

Title	Nanostructure materials based supercapattery for next generation pacemaker
Authors	Shao, Han
Publication date	2018
Original Citation	Shao, H. 2018. Nanostructure materials based supercapattery for next generation pacemaker. PhD Thesis, University College Cork.
Type of publication	Doctoral thesis
Rights	© 2018, Han Shao. - <a href="http://creativecommons.org/licenses/by-nc-nd/3.0/">http://creativecommons.org/licenses/by-nc-nd/3.0/</a>
Download date	2024-04-25 17:01:16
Item downloaded from	<a href="https://hdl.handle.net/10468/6907">https://hdl.handle.net/10468/6907</a>



DEPARTMENT OF CHEMISTRY  
NATIONAL UNIVERSITY OF IRELAND, CORK

# **NANOSTRUCTURE MATERIALS BASED SUPERCAPATTERY FOR NEXT GENERATION PACEMAKER**

A thesis submitted in accordance with the requirements for the degree of  
Doctor of Philosophy

**Han SHAO**

September 2018

Supervisor: Dr. Kafil M. Razeeb

Co-supervisor: Prof. Colm O'Dwyer



**Micro-Nano System Centre  
Tyndall National Institute  
Lee Malting, Dyke Parade, Cork Ireland**

## **Declaration**

This is to certify that the work I am submitting is my own and has not been submitted for another degree, either at University College Cork or elsewhere. All external references and sources are clearly acknowledged and identified within the contents. I have read and understood the regulations of University College Cork concerning plagiarism.

Han SHAO

## Abstract

With the rapid development of medical technology, implantable devices have been invented and widely used in many applications such as physiological monitoring, localized drug delivery, and biosensors. The artificial cardiac pacemaker, as one of the most important implantable medical devices, is used to stimulate the heart with electrical impulses in order to regulate heartbeats. Conventional rechargeable batteries are very expensive with limited cycle life and cannot be used in implantable applications due to their limited life cycle. Supercapattery is a new terminology to define the hybrid energy storage system, which combines the high energy-storage-capability of conventional batteries with the high power-delivery-capability of supercapacitors. With the benefit of combining battery-type material and capacitive material, supercapattery is able to obtain high energy from Faradaic redox reactions and high power from fast electron charge-transfer. Thereby, supercapattery has good electrical conductivity and a good capability to store huge amount of charges with long term stability compared to the conventional batteries. Consequently, supercapattery is an ideal hybrid energy storage device with superior storage capacity and long life, which can be employed in next-generation artificial cardiac pacemakers as a rechargeable energy source for the lifetime of the 20 years or more.

The aim of my PhD is to develop a supercapattery device based on novel nanostructured materials to store the energy from heartbeats through a piezoelectric device. Nickel foam with a porosity of 95% was used as substrate due to its high surface area to volume ratio and highly conductive 3D network architecture. By employing different hydrothermal processes, four different nanostructured materials including nickel oxide-indium oxide heterostructure, nickel phosphate nano/ microflakes, cobalt phosphate nano/ microflakes and cobalt phosphate nanoflake/ microflowers were synthesized. XRD, Raman, SEM, EDX, TEM, and XPS analysis were performed to characterize the morphology and structure of the materials. The electrochemical properties of the four synthesized electrode materials were investigated in a three electrode configuration in order to understand the charge-storage mechanism. Among these materials,  $\text{Co}_3(\text{PO}_4)_2$  nanoflake/ microflower material achieved a highest specific capacity of  $215.6 \text{ mAh g}^{-1}$  (equivalent to  $1990 \text{ F g}^{-1}$ ) with an excellent retention of 90.5% after 5000 charge-discharge cycles. In terms of complete devices, a symmetric and three asymmetric supercapatteries were assembled using synthesized electrode materials and activated carbon. Hybrid supercapattery assembled using cobalt phosphate as the positive and activated carbon as negative electrodes delivers a highest specific density of  $43.2 \text{ Wh kg}^{-1}$ . The initial capacity of the device dropped only 16% after first 20,000 cycles and even after 100,000 cycles, the device retained 68% of its initial capacity, which exhibited a long cyclability of 24 years. This device has been investigated under physiological conditions (25 - 45 °C) and showed stable electrochemical properties. Therefore, supercapattery fabricated from these materials can be a promising energy storage system for next generation pacemaker.

## Acknowledgements

First and foremost I would like to express my sincere gratitude to my supervisor Dr. Kafil M. Razeeb, and co-supervisor Prof. Colm O'Dwyer for their guidance, support, and encouragement throughout the entirety of my research. Their expertise in energy storage materials and electrochemical analysis have been a great source of inspiration for me.

I am very grateful to Dr. Alan O'Riordan for serving as my monitor on my graduate studies committee. He provided very fruitful discussion regarding my PhD progress and helpful guidance in the time management.

I am thankful to Dr. Padmanathan Narayanasamy, Dr. David McNulty, and Dr. Devendraprakash Gautam for sharing their valuable time and experience in guiding me with the important lab works.

I am also thankful to our colleagues in Tyndall, Dr. Giuseppe Alessio Vemi for training me XRD, Dr. Pierre Lovera for training me Raman, Mr. Vince Lodge for training me SEM, Mr. Donal O'Sullivan for package fabrication, Mr. Tony Compagno for the support on the fabrication process, and Ms. Orla Slattery for her support during my PhD study.

Lastly, I would like to thank Swatchith Lal, Dr. Xing Ouyang, Darragh Buckley, Jessie Doherty, Lin Lin, and other friends for their encouragement and friendship. I am also grateful to my parents and my husband Bo Yang and my other family members for their love, support, and encouragement throughout my PhD study.

## List of Publications

- A. **Han Shao**, N. Padmanathan, David McNulty, Colm O'Dwyer and Kafil M. Razeeb, Supercapattery based on binder-free  $\text{Co}_3(\text{PO}_4)_2 \cdot 8\text{H}_2\text{O}$  multilayer nano/microflakes on nickel foam. *ACS applied materials & interfaces*, 8, 28592–28598, (2016).
- B. N. Padmanathan, **Han Shao**, David McNulty, Colm O'Dwyer and Kafil M. Razeeb, Hierarchical NiO– $\text{In}_2\text{O}_3$  microflower (3D)/ nanorod (1D) hetero-architecture as a supercapattery electrode with excellent cyclic stability, *J. Mater. Chem. A*, 4, 4820–4830, (2016).
- C. N. Padmanathan, **Han Shao**, S. Selladurai, Colm Glynn, Colm O'Dwyer and Kafil M. Razeeb, Pseudocapacitance of  $\alpha\text{-CoMoO}_4$  nanoflakes in non-aqueous electrolyte and its bi-functional electro catalytic activity for methanol oxidation, *Int. J. Hydro. Energy*, 40, 16297-16305, (2015).
- D. N. Padmanathan, **Han Shao** and Kafil M. Razeeb. Multifunctional nickel phosphate nano/micro flakes 3D electrode for electrochemical energy storage, non-enzymatic glucose and sweat pH sensors, *ACS applied materials & interfaces*, (2018), DOI: 10.1021/acsami.7b17187
- E. **Han Shao**, N. Padmanathan, Kafil M. Razeeb, Robert Lynch, and Fernando M.F. Rhen, Issues in Environmental Science and Technology, Chapter 4 Energy Storage Options and Their Environmental Impacts, (2018). Accepted
- F. Mamun Jamal, Sumon Chakrabarty, **Han Shao**, David McNulty, Mohammad A Yousuf, Hidemitsu Furukawa, Ajit Khosla, Kafil M Razeeb, A non-enzymatic glutamate sensor based on nickel oxide nanoparticle, *Microsystem Technologies*, 1-7, (2017).
- G. **Han Shao**, Padman Narayanasamy, David McNulty, Colm O'Dwyer and Kafil M. Razeeb, Silver oxide-cobalt phosphate nanoparticle/ nanoflake as a high performance supercapattery electrode, 231st ECS Meeting, New Orleans, USA, May 28- Jun1, (2017).

- H. **Han Shao**, Padman Narayanasamy, David McNulty, Colm O'Dwyer and Kafil M. Razeeb, Supercapattery: A hybrid energy storage device for the next generation pacemaker, 2017 Smart System Integration, Cork, Ireland, Mar 8-9, (2017).
- I. **Han Shao**, Padman Narayanasamy, David McNulty, Colm O'Dwyer and Kafil M. Razeeb, Cobalt phosphate based supercapattery, 69<sup>th</sup> Irish Universities Chemistry Research Colloquium, Dublin, Ireland, June 22-23, (2017)
- J. **Han Shao**, Mamun Jamal, Sumon Chakrabarty, David McNulty, Mohammad A. Yousuf and Kafil M. Razeeb, Non-enzymatic glutamate sensor based on nickel oxide nanoparticle, 231st ECS Meeting, New Orleans, USA, May 28- Jun1, (2017).
- K. Mamun Jamal, Apu K. Dutta, Juel Islam, **Han Shao**, Mohammad A. Yousuf and Kafil M. Razeeb, Disposable chlorine sensor based on pencil graphite electrode, 231st ECS Meeting, New Orleans, USA, May 28- Jun1, (2017).
- L. Mamun Jamal, Irani Akhter, **Han Shao**, Mohammad A. Yousuf and Kafil M. Razeeb, Development of WO<sub>3</sub> nanoparticle based pH sensor, 231st ECS Meeting, New Orleans, USA, May 28- Jun1, (2017).
- M. Junaid U. Ahmed, **Han Shao**, Mohammad A. Yousuf, Kafil M. Razeeb, Mamun Jamal, Hydrothermal synthesis of metal oxide (NiO, CuO, ZnO and WO<sub>3</sub>) nanoparticles and their antimicrobial properties, 231st ECS Meeting, New Orleans, USA, May 28- Jun1, (2017).
- N. N. Padmanathana, **Han Shao**, S. Selladurai, Colm O'Dwyer and Kafil M. Razeeb, Design of  $\alpha$ -CoMoO<sub>4</sub> nanoflakes on carbon cloth and investigation of their pseudocapacitance in non-aqueous electrolyte and electro-oxidation of methanol, 227th ECS Meeting, Chicago, USA, May 24-28, (2015).

## List of Figures

**Figure 1.1** Wireless implanted medical devices.

**Figure 1.2** Schematic of the next generation leadless pacemaker (Sorin Copyrights used with permission).

**Figure 1.3** Current pacemaker vs. future leadless pacemaker.

**Figure 1.4** Schematic diagram of the different reaction mechanisms of lithium ion batteries.

**Figure 1.5** Schematic diagram of the supercapacitor working process and relative parameters.

**Figure 1.6** Schematic diagram of the supercapattery structure.

**Figure 1.7** Schematic illustration of selecting and pairing various electrodes to assemble different types of energy storage devices.

**Figure 1.8** Classification of energy storage devices with various selection and pairing of same or different electrodes.

**Figure 2.1** Schematic of heterogeneous nanostructures based on (a) 0D, (b) 1D, (c) 2D, and (d) 3D nanostructures.

**Figure 2.2** Electron microscopy images of high surface area carbon materials (a) activated carbon, (b) graphene, (c) carbon nanotubes, and (d) graphene sheets- carbon nanotubes.

**Figure 2.3** FESEM images of (a) the pristine CNTs, (b) the flower-like  $\text{MnO}_2$  powder, and (c-d) the  $\text{MnO}_2/\text{CNT}$  nanocomposite at different magnifications.

**Figure 2.4** Cyclic voltammograms of (a) NiO film electrode at different scan rates in 1 M KOH aqueous solution, (b) NiO/CFC nanostructure at different scan rates in 1 M TEABF<sub>4</sub>/PC organic electrolyte.

**Figure 2.5** Different nanostructured cobalt oxide materials.

**Figure 2.6** (a) SEM image of  $\text{FeCo}_2\text{O}_4$ -Nanoflowers on nickel foam after calcination at 400 °C for 2 h in air, (b) SEM image of  $\text{NiCo}_2\text{O}_4$  nanosheets after calcination at 200 °C for 3 h in air, (c) SEM image of  $\text{NiCo}_2\text{O}_4$  nanoflowers (d) SEM image of  $\text{CoMoO}_4$

nanoflakes structure on carbon fibre cloth.

**Figure 2.7** SEM images of (a) nickel phosphate nanoparticles, (b) nickel phosphate nanoflakes, (c) cobalt phosphate nanoflowers, and (d) cobalt phosphate nanorods.

**Figure 2.8** Approximate range of average discharge potentials and specific capacity of some of the conversion-type cathodes.

**Figure 3.1** Digital photograph of NiO, NiO-In<sub>2</sub>O<sub>3</sub> (1:2) and In<sub>2</sub>O<sub>3</sub> grown on NF substrate.

**Figure 3.2** Schematic description NiO-In<sub>2</sub>O<sub>3</sub> hybrid structure growth process with the corresponding SEM images.

**Figure 3.3** (a-f) SEM images of NiO-In<sub>2</sub>O<sub>3</sub>-NF (1:2) hybrid structure captured at different time of growth 3 h (a & b), 6 h (c & d) and 9 h (e & f).

**Figure 3.4** SEM images of pure NiO-NF (a and b) and pure In<sub>2</sub>O<sub>3</sub>-NF (c and d). EDX spectrum of (e) pure NiO-NF and (f) Pure In<sub>2</sub>O<sub>3</sub>-NF.

**Figure 3.5** (a-i) SEM images of NiO-In<sub>2</sub>O<sub>3</sub>-NF composites at various concentration of Ni and In, (a-c) 1:1, (d-f) 1:2 and (g-i) 2:1 at different magnifications.

**Figure 3.6** XRD patterns of NiO-In<sub>2</sub>O<sub>3</sub>-NF (1:2) hybrid structure before and after calcination at 400 °C for 2 h.

**Figure 3.7** (a) XRD pattern of pure NiO-NF and In<sub>2</sub>O<sub>3</sub>-NF with their stand JCPDS patterns and (b) XRD pattern of NiO-In<sub>2</sub>O<sub>3</sub>-NF composites prepared using different Ni/In concentrations.

**Figure 3.8** Raman spectra of pure NiO-NF, In<sub>2</sub>O<sub>3</sub>-NF and NiO-In<sub>2</sub>O<sub>3</sub>-NF composites with different concentrations.

**Figure 3.9** (a-d) SEM images of NiO-In<sub>2</sub>O<sub>3</sub>-NF (1:2) hybrid structure at different magnifications.

**Figure 3.10** (a-d) 45° tilted angle SEM images of NiO-In<sub>2</sub>O<sub>3</sub>-NF (1:2) hybrid structure.

**Figure 3.11** EDX spectrum of NiO-In<sub>2</sub>O<sub>3</sub>-NF hybrid composite at various concentration of Ni:In (a and b) 1:1, (c and d) 1:2, and (e and f) 2:1 scanned at different regions. The observed Cu peak was due to the copper tape used to attach the samples to the sample holder.

**Figure 3.12** Elemental mapping spectrum of NiO-In<sub>2</sub>O<sub>3</sub>-NF (1 : 2) hybrid composite

scanned at different regions.

**Figure 3.13** HRTEM images of (a) NiO-In<sub>2</sub>O<sub>3</sub> (1:2) hybrid structure, (b) nanorod region and (c) corresponding SAED pattern. (d) and (e) flower/ flakes region and (f) corresponding SAED pattern.

**Figure 3.14** (a-c) XPS spectra of pure and NiO-In<sub>2</sub>O<sub>3</sub> hybrid structure prepared at various concentrations.

**Figure 3.15** Digital photograph of Co<sub>3</sub>(PO<sub>4</sub>)<sub>2</sub>·8H<sub>2</sub>O grown on NF substrate prepared using different concentrations (2.5 mM, 5 mM, 10 mM and 20 mM).

**Figure 3.16** (a-b) SEM images with EDX analysis as inset of H<sub>2</sub>O/NF, PO<sub>4</sub>/NF samples, (c-d) SEM images of scratched Co<sub>3</sub>(PO<sub>4</sub>)<sub>2</sub>·8H<sub>2</sub>O/NF samples.

**Figure 3.17** (a-b) XRD pattern and Raman spectra of PO<sub>4</sub>/NF sample.

**Figure 3.18** (a) XRD pattern, (b) Raman spectra of pure nickel foam and 2.5 mM Co<sub>3</sub>(PO<sub>4</sub>)<sub>2</sub>·8H<sub>2</sub>O/NF nano/ microstructure, (c) XRD pattern of 2.5 mM, 5 mM, 10 mM and 20 mM Co<sub>3</sub>(PO<sub>4</sub>)<sub>2</sub>·8H<sub>2</sub>O/NF nano/ microstructure.

**Figure 3.19** (a-d) SEM images of 2.5 mM Co<sub>3</sub>(PO<sub>4</sub>)<sub>2</sub>·8H<sub>2</sub>O/NF nano/ microflakes at different magnifications (e) Elemental mapping spectrum of Co<sub>3</sub>(PO<sub>4</sub>)<sub>2</sub>·8H<sub>2</sub>O/NF nano/ microstructure scanned at different flake-powder. (f) Different magnification SEM images of 2.5 mM, 5 mM, 10 mM and 20 mM Co<sub>3</sub>(PO<sub>4</sub>)<sub>2</sub>·8H<sub>2</sub>O/NF nano/ microflakes.

**Figure 3.20** (a-c) HRTEM images of Co<sub>3</sub>(PO<sub>4</sub>)<sub>2</sub>·8H<sub>2</sub>O multilayer structure, (d) corresponding SAED pattern, (e) HRTEM image of Co<sub>3</sub>(PO<sub>4</sub>)<sub>2</sub>·8H<sub>2</sub>O at high magnification with particle analysis.

**Figure 3.21** (a-d) Ni2p, Co2p, O1s and P2p XPS spectra of pure nickel foam and Co<sub>3</sub>(PO<sub>4</sub>)<sub>2</sub>·8H<sub>2</sub>O/NF.

**Figure 3.22** (a) XRD and (b) Raman spectra of Ni<sub>3</sub>(PO<sub>4</sub>)<sub>2</sub>·8H<sub>2</sub>O/NF nano/ microflakes.

**Figure 3.23** (a-b) SEM images of Ni<sub>3</sub>(PO<sub>4</sub>)<sub>2</sub>·8H<sub>2</sub>O/NF captured at different magnifications, (c) HRTEM image of Ni<sub>3</sub>(PO<sub>4</sub>)<sub>2</sub>·8H<sub>2</sub>O nano/ microflakes, (d) Individual flake consists of pores, (e) Measured lattice space in layered flakes, and (f) the corresponding SAED pattern.

**Figure 3.24** EDS spectrum of Ni<sub>3</sub>(PO<sub>4</sub>)<sub>2</sub>·8H<sub>2</sub>O nano/ microflakes and their corresponding elemental composition.

**Figure 3.25** (a-d) XPS survey and core level XPS spectra of nickel phosphate multilayer nano/ microflakes.

**Figure 3.26** Digital photograph of  $\text{Co}_3(\text{PO}_4)_2$  grown on NF substrate before (left) and after (right) annealing.

**Figure 3.27** SEM images of 2, 4 and 8 hours growth at different magnifications. (d,h,l) schematic of growth process.

**Figure 3.28** Growth process identification by EDX mapping. (a) Phase distinguishable elemental mapping for 2h sample; (b-e) EDX elemental mapping for Co, P, O, Ni elements; (f-j), (k-o) and (p-t) are corresponding results for 4, 6 and 8h samples, respectively.

**Figure 3.29** (a) XRD patterns of cobalt phosphate electrode before and after annealing, (b) Raman spectra of cobalt phosphate electrode.

**Figure 3.30** (a) SEM images of cobalt phosphate electrode at different magnifications, (b) EDX analysis of cobalt phosphate electrode, (c) TEM image (1) and SAED pattern (2) of cobalt phosphate electrode.

**Figure 3.31** (a-d) Ni2p, O1s, P2p and Co2p XPS spectra of CP/NF.

**Figure 4.1** CV curves of bare NF before (black) and after (red) acid treatment measured at  $10 \text{ mV s}^{-1}$ .

**Figure 4.2** (a-b) SEM images and (c) EDX analysis of NOH/NF sample.

**Figure 4.3** (a-b) Ni2p and O1s XPS spectra of NOH/NF; (c) charge-discharge curves of NOH/NF sample at current density of  $5 \text{ mA cm}^{-2}$ .

**Figure 4.4** (a) Cyclic voltammograms of individual oxides and NiO-In<sub>2</sub>O<sub>3</sub>-NF hybrid oxides measured at  $10 \text{ mVs}^{-1}$  in 3 M KOH. (b) Scan rate dependent cyclic voltammograms of NiO-In<sub>2</sub>O<sub>3</sub>-NF (1:2) hybrid electrode. (c) Charge-discharge profile of NiO-In<sub>2</sub>O<sub>3</sub>-NF (1:2) hybrid structure (d) Cyclic stability of NiO-In<sub>2</sub>O<sub>3</sub>-NF (1:2) at  $20 \text{ A g}^{-1}$  and the inset represents the cyclic stability curves of pristine oxides.

**Figure 4.5** Variation of specific capacitance with respect current density for NiO-In<sub>2</sub>O<sub>3</sub>-NF (1:2) hybrid electrode in both three and two electrode configurations.

**Figure 4.6** Charge-discharge curves of (a) NiO-NF and (b) In<sub>2</sub>O<sub>3</sub>-NF at various current densities.

**Figure 4.7** Nyquist plot of In<sub>2</sub>O<sub>3</sub>-NF, NiO-NF and NiO-In<sub>2</sub>O<sub>3</sub>-NF electrode measured at 3 M KOH in three electrode configuration.

**Figure 4.8** Charge-discharge curves of (a) NiO-In<sub>2</sub>O<sub>3</sub>-NF (1:1) composite and (b) NiO-In<sub>2</sub>O<sub>3</sub>-NF (2:1) composite at various current densities.

**Figure 4.9** (a) Cyclic voltammograms of nickel foam, 2.5, 5, 10 and 20 mM Co<sub>3</sub>(PO<sub>4</sub>)<sub>2</sub>·8H<sub>2</sub>O/NF at a scan rate of 2 mV/s in 1 M NaOH. (b) Cyclic voltammograms of 5 mM Co<sub>3</sub>(PO<sub>4</sub>)<sub>2</sub>·8H<sub>2</sub>O/NF at different scan rate from 1 to 50 mV/s. (c-f) Discharge profile of 2.5, 5, 10 and 20 mM samples at different current densities.

**Figure 4.10** Nyquist plot for 2.5, 5, 10 and 20 mM Co<sub>3</sub>(PO<sub>4</sub>)<sub>2</sub>·8H<sub>2</sub>O/NF.

**Figure 4.11** (a) Cyclic voltammograms of 2.5 mM Co<sub>3</sub>(PO<sub>4</sub>)<sub>2</sub>·8H<sub>2</sub>O/NF at different scan rate from 1 to 50 mV/s in 1 M NaOH. (b) Charge-discharge profile of the electrode at different current densities. (c) Specific capacitance and capacity variation at different current densities. (d) Cyclic stability of the electrode. Inset represents continuous charge-discharge profile at 20 mA cm<sup>-2</sup>.

**Figure 4.12** Specific capacitance as a function of applied current densities for 2.5, 5, 10 and 20 mM samples.

**Figure 4.13** (a-b) SEM images of Co<sub>3</sub>(PO<sub>4</sub>)<sub>2</sub>·8H<sub>2</sub>O/NF electrode after 1000 charge-discharge cycles.

**Figure 4.14** (a) Cyclic voltammogram of Ni<sub>3</sub>(PO<sub>4</sub>)<sub>2</sub>·8H<sub>2</sub>O nano/ microflakes electrode at different scan rates of 2 – 100 mVs<sup>-1</sup>, (b) Charge-discharge profile at various applied current of 5 – 50 mAcm<sup>-2</sup>, (c) Cyclic stability of the electrode at 20 mAcm<sup>-2</sup> and inset represents the continuous charge discharge curve, (d) Nyquist plot of the electrode before and after 10,000 charge-discharge cycles and the corresponding equivalent circuit (inset).

**Figure 4.15** (a) Cyclic voltammograms of NF and CP/NF samples at a scan rate of 10 mV/s in 3.0 M KOH, (b) charge-discharge curves of NF and CP/NF samples at current density of 5 mA cm<sup>-2</sup>.

**Figure 4.16** (a) Cycle voltammograms, (b) plot of forward anodic peak current density and the square root of the scan rate, (c) the plot of log peak currents (I<sub>pa</sub>) against the log scan rate (v), (d) the plot of peak voltage vs. ln scan rate for CP/NF in three electrode

system, (e) raising part of CV curve of the cobalt phosphate electrode at different scan rates and the corresponding Tafel plot (f).

**Figure 4.17** (a) charge-discharge profiles and (b) cyclic stability of the cobalt phosphate electrode in three electrode system.

**Figure 5.1** Schematic of sandwich-type supercapattery ( $1 \times 1 \times 0.2 \text{ cm}^3$ ).

**Figure 5.2** (a) Cyclic voltammograms of symmetric supercapacitor fabricated with NiO-In<sub>2</sub>O<sub>3</sub>-NF (1:2) hybrid structure at different scan rates in 3 M KOH; (b) Charge-discharge curves of NiO-In<sub>2</sub>O<sub>3</sub>-NF (1:2) based symmetric supercapacitor at various current densities; (c) Cyclic stability of the symmetric supercapacitor and inset represents continuous charge-discharge profile at  $10 \text{ A g}^{-1}$ ; (d) Capacity retention and coulombic efficiency of the device at different current density.

**Figure 5.3** Cyclic voltammograms of NiO-In<sub>2</sub>O<sub>3</sub>-NF (1:2) based symmetric supercapacitor at high scan rates.

**Figure 5.4** (a-d) SEM images of NiO-In<sub>2</sub>O<sub>3</sub>-NF (1:2) electrode after 50,000 charge-discharge cycles.

**Figure 5.5** First few charge-discharge cycles of NiO-In<sub>2</sub>O<sub>3</sub>-NF (1:2) based symmetric supercapacitor measured before (black line) and after (red line) 1000 cycles at different current density (a)  $2 \text{ A g}^{-1}$ , (b)  $4 \text{ A g}^{-1}$ , (c)  $6 \text{ A g}^{-1}$  and (d)  $8 \text{ A g}^{-1}$ .

**Figure 5.6** (a) Cyclic voltammograms of NiO-In<sub>2</sub>O<sub>3</sub>-NF symmetric cell at different potential range and (b) the stable potential window of the device with respect to reference electrode.

**Figure 5.7** Ragone plot for NiO-In<sub>2</sub>O<sub>3</sub>-NF (1:2) based symmetric supercapacitor.

**Figure 5.8** NiO-In<sub>2</sub>O<sub>3</sub>-NF (1:2) based symmetric supercapacitor connected in series and their practical application of LED lighting.

**Figure 5.9** Nyquist plot for NiO-In<sub>2</sub>O<sub>3</sub>-NF (1:2) based symmetric supercapacitor before and after 50,000 cycles. Inset on the left is the equivalent circuit and inset on the right is showing the expanded view of the high frequency region.

**Figure 5.10** (a) Cyclic voltammograms of activated carbon at different scan rates in 1 M NaOH. (b) Charge-discharge curves of activated carbon at different current in 1 M NaOH. (c) Cyclic voltammograms of  $2.5 \text{ mM Co}_3(\text{PO}_4)_2 \cdot 8\text{H}_2\text{O}/\text{NF}$  and activated

carbon in a three electrode system where saturated calomel electrode (SCE) was used as a reference electrode (scan rate: 2 mV/s).

**Figure 5.11** (a) Cyclic voltammograms of the  $\text{Co}_3(\text{PO}_4)_2 \cdot 8\text{H}_2\text{O} // \text{AC}$  hybrid supercapattery at different scan rates in 1 M NaOH. (b) Charge-discharge curves of supercapattery at different current densities. (c) Cyclic stability of supercapattery. Inset represents continuous charge-discharge profile at  $20 \text{ mA cm}^{-2}$  (d) Ragone plots of supercapattery.

**Figure 5.12** Specific capacitance as a function of applied current densities for hybrid supercapattery.

**Figure 5.13** Nyquist plot for  $\text{Co}_3(\text{PO}_4)_2 \cdot 8\text{H}_2\text{O} // \text{AC}$  hybrid supercapattery before and after 1000 cycles.

**Figure 5.14** CV curves of AC/NF and  $\text{Ni}_3(\text{PO})_4 \cdot 8\text{H}_2\text{O} / \text{NF}$  at  $10 \text{ mV s}^{-1}$  in 1 M NaOH.

**Figure 5.15** (a) Cyclic voltammogram of  $\text{Ni}_3(\text{PO}_4)_2 \cdot 8\text{H}_2\text{O} / \text{NF} || \text{AC} / \text{NF}$  supercapattery at different scan rates of  $10 - 100 \text{ mVs}^{-1}$ , (b) Charge-discharge profile for the device at different specific current of  $2.5 - 20 \text{ mA cm}^{-2}$ , (c) Cyclic stability and coulombic efficiency of the device at  $10 \text{ mA cm}^{-2}$  and inset represents the corresponding charge discharge profile, (d) Ragone plot related to the specific energy and power of the device.

**Figure 5.16** Nyquist Plot of  $\text{Ni}_3(\text{PO})_4 \cdot 8\text{H}_2\text{O} / \text{NF} || \text{AC} / \text{NF}$  supercapattery before and after 10,000 charge-discharge cycles.

**Figure 5.17** Cyclic voltammograms of CP/NF and activated carbon in a three electrode system where saturated calomel electrode (SCE) was used as a reference electrode (scan rate: 10 mV/s).

**Figure 5.18** (a) Cycle voltammograms, (b) charge-discharge profiles and (c) cyclic stability of the CP/NF // AC/NF supercapattery.

**Figure 5.19** (a) SEM and EDX images of cobalt phosphate electrode after 20,000 charge-discharge cycles, (b) SEM and EDX images of cobalt phosphate electrode after 100,000 charge-discharge cycles, (c) XRD patterns of cobalt phosphate electrode after 100,000 charge-discharge cycles.

**Figure 5.20** (a) 3D gravimetric Ragone plots of the supercapattery and comparison with other works, the z-axis indicates the charge-discharge cycles reported for each device

and the colour-gradient map, (b) volumetric Ragone plots of the CP/NF//AC/NF supercapattery and comparison with other energy devices.

**Figure 5.21** Cobalt phosphate based hybrid supercapatteries connected in series and the application of LED lighting.

**Figure 5.22** (a) self-discharge curves of supercapattery at different temperature from 25 °C to 45 °C, (b) Plot of forward anodic peak current density and the square root of the scan rate for CP/NF at different temperature from 25 °C to 45 °C in three electrode system, (c-d) discharge curve (at 40 mA cm<sup>-2</sup>) and Nyquist plots of the hybrid device at different temperature from 25 °C to 45 °C.

**Figure 5.23** (a) Plot of forward anodic peak current density and the square root of the scan rate for CP/NF at different temperature from 25 °C to 45 °C in three electrode system, (b) plot of forward anodic peak current density and the square root of the scan rate for AC/NF at different temperature from 25 °C to 45 °C in three electrode system.

## List of Tables

**Table 2.1** Electrochemical performance of activated carbons in the earlier reports.

**Table 2.2** Electrochemical performance of carbon nanotubes in the earlier reports.

**Table 2.3** Electrochemical performance of graphene electrode in the earlier reports.

**Table 2.4** Electrochemical performance of ion capacitors in the earlier reports.

**Table 2.5** Comparison of electrochemical performance for different metal phosphate based electrode in three electrode configuration.

**Table 2.6** Comparison of ion capacitor and supercapattery.

**Table 3.1** Parameters of the fabricated nanostructured materials.

**Table 4.1** Electrochemical performances of fabricated materials in different electrolytes.

**Table 4.2** Comparison of electrochemical performance for different hetero-composite electrodes in three electrode configuration.

**Table 4.3** Comparison of electrochemical performance for different metal phosphate based electrode in three electrode configuration.

**Table 4.4** Comparison of electrochemical performance for fabricated phosphate based electrode and other nickel or/ and cobalt oxide based electrode in three electrode configuration.

**Table 5.1** Electrochemical characteristics of the assembled supercapatteries.

**Table 5.2** Comparison of electrochemical performance for various metal-phosphate based asymmetric cell.

# TABLE OF CONTENTS

<b>DECLARATION</b> .....	<b>I</b>
<b>ABSTRACT</b> .....	<b>II</b>
<b>ACKNOWLEDGEMENTS</b> .....	<b>III</b>
<b>LIST OF PUBLICATIONS</b> .....	<b>IV</b>
<b>LIST OF FIGURES</b> .....	<b>VI</b>
<b>LIST OF TABLES</b> .....	<b>XIV</b>
<b>TABLE OF CONTENTS</b> .....	<b>XV</b>
<b>CHAPTER 1 BACKGROUND AND MOTIVATION</b> .....	<b>1</b>
1.1    EVOLUTION OF IMPLANTABLE MEDICAL DEVICES.....	1
1.2    CLASSIFICATION OF ENERGY STORAGE DEVICES .....	4
1.2.1    Similarities and Differences between Batteries, Supercapacitors and Supercapatteries. ....	5
1.2.2    Classification of Supercapattery.....	13
1.3    RESEARCH OBJECTIVES .....	15
1.4    THESIS OUTLINE.....	16
<b>CHAPTER 2 DEVELOPMENT TRENDS OF SUPERCAPATTERY ELECTRODE MATERIALS</b> .....	<b>19</b>
2.1    INTRODUCTION .....	19
2.2    CAPACITIVE MATERIALS.....	20
2.2.1    Activated carbon .....	21
2.2.2    Carbon nanotubes.....	22
2.2.3    Graphene.....	23
2.2.4    Carbon based material composites .....	25
2.3    PSEUDOCAPACITIVE MATERIALS .....	27
2.4    BATTERY-TYPE MATERIALS .....	28
2.5    PSEUDO-BATTERY-TYPE MATERIALS .....	30
2.5.1    Metal oxide based materials .....	31
2.5.2    Metal phosphate based materials.....	35
2.5.3    Other materials .....	38
2.6    SUPERCAPATTERY PERFORMANCES.....	39
2.6.1    Selection of Electrode Materials and Electrolytes .....	40
2.6.2    Comparison of Different Types of Supercapatteries.....	40
2.7    PROSPECTS AND FUTURE .....	41
<b>CHAPTER 3 FABRICATION AND MATERIAL CHARACTERIZATION</b> .....	<b>43</b>
3.1    INTRODUCTION .....	43
3.2    NiO-IN <sub>2</sub> O <sub>3</sub> MICROFLOWER (3D)/ NANOROD (1D) HETERO-ARCHITECTURE ON NICKEL FOAM	
44	

3.2.1	Synthesis and growth mechanism .....	44
3.2.2	Structure Analysis (XRD and Raman).....	50
3.2.3	Morphology under SEM and TEM.....	53
3.2.4	XPS analysis .....	58
3.3	$\text{CO}_3(\text{PO}_4)_2 \cdot 8\text{H}_2\text{O}$ MULTILAYER NANO/ MICROFLAKES ON NICKEL FOAM.....	61
3.3.1	Synthesis and growth mechanism .....	61
3.3.2	Structure Analysis (XRD and Raman).....	65
3.3.3	Morphology under SEM and TEM.....	66
3.3.4	XPS Analysis.....	68
3.4	$\text{Ni}_3(\text{PO}_4)_2 \cdot 8\text{H}_2\text{O}$ 3D NANO/ MICRO FLAKES ON NF .....	70
3.4.1	Synthesis and growth mechanism .....	70
3.4.2	Structure Analysis (XRD and Raman).....	71
3.4.3	Morphology under SEM and TEM.....	72
3.4.4	XPS Analysis.....	74
3.5	$\text{CO}_3(\text{PO}_4)_2 \cdot 8\text{H}_2\text{O}$ NANOFLAKES/ MICROFLOWER ON NF .....	75
3.5.1	Synthesis and growth mechanism .....	75
3.5.2	Structure Analysis (XRD and Raman).....	78
3.5.3	Morphology under SEM and TEM.....	79
3.5.4	XPS Analysis.....	80
3.6	CONCLUSION .....	81
<b>CHAPTER 4 ELECTROCHEMICAL PERFORMANCES OF MATERIALS .....</b>		<b>83</b>
4.1	INTRODUCTION .....	83
4.2	ELECTROCHEMICAL PERFORMANCE OF NICKEL FOAM.....	85
4.3	ELECTROCHEMICAL PERFORMANCE OF NiO-IN <sub>2</sub> O <sub>3</sub> /NF HETERO-MICROFLOWER.....	88
4.4	ELECTROCHEMICAL PERFORMANCE OF $\text{CO}_3(\text{PO}_4)_2 \cdot 8\text{H}_2\text{O}$ /NF NANOFLAKES .....	96
4.5	ELECTROCHEMICAL PERFORMANCE OF $\text{Ni}_3(\text{PO}_4)_2 \cdot 8\text{H}_2\text{O}$ /NF NANOFLAKES .....	103
4.6	ELECTROCHEMICAL PERFORMANCE OF $\text{CO}_3(\text{PO}_4)_2$ /NF NANOFLAKES/MICROFLOWER STRUCTURE .....	106
4.7	CONCLUSION .....	112
<b>CHAPTER 5 ELECTROCHEMICAL PERFORMANCES OF DEVICES .....</b>		<b>115</b>
5.1	INTRODUCTION .....	115
5.2	NiO-IN <sub>2</sub> O <sub>3</sub> /NF SYMMETRIC SUPERCAPATTERY .....	117
5.3	$\text{CO}_3(\text{PO}_4)_2 \cdot 8\text{H}_2\text{O}$ /NF HYBRID SUPERCAPATTERY.....	125
5.4	$\text{Ni}_3(\text{PO}_4)_2 \cdot 8\text{H}_2\text{O}$ /NF HYBRID SUPERCAPATTERY .....	130
5.5	$\text{CO}_3(\text{PO}_4)_2$ /NF SUPERCAPATTERY .....	133
5.5.1	Supercapattery performance .....	133
5.5.2	Self-discharge avoidance in pacemaker supercapattery.....	139
5.5.3	Operation under physiological conditions (25 - 45 °C).....	140
5.6	CONCLUSION .....	142
<b>CHAPTER 6 CONCLUSIONS AND FUTURE WORK.....</b>		<b>143</b>
6.1	THESIS SUMMARY AND MAIN RESULTS .....	143
6.2	RECOMMENDATIONS FOR FUTURE WORK.....	146

6.2.1	Development of Novel Materials .....	146
6.2.2	Optimization of the Complete Supercapattery Cell.....	146
<b>BIBLIOGRAPHY.....</b>		<b>148</b>

# Chapter 1 Background and Motivation

## 1.1 Evolution of Implantable Medical Devices

Global average life expectancy has risen to 71.5 years over the period 2010–2015, consequently, the number of age-related diseases has also increased. Therefore, treatment techniques such as implants, prostheses and long-term pharmaceutical usage have drawn much attention in the scientific and medical industries. In particular, implanted medical devices (IMDs), including implantable neuro-stimulators, cochlear implants, artificial cardiac pacemakers, gastric electrical stimulators, insulin pumps and foot-drop implants, are being used in many different parts of the body for various applications as shown in Figure 1.1.

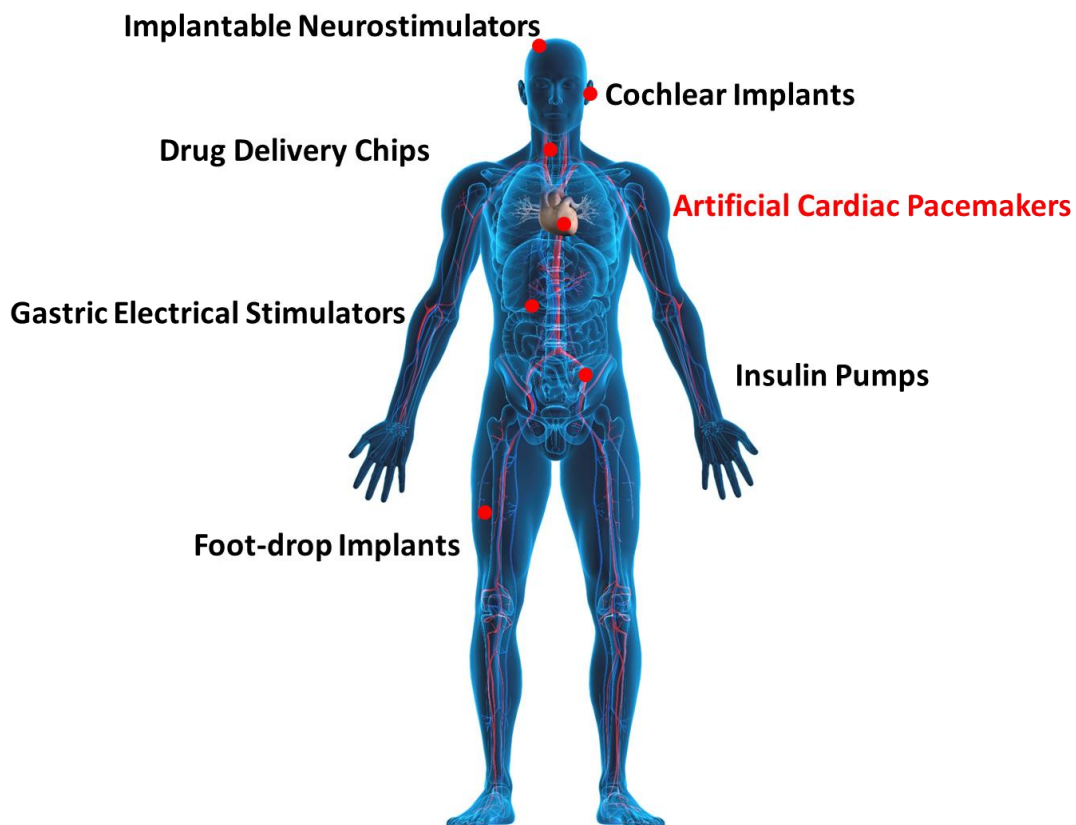


**Figure 1.1** Wireless implanted medical devices.

In the past decade, wireless sensor networks and communication technologies have become an intrinsic part of many IMDs for in-home monitoring and diagnosis. At present, existing medical equipment is able to monitor diabetes and chronic heart failure patients' vital signs remotely and devices to track chronic kidney diseases and lung diseases are under development. Ultimately, adding a wireless system to IMDs will improve the medical treatment services and lead to a better health care system<sup>1</sup>. Further to this, the miniaturization of IMDs is another crucial challenge. The size and shape of the IMDs are restricted by the implantation spot in the human body. In order to meet the miniaturization requirement, further advances in low power design techniques, integrated circuits, system optimization, packaging, and power source are desired.<sup>2</sup>

In particular, approximately 300,000 IMDs are implanted in U.S. every year, and two-thirds of them are artificial cardiac pacemakers.<sup>3,4</sup> The artificial cardiac pacemaker is used to stimulate the heart effectively with electrical impulses in order to regulate heartbeats, and are powered by batteries. Since its invention, pacemaker technology has grown immensely and continuously developed over the last 50 years. These devices are currently powered by Li-batteries. The average pacemaker lithium battery has about 0.5-2 Ah of storage capacity<sup>5</sup> and an estimated life of around 6 to 11 years<sup>6</sup>. Recently, the micra<sup>TM</sup> transcatheter pacing system has been developed with an expected battery longevity of 12 years.<sup>7</sup> Due to the toxicity and uncontrolled environmental issues of lithium and to exclude patients from unnecessary injury by battery-replacement surgery, researchers are now working on different types of self-powered or self-rechargeable energy sources for pacemakers, such as generating electricity from glucose<sup>8</sup>, heart movement<sup>9</sup>, radioactive material<sup>10</sup>, etc. to recharge the battery. However, the power source for self-rechargeable pacemakers remains the biggest challenge for developers and manufacturers. In the development of a leadless pacemaker, inserted inside the right ventricular of the heart, the power source cannot be replaced and should ideally last for 20 years or more.

Silicon-based piezoelectric devices have been proposed to generate electrical power

from the mechanical energy of heartbeats to operate the pacemaker<sup>11</sup>, where the electrical energy is stored using a battery to power the electronics of the pacemaker, and to deliver the electrical impulses during emergency. However, the state of the art rechargeable Li-ion battery cyclability is limited to only 1,000+ cycles<sup>12</sup> which is far from the requirement to be recharged for more than 10 years lifetime<sup>6</sup> (or at least 20,000 cycles) without loss of power, which is a significant health issue for a pacemaker. This then poses a significant concern for the long term operation of a pacemaker and the safety of the recipient. For a pacemaker energy source, intermittent needs for fast charge or discharge kinetics are required, often in emergency situations but without loss of power. Typically, the higher voltage battery ‘component’ is kinetically more sluggish than the higher rate capacitor, which the hybrid supercapattery addresses directly. Therefore, the development of a new type of energy storage device is necessary with enhanced cyclability and storage capacity for the next generation leadless pacemakers.

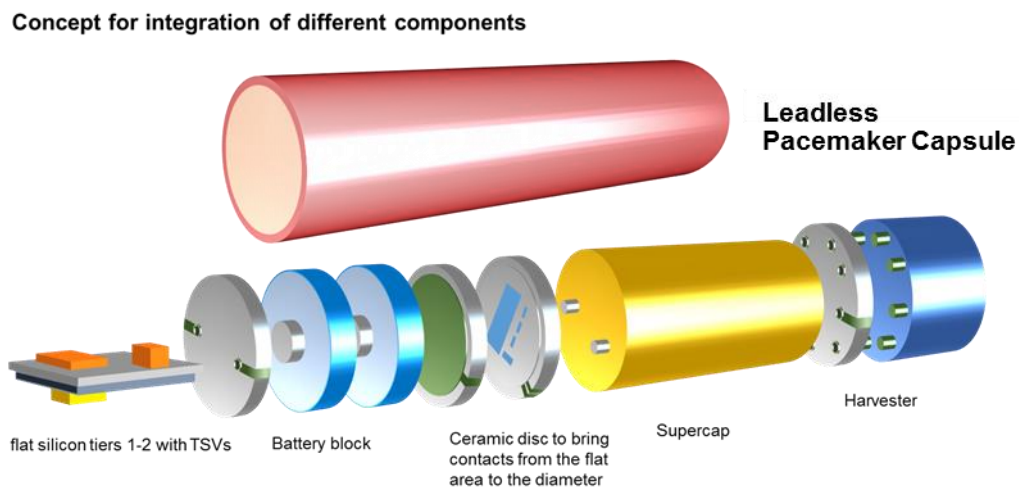


**Figure 1.2** Schematic of the next generation leadless pacemaker (Sorin Copyrights used with permission).

In addition, the typical size of a pacemaker is  $\sim 46 \text{ mm} \times 52 \text{ mm} \times 6 \text{ mm}$ ,<sup>6</sup> and the energy storage device usually occupies 2/3 of this volume. For the next generation leadless pacemaker, it is necessary to reduce the average size of the energy storage device considerably (6 mm diameter  $\times$  15 mm height) with a cell voltage of 2.8 V.<sup>6</sup>

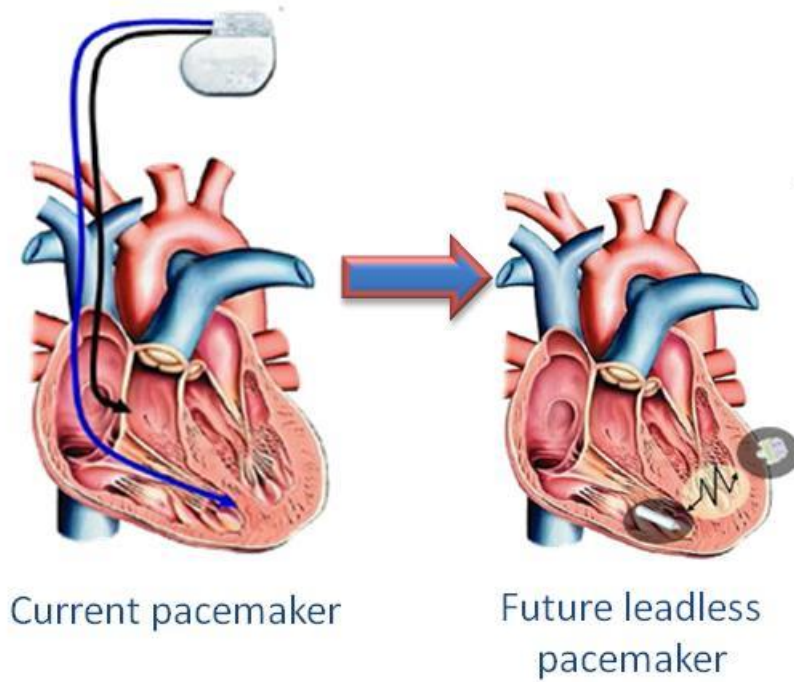


**Figure 1.3** Current pacemaker vs. future leadless pacemaker.<sup>13</sup>

In general, conventional rechargeable batteries are very expensive with limited cycle life and cannot be used in implantable applications due to their limited life cycle. The supercapattery is a device that combines the high power capacity and short charging/discharging times of a supercapacitor with the greater energy density of batteries and is therefore an attractive power source for next generation self-rechargeable pacemakers. Consequently, this hybrid device has attracted the attention of biomedical industries as an ideal alternative rechargeable power source replacing current battery technology. With high energy density, the device should be able to provide enough power during cardiac emergency, which requires good stability once fully charged. Therefore, supercapatteries are a promising power source for a number of implanted medical devices requiring fast charging/discharging, good capacity and ultra-long cycle life.

## **1.2 Classification of energy storage devices**

With increasing levels of fossil fuel consumption and rising global pollution, alternative

energy storage devices such as fuel cells, chemical batteries, supercapacitors, and supercapatteries have been the focus of a great deal of research over recent decades. Samsung launched a new smartphone called Galaxy S9 which contains a battery that can be fully charged in twelve minutes<sup>14</sup>. Coincidentally, a team in Stanford developed an ultrafast rechargeable aluminium-ion battery which can be charged in only one minute with a specific capacity of  $70 \text{ mA h g}^{-1}$ , and able to withstand more than 7,500 cycles without decay.<sup>15</sup> Compared to the traditional lithium battery, these two novel batteries represent a potential significant advancement of the chemical battery. As another type of energy storage device, supercapacitors have been intensively investigated due to their high specific power density and long lifetime. The best commercial carbon based supercapacitor obtained a power density of  $8.5 \text{ kW kg}^{-1}$ , with only 20% capacitance decay after 1,000,000 cycles,<sup>4</sup> but the energy density is limited to  $7.4 \text{ Wh kg}^{-1}$ . In the last decade there has been a surge of research and development in developing high power and high energy density supercapatteries to bridge the gap between conventional high-power capacitor and the high-energy battery where it bridges the gap in the Ragone plot between conventional capacitors and Li batteries. Therefore, the three different types of energy storage devices are suitable for a variety of applications.

### **1.2.1 Similarities and Differences between Batteries, Supercapacitors and Supercapatteries.**

**Batteries** are one of the most common energy storage devices in our day to day lives, and are used to provide power for electric devices such as smartphones, flashlights, and electric cars. Batteries are classified into two types: primary and secondary. Primary batteries are also called single-use or disposable batteries, which are only used once and discarded. Primary batteries are widely used for small electronic devices with low power consumption, which is convenient but detrimental for the environment. Secondary batteries are rechargeable batteries which are able to be charged and discharged multiple times along with reversible chemical reactions. Comparing to other

existing secondary batteries such as lead-acid batteries<sup>16,17</sup> and nickel-cadmium batteries<sup>18,19</sup>, lithium ion (Li-ion) batteries have drawn great attention due to their high capacity, high energy density, small self-discharge, good cyclic stability, and safety issues.<sup>20,21</sup>

Li-ion batteries are different from lithium batteries. The main difference is that lithium batteries are primary batteries using lithium in its pure metallic form, while Li-ion batteries are a type of rechargeable battery using an intercalated lithium compound as one electrode material. In the Li-ion battery system, Li ions move between the positive electrode and the negative electrode during charge and discharge process. The charge storage mechanisms for Li-ion batteries are typically split into three different groups: intercalation, conversion and alloying<sup>22,23</sup> (Figure 1.4). In general, intercalation materials are supposed to provide better cyclic stability, but the theoretical capacity is low, while the other two mechanisms offer ultra-high capacity but the large volume change limits the coulombic efficiency and cyclic stability.<sup>22,23</sup>

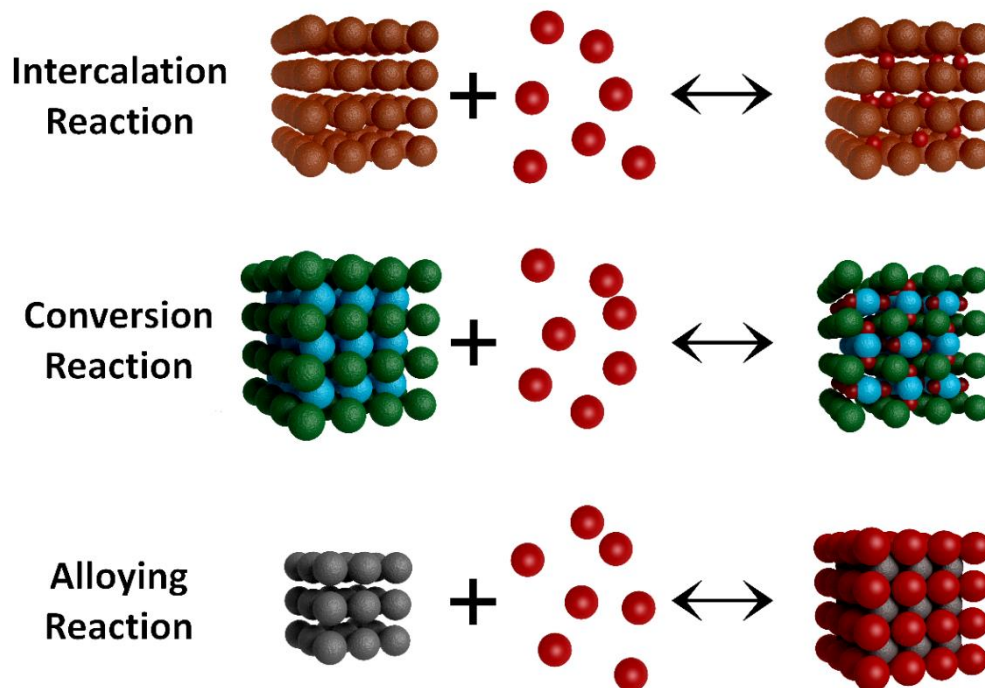
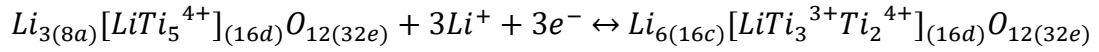


**Figure 1.4** Schematic diagram of the different reaction mechanisms of lithium ion batteries.

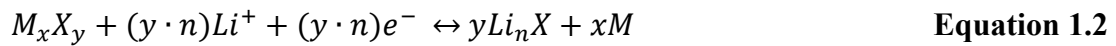
In detail, classic intercalation materials such as  $\text{LiMn}_2\text{O}_4$ <sup>24,25</sup>,  $\text{Li}_4\text{Ti}_5\text{O}_{12}$ <sup>26,27</sup>, and graphite<sup>28-30</sup> with a two-dimensional layered or three-dimensional network structure can allow lithium ions to reversibly intercalate without destroying the crystal structure. For instance,  $\text{Li}_4\text{Ti}_5\text{O}_{12}$  can be described as  $\text{Li}_{3(8a)}[\text{LiTi}_5^{4+}]_{(16d)}\text{O}_{12(32e)}$ . During the intercalation process, lithium ions are inserted into the lattice and located at the octahedral (16d) sites, while the existing tetrahedral (8a) lithium ions also transported to the octahedral (16c) sites. The reversible reaction process of  $\text{Li}_4\text{Ti}_5\text{O}_{12}$  is formulated as following equation<sup>31</sup>:



**Equation 1.1**

Though these metal oxide materials exhibit good cyclic stability due to the limited volume changing during the intercalation process, the rate performance is limited by slow diffusion of lithium ions and low electronic conductivity. Thereby, many efforts are now focusing on enhancing the transport of lithium ion and electrons in battery materials using element doping, surface coating, and other methods.<sup>32-35</sup>

Moreover, the conversion reaction occurs based on a displacement reaction as following<sup>36</sup>:



**Equation 1.2**

Where,  $M$  represents transition metal = Mn, Fe, Co, Ni, Cu, Ru, Cr, Mo, W, etc.,  $X$  represents H, N, O, F, P, S, etc., and  $n$  is the oxidation state of  $X$ . During the conversion process, all these transition metal compounds firstly convert to metal cluster then dispersed into  $\text{Li}_nX$  matrix. Consequently, conversion reactions involve a multiple electron transfer process, which will deliver remarkably high specific capacity compared to the intercalation process. However, the large structure reconstruction and the volume change can cause mechanical fracture and pulverization of active materials,

which limits the battery cyclic life<sup>37,38</sup>. With the purpose of improving the battery performance, recent investigations of these material are mainly focusing on nano-crystallization, morphology modification, and surface treatments<sup>35,39,40</sup>.

Furthermore, elements like Si and Sb or metals like Sn, Zn and Cd can form alloys with lithium<sup>41</sup>, which can be classified to alloying/de-alloying mechanism. (Equation 1.3)



Among all alloying materials, Si has drawn the most attention due to its relatively low delithiation potential, extremely high capacity (Li<sub>15</sub>Si<sub>14</sub>) low cost, and non-toxicity,<sup>42</sup> while Sn exhibits higher electrical conductivity but lower capacity and cell voltage<sup>43</sup>. In addition, Sn can be easily fractured even at small particle size around 10 nm<sup>44</sup>. However, other alloying metals like Zn, Cd suffer from low capacity according to the high molecular weight. Compared to intercalation and conversion mechanisms, alloying materials have the highest theoretical capacity but do suffer from issues associated with the large volume change rate caused by the alloying process. Thereby, to reduce the impact of material pulverization, investigations into the development of novel metal alloy and variations of their morphology are under progress<sup>45-47</sup>. Thus, alloy electrodes have been considered as one of the most promising electrode materials for next-generation lithium-ion batteries due to their high energy densities, relatively low cost, environmental compatibility and safe operation potentials.

In summary, Li-ion batteries have become commonplace for most of the daily electronic devices including communication, transportation, and entertainment applications. The study of improving the existing materials of Li-ion battery electrodes are under progress. Though the Li-ion batteries can provide large operation voltage and high energy density, the poor cyclic stability and low power output limit the applications so that an alternative type of energy storage device with higher power density and longer lifetime is required.

**Supercapacitors**, due to their fast charge-discharge capability and high power density,

give unique energy storage properties as compared to the conventional energy storage system. A supercapacitor consists of positive and negative electrodes, which are electrically isolated from each other by a separator. (Figure 1.5) In a classic electric double layer capacitors (EDLC), an electrical double layer is formed at the interface between the surface of a conductor electrode and electrolyte. Activated carbon, graphene, and other carbon based materials are widely investigated as high performance supercapacitor electrode materials due to their high surface area, good stability, and high conductivity.

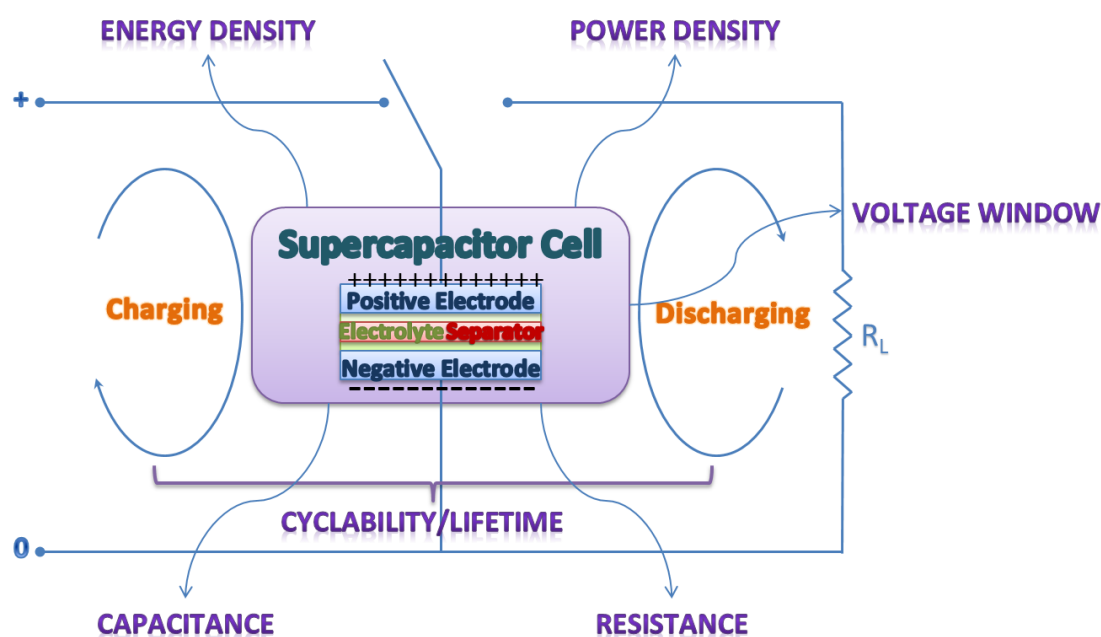


**Figure 1.5** Schematic diagram of the supercapacitor working process and relative parameters.

Interestingly, some metal oxide materials like  $\text{RuO}_2$ <sup>48,49</sup> and  $\text{MnO}_2$ <sup>50,51</sup> can exhibit capacitive behavior achieved by Faradaic reaction on the surface of the electrode by specifically adsorbed electrolyte ions. Due to the different electron transfer mechanisms of capacitive behavior, these materials have been classified as pseudocapacitive materials. As a matter of fact, due to the Faradaic process involved in redox reduction-oxidation reactions, these metal oxides have higher theoretical capacitance than carbon

based materials, but also suffer from lack of cyclic stability and lower power density<sup>52-55</sup>. Thus, the study of hybrid materials has drawn much attention in recent years. Hybrid materials involve a combination of carbon based materials with either metal oxides or conducting polymers<sup>56-58</sup>, incorporating benefits of both capacitive double layer of charge and Faradaic pseudocapacitive mechanisms. Thereby, further research is necessary to maximize both the capacitance and cyclic stability of the supercapacitor materials in near future.

Supercapacitors can be classified into three different types, EDLC, pseudocapacitors and hybrid devices of their combination. Generally, EDLC is a symmetric cell consisting two carbon based electrodes, electrolyte, and the separator, which keeps the two electrodes apart. EDLC exhibit a classic capacitive behaviour with a linear dependence of the charge stored with changing potential within the window of interest. Thereby, the capacitance, energy density and power density of the cell can be calculated from galvanostatic charge/discharge curves using the following equations, respectively:

$$C_{cell} = \frac{I \times \Delta t}{\Delta V} \quad \text{Equation 1.4}$$

$$E = \frac{1}{2} C_{cell} V^2 \quad \text{Equation 1.5}$$

$$P = \frac{E}{t} \quad \text{Equation 1.6}$$

where,  $I$  (A) is the discharge current,  $t$  (s) is the discharge time,  $V$  (V) is the potential window.

Since the two electrodes form a series circuit of two individual capacitors in the EDLC, so that the capacitance of the cell is half of the capacitance of each electrode. Thereby, the specific capacitance of the electrode material can be calculated as following:

$$C_{sp} = \frac{2 \times C_{cell}}{m_{electrode}} = \frac{2 \times I \times \Delta t}{\Delta V \times m_{electrode}} = \frac{4 \times I \times \Delta t}{\Delta V \times m} \quad \text{Equation 1.7}$$

Where  $m_{electrode}$  (g) is the loading mass of the active material in the electrode, and  $m$  (g) is the total mass of the two electrode materials.

Though pseudocapacitors utilize a Faradaic redox reaction mechanism, they also behave like capacitors. Thus the related calculations for pseudocapacitors are following the formulas as EDLC. The capacitance of a pseudocapacitor can be 10 to 100 times higher than EDLC. However, due to the slower Faradaic reactions, the power output of pseudocapacitor is normally lower than EDLC and the cyclic stability is also limited. Thereby further development of hybrid materials and hybrid cells are necessary to optimize the supercapacitor performance.<sup>59</sup>

It is worth pointing out that not all the catalytic materials exhibit pseudocapacitive behaviour, such as NiO<sup>60,61</sup>, Co<sub>3</sub>O<sub>4</sub><sup>62</sup>. Due to the misconception in the literature of the term “pseudocapacitance”, many researchers have classified their materials with a behaviour of a noticeable discharge plateau to be capacitive<sup>63-65</sup> and used the same equation to estimate the charge storage capacity. However, these materials demonstrate either diffusion controlled or surface controlled reversible redox reactions on the electrode surface with a behaviour of a noticeable discharge plateau. Thus, they should be classified as pseudo-battery type due to no intercalation/ de-intercalation process involved. Thereby the new terminology of **supercapattery** was created to define the electrochemical behaviour between capacitor-like and battery-like hybrids.<sup>66,67</sup> Generally, the electrodes of a supercapattery cell consists of a pseudo-battery type material and a supercapacitor-type material as shown in Figure 1.6. Due to the combination of two mechanisms, the supercapattery devices could obtain high energy from the battery-type material and coupling this with the ability to deliver high power from supercapacitor-type material. Moreover, the supercapattery could also potentially broaden the cell voltage and extend the cell lifetime.<sup>66,68</sup>

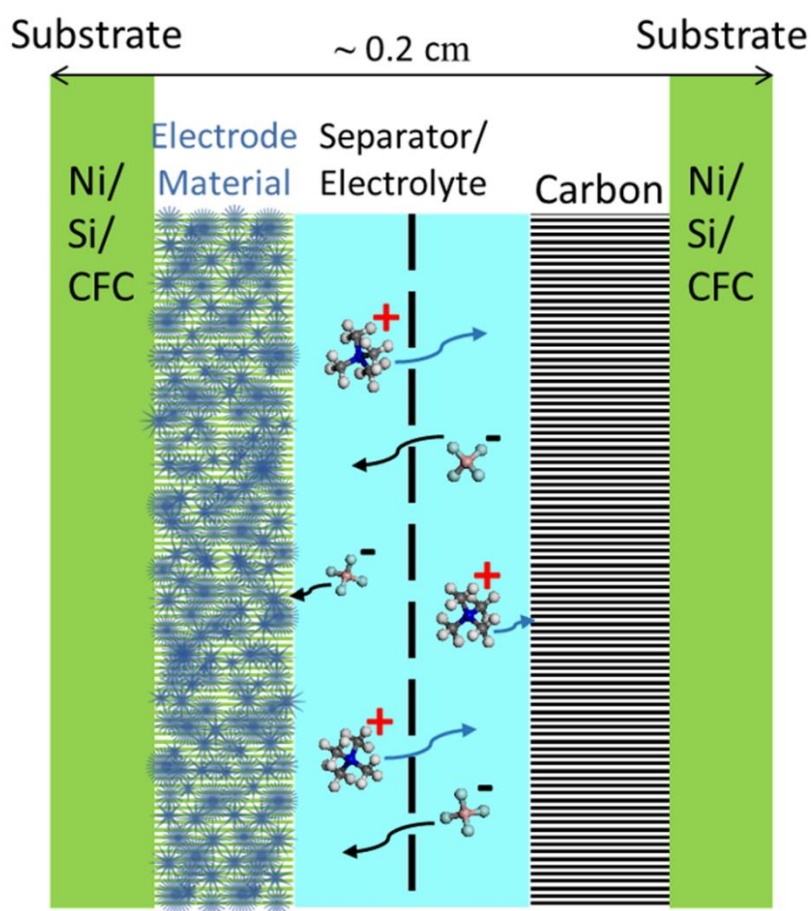


**Figure 1.6** Schematic diagram of the supercapattery structure.

However, with rapid development of the high performance energy storage devices, more and more novel devices have been investigated. Thereby, the definition classification of supercapattery remains controversial. For instance, lithium/ sodium-ion capacitor, which is a hybrid electrochemical energy storage device couples a high capacity bulk intercalation based battery-style negative electrode (anode) and a high rate surface adsorption based capacitor-style positive electrode (cathode), has drawn much attention recently. The lithium/ sodium ion can intercalate into the anode and counter-ions will form the double layer at the cathode (i.e. activated carbon) during the charge process. Though the ion capacitor exhibits a capacitance-type behaviour, which is a rectangular cyclic voltammetry (CV) and linear charge-discharge curve, it is hard to categorise the ion capacitor as supercapacitor or supercapattery due to the different storage mechanism. Some researchers claim that the Li/ Na ion capacitor is a hybrid device, which belongs to supercapattery<sup>69</sup>, because discharging voltage reach zero

instead of  $V_{\min}$  as like batteries, however it is hard to distinguish from the devices which can store the energy by chemical redox reaction but without involving intercalation mechanism. Furthermore, another type of symmetric device (in which both the positive and negative electrodes are made from same materials) fabricated by low cost pseudo-battery type materials normally exhibit a noticeable discharge plateau or quasi linear discharge behaviour<sup>64</sup>, with higher energy density than supercapacitors and higher power density, and much better cyclic stability than battery. Thereby, they are worthy for further investigation and needed to be classified properly.

## 1.2.2 Classification of Supercapattery

In general, the electrode materials of energy storage devices can be classified into four different types due to their different energy storage mechanisms: capacitive materials (activated carbon, graphite, graphene, etc.<sup>70-74</sup>), pseudocapacitive materials ( $\text{MnO}_2$ ,  $\text{RuO}_2$ , etc.<sup>48,50,51</sup>), battery-type materials ( $\text{LiTi}_4\text{O}$ ,  $\text{LiFePO}_4$ , etc.<sup>25,27,34</sup>), and pseudo-battery type materials ( $\text{NiO}$ ,  $\text{Co}_3\text{O}_4$ ,  $\text{CoMoO}_4$ ,  $\text{Co}_3(\text{PO}_4)_2$ , etc.<sup>66,75-77</sup>). Theoretically, these materials all can be used as either positive electrodes or negative electrodes to assemble an energy storage device according to their voltage window. Different electrolytes also determine the charge storage characteristics of an energy storage device, where each electrode exhibits a specific voltage window in a particular electrolyte. Thereby, quite a large number of energy storage devices are fabricated by selecting and pairing various electrodes and electrolytes. In order to maximize the electrochemical performance of the device, researchers are now focusing on developing asymmetric cells assembled using two different electrodes with positive and negative working potential in a specific electrolyte. Compared to symmetric cells (same electrode applied), asymmetric cells can broaden the cell voltage so that the energy density may increase accordingly. Figure 1.7 illustrates the CV of the electrodes and the charge/ discharge behaviour of the devices with different paired electrodes.

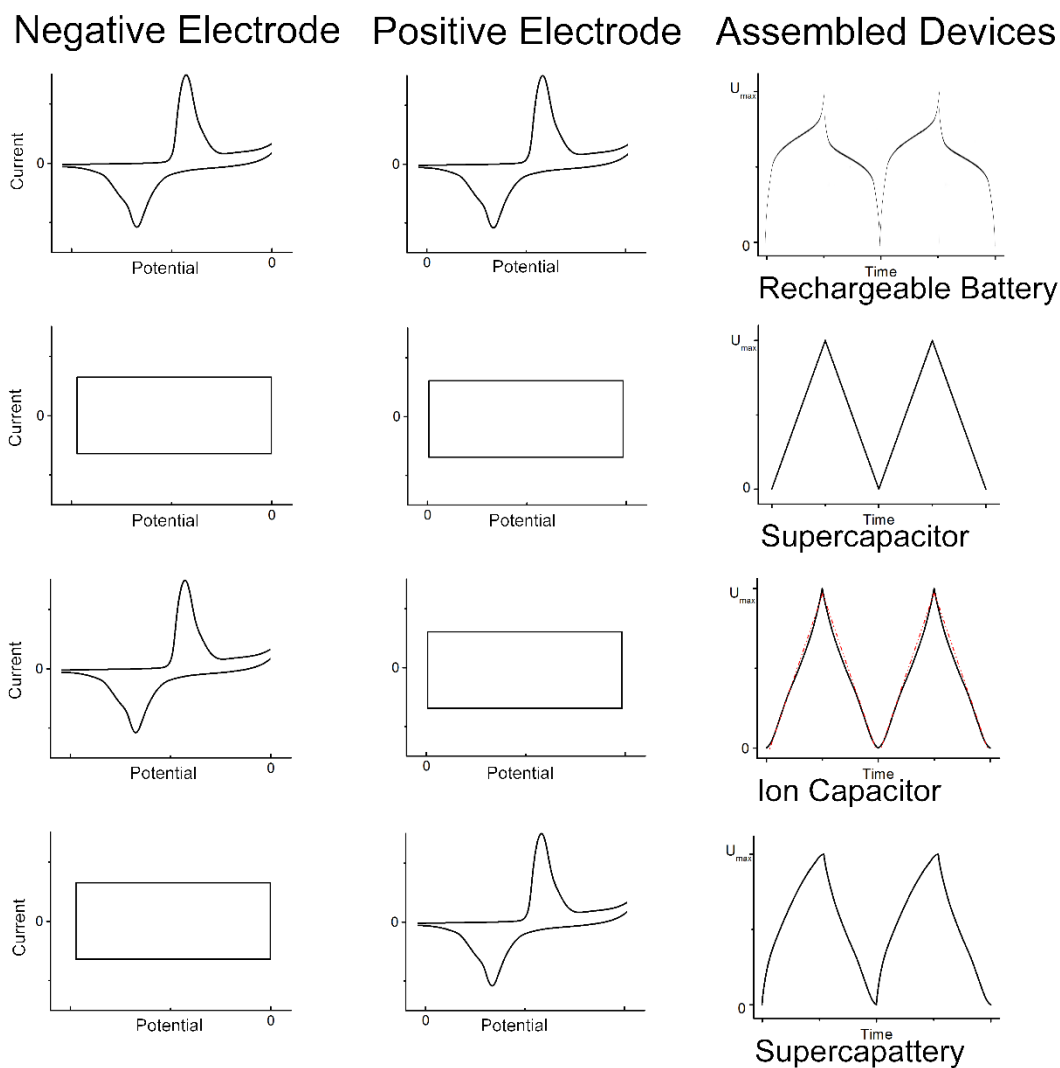


**Figure 1.7** Schematic illustration of selecting and pairing various electrodes to assemble different types of energy storage devices.

Obviously, a rechargeable battery consists of two battery-type electrodes while a supercapacitor consists two capacitive-type electrodes. Besides, there are also many other choices for selection and pairing of electrodes. Typically, ion capacitors are fabricated by pairing battery-type electrode and capacitive-type electrode, and supercapatteries are assembled with pseudo-battery type electrodes. However, there may still be many devices that cannot fit in to any of the above terminologies, then the denotation of supercapattery may extend to describe all the energy storage devices apart from rechargeable battery and supercapacitor. Figure 1.8 presents the classification of

energy storage devices with various selection and pairing of same or different electrodes. Further discussion on the detailed mechanisms will be explained in chapter 2.

Energy Storage Devices	Supercapacitor					Supercapattery				Battery	
	EDLC		Pseudocapacitor			Supercapattery					Ion capacitor
Electrode Materials	CM	CM	CM	PCM	PCM	CM	PCM	PBM	PBM	CM	BM
	I	II	II	I	II	II	II	I	II	II	II
	CM	CM	PCM	PCM	PCM	PBM	PBM	PBM	PBM	BM	BM

CM: capacitive material  
 PCM: pseudocapacitive material  
 BM: battery material  
 PBM: pseudo battery material  
 I: symmetric device using same electrode material  
 II: asymmetric device using different electrode material

**Figure 1.8** Classification of energy storage devices with various selection and pairing of same or different electrodes.

### 1.3 Research Objectives

The evolution of implantable medical devices has led towards leadless systems, which require a miniaturized power source with long cyclic stability. Conventional rechargeable batteries are very expensive and cannot be used in implantable application due to their limited life cycle. Among all the different types of energy storage devices described in the previous section, supercapatteries, which combines the high power capacity and short charging/discharging times of a supercapacitor with the greater energy density of batteries, can be an attractive power source for the next generation self-rechargeable pacemaker. With high energy density, the device should be able to provide enough power during cardiac emergency, which requires good stability once fully charged.

Thereby, the aim of this study is to develop nanomaterial based supercapatteries to store the energy from heartbeats through a piezoelectric device and drive the pacemaker to deliver the electrical impulses during emergency. This device is required to survive for at least 20 years inside the pacemaker with enough retention capability after thousands of charge-discharge cycles.

To fulfil the objectives, the main tasks of this research work include:

- Development of different nanostructured electrode materials and the growth mechanism study
- Characterization of the synthesized nanomaterials and the modification of their morphologies
- Understand the electrochemical storage mechanism of the fabricated electrodes and electrochemical performance characterizations
- Design of prototype supercapattery devices
- Measure electrochemical performance of assembled supercapattery devices
- Self-discharge behaviour and leakage current study on the fabricated supercapattery devices
- Investigate performance of the supercapattery under physiological temperature range

## **1.4 Thesis Outline**

This thesis is organized in six chapters, and the general content of each chapter can be summarized as below:

In Chapter 1, implantable medical devices, evolution and their power sources are introduced. The similarities and differences of three different energy storage devices are elucidated. The classification of different types of supercapatteries are clarified.

In Chapter 2, a literature review is performed on the energy storage mechanism in electrode materials, including capacitive materials, pseudocapacitive materials, battery-type materials and pseudo-battery type materials. Selection and pairing of electrode materials and electrolytes are introduced.

In Chapter 3, the experiments associated with nickel foam (NF) supported materials

fabrication, structural and characterizations of the fabricated materials are described. The crystal structures of fabricated materials were analysed using X-ray diffractometer (XRD Philips PW3710-MPD diffractometer with Cu K $\alpha$  radiation,  $\lambda=1.54$  Å). The surface morphology and compositional analysis of the fabricated electrode materials were studied using scanning electron microscope (FEI QUANTA 650 HRSEM) with an energy-dispersive X-ray spectrometer (EDX Oxford Instruments INCA energy system) and high resolution transmission electron microscope (JEOL HRTEM-2100 at 200 kV). The Raman spectra was recorded with the Renishaw (RA 100) in Via confocal Raman Microscope at 514.5 nm excitation and the X-ray photoelectron spectroscopy (XPS) analysis was performed on a Kratos Ultra DLD spectrometer with Al K  $\alpha$  (1486.6 eV) as the X-ray source. To avoid contribution of Ni from the NF, the EDX and TEM measurements were carried out for the powder samples scratched off from the NF.

In Chapter 4, the four different fabricated materials were investigated using a three electrode system using platinum wire (Pt) and saturated calomel electrode (SCE) as counter and reference electrodes, respectively. The synthesized electrodes were cut into  $1 \times 1$  cm<sup>2</sup> size and tested in inorganic aqueous sodium hydroxide / potassium hydroxide solution. The electrochemical measurements, including CV, chronopotentiometry (CP), and alternative current impedance techniques were conducted using a CHI 660C electrochemical workstation and a Biologic VSP Modular 5 channel potentiostat. The electrochemical mechanism of the synthesized materials was understood, and the electrochemical properties of the materials were analyzed. In addition, the studies on the electrochemical properties of cobalt phosphate electrode was carried out between 25 - 45 °C and explained.

In Chapter 5, four different supercapatteries were assembled using synthesized materials as positive electrode and activated carbon as negative electrode. The balancing of two electrode were discussed and approved by experiments. The electrochemical properties of the fabricated supercapatteries were investigated using CV, chronopotentiometry, and alternative current impedance techniques using a CHI

660C electrochemical workstation and a Biologic VSP Modular 5 channel potentiostat. The electrochemical properties of the supercapattery device were analyzed and discussed. The application of LED lighting was investigated for the devices and moreover cobalt phosphate based supercapattery was investigated between 25 - 45 °C and discussed.

In Chapter 6, a summary of the current work presented in the thesis and its novelty are provided. Suggestions provided for future works that will be necessary to develop new 3D structured on carbon/silicon based substrate as supercapattery electrode for next generation pacemaker and other applications.

# Chapter 2 Development Trends of Supercapattery electrode materials

## 2.1 Introduction

Recent research efforts that have been devoted to advancing electrode materials for energy storage devices, most often involved lithium or sodium based intercalation materials<sup>78-82</sup>, carbon based materials<sup>72,83,84</sup>, metal oxides<sup>64,85,86</sup>, conducting polymers<sup>87,88</sup> and in recent year's metal-organic frameworks (MOFs)<sup>89-91</sup>. In order to achieve high electrochemical performance, optimization of the material structure and morphology is crucial. Nanostructure morphology of the electrode material can bring drastic variation in their electrochemical properties. Due to the high surface to volume ratio of the nanostructure, the specific surface area of the electrode material can be increased and consequently enhance the electrochemical performance of the storage device. Nanostructure morphology of different materials may vary significantly depending on their material composition, crystal structure and manufacturing method. The various structures of different electrode nanomaterials are depicted in Figure 2.1. In general, nanomaterials can be classified in four major categories based on their structural complexity from zero dimensional (0D) to three dimensional (3D) nanostructures. Basically, 0D nanostructure refers to spherical nanoparticles with diameters ranging from a few to tens of nanometers, including core-shell nanoparticles and nanoparticles loaded with nanospheres, while 1D nanostructure such as nanowires and nanotubes can provide a direct pathway for efficient charge transport. More complex 2D and 3D nanostructures often refer to nanosheets/ nanofilms and stereoscopic heterogeneous architectures, respectively. Due to the structural interconnectivities, the nanomaterials demonstrate great potential as candidate electrodes for electrochemical energy storage devices. In this chapter, fabrication techniques, nanostructure morphology, and electrochemical properties of these different types of nanomaterials will be discussed.

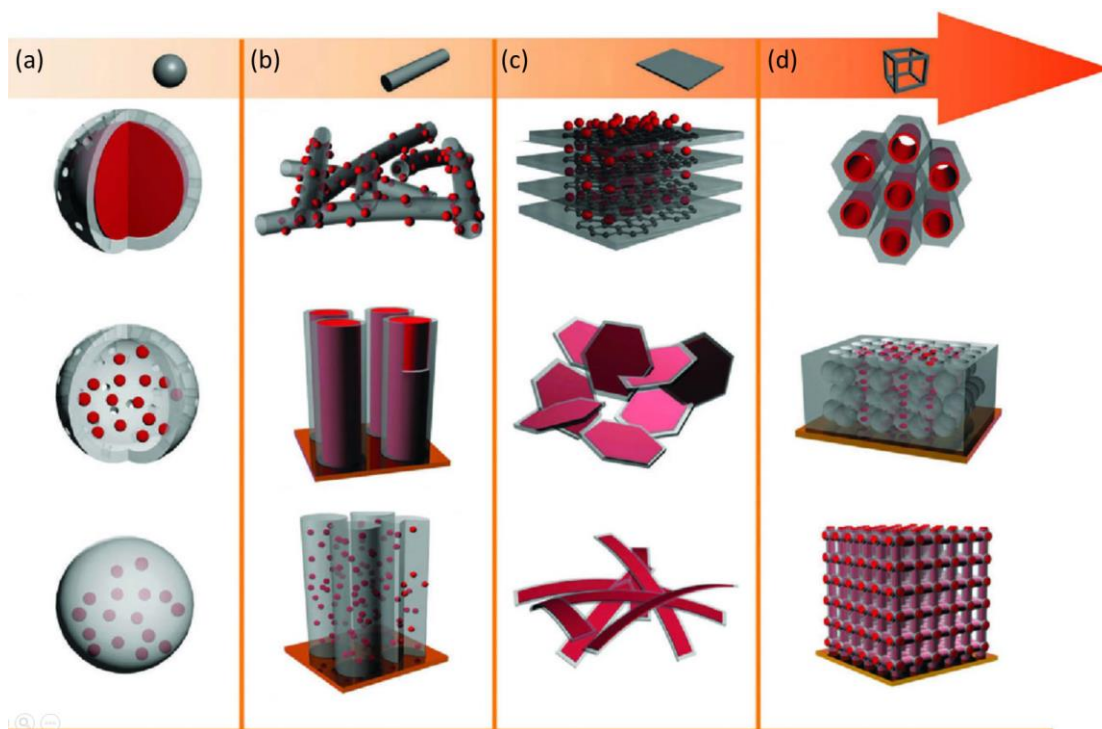


**Figure 2.1** Schematic of heterogeneous nanostructures based on (a) 0D, (b) 1D, (c) 2D, and (d) 3D nanostructures.<sup>92</sup>

## 2.2 Capacitive Materials

Carbon based materials are widely investigated as high performance supercapacitor electrode materials due to their high surface area, high conductivity, low cost, and established electrode production technologies. As discussed in section 1.2.1, the energy storage mechanism of these material is the double layer formed at the interface between the surface of electrode and electrolyte. Many studies aim at fabricating different types of carbon based materials such as activated carbon<sup>93-95</sup>, carbon nanotubes<sup>73,96,97</sup>, graphene<sup>98-100</sup> and their composites<sup>97,101</sup> (Figure 2.2), some of which will be described in the subsequent sections.

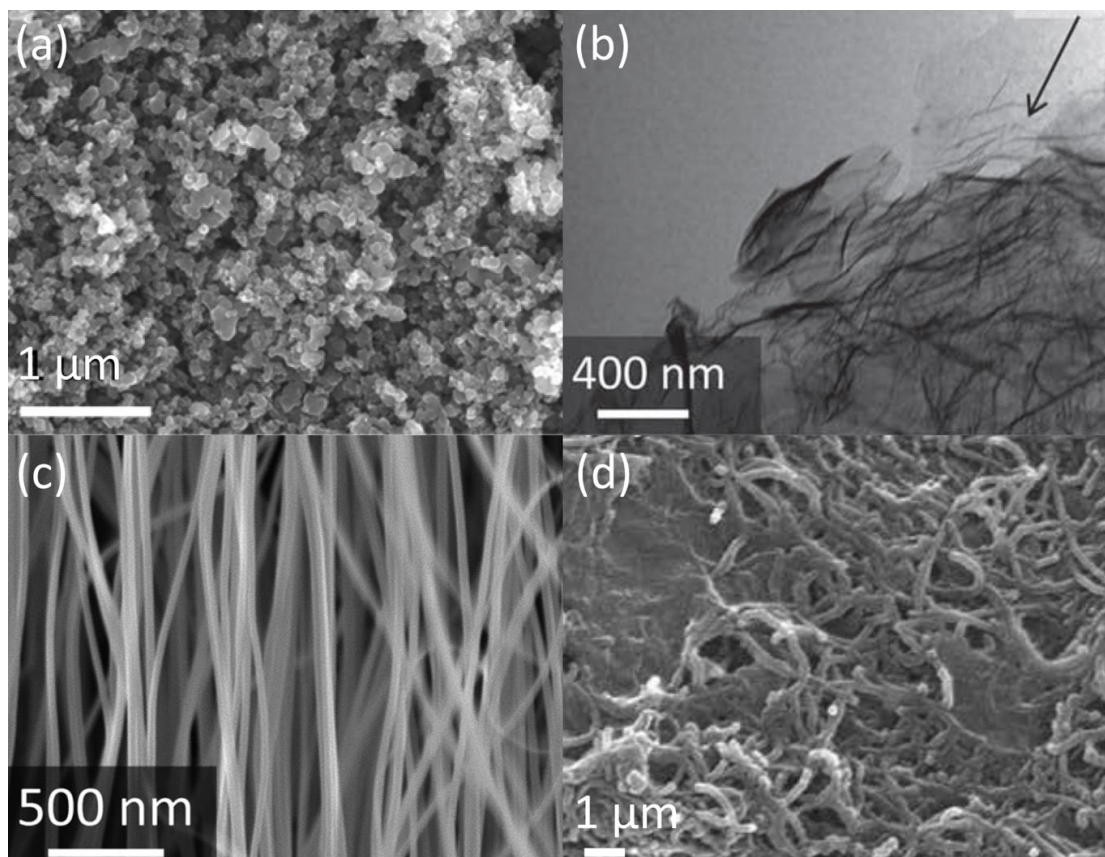


**Figure 2.2** Electron microscopy images of high surface area carbon materials <sup>93,102-104</sup>: (a) activated carbon, (b) graphene, (c) carbon nanotubes, and (d) graphene sheets-carbon nanotubes

### 2.2.1 Activated carbon

Among different carbon based materials, activated carbons (AC) are widely used as electrode materials in supercapacitors. Activated carbons (AC) are obtained from different carbon based organic precursors, such as cola, corn grain, wood, peat, nutshells, leaves, and straw.<sup>97,105-109</sup> Generally, AC can be obtained by either thermal (also called physical) or chemical activation process. The physical activation involves carbonization and gasification by the treatment of high temperature (700 to 1200°C) treatment in the presence of an oxidizing agent like CO<sub>2</sub> or steam.<sup>110,111</sup> in the case of chemical activation, the precursor reacts with chemical reagent such as sodium hydroxide, potassium hydroxide, phosphoric acid, and sulfuric acid.<sup>111-115</sup> The obtained

porous structure of AC can be broken down and named as micropores ( $< 2$  nm), mesopores (2 – 50 nm) and macropores ( $> 50$  nm) according to their size. Thereby, the surface area of AC is usually in the range of 1000-2000  $\text{m}^2 \text{g}^{-1}$ , and even up to 3000  $\text{m}^2 \text{g}^{-1}$  in some reports, which can enhance the electrochemical capacitance.<sup>116,117</sup> Table 2.1 summarizes different precursors, the Brunauer–Emmett–Teller surface area (BET-SA) and capacitance of some previously reported ACs.

**Table 2.1** Electrochemical performance of activated carbons in the earlier reports.

Precursor	Activation Method	BET-SA	Capacitance	Ref.
		$\text{m}^2 \text{g}^{-1}$	$\text{F g}^{-1}$	
Melamine mica	30% HNO <sub>3</sub> + ammonia treatment	3487	148	118
Polyvinyl alcohol	Chemical-KOH	2218	147	119
Glucose	Chemical-ZnCl <sub>2</sub> KOH	2150		74
Tobacco	Chemical-KOH	1297.6	148	120
Rubber wood sawdust	Chemical-NaOH H <sub>3</sub> PO <sub>4</sub>	693	129	121
Poly	Physical-CO <sub>2</sub>	1360	196	122
Carbon aerogels	Chemical-KOH	428	152.6	123
Celtuce leaves	Chemical-KOH	3404	273	106
Seed shell	Chemical-KOH	2100	355	124
Camellia oleifera shell	Chemical-ZnCl <sub>2</sub>	2080	230	107

One of the disadvantages of activated carbon powders is that they needed to be mixed with binders to coat on the current collectors, which may block some of the pores and reduce the effective area. In addition, the pore size distribution in AC powders is hard to optimize during the activation process. Thereby, some regions of the activated material do not contribute to capacitance.

## 2.2.2 Carbon nanotubes

Carbon nanotubes (CNT) have drawn much attention due to their unique structure

obtained by the catalytic decomposition of certain hydrocarbons under different manipulation parameters.<sup>112</sup> As CNTs can be grown on the conductive substrates directly, the whole surface of the CNT can be exposed to the electrolyte during the energy storage process, which may enhance the performance. Moreover, the resistance between the activated material and the current collector is less as compared to activated carbon. Thereby, the specific capacitance of CNTs is mainly controlled by the purity and morphology of the material. The capacitance of CNT is normally limited to 200 F g<sup>-1</sup> due to the hydrophobic property of the surface. Table 2.2 summarized the capacitance of reported CNT electrodes.

**Table 2.2** Electrochemical performance of carbon nanotubes in the earlier reports

Activation Method	BET-SA	Capacitance	Electrolyte	Ref
	m <sup>2</sup> g <sup>-1</sup>	F g <sup>-1</sup>		
Chemical KOH	1050	65	1.4 M TEABF <sub>4</sub> in AN	125
Catalytically grown + HNO <sub>3</sub>	430	102	38 wt % H <sub>2</sub> SO <sub>4</sub>	126
Ammonia plasma	86.5	207	6 M KOH	127
Chemical KOH	1050	90	6 M KOH	125
CVD method	259	300	6 M KOH	128
Chemical HNO <sub>3</sub>	430	104	38 wt % H <sub>2</sub> SO <sub>4</sub>	129

CNTs can be categorized as single walled carbon nanotubes (SWCNTs), multi-walled carbon nanotubes (MWCNTs), and both are widely investigated as electrode materials. Due to the low CNT density and surface area, the capacitance and energy density of CNT based EDLS is limited. Thereby, recent efforts are focusing on developing composite materials over CNTs to enhance the electrochemical performance. Further details are discussed in section 2.2.4.

### 2.2.3 Graphene

Graphene is a one atom thick sheet 2D structure of sp<sup>2</sup> bonded carbon atoms arranged

in a hexagonal lattice, which can be an ideal material for energy storage devices due to its large surface area, rate and cyclic stability, excellent electrical conductivity, and good chemical and thermal stability.<sup>97,130</sup> Compared to the other carbon based material such as activated carbon and carbon nanotubes, graphene has drawn much attention due to the wide potential window it can be cycled in, abundant surface functional groups and having no issues associated with the distribution of pore sizes. The theoretical capacitance of fully utilized graphene is 550 F g<sup>-1</sup>, however, the fabrication process is crucial to achieve this capacitance. There are many methods of producing different types of graphene such as thermal reduction, chemical vapor deposition (CVD), and chemical exfoliation.<sup>131</sup> Graphene has been widely investigated in different electrolytes including inorganic electrolyte (H<sub>2</sub>SO<sub>4</sub>, KOH)<sup>70,132</sup>, organic electrolyte (TEATFB)<sup>70</sup>, and ionic liquid (N-butyl-N-methylpyrrolidiniumbis (trifluoromethanesulfonyl) imide (PYR14TFSI), IMIMTFB)<sup>71,133</sup>. Table 2.3 summarized the graphene electrode developed through different methods and their performance.

**Table 2.3** Electrochemical performance of graphene electrode in the earlier reports

Exfoliation Method	BET-SA	Capacitance	Electrolyte	Ref
	m <sup>2</sup> g <sup>-1</sup>	F g <sup>-1</sup>		
Thermal exfoliation	737	233	2 M KOH	134
Electrochemical reduction		165	0.1 Na <sub>2</sub> SO <sub>4</sub>	133
Chemically reduced	320	205	30 wt% KOH	135
Microwave expanded	463	191	5 M KOH	136
CVD + N-doping	-	282	6 M KOH	137
	-	220	TEATFB	
Hydrothermal	830	223	H <sub>2</sub> SO <sub>4</sub>	138
N-doping	190	217	6 M KOH	139

It is worthy to point out that graphene suffers from the agglomeration of restacking back to graphite, and the reported surface area is far below the theoretical specific value of 2630 m<sup>2</sup> g<sup>-1</sup>. Thereby, the structure modification is crucial. The last three electrodes

in Table 2.3 exhibit better electrochemical performance, which may be due to manipulation of local electronic structures by nitrogen doping. Furthermore, there are also ongoing efforts to develop graphene based composites with conducting polymers and metal oxides, which are discussed in the following section.

#### **2.2.4 Carbon based material composites**

The study of hybrid materials has drawn much attention in recent years. As a matter of fact, most investigated hybrid materials combine highly conductive carbon allotropes, conducting polymer, and electroactive oxides to improve the energy density in supercapacitors.<sup>140,141</sup> A co-reduction process was developed to reduce dispersed graphene oxide and single walled carbon nanotubes simultaneously and obtained a high specific capacitance of 261 F g<sup>-1</sup> for a single electrode and a high energy density of 123 Wh kg<sup>-1</sup> in the two-electrode configuration.<sup>58</sup> A hollow polypyrrole (PPy) modified nitrogen-doped graphene (NG/H-PPy) was prepared by in situ chemical oxidative polymerization process. The specific capacitance of NG/H-PPy composites was 575 F g<sup>-1</sup> and the energy density was 47.92 Wh kg<sup>-1</sup>.<sup>142</sup> Research was carried out on the comparison between pure carbon nanotubes, pure MnO<sub>2</sub> and their composites (Figure 2.3)<sup>141</sup>. MnO<sub>2</sub> microsphere-coated CNTs exhibited a highly porous structure. The surface area of the composite was found to be 237.8 m<sup>2</sup> g<sup>-1</sup>, which is much higher than that of the pure MnO<sub>2</sub> (42.1 m<sup>2</sup> g<sup>-1</sup>) and pristine CNTs (95.7 m<sup>2</sup> g<sup>-1</sup>). In another study, MnO<sub>2</sub> modified CNTs were prepared via electrochemical deposition technique, where the addition of 2-3 nm MnO<sub>2</sub> layer improve the composite capacitance significantly (465 F g<sup>-1</sup>).<sup>57</sup>

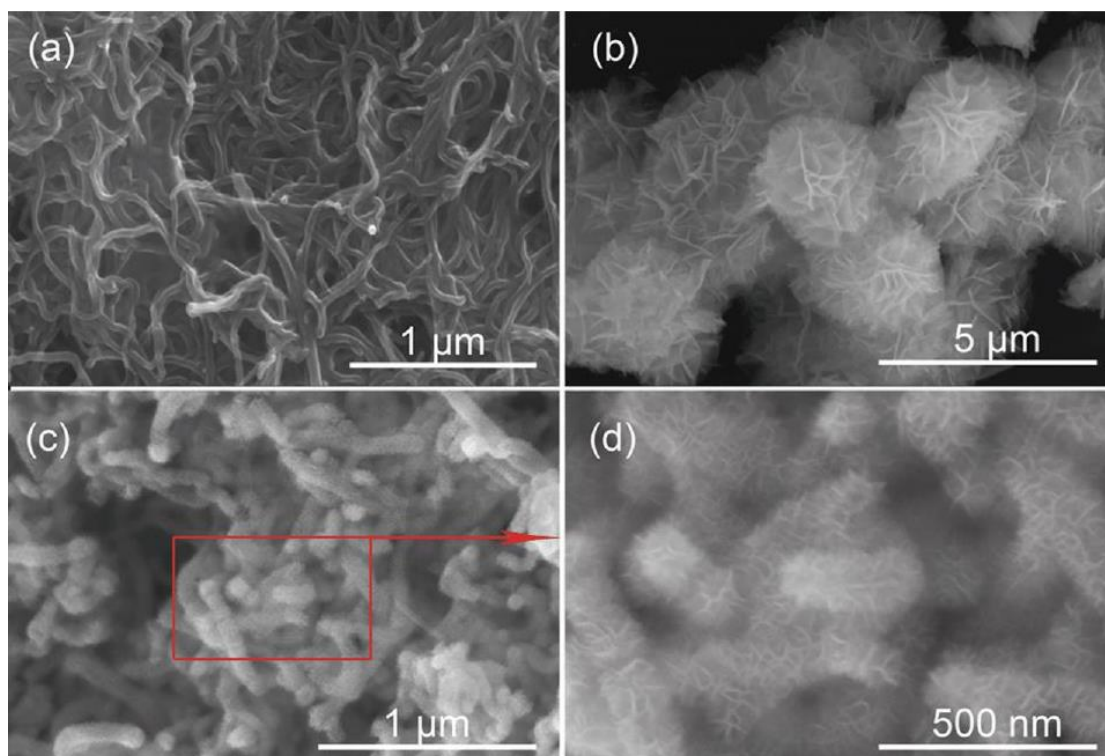


**Figure 2.3** FESEM images of (a) the pristine CNTs, (b) the flower-like MnO<sub>2</sub> powder, and (c-d) the MnO<sub>2</sub>/CNT nanocomposite at different magnifications.

The structure of graphene composites can help to avoid the retracking of graphene sheets, while graphene offers a uniformly dispersed controlled nanostructure to enhance the overall surface area. The obtained capacitance of the composite is usually higher than the individual material. Also, other electrochemical performance such as cyclic stability, rate capability, energy density, and power density may also be improved owing to the integrated three dimensional (3D) structure. As an example, a nanocomposite of mesoporous MnO<sub>2</sub> nanospheres anchored on reduced graphene oxide was synthesized by a simple and inexpensive reflux reaction delivered a specific capacitance of 466.7 F g<sup>-1</sup>.<sup>56</sup> Another composite of α-MnS anchored nitrogen-doped reduced graphene oxide nanosheets was fabricated by one-pot solvothermal approach, and exhibit a high specific capacitance of 933.6 F g<sup>-1</sup>.<sup>143</sup>

In summary, the carbon based material exhibit a negative potential window and limited capacitance up to 300 F g<sup>-1</sup> due to the electrostatic storage mechanism and exceptional

cyclic stability over 100,000 charge-discharge cycles. The electrochemical performance may be enhanced by coating a layer of activated material with multiple functional groups. Further study is required to develop novel carbon based composite for energy storage devices.

### 2.3 Pseudocapacitive Materials

Pseudocapacitance is used to describe the materials such as  $\text{RuO}_2$ <sup>48,49</sup>,  $\text{MnO}_2$ <sup>50,51</sup>, which show capacitive electrochemical properties (like carbon) through Faradaic reaction mechanism. In detail, these materials exhibit a rectangular shape current/ voltage profile and linear dependence of the charge stored with charging potential by chemical redox reaction.  $\text{RuO}_2$  and  $\text{MnO}_2$  based materials have been widely investigated due to their high theoretical capacitance of 2000 and 1370  $\text{F g}^{-1}$ , respectively.  $\text{RuO}_2$  has a good stability in acidic electrolyte<sup>144</sup>, while  $\text{MnO}_2$  is more suitable for the neutral solution.<sup>50</sup> The pseudocapacitive mechanism of these material is the chemical reversible redox reaction between the activated material and the specific electrolyte ions. The reactions of  $\text{RuO}_2$  and  $\text{MnO}_2$  can be expressed using the following equations:<sup>145-147</sup>



Where  $x$  is the number of transferred protons during the reaction and  $\text{M}^+$  represents the protons or alkali metal cations in the electrolyte such like  $\text{Li}^+$ ,  $\text{Na}^+$  and  $\text{K}^+$ .

It is a remarkable fact that  $\text{RuO}_2$  has a wide potential window of 1.2 V in inorganic electrolyte.<sup>130</sup> Besides, it exhibits high proton conductivity, long cyclic stability, high rate capability and good thermal stability.<sup>130,148</sup> So far, a specific capacitance of 1500  $\text{F g}^{-1}$  has been achieved by electroplating  $\text{RuO}_2$  on highly conductive nanoporous gold, which is close to the theoretical value.<sup>149</sup> However, the high cost and rarity of Ru make it difficult for large scale production. Thereby, the study on developing  $\text{RuO}_2$  based composites are now highly focused.  $\text{RuO}_2/\text{TiO}_2$  nanotubes composites were

synthesized by loading various amounts of RuO<sub>2</sub> on TiO<sub>2</sub> nanotubes, and a maximum specific capacitance of 1263 F/g was obtained for the RuO<sub>2</sub>.<sup>150</sup> Furthermore, RuO<sub>2</sub> modified carbon based materials have also been widely studied, including RuO<sub>2</sub>·xH<sub>2</sub>O/carbon nanofibers<sup>151</sup>, polyaniline/Nafion/hydrous RuO<sub>2</sub><sup>152</sup>, RuO<sub>2</sub> nanoparticles/carbon nanotubes<sup>153</sup>, and cone-shaped polypyrrole/RuO<sub>2</sub><sup>154</sup>.

MnO<sub>2</sub> is an alternative ideal pseudocapacitive type material due to the low cost, low toxicity and environmental safety.<sup>130</sup> The capacitance and cycling stability of MnO<sub>2</sub> is mainly determined by the microstructure and chemical hydrous state.<sup>155</sup> Since the high crystallinity of manganese oxide may limit the proton exchange, the modification of morphology and composition is crucial during the fabrication process.<sup>156</sup> Various allotropic forms of MnO<sub>2</sub> were synthesized following dedicated preparation routes and the 3D structure delivered the best performance.<sup>145</sup> Moreover, the electrochemically active surface area of MnO<sub>2</sub> could also be enhanced by growing over specific substrate or other material.<sup>157,158</sup> Interestingly, MnS and Mn<sub>3</sub>(PO<sub>4</sub>)<sub>2</sub> also demonstrates pseudocapacitive behaviour<sup>159-161</sup>, which is due to the successive surface redox reaction during the process.<sup>162</sup> Manganese based material are not suitable for symmetric energy storage devices owing to the positive working potential, however, they have the potential to assemble the hybrid system as a good positive electrodes.<sup>162</sup>

## 2.4 Battery-type Materials

Ion capacitors are hybrid devices that combine a battery type material as anode and carbon based material (usually activated carbon) as cathode, which demonstrate an electrochemical behaviour similar to capacitors. Theoretically, ion capacitors can combine the advantages of batteries and supercapacitors, which means high energy density, high power density, large potential window, and long cyclic stability. Ion capacitors combine the two different mechanism of adsorbing/ desorbing on one electrode surface and Li<sup>+</sup>/Na<sup>+</sup> ion intercalating/ de-intercalating in the bulk of the other electrode.<sup>163</sup> Various battery type electrode materials can be used as anode such as

LiMn<sub>2</sub>O<sub>4</sub>, TiO<sub>2</sub>, LiNi<sub>0.5</sub>Mn<sub>1.5</sub>O<sub>4</sub>, Li<sub>3</sub>V<sub>2</sub>(PO<sub>4</sub>)<sub>3</sub>.<sup>79,164-166</sup> So far, these materials are usually tested in liquid electrolytes, which may cause serious safety issues due to the leakage.

Table 2.4 summarizes the reported ion capacitor and their performance.

**Table 2.4** Electrochemical performance of ion capacitors in the earlier reports.

Electrode materials		Electrolyte	Energy density	Cyclic stability	Ref
Cathode	Anode		Wh kg <sup>-1</sup>		
LiMn <sub>2</sub> O <sub>4</sub> /graphene	Activated carbon	1 M LiPF <sub>6</sub> in EC:DEC:DMC = 1 : 1 : 1, vol%	38.8	500 (90.6%)	164
Li <sub>5</sub> ReO <sub>6</sub>	Activated carbon	1M LiPF <sub>6</sub> in EC:DMC = 1:1, vol %	40	-	167
MoO <sub>2</sub>	Activated carbon	1M LiPF <sub>6</sub> in EC:DMC = 1:1, vol %	150	4000 (85%)	168
Li <sub>4</sub> Ti <sub>5</sub> O <sub>12</sub>	Carbon nanosheet	1 M TEABF <sub>4</sub>	63	6000 (97%)	169
TiO <sub>2</sub> -rGO	Activated carbon	1M LiPF <sub>6</sub> in EC:DMC = 1:1, vol %	50	4000 (82%)	166
MnO/C	Carbon nanosheets	1M LiPF <sub>6</sub> in EC:DMC = 1:1, vol %	100	5000 (70%)	170
Core-derived carbon sheets	Core-derived carbon sheets	1M LiPF <sub>6</sub> in EC:DMC = 1:1, vol %	124.8	5000 (66%)	171
Peanut shell nanosheet carbon	Peanut shell ordered carbon	1 M NaClO <sub>4</sub> in EC:DMC = 1:1, vol %	201	10,000 (72%)	81
High-quality Prussian blue	Activated carbon	0.5 M Na <sub>2</sub> SO <sub>4</sub>	30	1000 (97%)	172

Apart from the Li ion system, Na, K and Al ions have the potential to be applied in the

ion capacitor. Na and K has a low redox potential of -2.71 V for Na<sup>+</sup>/Na vs. SHE and -2.93 V for K<sup>+</sup>/K vs. SHE, while Al engages a three-electron transportation during the redox reaction.<sup>15,173</sup> However the investigation in ion capacitor is still rare in the literature, where more study on the in situ characterization techniques and the evidence about the reaction mechanism is desired.

## 2.5 Pseudo-battery-type Materials

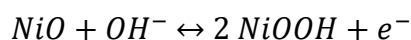
As mentioned in chapter 1.2.1 many materials such as NiO<sup>60,61</sup>, Co<sub>3</sub>O<sub>4</sub><sup>62</sup>, Ni(OH)<sub>2</sub><sup>174</sup>, and CoHPO<sub>4</sub><sup>175</sup> are presented in the literature as pseudocapacitive materials, which is technically inaccurate.<sup>65</sup> These materials do not exhibit capacitive behaviour of rectangular CV and linear charge-discharge curve like carbon based material. On the other hand, their Faradaic reactions are not dominated by intercalation/ de-intercalation mechanisms like a lithium/ sodium ion battery, but are controlled by diffusion and absorption on the electrode surface. The word pseudo means almost and approaching, thereby these materials, which have battery-like behaviour but no intercalation or huge structure changing by alloying and conversion, should be named pseudo-battery-type material.

In terms of fabrication, different methods were used for preparation of the nanostructure oxide materials, such as hydrothermal, sol-gel, microwave, electrodeposition etc.<sup>176</sup> The hydrothermal method is one of the simplest and cheapest ways to fabricate the materials using water soluble metal precursors at high pressure and temperature. Using this method, not only powder samples can be fabricated, but it also allow materials to be grown on different substrates.<sup>64,77</sup> Another easy and effective procedure to obtain pure and homogeneous nanomaterials is sol-gel.<sup>177</sup> The concentration of the component, solvents, temperature and reaction time are the main factors to determine the purity, homogeneity and porosity of the final product. Electrochemical deposition is a process by which a thin and tightly adherent desired coating of metal, oxide, or salt can be deposited onto the surface of a conductor substrate by simple electrolysis of a solution

containing the desired metal ion or its chemical complex. Electrochemical deposition of metals and alloys involves the reduction of metal ions from aqueous, organic, and fused-salt electrolytes.<sup>178</sup>

## 2.5.1 Metal oxide based materials

It is well accepted that metal oxides are promising materials for energy storage devices due to their high theoretical capacity (NiO<sup>179</sup> 359 mAh g<sup>-1</sup>/ 2584 F g<sup>-1</sup>, Co<sub>3</sub>O<sub>4</sub><sup>180</sup> 445 mAh g<sup>-1</sup>/ 3560 F g<sup>-1</sup>), controllable structure and simple fabrication methods.<sup>181</sup> Nickel oxide has been widely investigated because of its low cost, easy synthesis, and environmental friendliness.<sup>75</sup> Figure 2.4a shows the CV graph of NiO in 1 M KOH electrolyte at different scan rates. Two obvious redox peaks indicate the electron transfer and the valence change of the nickel during the process. The peak shifted with increasing the scan rate exhibit the quasi-reversible reaction of nickel oxide. The Faradaic reaction of NiO in alkaline electrolyte is:



**Equation 2.3**

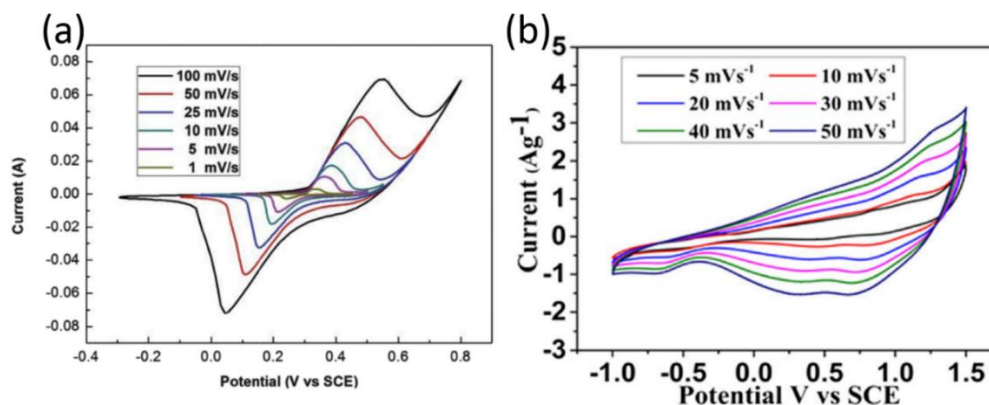


**Figure 2.4** Cyclic voltammograms of (a) NiO film electrode at different scan rates in 1 M KOH aqueous solution,<sup>182</sup> (b) NiO/CFC nanostructure at different scan rates in 1 M TEABF<sub>4</sub>/PC organic electrolyte.<sup>75</sup>

The maximum capacitance (2018 F g<sup>-1</sup> at 2.27 A g<sup>-1</sup>) of NiO was obtained by Zhiyi et al,<sup>61</sup> and the rate capacity was over 76% (1536 F g<sup>-1</sup> at 22.7 A g<sup>-1</sup>). NiO also showed

stable electrochemical activity in organic electrolyte (1 M TEABF<sub>4</sub> Figure 2.4b)<sup>75</sup>. The assembled symmetric device demonstrated a wide potential window of 2 V with a good energy density of 19.4 Wh kg<sup>-1</sup>.

Similarly, cobalt oxide has attracted much attention due to its various nanostructure possibilities (Figure 2.5) and excellent reversible redox behaviour during the chemical reactions. Co<sub>3</sub>O<sub>4</sub> nanotubes displayed good specific capacitance of 574 F g<sup>-1</sup> in 6 M KOH solution,<sup>183</sup> while Co<sub>3</sub>O<sub>4</sub> nanowires delivered a high specific capacitance of 1525 F g<sup>-1</sup>.<sup>62</sup>

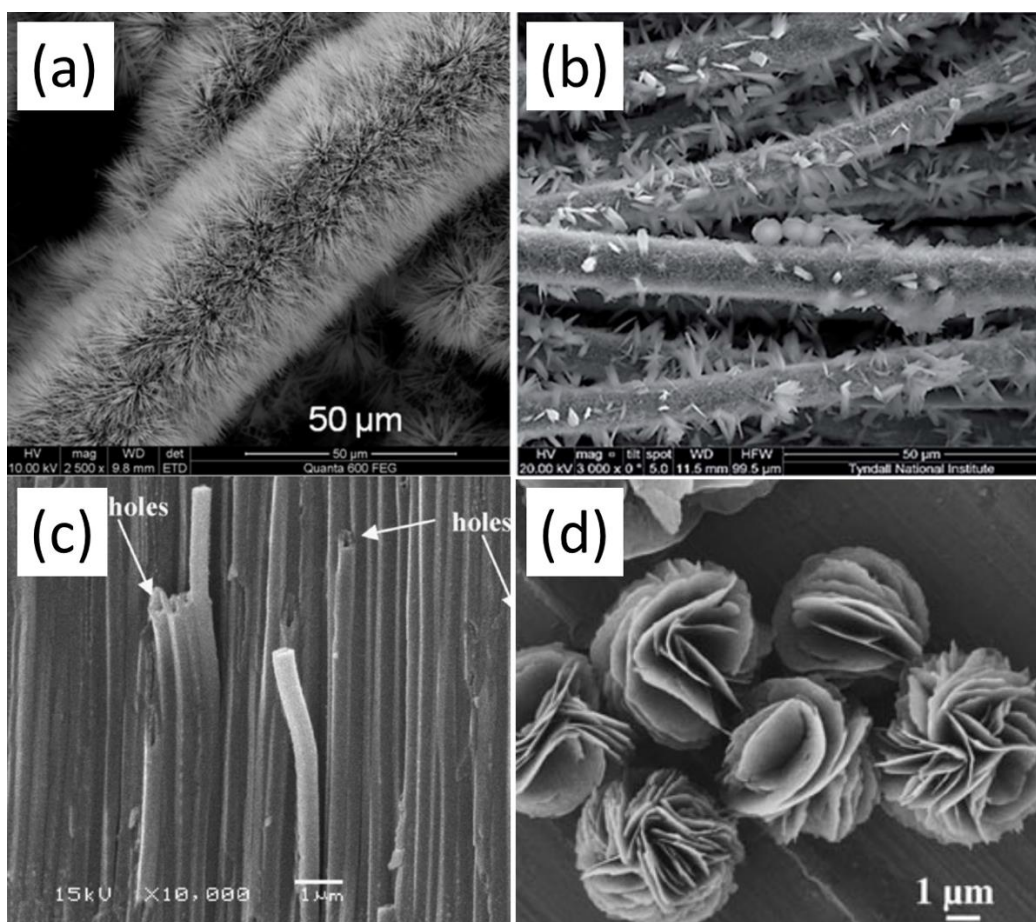


**Figure 2.5** Different nanostructured cobalt oxide materials. <sup>62,76,183,184</sup>

Instead of single metal oxides, binary transition metal oxides have drawn attention as active materials for energy storage device, which possess multiple oxidation states to realize multiple redox reactions. Different binary transition metal oxides have been

reported to exhibit better electrochemical properties than single component metal oxides, such as  $\text{NiFe}_2\text{O}_4$ <sup>185</sup>,  $\text{FeCo}_2\text{O}_4$ <sup>186</sup>,  $\text{NiCo}_2\text{O}_4$ <sup>187</sup> with a high specific capacitance of  $1135.5 \text{ F g}^{-1}$ ,  $2445 \text{ mA h g}^{-1}$ , and  $506 \text{ F g}^{-1}$ . These materials show unique performance due to the coexistence of two different cations in highly porous nanoflake/nanoflower structure (Figure 2.6). The surface area of binary metal oxides may be larger than single metal oxides, thereby it may enhance the overall electrochemical performance of the electrode materials.

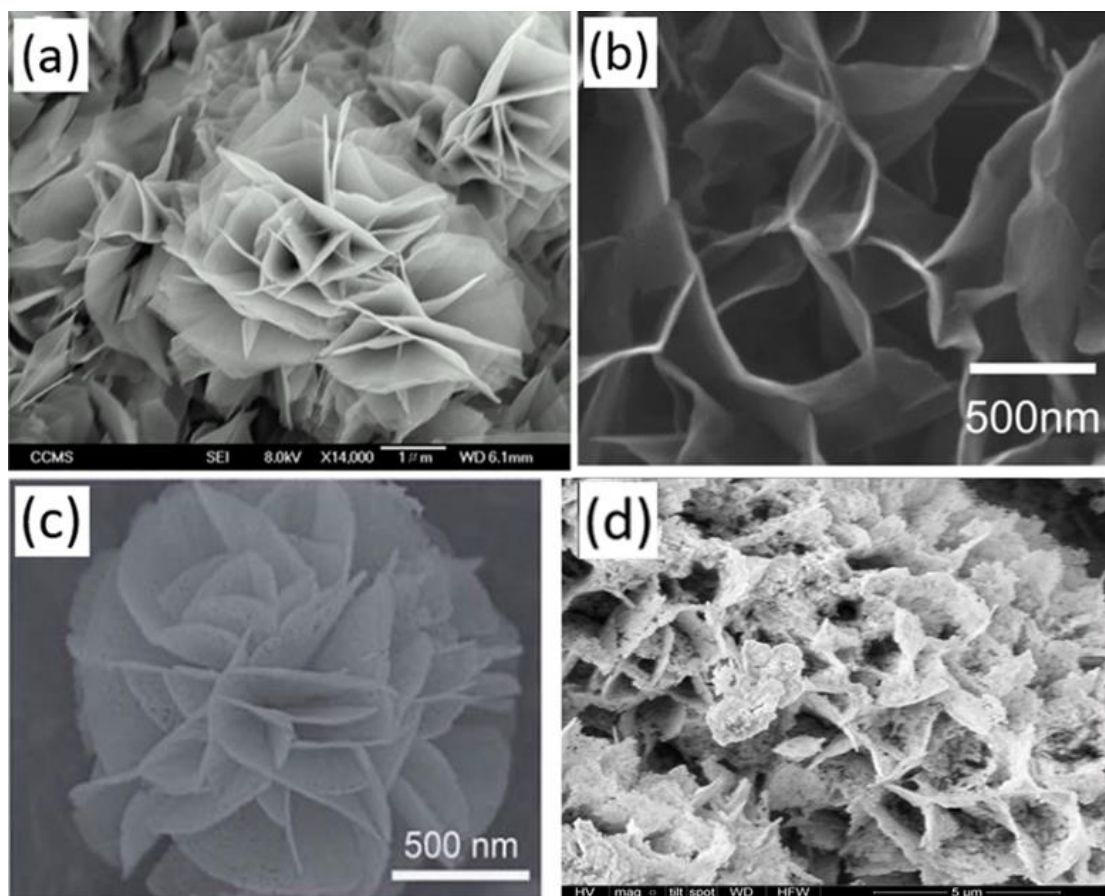


**Figure 2.6** (a) SEM image of  $\text{FeCo}_2\text{O}_4$ -Nanoflowers on nickel foam after calcination at  $400 \text{ }^\circ\text{C}$  for 2 h in air, (b) SEM image of  $\text{NiCo}_2\text{O}_4$  nanosheets after calcination at  $200 \text{ }^\circ\text{C}$  for 3 h in air, (c) SEM image of  $\text{NiCo}_2\text{O}_4$  nanoflowers (d) SEM image of  $\text{CoMoO}_4$  nanoflakes structure on carbon fibre cloth.<sup>77,186-188</sup>

Among different types of binary systems,  $\text{NiCo}_2\text{O}_4$  is one of the most investigated materials due to its much better electrical conductivity and higher electrochemical

activity compared to monometallic nickel oxide or cobalt oxide. However, due to the powder-form of this material, to fabricate the bulk electrode requires a polymer binder, which hinders the electron transport from the oxide materials to the current collector. Thus the ion transport kinetics in the electrode and electrolyte is limited. To solve this issue, growing the materials over a conductive substrate becomes an attractive choice. Yunhuai et al.<sup>189</sup> reported the fabrication of self-supported Ni-Co oxide nanowires grown on TiO<sub>2</sub> nanotubes. By controlling the molar ratio of 1:1, the specific capacitance of single electrode was calculated to be 2545 F g<sup>-1</sup> while the theoretical capacitance was calculated to be 3108 F<sup>-1</sup>. A symmetric device based on this material was also investigated. Due to the limited diffusion space in a two electrode system, the lab handmade cell only demonstrated 187 F g<sup>-1</sup> at current density of 1A g<sup>-1</sup>.

Since both nickel and cobalt are heavy metals and are harmful to the environment, an abundance, cheap, and environmentally friendly metal such as iron becomes an ideal candidate to replace nickel or cobalt in NiCo<sub>2</sub>O<sub>4</sub>. Due to serious aggregation and low specific surface area of active sites, both NiFe<sub>2</sub>O<sub>4</sub> and FeCo<sub>2</sub>O<sub>4</sub> were reported as grown on some 3-dimensional conductive substrates like nickel foam or carbon fibre cloth. Hong et al. fabricated high performance NiFe<sub>2</sub>O<sub>4</sub> nanoparticles over carbon cloth with a specific capacitance of 1032 F g<sup>-1</sup> in H<sub>2</sub>SO<sub>4</sub> and 871 F g<sup>-1</sup> in KOH.<sup>185</sup> In addition, after 3000 cycles, the capacitance remains more than 91% in both electrolyte systems. In the case of PVA-H<sub>2</sub>SO<sub>4</sub> gel electrolyte based symmetric device, an energy density of 2.07 mW h cm<sup>-3</sup> was calculated at 2 mA cm<sup>-2</sup>. Even at a current density of 10 mA cm<sup>-2</sup>, the energy density remains at 0.56 mW h cm<sup>-3</sup>.

Compared to carbon materials, metal oxide materials give higher specific capacitance because of the different mechanism of chemical redox reaction. However, the surface area of metal oxide materials are limited to 300 m<sup>2</sup> g<sup>-1</sup>, mostly around 100 m<sup>2</sup> g<sup>-1</sup> or even less. Due to the big atom size, aggregated particles form by the fabrication method, and the small pore on the layer-by-layer structure, increasing the surface area becomes a big challenge for metal oxide materials. Recently, much effort was focused on

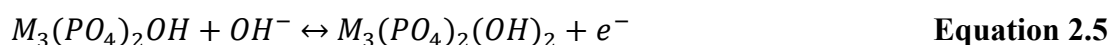
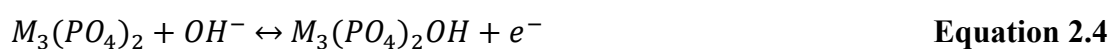
developing core-shell structured material such as  $\text{MnCo}_2\text{O}_4@\text{Ni}(\text{OH})_2$ <sup>190</sup>,  $\text{NiCo}_2\text{S}_4$  nanosheets@ $\text{NiCo}_2\text{S}_4$  nanotube<sup>191</sup>. These hybrid electrodes exhibit a significant improvement on the surface area and further improves the electrochemical properties of the material.

## 2.5.2 Metal phosphate based materials

Metal phosphate based materials exhibit huge potential as promising electrode material for energy storage devices. Phosphorus can react with most of the elements in the periodic table to form various phosphides and phosphates. Many lithium metal phosphates have already been commercialized in battery manufacturing,<sup>192,193</sup> while nickel or/and cobalt phosphates were widely investigated in the past decade as positive electrode for hybrid devices. The phosphates present good ion conductivity and charge storage capacity due to the open structure with large channels and cavities,<sup>194</sup> and good chemical stability according to the covalent bonds of P-O.

In general, metal phosphate electrodes are synthesised via simple hydrothermal process with controllable synthesis temperature, fabrication time, and other conditions. Various structures can be obtained such as nanoparticles, nanoflakes, nanoflowers, and nanorods. (Figure 2.7). Other methods such as chemical precipitation and aqueous-based reflux can also be applied due to the low cost and simple process, and the structure and morphology can be modified by an extra calcination process to obtain highly stable phosphates.<sup>195,196</sup>

The phosphate-based materials exhibit a pseudo-battery type behaviour similar to the oxide based materials. The Faradaic reaction of metal phosphate in alkaline electrolyte is as follows:





where,  $M$  represent transition metals like Ni, Co, etc.

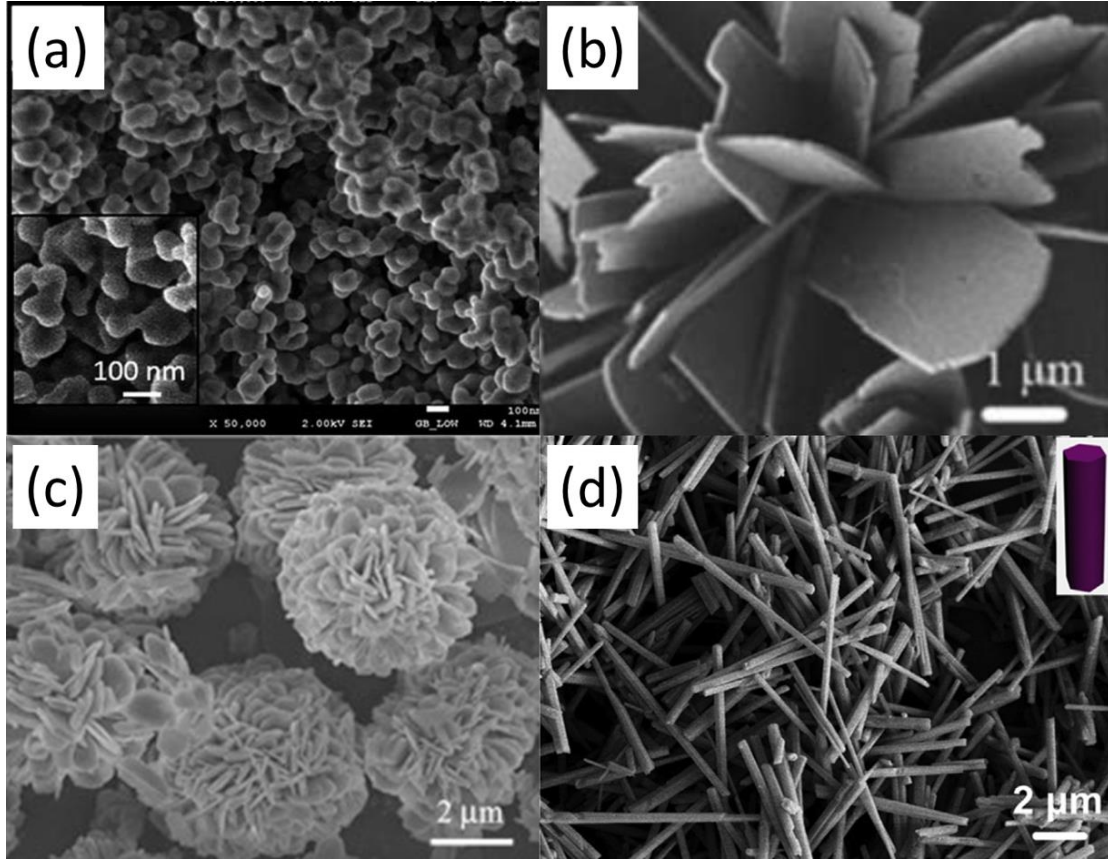


**Figure 2.7** SEM images of (a) nickel phosphate nanoparticles, (b)nickel phosphate nanoflakes, (c) cobalt phosphate nanoflowers, and (d) cobalt phosphate nanorods.<sup>197-200</sup>

To date, a specific capacitance of 1876 and 1578 F g<sup>-1</sup> have been achieved for nickel and cobalt phosphates.<sup>66,201</sup> The nickel-cobalt binary phosphates demonstrate higher electrochemical performance due to the synergistic effect of nickel-cobalt species. Thereby, the Ni<sub>3</sub>P<sub>2</sub>O<sub>8</sub>-Co<sub>3</sub>P<sub>2</sub>O<sub>8</sub> nano/ microflower achieved 1980 F g<sup>-1</sup> in 6 M KOH solution with excellent cyclic stability over 90% after 1,000 cycles.<sup>202</sup> Table 2.5 presents a comparison of electrochemical performance for different metal phosphate based electrode in three electrode configuration. There still remain doubts on how many electrons are transferred during the redox reaction for this phosphate. Thereby, further in-situ characterizations are crucial to understand the behaviour of the phosphates in

the chemical redox process.

**Table 2.5** Comparison of electrochemical performance for different metal phosphate based electrode in three electrode configuration.

Material	Electrolyte	Specific Capacitance	Applied Current	Cycles	Retention	Ref
		F g <sup>-1</sup>	A g <sup>-1</sup>		%	
(NH <sub>4</sub> )(NiCo)PO <sub>4</sub> ·0.67H <sub>2</sub> O	6M KOH	1128	0.5	5000	95.6	203
Co <sub>0.4</sub> Ni <sub>1.6</sub> P <sub>2</sub> O <sub>7</sub>	3M KOH	1259	1.5	1000	34.09	204
Co <sub>0.86</sub> Ni <sub>2.14</sub> (PO <sub>4</sub> ) <sub>2</sub>	2M KOH	1409	0.25	2500	57.8	205
Co <sub>11</sub> (HPO <sub>3</sub> ) <sub>8</sub> (OH) <sub>6</sub>	3M KOH	312	1.25	3000	89.4	206
Co <sub>2</sub> P <sub>2</sub> O <sub>7</sub>	3M KOH	367	0.625	3000	96.2	196
Co <sub>3</sub> (PO <sub>4</sub> ) <sub>2</sub>	3M KOH	210	10 mVs <sup>-1</sup>	800	95	207
Co <sub>3</sub> (PO <sub>4</sub> ) <sub>2</sub>	3M KOH	1174	2	-	-	208
Co <sub>3</sub> (PO <sub>4</sub> ) <sub>2</sub> ·8H <sub>2</sub> O	3M KOH	350	1	500	102	199
CoHPO <sub>4</sub> ·3H <sub>2</sub> O	3M KOH	413	1.5	3000	85.1	175
MOF-Ni <sub>x</sub> P <sub>y</sub> O <sub>2</sub>	2M KOH	1627	1	2000	76.82	195
NH <sub>4</sub> Co <sub>2</sub> Ni <sub>3</sub> PO <sub>4</sub> ·H <sub>2</sub> O	3M KOH	1567	1	3000	97.6	209
NH <sub>4</sub> CoPO <sub>4</sub> ·H <sub>2</sub> O	3M KOH	662	1.5	3000	92.7	210
NH <sub>4</sub> CoPO <sub>4</sub> ·H <sub>2</sub> O	3M KOH	369.4	0.625	400	99.7	200
Ni <sub>11</sub> (HPO <sub>3</sub> ) <sub>8</sub> (OH) <sub>6</sub>	3M KOH	558	0.5	10000	97.6	211
Ni <sub>11</sub> (HPO <sub>3</sub> ) <sub>8</sub> (OH) <sub>6</sub>	3M KOH	1876	0.625	2000	95	201
Ni <sub>2</sub> P <sub>2</sub> O <sub>7</sub>	3M KOH	1050	0.5	6000	90.5	212
Ni <sub>3</sub> (PO <sub>4</sub> ) <sub>2</sub>	3M KOH	265	20 mVs <sup>-1</sup>	1000	97	213
Ni <sub>3</sub> P <sub>2</sub> O <sub>8</sub> -Co <sub>3</sub> P <sub>2</sub> O <sub>8</sub>	6M KOH	1980	0.5	1000	90.9	202
Ni <sub>x</sub> Co <sub>3-x</sub> (PO <sub>4</sub> ) <sub>2</sub>	1M KOH	940	1	1000	84.5	214
Ni <sub>x</sub> Co <sub>3-x</sub> (PO <sub>4</sub> ) <sub>2</sub>	3M KOH	1132	1	8000	93	215

### 2.5.3 Other materials

Other materials like sulphides and phosphides have also been studied in the past decades.<sup>216,217</sup> Ni<sub>3</sub>S<sub>2</sub> coated indium tin oxide core-shell structures exhibited excellent capacitance of 1865 F g<sup>-1</sup> and the assembled symmetric devices delivered a maximum energy density of 1.02 mWh cm<sup>-3</sup>.<sup>216</sup> Ni<sub>1-x</sub>Zn<sub>x</sub>S multilayers showed a capacitance of 1815 F g<sup>-1</sup> and the complete cell demonstrated a specific energy of 38.9 Wh kg<sup>-1</sup>.<sup>217</sup> In addition, NiP amorphous delivered a capacitance of 1597.5 F g<sup>-1</sup> at an applied current of 0.5 A g<sup>-1</sup>, and ~50% of the capacitance remained when the current increased to 8 A g<sup>-1</sup>. An asymmetric supercapattery was assembled using Co<sub>2</sub>P nanoflowers as positive electrode and graphene as the negative one. The device demonstrated a specific energy of 24 Wh kg<sup>-1</sup> with 97% retention after 6,000 charge-discharge cycles.<sup>218</sup> Interestingly, fluorides and chlorides offer a high theoretical specific and volumetric capacities so that they are investigated as supercapattery electrodes.<sup>12,219</sup> (Figure 2.8) A 3D nanoporous NiF<sub>2</sub>-dominant film was deposited on a flexible PET substrate, and produced a maximum capacitance of 66 mF cm<sup>-1</sup>.<sup>220</sup> A wide potential window of -1.4 V to 1.4 V was applied to convert NiF<sub>2</sub> to Ni(OH)<sub>2</sub> to obtain good electrochemical performance. However, conversion of NiF<sub>2</sub> and Ni(OH)<sub>2</sub> is not reversible so that it is hard to distinguish the contribution of fluoride and hydroxide in the system. Furthermore, the cyclic stability may be limited.

In summary, four categories of the supercapattery electrode materials were discussed in terms of their preparation process, microstructure, and electrochemical applications. Carbon based materials have extremely high stability during long charge-discharge cycles but suffer from the low capacitance and energy density. Battery type materials (for ion capacitors) are facing the safety issues due to the leakage of liquid electrolytes. Pseudo-battery type materials have a huge potential for supercapattery applications due to the abundant resources, high theoretical capacity, easy fabrication process, various morphologies, good cyclic stability, low toxicity, and environmental friendliness.

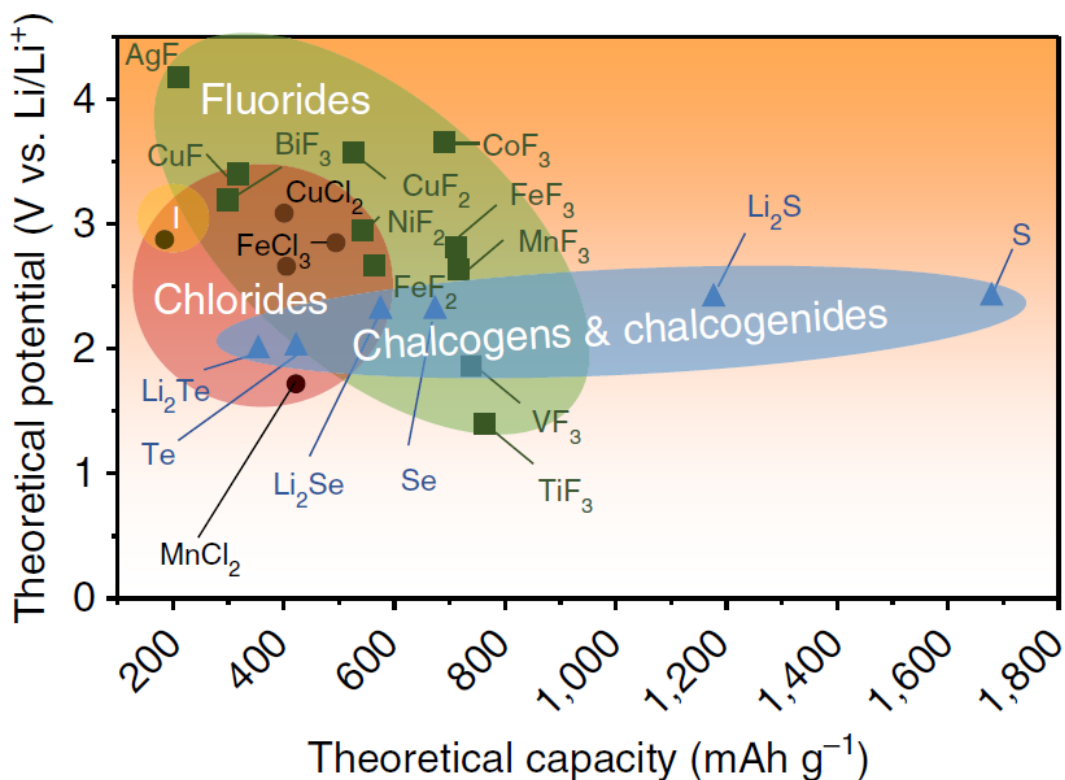


**Figure 2.8** Approximate range of average discharge potentials and specific capacity of some of the conversion-type cathodes.<sup>12</sup>

## 2.6 Supercapattery Performances

Different nanostructured electrode materials have been investigated recently as electrodes for the fabrication of supercapattery cell. However, to bring a material study to a commercial product is a long process and therefore, fabrication of complete supercapattery cells in the lab has started to draw more attention in recent years. Both the symmetric (using same material) and asymmetric (pairing different materials) supercapattery cells were reported and the asymmetric cells give better electrochemistry properties due to the combination of two different materials, which can easily broaden the potential window and enhance the performance of the complete cell.

### **2.6.1 Selection of Electrode Materials and Electrolytes**

Since one specific material normally displays either positive or negative working potentials in the specific electrolyte, a large potential range may be obtained by combining a positive potential material and a negative one. Notably, supercapattery attracted much interest because it combines two different mechanism in one system. The benefit of building a hybrid device is to obtain high energy from the battery-type/pseudo-battery type material and coupling this with the ability to deliver high power from supercapacitor-type material is attractive for the energy storage community. As a capacitive material, activated carbon is now the most popular electrode for both hybrid supercapatteries and ion capacitors due to its excellent electrochemical performance in inorganic, organic and ionic electrolytes. Interestingly, the material behaves differently in different electrolytes, which is related to the different reaction mechanism, diffusion efficiency, and charge transfer efficiency. Thereby, it is crucial to select an electrolyte which is suitable for both electrode materials. Overall, aqueous electrolytes are widely used in various energy storage devices due to their high conductivity and high ionic concentration.<sup>221</sup> However, the aqueous electrolytes suffer from small working potential windows, which limits the energy capability. Organic electrolytes can offer a wider working potential, but may cause serious safety issues, while ionic liquids have an acceptable conductivity and are not flammable, they are not cost-effective.<sup>222</sup> Thereby, the understanding and optimisation of electrode pairings and electrolyte selection are needed to be explored further through fundamental study on their electrochemical mechanism.

### **2.6.2 Comparison of Different Types of Supercapatteries**

Much effort has been made in studying ion capacitors and hybrid supercapatteries. Both of these devices belong to supercapattery group (as discussed in chapter 1.2.1-1.2.2), but the energy storage mechanism and electrochemical properties are significantly different. In general, the hybrid ion capacitor couples a high capacity bulk intercalation

based battery-style negative electrode and a high rate surface adsorption based capacitor-style positive electrode. The anode material is usually a Li/ Na doped material, while the cathode materials are usually carbon based materials and the electrolyte is an organic electrolyte with dissolved lithium/ sodium ion salt. The energy storage mechanism in ion capacitors is dominated by intercalation/ de-intercalation mechanism like a lithium/ sodium ion battery. However, the hybrid supercapattery is another type of storage device, which has no intercalation/ de-intercalation ions in the system. In supercapattery, the energy storage mechanism is a diffusion controlled reversible redox reaction on the electrode surface. Thereby, ion capacitors exhibit several times higher energy than the hybrid supercapattery, but the latter can survive more than 10,000 charge/ discharge cycles. Table 2.6 enumerates the differences between the two different supercapatteries.

**Table 2.6** Comparison of ion capacitor and supercapattery.

<b>Specification</b>	<b>Ion Capacitor</b>	<b>Hybrid Supercapattery</b>
Positive Electrode	Ion adsorption electrode	Metal oxide/sulphate/phosphate, etc.
Negative electrode	Li/Na doped electrode	Activated carbon or other material with negative window
Electrolyte	Organic electrolyte with dissolved lithium/sodium ion salt	Inorganic aqueous solution KOH/NaOH/H <sub>2</sub> SO <sub>4</sub>
Mechanism	intercalation/de-intercalation	Non-capacitive Faradaic redox reaction

## 2.7 Prospects and Future

The study of supercapattery has entered a high-speed development period through the development of electrode materials and complete cells. However, the following aspects are needed to be considered during the development of a complete cell: packaging volume, packaging materials, electrolyte materials, operating temperature range,

environmental friendliness, large scale production, toxicity, cost, safety, and reliability. The specific energy/ energy density would decrease tremendously by considering the whole packaging mass and volume when comparing to the values calculated from the mass and area of the active materials and electrodes. Another issue is that previous research was carried out under an ideal repeatable process, for instance, charging/ discharging measurements were operating under a fully or half voltage window setup. However, it is sometimes impossible to achieve a fully charged or discharged condition in the real life. Thereby, more investigation under realistic condition are needed, including various partial charge/ discharges, self-leakage current testing and the performance under a wide range of temperatures.

# Chapter 3 Fabrication and Material Characterization

## 3.1 Introduction

For the specific application as the energy storage device of the next generation self-charged pacemaker, the supercapattery device should work effectively, steadily, and safely inside the human body for at least 15 to 20 years, which requires the nano/ micro structure to offer high capacity and excellent stability. The aim of this task is to develop novel electrode materials with enhanced electrochemical performance to be used as supercapattery electrodes. Three dimensional network structured nickel foam substrates have recently attracted great attention owing to the high surface area to volume ratio offered by the highly porous structure. A nanostructured electrode material is grown over a nickel foam homogenously, which can bring drastic variations in the capacitive nature of electrode material and consequently increase the energy capacity of the supercapattery device.

Precipitating nanoparticles from a solution of chemical compounds can be classified into several major categories such as colloidal methods, sol-gel processing, water-oil micro-emulsions, hydrothermal synthesis and polyol method. Hydrothermal method was carried out for the nanomaterial synthesis, due to the low cost, simple operation and fully controllable variables (temperature, pressure and composition)<sup>223</sup>. The following Table 3.1 shows the parameters of nanostructured materials synthesis process. Further fabrication process and characterizations of each material are discussed in this chapter.

**Table 3.1** Parameters of the fabricated nanostructured materials.

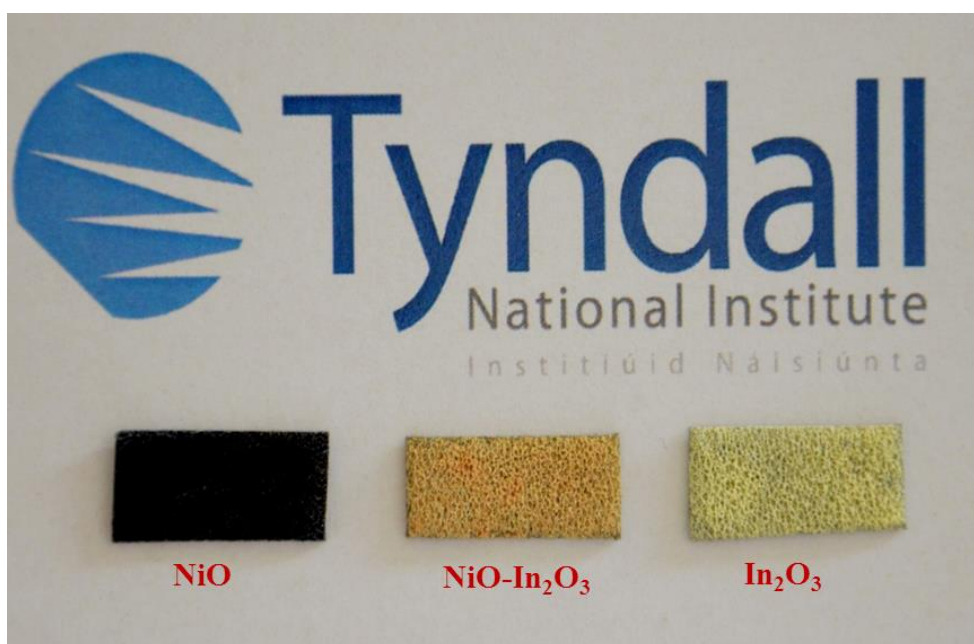
Material	Cation	Anion	Substrate	Temperature rate (°C/ h)	Temperature (°C)	Time (h)
NiO-In <sub>2</sub> O <sub>3</sub>	5 mM Ni <sup>2+</sup> 10 mM In <sup>3+</sup>	Urea	NF	1.5	120	12
Co <sub>3</sub> (PO <sub>4</sub> ) <sub>2</sub> ·8H <sub>2</sub> O	2.5 mM CO <sup>2+</sup>	2.5 mM PO <sub>4</sub> <sup>3-</sup>	NF	1.5	120	8
Ni <sub>3</sub> (PO <sub>4</sub> ) <sub>2</sub> ·8H <sub>2</sub> O	10 mM Ni <sup>2+</sup>	10 mM PO <sub>4</sub> <sup>3-</sup>	NF	1.5	120	4
Co <sub>3</sub> (PO <sub>4</sub> ) <sub>2</sub>	2.5 mM CO <sup>2+</sup>	2.5 mM PO <sub>4</sub> <sup>3-</sup>	NF	0.5	120	8

## 3.2 NiO-In<sub>2</sub>O<sub>3</sub> Microflower (3D)/ Nanorod (1D) Hetero-Architecture on Nickel Foam

### 3.2.1 Synthesis and growth mechanism

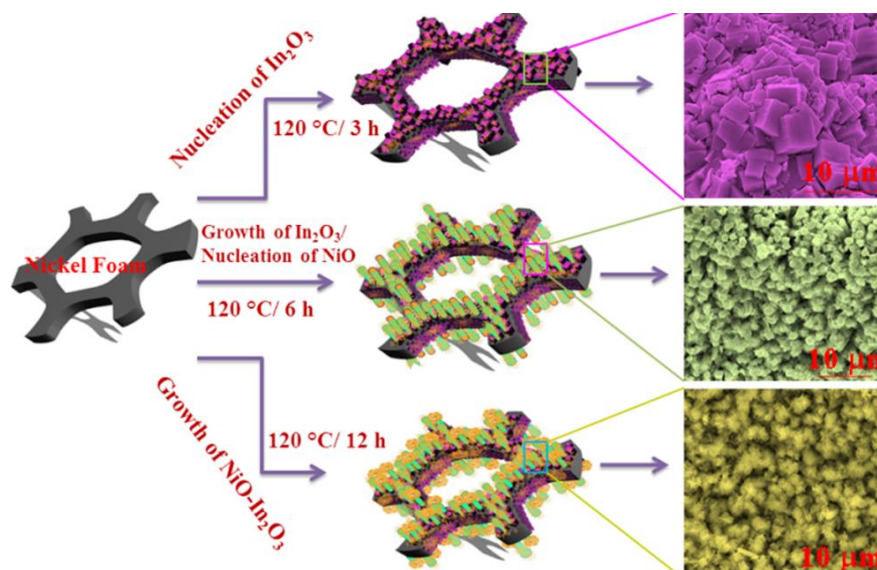
Growth of NiO-In<sub>2</sub>O<sub>3</sub> hybrid structure on nickel foam: nickel foam was cleaned ultrasonically in 3 M HCl, deionized (DI) water and ethanol for 15 min, respectively, and then dried in air. In a typical process, 0.1 g NiCl<sub>2</sub>·6H<sub>2</sub>O, 0.2 g of InCl<sub>3</sub>, 0.6 g of urea were dissolved into equal volume of DI water (40 ml) and ethanol (40 ml) mixed solvent to form a transparent green solution. After putting in a piece of cleaned nickel foam (4 cm × 4 cm), the solution was then transferred to a reaction vessel and kept at 120 °C for 12 h. After hydrothermal growth, the nickel foam covered with NiIn-precursor was carefully rinsed several times with de-ionized water, absolute ethanol and acetone with the assistance of ultrasonication, and finally dried in air. Then, the sample was put in a muffle furnace and calcined at 400 °C for 2 h to get well defined crystallized NiO-In<sub>2</sub>O<sub>3</sub> microflower/ nanorod hybrid structures on nickel foam. For the sake of comparison, pure NiO, In<sub>2</sub>O<sub>3</sub> and NiO-In<sub>2</sub>O<sub>3</sub> hybrid composites with different concentrations of Ni/ In (1:1 and 2:1) also prepared using the same procedure. The mass

of the hybrid structure on nickel foam was determined by subtracting the weight before deposition from the weight after deposition. Typical mass densities of active materials were about  $\sim 0.5 \text{ mg cm}^{-2}$ ,  $\sim 0.5 \text{ mg cm}^{-2}$ ,  $\sim 1.5 \text{ mg cm}^{-2}$ ,  $\sim 1.8 \text{ mg cm}^{-2}$  and  $\sim 1 \text{ mg cm}^{-2}$  for NiO-NF,  $\text{In}_2\text{O}_3$ -NF, NiO- $\text{In}_2\text{O}_3$ -NF (1:1), NiO- $\text{In}_2\text{O}_3$ -NF (1:2) and NiO- $\text{In}_2\text{O}_3$ -NF (2:1) respectively. Figure 3.1 shows the photograph of NiO, NiO- $\text{In}_2\text{O}_3$  (1:2) and  $\text{In}_2\text{O}_3$  grown on NF substrate.



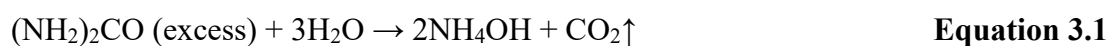
**Figure 3.1** Digital photograph of NiO, NiO- $\text{In}_2\text{O}_3$  (1:2) and  $\text{In}_2\text{O}_3$  grown on NF substrate.

To confirm the heterogeneous growth process, a time dependent synthesis was conducted using the same fabrication procedure with different timings of 3, 6 and 9 hours and the growth process is schematically represented in Figure 3.2. As evidenced from the time dependent experiments,  $\text{In}_2\text{O}_3$  nucleates first as nanocubes and then grows as 1D nanorods. Simultaneously, NiO nucleated as 2D nanosheets and subsequently into a 3D microflower-like hierarchical architecture possibly due to crystal-face attraction, van der Waals force and hydrogen bonds.<sup>224</sup>



**Figure 3.2** Schematic description NiO-In<sub>2</sub>O<sub>3</sub> hybrid structure growth process with the corresponding SEM images

Finally, at the end of calcination, a well-defined and stable NiO-In<sub>2</sub>O<sub>3</sub> hetero-microflower structure is formed as observed in the SEM images as shown in Figure 3.3 (a-f). After 3 h, only nanorods covered with irregular microcubes mainly composed of In<sub>2</sub>O<sub>3</sub> were present (Figure 3.3 (a and b)). At the end of 6 h, (Figure 3.3 (c and d)) a distinct microstructure of microcubes and nanoflowers are visible. Further increase of the growth time to 9 h, resulted in extensive growth of nano/ microflowers as seen in Figure 3.3 (e and f). At the end of 12 h, a typical 3D-1D hybrid microstructure was formed with the NiO-In<sub>2</sub>O<sub>3</sub> hetero-composite. The growth process can be explained by the following chemical processes:



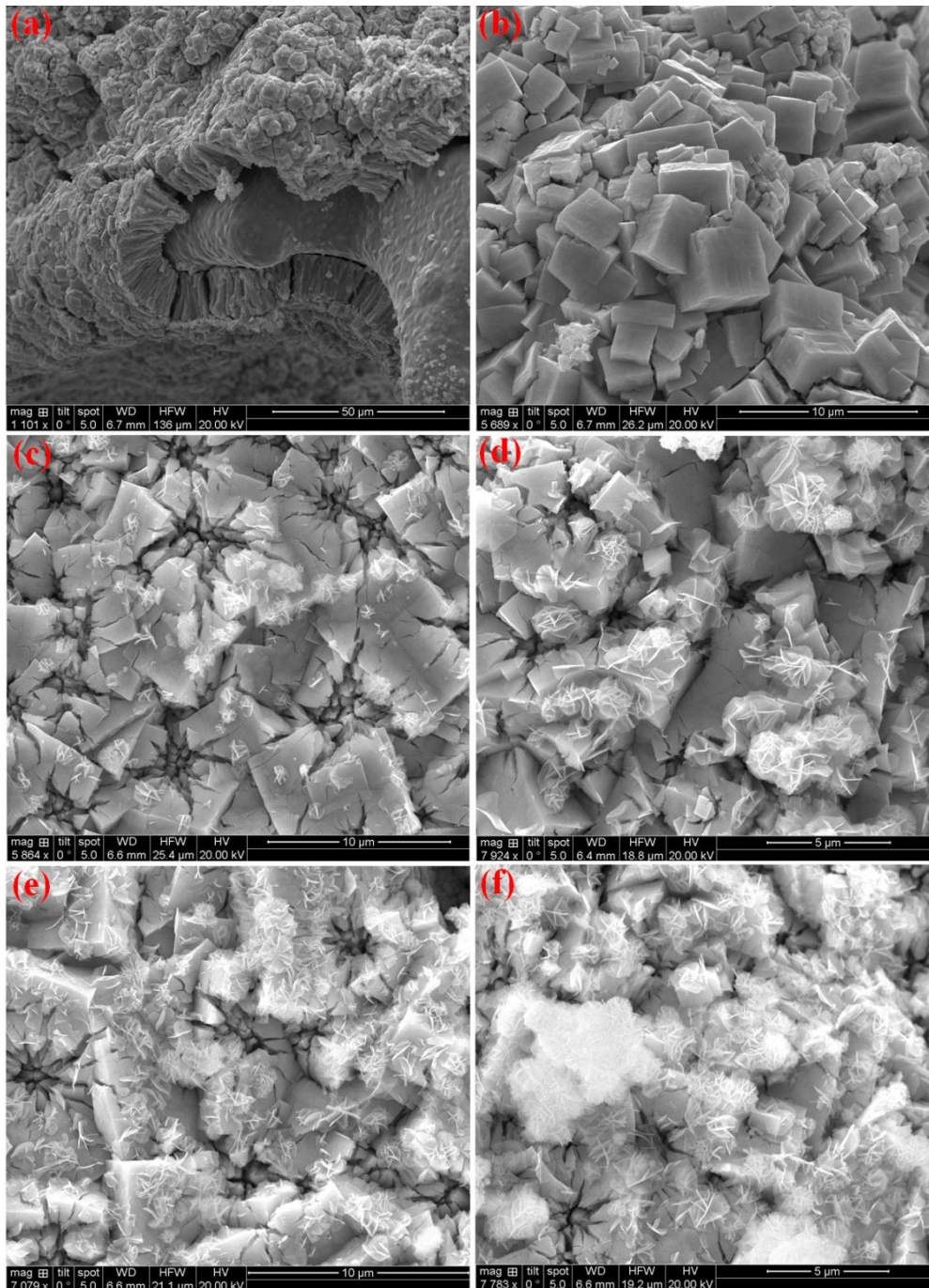


**Figure 3.3** (a-f) SEM images of NiO-In<sub>2</sub>O<sub>3</sub>-NF (1:2) hybrid structure captured at different time of growth 3 h (a & b), 6 h (c & d) and 9 h (e & f).

Generally, the hierarchical nanostructure can be grown under the surfactant mediated experimental conditions and the oriented attaching growth might be used to explain the formation mechanism.<sup>225</sup> Since the absence of surfactant during the synthesis, it is proposed the Oswald ripening mechanism for this anisotropic growth of hybrid

structure.<sup>225</sup> In this study, water/ ethanol mixed solvent and urea plays an important role in the formation of this hybrid microflower structure. It is reported that the polarity of the solvents can affect the dispersity of the reactants in the reaction medium, the nucleus formation in the products and their growth directions. Since the solvents are of different polarities, the less polar solvent could act as a surfactant over the metal-hydroxide surface and leads to the further particle assembly and their growth.<sup>226</sup> First, the hydrolysis of urea under mild (120 °C) hydrothermal condition, slowly produces the OH<sup>-</sup> ions in the reaction system.<sup>227,228</sup> The slow reaction rates lead to the low degree of supersaturation in solution and eventually the nucleation between metal (In<sup>3+</sup> and Ni<sup>2+</sup>) and OH<sup>-</sup> ions occurs. In this case, the nucleation occurs heterogeneously and forms the hybrid microstructure at the end.<sup>228-230</sup> To investigate this heterogeneous growth, pure NiO, In<sub>2</sub>O<sub>3</sub> and various composition of NiO-In<sub>2</sub>O<sub>3</sub> such as 1:1, 1:2 and 2:1 (Ni:In) have been grown over nickel foam under the same experimental conditions. Also, time dependent experiments were carried out for 1:2 (Ni:In) composition. The SEM images of the samples are shown in Figure 3.4 (a-d) and Figure 3.5 (a-i). From these figures it may be seen that the networked nanosheets like microstructure for pure NiO (Figure 3.4 (a and b)) and irregular aggregated nanocubes for pristine In<sub>2</sub>O<sub>3</sub> (Figure 3.4 (c and d)). Ultimately, all the Ni-In mixed composites exhibited the hybrid microstructure as shown in Figure 3.5 (a-i) indicating the heterogeneous growth of NiO-In<sub>2</sub>O<sub>3</sub> mixed oxide. These results were in good agreement with the time dependent experiments as discussed earlier.

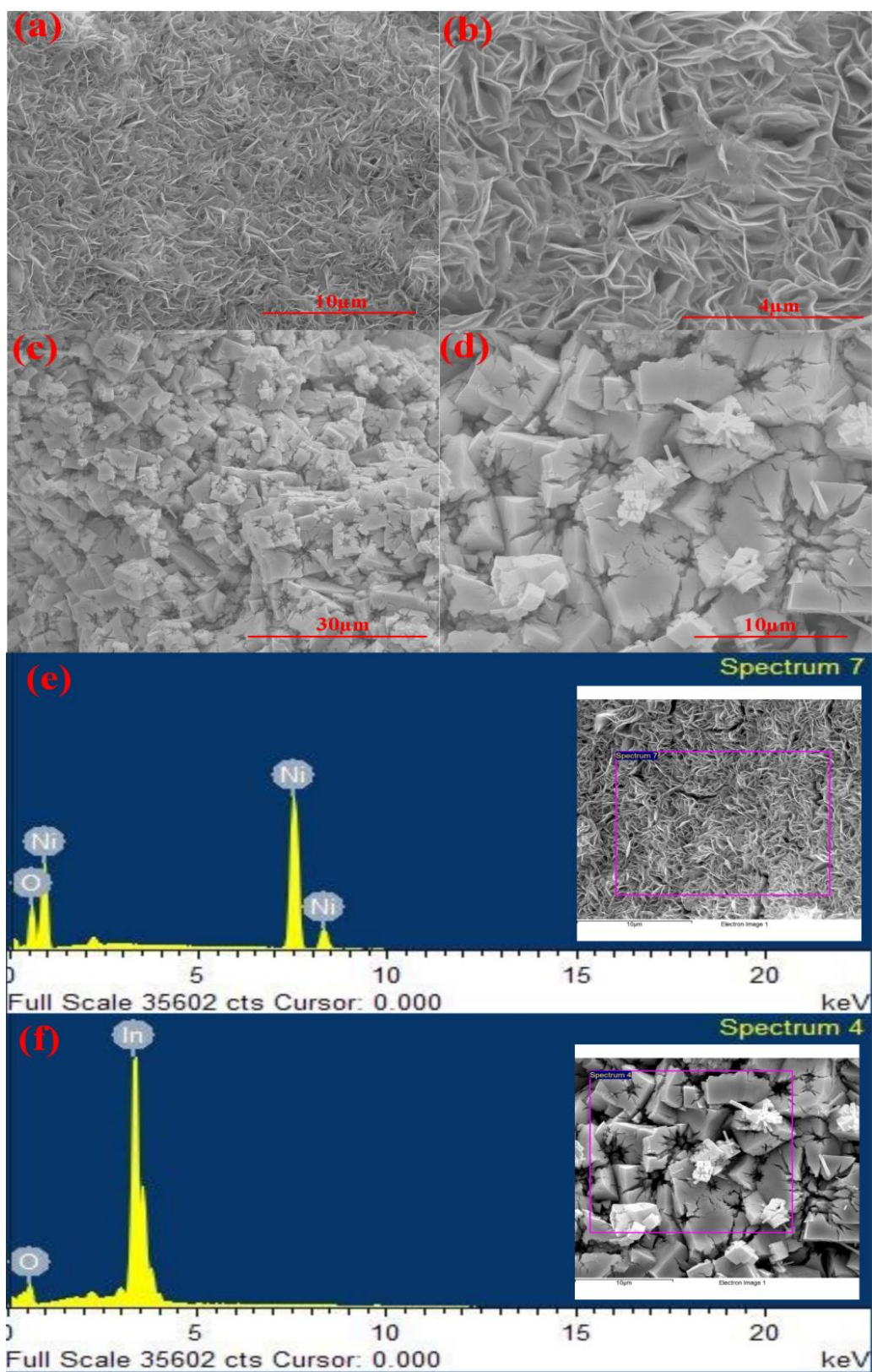


**Figure 3.4** SEM images of pure NiO-NF (a and b) and pure In<sub>2</sub>O<sub>3</sub>-NF (c and d). EDX spectrum of (e) pure NiO-NF and (f) Pure In<sub>2</sub>O<sub>3</sub>-NF.

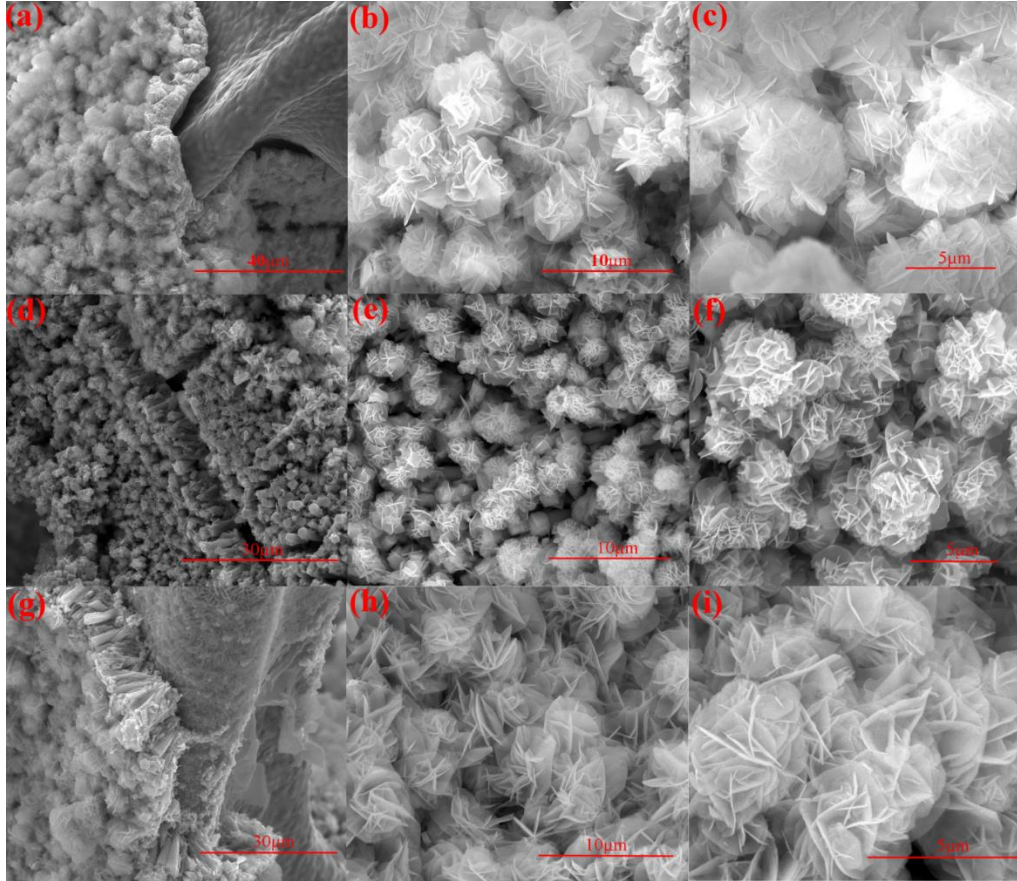


**Figure 3.5** (a-i) SEM images of NiO-In<sub>2</sub>O<sub>3</sub>-NF composites at various concentration of Ni and In, (a-c) 1:1, (d-f) 1:2 and (g-i) 2:1 at different magnifications.

### 3.2.2 Structure Analysis (XRD and Raman)

To understand the crystal structure and phase of NiO-In<sub>2</sub>O<sub>3</sub> hetero-structure, powder X-ray diffraction (XRD) was used. Figure 3.6 shows the XRD patterns of pure nickel foam and nickel indium oxide heterostructure (Ni:In/1:2) before and after calcination. In the mixed oxide, well-defined diffraction peaks are observed, which indicates the crystalline nature of the compound. Before the heat treatment at 400 °C, mixed hydroxide phases of In(OH)<sub>3</sub> and Ni(OH)<sub>2</sub> can be indexed to the corresponding JCPDS cards (#06-0202 and #22-0444).<sup>228,231</sup> Also some of the un-assigned peaks ( $\approx 49^\circ$ ,  $53.3^\circ$ ,  $54.5^\circ$ ,  $56.3^\circ$ ,  $71.6^\circ$  and  $75.9^\circ$ ) can be visible in the mixed hydroxides due to intercalated charge balancing anions (i.e. CO<sub>3</sub><sup>-</sup>, Cl<sup>-</sup>) or water molecules.<sup>232</sup> After calcination, the hydroxides phases were completely converted to oxide phases, as evidenced from the

corresponding EDX elemental mapping analysis that correlates composition to structural morphology.

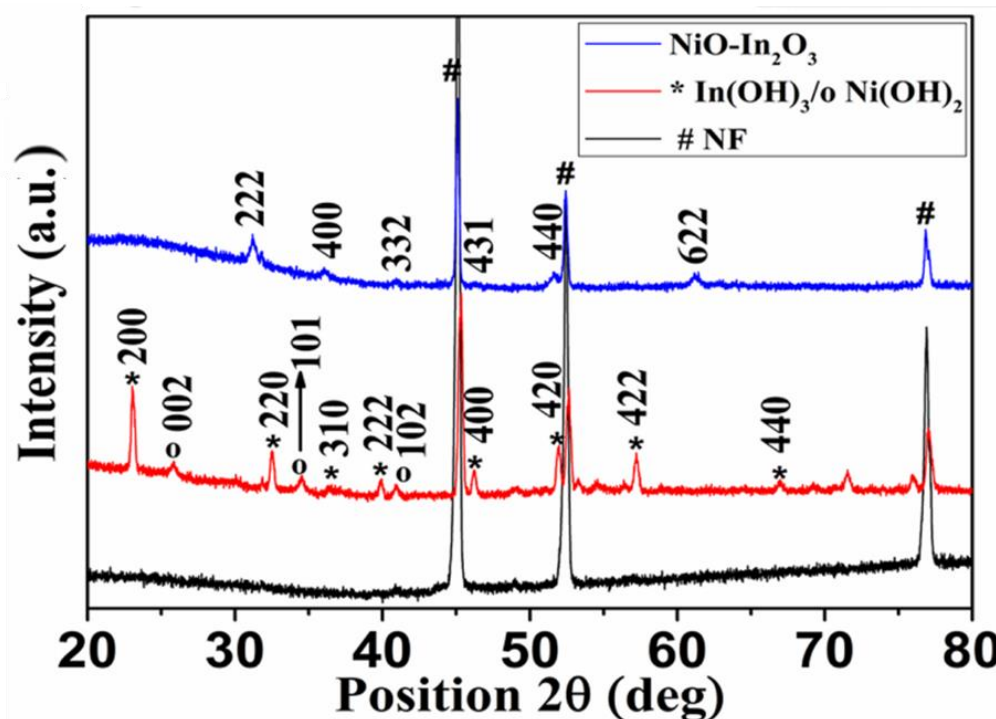


**Figure 3.6** XRD patterns of NiO-In<sub>2</sub>O<sub>3</sub>-NF (1:2) hybrid structure before and after calcination at 400 °C for 2 h.

When compared to pure monometallic oxides, the diffraction peaks in the XRD pattern of nickel indium oxide is well-matched to the cubic In<sub>2</sub>O<sub>3</sub> phase (JCPDS # 06-0416)<sup>225,232</sup> as shown in Figure 3.7 (a). Interestingly, there is no evidence of Ni based secondary phases in the NiO-In<sub>2</sub>O<sub>3</sub> samples after calcination and it may be due to either the diffusion of Ni into the In<sub>2</sub>O<sub>3</sub> lattice or insufficient/ amorphous NiO phase formation, which is below the detection limit of the XRD (Figure 3.7 (b)).<sup>233</sup> The crystallite size of the hybrid material was estimated using Debye-Scherrer equation:  $D = \frac{K\lambda}{\beta \cos \theta}$ <sup>234</sup>, where  $D$  is the mean size of crystallites (nm),  $K$  is crystallite shape factor (a good approximation is 0.9),  $\lambda$  is the X-ray wavelength ( $\lambda = 1.5406 \text{ \AA}$ ),  $\beta$  is the full width at half the maximum (FWHM) in radians of the X-ray diffraction peak and  $\theta$  is the Bragg's angle (degree). The average diameter of the crystallites was found to be ~15.7 nm for

NiO-In<sub>2</sub>O<sub>3</sub> composite.

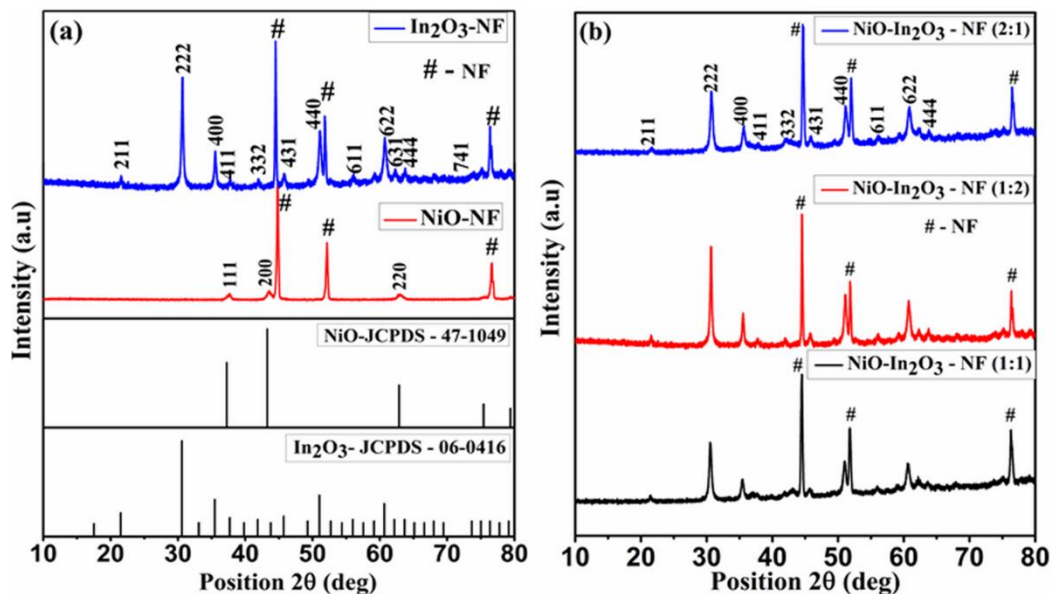


**Figure 3.7** (a) XRD pattern of pure NiO-NF and In<sub>2</sub>O<sub>3</sub>-NF with their stand JCPDS patterns and (b) XRD pattern of NiO-In<sub>2</sub>O<sub>3</sub>-NF composites prepared using different Ni/In concentrations.

It is well recognized that Raman spectroscopy as a powerful tool to ascertain the secondary phases in the composites. Figure 3.8 shows the Raman spectra of NiO-NF, In<sub>2</sub>O<sub>3</sub>-NF and NiO-In<sub>2</sub>O<sub>3</sub>-NF with different compositions. In the Raman spectra of NiO-NF sample, NiO shows two broad absorption bands at  $\sim 500\text{ cm}^{-1}$  and  $1060\text{ cm}^{-1}$  correspond to the Ni-O stretching. Similarly, the In<sub>2</sub>O<sub>3</sub>-NF shows the vibrational modes at  $131, 306, 367, 497$  and  $630\text{ cm}^{-1}$ , associated to the vibrations of body centred cubic In<sub>2</sub>O<sub>3</sub> structure. In the NiO-In<sub>2</sub>O<sub>3</sub>-NF mixed oxides, a considerable variation in the peak positions is observed, especially in the frequency region around  $450\text{--}650\text{ cm}^{-1}$  (marked as a circle in Figure 3.8) compared to their mono-metallic oxides. These peak-shifts are due to the interaction between NiO and In<sub>2</sub>O<sub>3</sub>. Also, the peaks due to the Ni-O stretching at  $557\text{ cm}^{-1}$  and  $1060\text{ cm}^{-1}$  in the mixed oxide further confirm the formation NiO-In<sub>2</sub>O<sub>3</sub> nanocomposite.

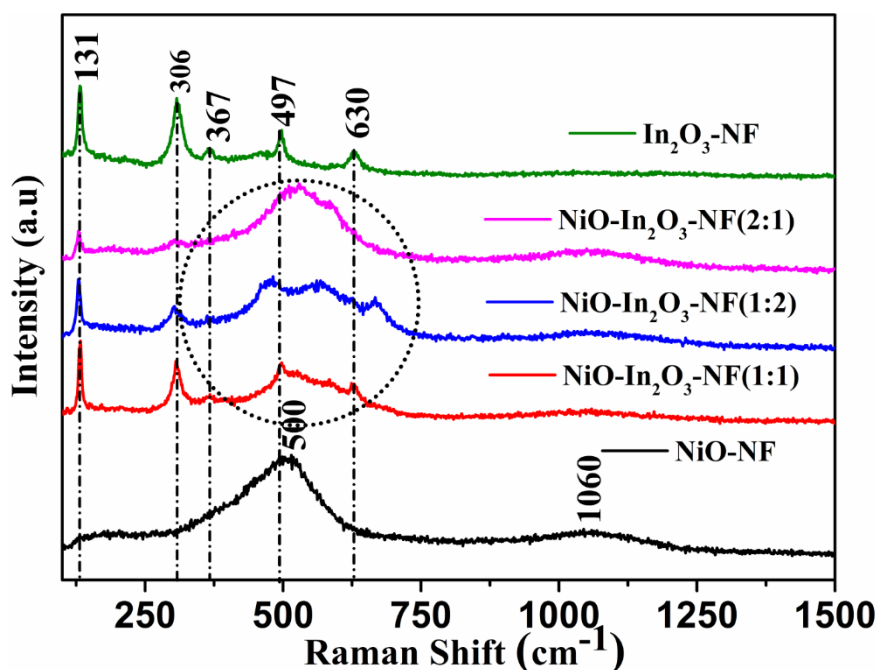
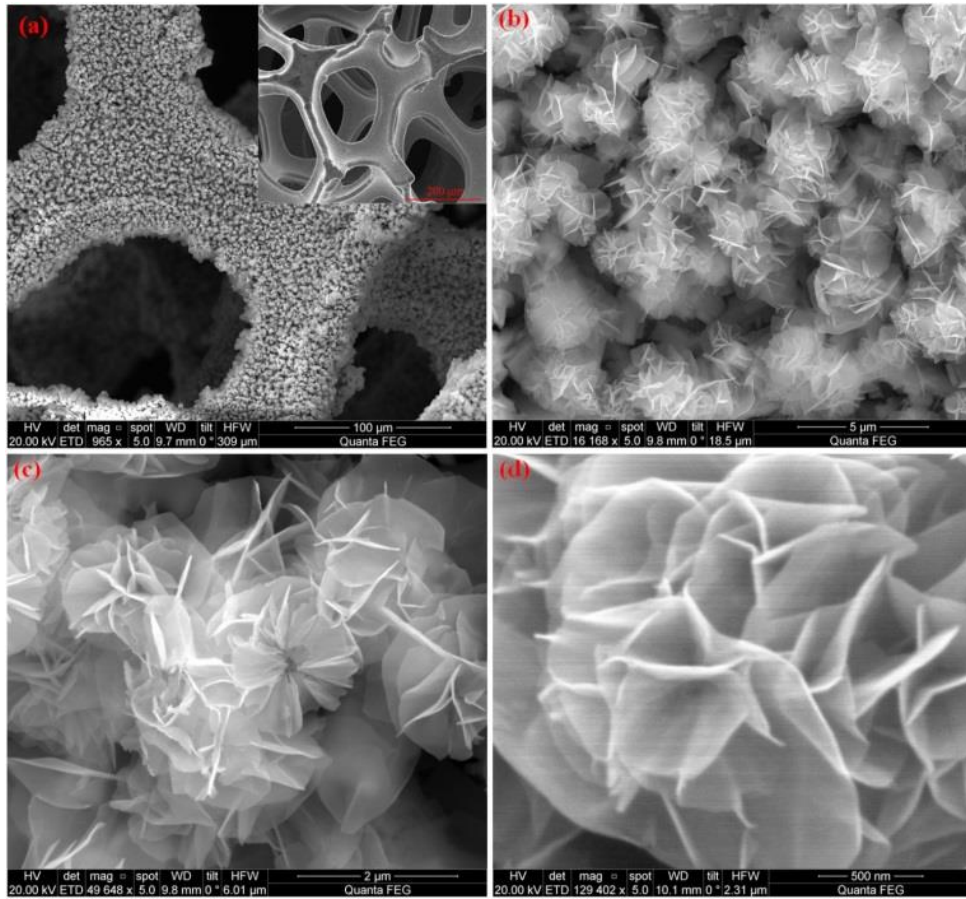


**Figure 3.8** Raman spectra of pure NiO-NF, In<sub>2</sub>O<sub>3</sub>-NF and NiO-In<sub>2</sub>O<sub>3</sub>-NF composites with different concentrations.

The equal molar concentration of Ni/In shows both the Ni-O and In-O-In stretching. Followed by the high Ni and low In concentration (Ni:In/2:1) shows predominant Ni-O vibrations in addition to the In-O-In stretching. However, the exact phase of the Ni compound is still unpredictable and can be attributed to the existence of low crystalline structure with many defects.

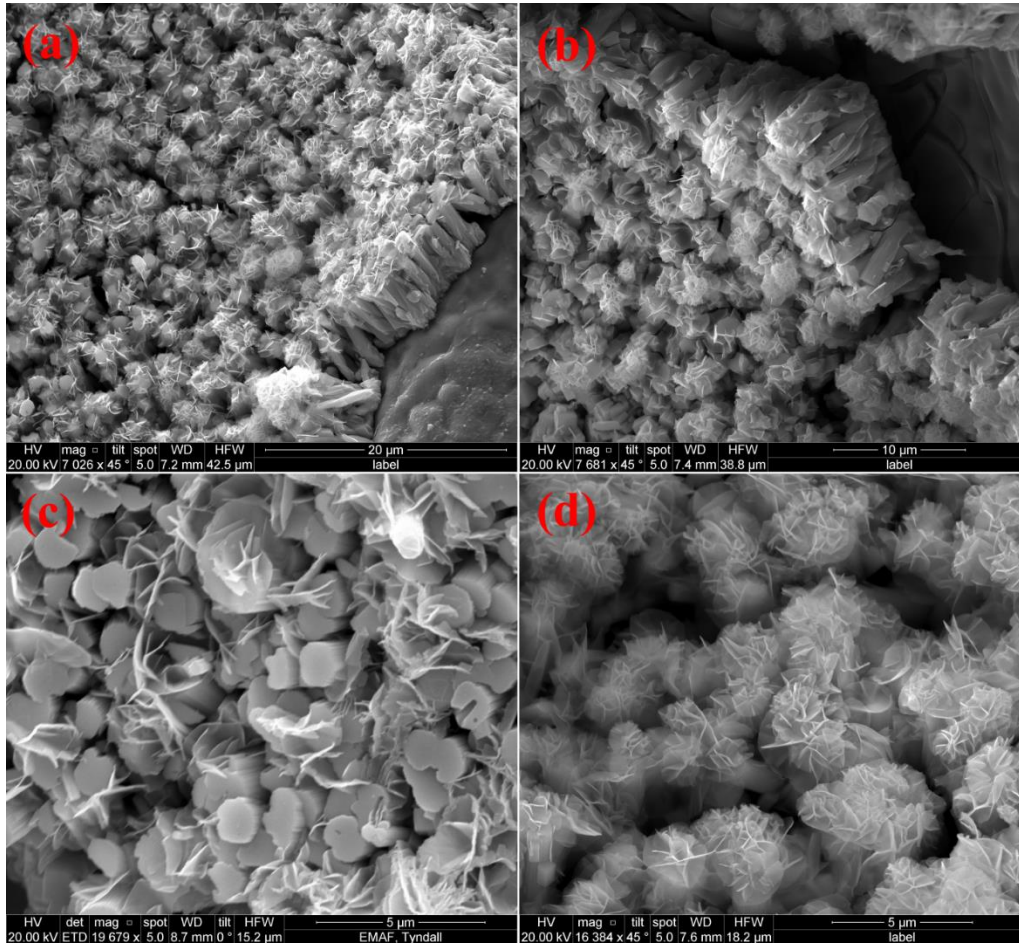
### 3.2.3 Morphology under SEM and TEM

Figure 3.9 shows SEM images of the structure and morphology of the nickel-indium oxide on nickel foam (NF). Low magnification SEM image of Figure 3.9 (a) shows the formation of well integrated NiO-In<sub>2</sub>O<sub>3</sub> hetero-microstructure over the nickel foam surface (inset of Figure 3.9 (a)). It contains uniformly grown flowers (Figure 3.9 (b and c)) comprised of ultra-thin nanosheets (Figure 3.9 (d)) with diameters ranging from 0.8-2  $\mu\text{m}$ . Each nanosheet has a thickness in the range of 10-14 nm and has long planar dimensions.



**Figure 3.9** (a-d) SEM images of NiO-In<sub>2</sub>O<sub>3</sub>-NF (1:2) hybrid structure at different magnifications.

Interestingly, all the flowers are supported by the nanorod arrays of several hundreds of nanometre in length with an average diameter of ~80 nm, as evidenced from the tilted angle SEM images in Figure 3.10 (a-d).



**Figure 3.10** (a-d) 45° tilted angle SEM images of NiO-In<sub>2</sub>O<sub>3</sub>-NF (1:2) hybrid structure.

The energy dispersive X-ray spectroscopy (EDX) (Figure 3.11 (a-f)) of the NiO-In<sub>2</sub>O<sub>3</sub> hetero-structures fabricated using 3 different mole concentrations of Ni:In (1:1, 1:2 and 2:1) confirms the presence of individual elements (Ni, In and O). However, hetero-structures showed variation in their elemental compositions, which may be attributed to the diffusion or formation of intermetallic compounds. Interestingly, for all the compositions, the regions over flowers (Figure 3.11 (a, c & e)) show a dense distribution of Ni and a limited amount of In. On the other hand, the nanorod portion (Figure 3.11 (b, d & f)) shows a dominant In distribution and low quantity of Ni. This observation further supports the formation of the hetero-composites. The deviation from initial concentration (Ni:In) suggests the partial incorporation of In and Ni ions within the NiO and In<sub>2</sub>O<sub>3</sub> lattices during hydrothermal growth, which substantiates the formation of a solid solution. For better understanding of this microcube-nanorod-nano/

microflower heterostructure formation, monometallic oxide of pure NiO and In<sub>2</sub>O<sub>3</sub> were grown on the NF using similar fabrication method. Figure 3.4 (a) and (b) are the SEM images and the corresponding EDX analysis of the NiO-NF (Figure 3.4 (e)) confirms the formation of highly dense networked nanosheets of NiO grown on the NF. By contrast, Figure 3.4 (c) and (d) and the EDX of (f) reveal the irregular aggregates of In<sub>2</sub>O<sub>3</sub> microcubes growth on the NF.

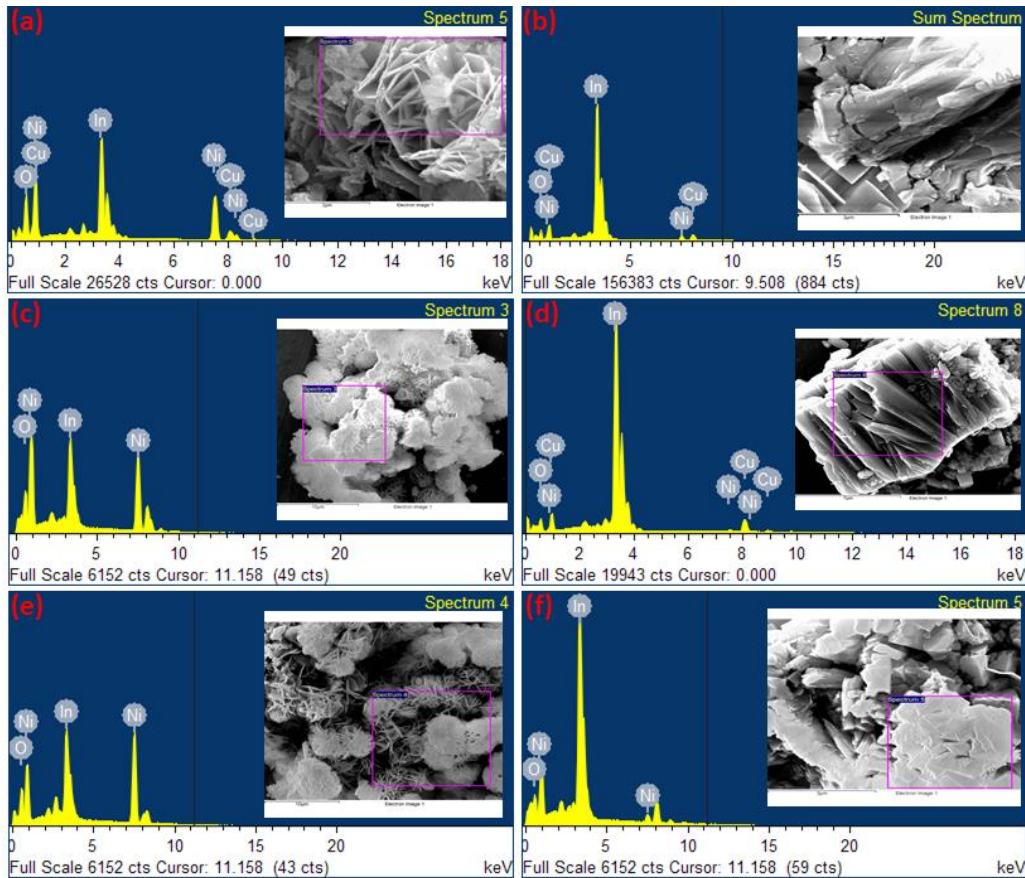


**Figure 3.11** EDX spectrum of NiO-In<sub>2</sub>O<sub>3</sub>-NF hybrid composite at various concentration of Ni:In (a and b) 1:1, (c and d) 1:2, and (e and f) 2:1 scanned at different regions. The observed Cu peak was due to the copper tape used to attach the samples to the sample holder.

The elemental mapping of the sample scanned at different regions of nanorods, flowers and microflower/ nanorod areas of the NiO-In<sub>2</sub>O<sub>3</sub> (1:2) are displayed in Figure 3.12, which shows the elemental distribution of Ni, In and O. Over the nanorod region, In is

predominant with oxygen demonstrating the formation of  $\text{In}_2\text{O}_3$ . Alternatively, the flower area is extensively covered by the Ni with O, which reveals the growth of NiO microflowers over  $\text{In}_2\text{O}_3$  nanorods. The dispersion of Ni and In in their respective nanorod and microflower regions indicates the partial diffusion/ incorporation of metal ions in the hybrid composite lattices.

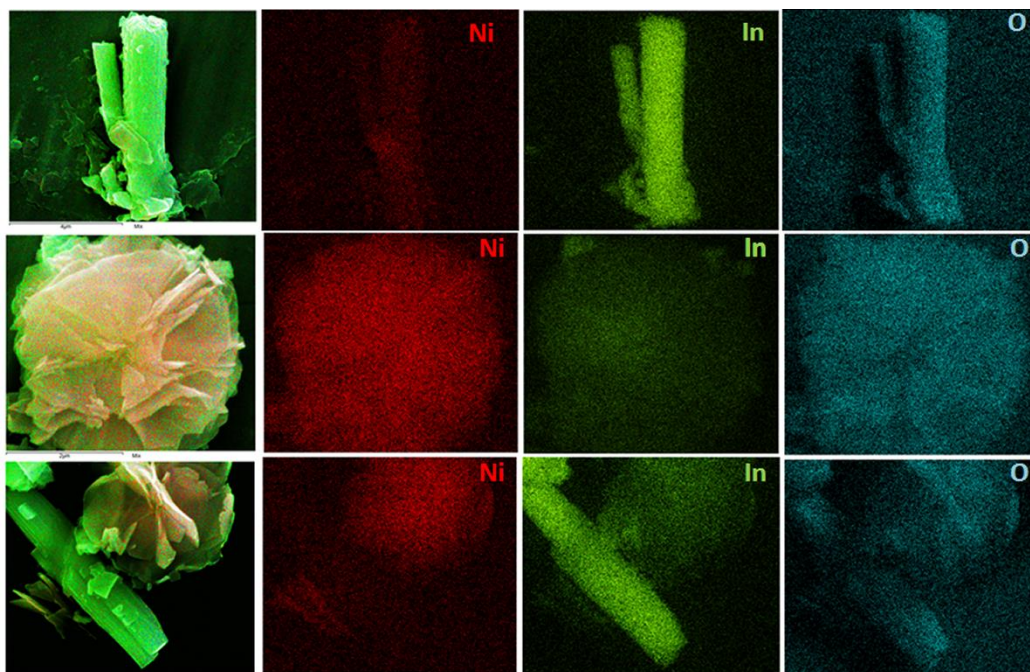


**Figure 3.12** Elemental mapping spectrum of NiO– $\text{In}_2\text{O}_3$ –NF (1 : 2) hybrid composite scanned at different regions

Further inspection using high-resolution TEM (HRTEM) and the corresponding selected-area electron diffraction (SAED) are shown in Figure 3.13 (a-f) reveal that these hybrid microflower/ nanorods are polycrystalline in nature, as seen by the well-defined diffraction rings. TEM image in Figure 3.13 (a) clearly shows a distribution of fine nanocrystals of  $\sim 8$ -11 nm (inset Figure 3.13 (b)) in the nanorod region which is consistent with XRD analysis. Figure 3.13 (b) is the high magnification TEM image on nanorod portion showing the d-spacing of 0.29 nm for (222) planes of  $\text{In}_2\text{O}_3$  oxide and 0.21 nm for (200) planes of NiO. The corresponding SAED pattern as shown in Figure 3.13 (c) reflects the diffused rings of  $\text{In}_2\text{O}_3$  and nearly amorphous NiO referring to the

growth of nanocomposite. Figure 3.13 (d) shows the petals of microflower structure comprised of fine nanocrystals with uniform particle distribution. These interconnected thin sheets (Figure 3.13 (e) and inset) self-assembled in such a way to form the final microflower structure where both 0.21 and 0.29 nm lattice spacings are visible. A typical SAED image (Figure 3.13 (f)) shows the lattice spacing of 0.29, 0.18, 0.25, and 0.15 nm, in agreement with the (222), (440), (400) and (622) planes of  $\text{In}_2\text{O}_3$ , which is followed by the estimated lattice spacing of 0.21 nm for the (200) plane of  $\text{NiO}^{235}$  and ultimately confirms the formation of nickel indium nanocomposite. All the rings in the SAED pattern in Figure 3.13 (f) can be indexed to the cubic  $\text{In}_2\text{O}_3$  (# 06-0416) and  $\text{NiO}$  (# 47-1049).

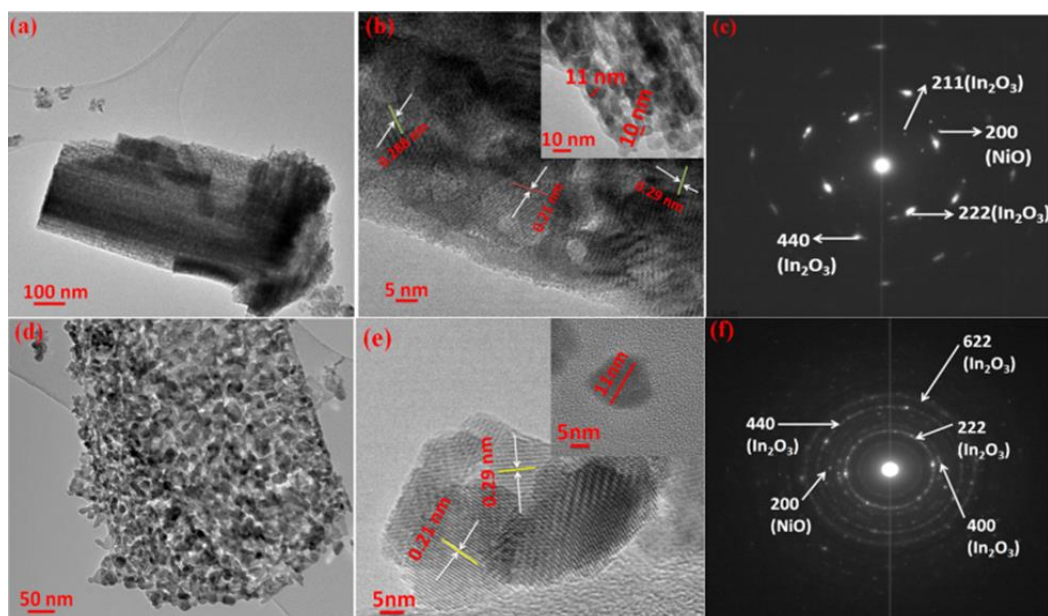


**Figure 3.13** HRTEM images of (a)  $\text{NiO-In}_2\text{O}_3$  (1:2) hybrid structure, (b) nanorod region and (c) corresponding SAED pattern. (d) and (e) flower/ flakes region and (f) corresponding SAED pattern.

### 3.2.4 XPS analysis

The samples were further analysed using XPS to investigate the formation  $\text{NiO-In}_2\text{O}_3$  nanocomposite, and their appropriate valence states. Figure 3.14 (a-c) represents the fine scan XPS spectra of pure  $\text{NiO}$ ,  $\text{In}_2\text{O}_3$  and different  $\text{NiO-In}_2\text{O}_3$  composites. The de-

convoluted XPS spectra of NiO-In<sub>2</sub>O<sub>3</sub> composites obviously validate the perception of the hetero-structured composite which is composed of NiO-In<sub>2</sub>O<sub>3</sub>. The Ni2p, In3d and O1s XPS spectra of pure and NiO - In<sub>2</sub>O<sub>3</sub> mixed oxides are shown in Figure 3.14 (a-c). The Ni2p spectrum of NiO shows the asymmetric main and multiplet-split Ni2p<sub>3/2</sub> (NiO) peaks at the corresponding binding energies of 853.8 (Ni<sup>2+</sup>) and 855.9 (Ni<sup>3+</sup>) eV, respectively. The satellite peaks in the respective binding energies further confirm the existence of Ni<sup>2+</sup>/Ni<sup>3+</sup> in the NiO sample.<sup>233,236-238</sup> The slight deviation in the peaks position from the binding energy value of pure NiO (854.2) is mainly attributed to the oxygen defects on the NiO surface.<sup>239</sup> The observed O1s spectrum (Figure 3.14 (c)) further proves this speculation. It shows a distinct peak at 529.3 eV and the shoulders at 531 and 532.5 eV related to the oxygen ions in the NiO crystal lattice and defects sites within the oxide crystals such as adsorbed oxygen (O<sub>x</sub><sup>-</sup>) or hydroxide species.<sup>239,240</sup> Similarly, the pure In<sub>2</sub>O<sub>3</sub> (Figure 3.14 (b)) show the dominant bands related to In3d<sub>5/2</sub> and In3d<sub>3/2</sub> at the binding energies of 444.5 eV and 452 eV, respectively. The existence of symmetric peaks indicates the oxidized state of In, rather than the metallic state. The strong O1s peak at 529.8 eV with a shoulder peak at 531.6 eV reveals the existence of In-O bonding with some adsorbed surface oxygen defects. The observed binding energies are in good agreement with earlier reports for In<sub>2</sub>O<sub>3</sub> nanostructures (443.9 eV & 443.8 eV).<sup>230,238,240,241</sup>

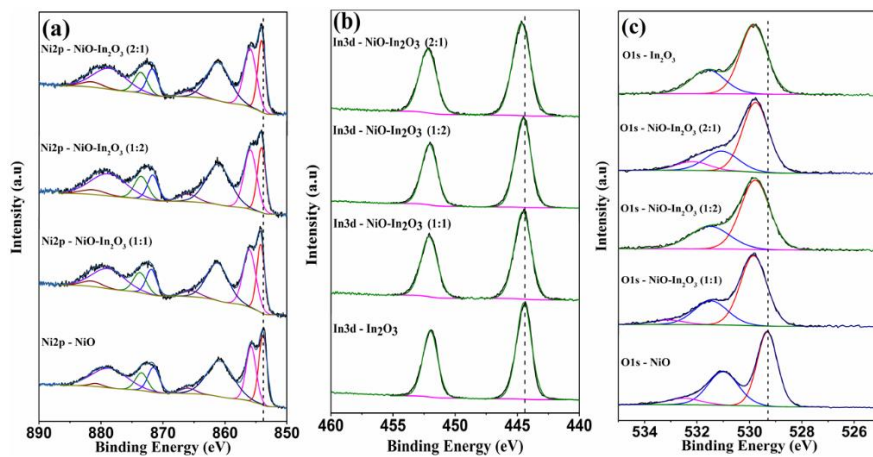


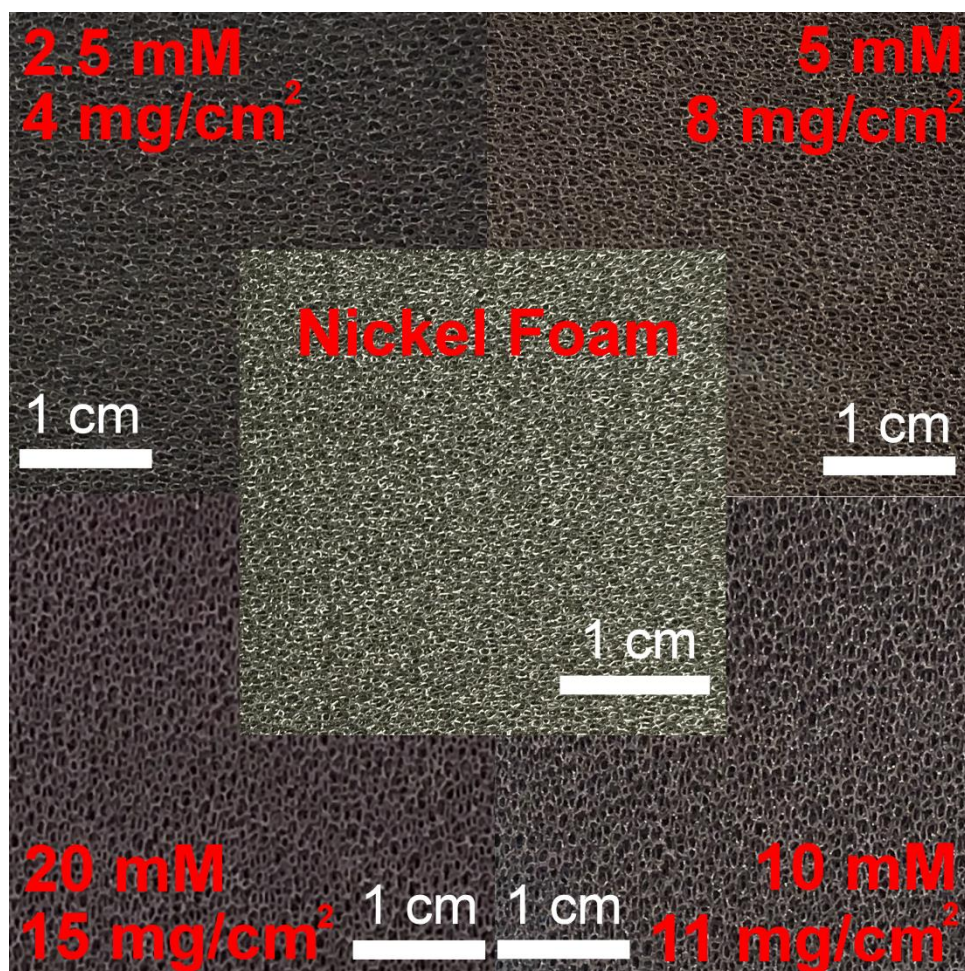
**Figure 3.14** (a-c) XPS spectra of pure and NiO-In<sub>2</sub>O<sub>3</sub> hybrid structure prepared at various concentrations.

When compared to individual oxides, the XPS spectra of mixed compounds showed significant variations in the Ni2p<sub>3/2</sub> peak positions due to the addition of In<sub>2</sub>O<sub>3</sub> as shown in Figure 3.14 (a). In particular, the intensity ratio of Ni<sup>2+</sup>/Ni<sup>3+</sup> has been varied according to the Ni:In concentrations. The NiO-In<sub>2</sub>O<sub>3</sub> with equal concentration Ni:In(1:1) and Ni rich concentration Ni:In (2:1) showed the Ni<sup>2+</sup>/Ni<sup>3+</sup> intensity ratio of 0.62. Meantime, for the In rich NiO-In<sub>2</sub>O<sub>3</sub> (1:2) hetero composite, the ratio was increased to 0.66 due to the high concentration of defects as supported by the Raman spectra. However, these values are quite lower than the pure NiO sample (0.84), which may be due to the decrease in hole concentration of p-type NiO semiconductors as a results of In incorporation.<sup>233</sup> This indicates that a limited amount of the In ions were incorporated into NiO lattice for all the composites. Similarly, the In3d spectra of NiO-In<sub>2</sub>O<sub>3</sub> hetero-composites (Figure 3.14 (b)) showed the characteristic spin-orbit splits at the binding energies ranging from 444.4-444.7 eV and 452-452.2 eV corresponds to the In3d<sub>5/2</sub> and In3d<sub>3/2</sub>, respectively.<sup>233,239-241</sup> This indicated that element indium in NiO-In<sub>2</sub>O<sub>3</sub> hetero-structures existed in the oxide state only.<sup>241</sup> The relation between metal and oxygen is further evaluated by the O1s XPS spectral analysis and depicted in Figure 3.14 (c) for the pure and NiO-In<sub>2</sub>O<sub>3</sub> (1:1), NiO-In<sub>2</sub>O<sub>3</sub> (1:2) and NiO-In<sub>2</sub>O<sub>3</sub> (2:1) samples. Typical O1s spectra of all the composites showed a distinct peak at 529.8±0.1 eV associated to the O<sup>2-</sup> species in Ni-O and In-O. Also, there is a visible shoulder peaks between 531.1-532.2 eV and can be proposed to the defects sites within oxide crystal in addition to the adsorbed oxygen and hydroxides.<sup>238</sup> The ratio of the shoulder peak versus the total O1s peak for NiO:In<sub>2</sub>O<sub>3</sub> composites are found to be 28.5%, 30.6% and 23.6% for Ni:In (1:1), Ni:In (1:2) and Ni:In (2:1) respectively, confirming the existence of more surface defects in Ni:In (1:2) sample than the other two compositions. These results are in good agreement with the observed Ni2p and In3d spectra as well as with the XRD and Raman analysis and contribute to the perception of the heterostructured composite, which is composed of NiO and In<sub>2</sub>O<sub>3</sub>.

### **3.3 $\text{Co}_3(\text{PO}_4)_2 \cdot 8\text{H}_2\text{O}$ Multilayer Nano/ Microflakes on Nickel Foam**

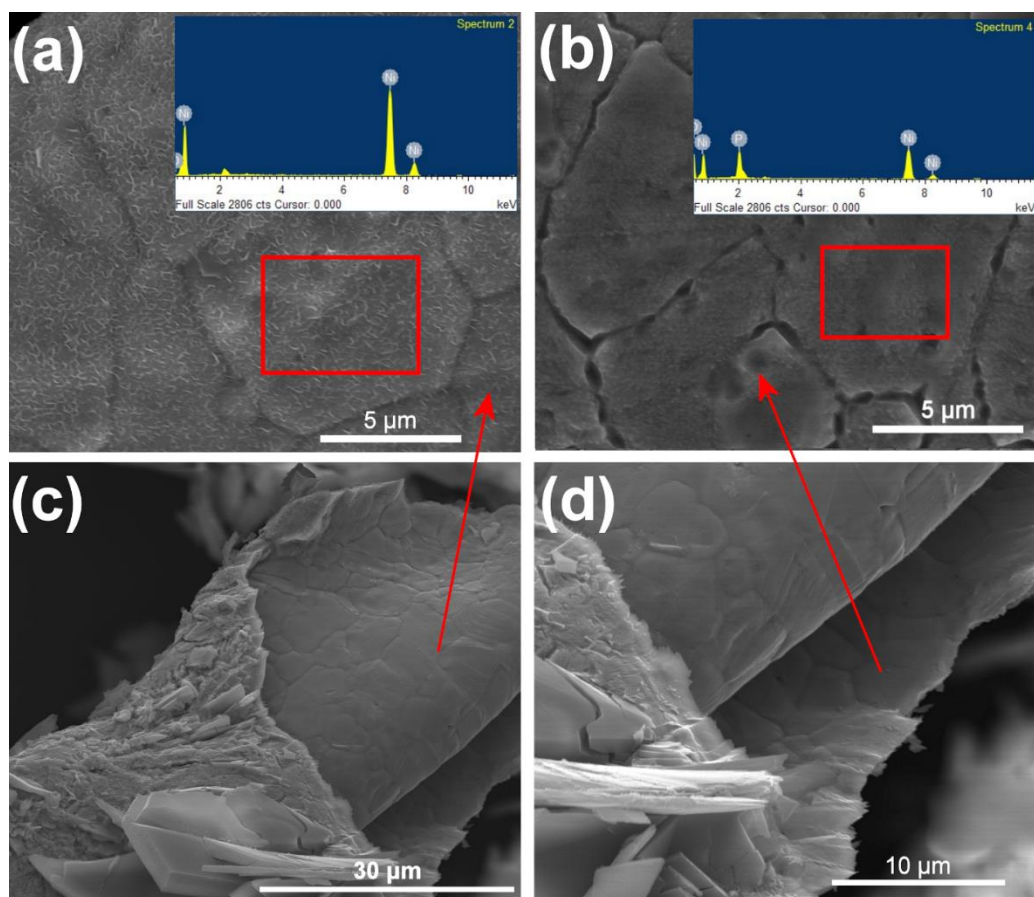
#### **3.3.1 Synthesis and growth mechanism**

$\text{Co}_3(\text{PO}_4)_2 \cdot 8\text{H}_2\text{O}$  nano/ microflakes were synthesized by hydrothermal method on nickel foam (NF). In detail, equal concentration (2.5 mM) of  $\text{Co}(\text{NO}_3)_2 \cdot 6\text{H}_2\text{O}$  and  $\text{NH}_4\text{H}_2\text{PO}_4$  were dissolved in deionized (DI) water under stirring for 15 min. The solution was transferred to a 100 ml reaction vessel, which contained the pre-treated nickel foam substrate and was then kept at 120 °C for 8 h in oven. After this time, the reaction vessel was allowed to cool down to room temperature naturally. Finally, substrates covered with  $\text{Co}_3(\text{PO}_4)_2 \cdot 8\text{H}_2\text{O}$  were washed with DI water several times with the assistance of ultrasonication, and then dried in air. For the mass loading study, different concentrations (5 mM, 10 mM, 20 mM) of  $\text{Co}^{+2}$  and  $\text{PO}_4^{-3}$  were prepared using the same procedure. The amount of  $\text{Co}_3(\text{PO}_4)_2 \cdot 8\text{H}_2\text{O}$  was measured from the weight difference of the pure nickel foam and  $\text{Co}_3(\text{PO}_4)_2 \cdot 8\text{H}_2\text{O}$  grown nickel foam. Figure 3.15 shows a photograph of  $\text{Co}_3(\text{PO}_4)_2 \cdot 8\text{H}_2\text{O}/\text{NF}$  samples prepared using different concentrations (2.5 mM, 5 mM, 10 mM, 20 mM). Pink-purple nano/ microstructure was grown over the nickel foam. The color becomes brighter with increasing concentration, which indicates the larger loading mass for the  $\text{Co}_3(\text{PO}_4)_2 \cdot 8\text{H}_2\text{O}$ . The samples were measured before and after the synthesis. Typical mass of the active electrode material is ~4, ~8, ~11, 15  $\text{mg cm}^{-2}$ , respectively.



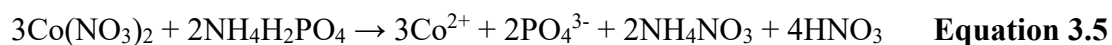
**Figure 3.15** Digital photograph of  $\text{Co}_3(\text{PO}_4)_2 \cdot 8\text{H}_2\text{O}$  grown on NF substrate prepared using different concentrations (2.5 mM, 5 mM, 10 mM and 20 mM).

In order to study growth mechanism of  $\text{Co}_3(\text{PO}_4)_2 \cdot 8\text{H}_2\text{O}$  multilayer nano/ microflakes during the hydrothermal process, two samples were made using the following method: two pieces of nickel foam ( $3 \times 3 \text{ cm}^2$ ) treated with 3 M HCl followed by washing with ethanol and deionized water for 15 minutes was used as substrate. One reaction vessel was filled only with 80 ml deionized water, while the other one contained 2.5 mM  $\text{NH}_4\text{H}_2\text{PO}_4$  dissolved in 80 ml deionized water. Two reaction vessel with the pre-treated nickel foam substrate was kept at  $120 \text{ }^\circ\text{C}$  for 8 h in oven. Then, the reaction vessel was allowed to cool down to room temperature naturally. Finally, water treated NF ( $\text{H}_2\text{O}/\text{NF}$ ) and ammonium phosphate treated NF ( $\text{PO}_4/\text{NF}$ ) samples were washed with deionized water several times with the assistance of ultrasonication, and then dried in air.



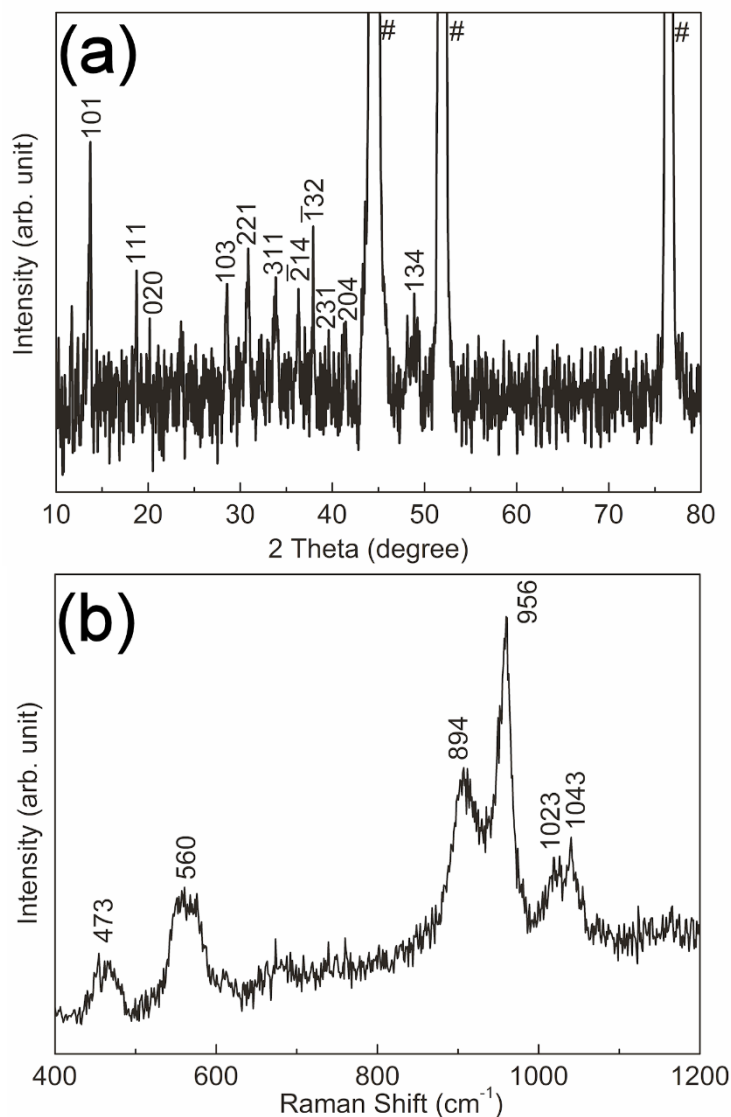
**Figure 3.16** (a-b) SEM images with EDX analysis as inset of H<sub>2</sub>O/NF, PO<sub>4</sub>/NF samples, (c-d) SEM images of scratched Co<sub>3</sub>(PO<sub>4</sub>)<sub>2</sub>·8H<sub>2</sub>O/NF samples.

Figure 3.16 shows the SEM images of H<sub>2</sub>O/NF, PO<sub>4</sub>/NF, and scratched Co<sub>3</sub>(PO<sub>4</sub>)<sub>2</sub>·8H<sub>2</sub>O/NF samples. In Figure 3.16 (a), fiber like morphology was formed on the nickel foam and start to crack, which is a thin layer of NiO. In the SEM image of PO<sub>4</sub>/NF sample as shown in Figure 3.16 (b), no fibre like structure can be seen and the rift are deeper than the H<sub>2</sub>O/NF sample. In Figure 3.16 (c-d), part of scratched Co<sub>3</sub>(PO<sub>4</sub>)<sub>2</sub>·8H<sub>2</sub>O/NF sample shows the same morphology as H<sub>2</sub>O/NF and PO<sub>4</sub>/NF. Therefore, according to the EDX analysis, the growth process can be explained as follows: First NiO thin layer was formed on the nickel foam, then nickel phosphate layer and finally the cobalt phosphate hydrate micro/ nanoflakes as following equations:





**Equation 3.6**



**Figure 3.17** (a-b) XRD pattern and Raman spectra of PO<sub>4</sub>/NF sample.

XRD and Raman spectroscopy were used to explore the phase structure of PO<sub>4</sub>/NF sample. In XRD result (Figure 3.17 (a)), except the marked (#) peaks of nickel foam, nickel phosphate (Ni<sub>2</sub>P<sub>4</sub>O<sub>12</sub>) phase were formed (JCPDS NO. 86-2160). In Raman spectroscopy (Figure 3.17 (b)), PO<sub>4</sub>/NF sample shows two bands at 473 cm<sup>-1</sup> and 560 cm<sup>-1</sup> correspond to the Ni-O stretching.<sup>242</sup> The symmetric O-P-O stretching vibrations are observed at 956, 1023 and 1046 cm<sup>-1</sup> while the asymmetric P-O-P stretching vibration was obtained at 894 cm<sup>-1</sup>.<sup>243-245</sup> All these modes confirm the formation of

$\text{Ni}_2\text{P}_4\text{O}_{12}$  composite on nickel foam. The XRD and Raman results are in good agreement with the SEM and EDX analysis.

### 3.3.2 Structure Analysis (XRD and Raman)

X-ray diffraction (XRD) and Raman spectroscopy were used to explore the phase structure of  $\text{Co}_3(\text{PO}_4)_2 \cdot 8\text{H}_2\text{O}$  nano/ microflakes. As shown in Figure 3.18a, except the marked peaks of nickel foam (peaks at  $44.6^\circ$ ,  $51.9^\circ$  and  $76.6^\circ$ ) single phase of  $\text{Co}_3(\text{PO}_4)_2 \cdot 8\text{H}_2\text{O}$  were formed. All the other peaks can be indexed to the planes of cobalt phosphate hydrate (JCPDS NO. 41-0375). With increasing concentration, the peak intensity of  $\text{Co}_3(\text{PO}_4)_2 \cdot 8\text{H}_2\text{O}$  increased (Figure 3.18c), while the peak intensity of nickel decreased due to larger mass loading for higher concentration samples.

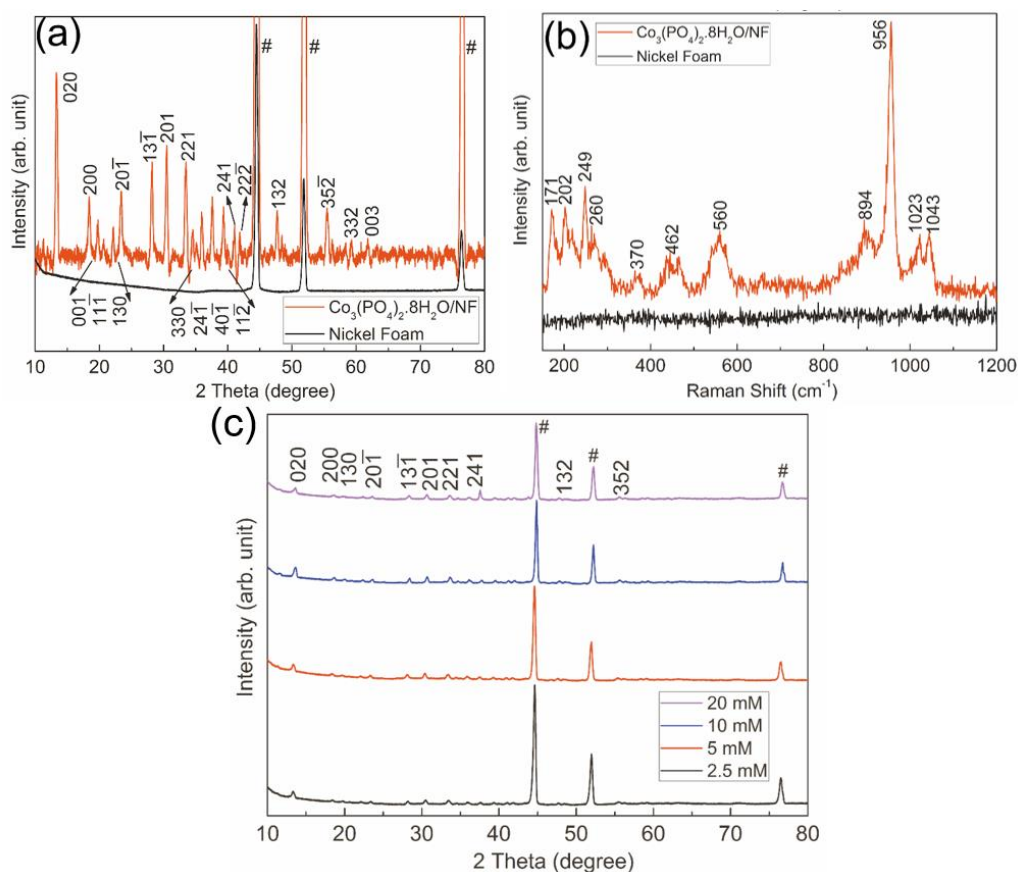
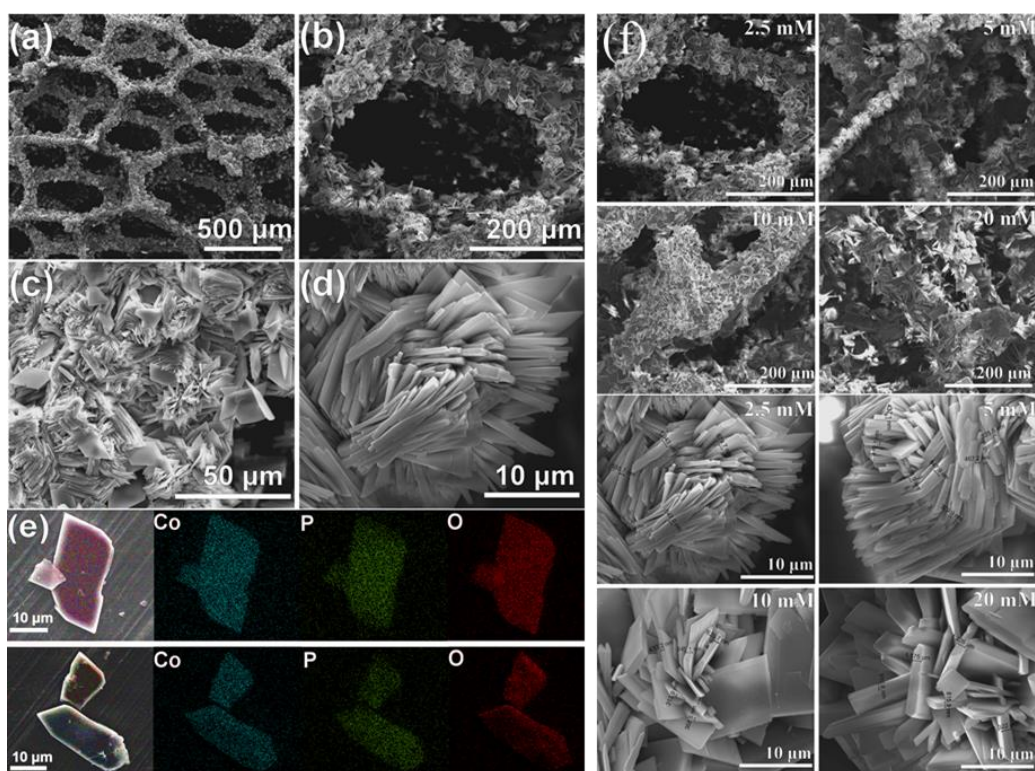


**Figure 3.18** (a) XRD pattern, (b) Raman spectra of pure nickel foam and 2.5 mM  $\text{Co}_3(\text{PO}_4)_2 \cdot 8\text{H}_2\text{O}/\text{NF}$  nano/ microstructure, (c) XRD pattern of 2.5 mM, 5 mM, 10 mM and 20 mM  $\text{Co}_3(\text{PO}_4)_2 \cdot 8\text{H}_2\text{O}/\text{NF}$  nano/ microstructure.

Figure 3.18b shows the Raman spectra of nickel foam and  $\text{Co}_3(\text{PO}_4)_2 \cdot 8\text{H}_2\text{O}/\text{NF}$ . No obvious peaks were obtained from acid pre-treated pure nickel foam spectroscopy, because of no changes in polarization in the pure metal. In the spectroscopy of  $\text{Co}_3(\text{PO}_4)_2 \cdot 8\text{H}_2\text{O}/\text{NF}$ , the peaks due to the Ni-O stretching at  $560\text{ cm}^{-1}$  indicated the conversion of the nickel foam which is presented in section 3.3.1.<sup>242</sup> O-Co-O bending appears at  $260$  and  $370\text{ cm}^{-1}$ .<sup>244</sup> The O-P-O bending modes are located at  $462\text{ cm}^{-1}$ ,<sup>243,245</sup> while the symmetric O-P-O stretching vibrations are observed at  $956$ ,  $1023$  and  $1046\text{ cm}^{-1}$ .<sup>243-245</sup> The asymmetric P-O-P stretching vibration was obtained at  $894\text{ cm}^{-1}$ .<sup>245</sup> The external modes are found in the  $160$ - $250$  region.<sup>245,246</sup> All these modes confirm the formation of  $\text{Co}_3(\text{PO}_4)_2 \cdot 8\text{H}_2\text{O}$  composite on nickel foam.<sup>244,245,247,248</sup>

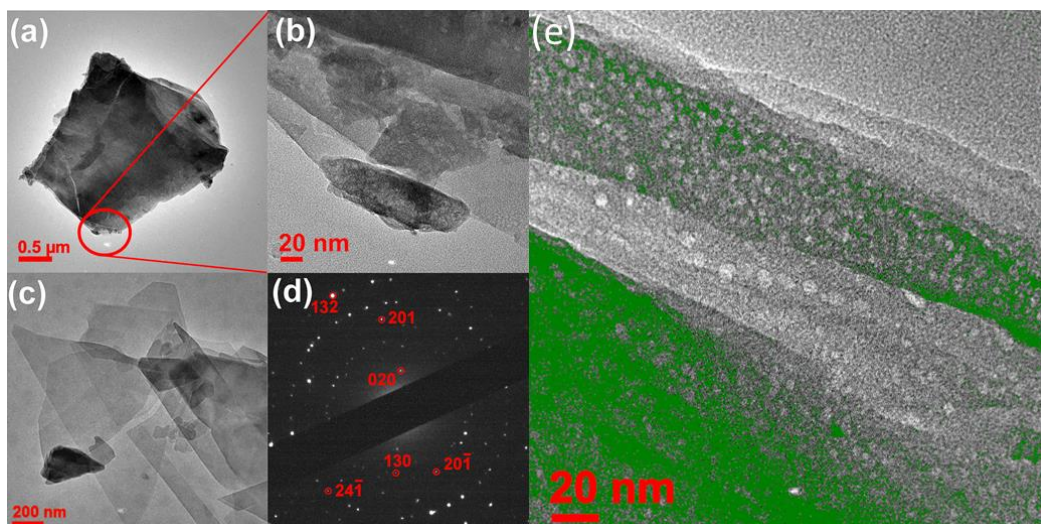
### 3.3.3 Morphology under SEM and TEM

Figure 3.19 shows the SEM images of nickel foam supported  $\text{Co}_3(\text{PO}_4)_2 \cdot 8\text{H}_2\text{O}$  nano/microflakes at different magnifications fabricated from  $2.5\text{ mM}$  concentration. Low magnification images (Figure 3.19a-b) shows the homogeneous growth of the  $\text{Co}_3(\text{PO}_4)_2 \cdot 8\text{H}_2\text{O}$  multilayer nano/microflakes. These nano/microflakes were formed layer by layer with an average thickness ranging from  $400\text{ nm}$  to  $1\text{ }\mu\text{m}$  as can be seen in Figure 3.19c-d. With increasing concentration (from  $2.5$  to  $20\text{ mM}$ ), individual layer of the multilayer structures grew thicker ( $600\text{ nm}$  to  $1.2\text{ }\mu\text{m}$ ) in a disorderly fashion into different directions as can be observed in Figure 3.19f. Thicker flakes easily block the interspace of the nickel foam and might reduce the overall surface area of the electrode. To analyze the component in the nano/microflakes structure, thin flake-powder was scratched off from the nickel foam and stuck to the copper tape. The elemental mapping on the flakes in Figure 3.19e clearly shows the distribution of Co, P and O, which is in good agreement with the XRD and Raman analysis.



**Figure 3.19** (a-d) SEM images of 2.5 mM  $\text{Co}_3(\text{PO}_4)_2 \cdot 8\text{H}_2\text{O}/\text{NF}$  nano/microflakes at different magnifications (e) Elemental mapping spectrum of  $\text{Co}_3(\text{PO}_4)_2 \cdot 8\text{H}_2\text{O}/\text{NF}$  nano/microstructure scanned at different flake-powder. (f) Different magnification SEM images of 2.5 mM, 5 mM, 10 mM and 20 mM  $\text{Co}_3(\text{PO}_4)_2 \cdot 8\text{H}_2\text{O}/\text{NF}$  nano/microflakes.

In addition, high-resolution transmission electron microscopy (HR-TEM) measurements were carried out for the powder samples scratched off from the nickel foam to avoid the contribution of the substrate. The HR-TEM and corresponding selected-area electron diffraction (SAED) images are shown in Figure 3.20. Different thicknesses of scratched powder sample were selectively analyzed. Figure 3.20a-b clearly show a single layer found at the edge of a thick sample piece, which is comprised of several layers. Similarly, Figure 3.20c demonstrates the obvious layer-by-layer structure, confirming the multilayer structure shown in the SEM images in Figure 3.19 (c-d). The corresponding SAED pattern in Figure 3.20d shows the electron diffraction from different planes and is consistent with XRD results.



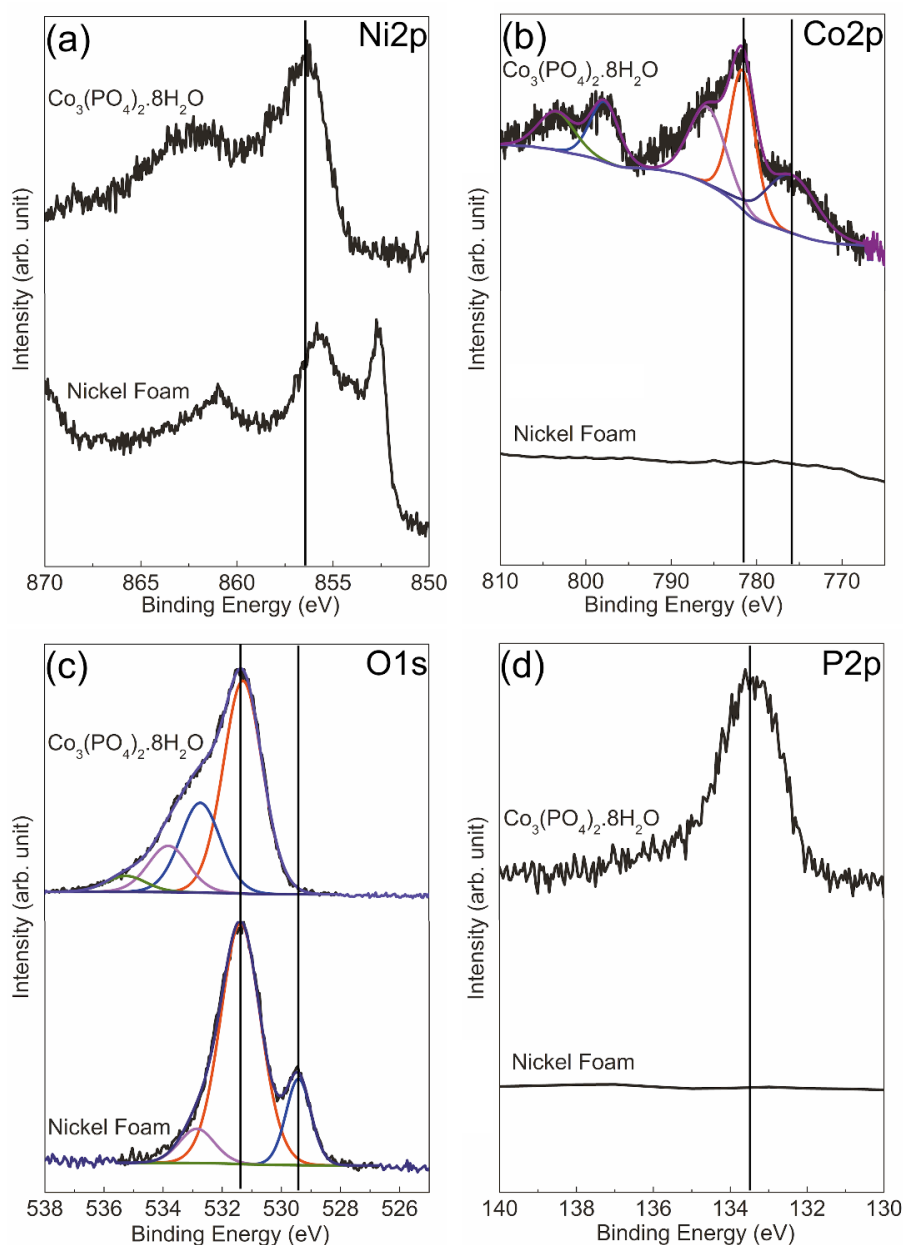
**Figure 3.20** (a-c) HRTEM images of  $\text{Co}_3(\text{PO}_4)_2 \cdot 8\text{H}_2\text{O}$  multilayer structure, (d) corresponding SAED pattern, (e) HRTEM image of  $\text{Co}_3(\text{PO}_4)_2 \cdot 8\text{H}_2\text{O}$  at high magnification with particle analysis.

Figure 3.20e presents the edge of the thick piece at high magnification (treated by particle size analysis), which shows the honeycomb-like pores with an average size of  $\sim 5$  nm. The porous structure in scratched powder can be ascribed to the hydrated water in  $\text{Co}_3(\text{PO}_4)_2 \cdot 8\text{H}_2\text{O}$  structure.

### 3.3.4 XPS Analysis

The samples were further analyzed by XPS to investigate the appropriate valence states. The Ni2p, Co2p, O1s and P2p XPS spectra are shown in Figure 3.21a-d. The Ni2p spectrum of pure nickel foam (Figure 3.21a) shows the peaks at 855.7 eV ( $\text{Ni}(\text{OH})_2$ ), 845.2 eV ( $\text{NiO}$ ) 852.6 eV ( $\text{Ni}$ ) and 861 eV (satellite). This may be caused by the slow oxidation reaction in the air of the nickel foam. After synthesis process the nickel peak at 852.6 eV vanished may due to the surface reaction on the nickel foam as explained in the section 3.3.1. The O1s spectrum of Figure 3.21c further proves the existence of  $\text{Ni}(\text{OH})_2$  and  $\text{NiO}$ , which shows a distinct peak at 531.3 eV ( $\text{Ni}(\text{OH})_2$ ) and the shoulders at 529.4 eV ( $\text{NiO}$ ). For Co2p and P2p scan in Figure 3.21b and d, no obvious peaks were obtained from the pure nickel foam sample. The binding energy peak of  $\text{Co}2p_{3/2}$

at 781.5 eV in Figure 3.21b, along with a satellite peak at 785.8 eV, indicates that +2 valence are the main state for cobalt.<sup>249,250</sup> The peaks of Co2p correspond to Co2p<sub>1/2</sub> orbits at 797.8 eV and 803.5 eV further prove the speculation.<sup>250-252</sup> As expected, in P2p region (Figure 3.21d), a single binding energy peak of P2p was detected at 133.6 was assigned to the P-O bonding<sup>253,254</sup>, which corresponds with the O1s peak at 531.3 eV.<sup>251</sup> The other O1s peaks at 532.7 eV, 532.9 eV, 533.8 eV and 535.3 eV were obtained from adsorbed oxygen, hydroxides and moisture. Therefore, the XPS spectrum confirmed that the Co<sub>3</sub>(PO<sub>4</sub>)<sub>2</sub>·8H<sub>2</sub>O was successfully grown over the nickel foam.<sup>252-258</sup>



**Figure 3.21** (a-d) Ni2p, Co2p, O1s and P2p XPS spectra of pure nickel foam and  $\text{Co}_3(\text{PO}_4)_2 \cdot 8\text{H}_2\text{O}/\text{NF}$ .

### 3.4 $\text{Ni}_3(\text{PO}_4)_2 \cdot 8\text{H}_2\text{O}$ 3D Nano/ Micro flakes on NF

#### 3.4.1 Synthesis and growth mechanism

Analytical grades of Nickel chloride hexahydrate ( $\text{NiCl}_2 \cdot 6\text{H}_2\text{O}$ ), Ammonium dihydrogen phosphate ( $\text{NH}_4\text{H}_2\text{PO}_4$ ) and polyethylene glycol (PEG) were purchased

from Sigma Aldrich, and used as received without further purifications. For typical synthesis, 10 mM of  $\text{NH}_4\text{H}_2\text{PO}_4$  was first dissolved in 80 ml of deionized water followed by the addition of equal mole of  $\text{NiCl}_2 \cdot 6\text{H}_2\text{O}$  to the above solution under vigorous stirring at room temperature. Subsequently, 5 ml of PEG was added into the above mixture to form a homogeneous solution. After stirring for 20 min, the solution was transferred to reaction vessel of volume 100 ml, which contains pretreated NF ( $3 \times 3 \text{ cm}^2$ ) and kept at  $120^\circ\text{C}$  for 4 h. Finally, after cooling down to room temperature, the  $\text{Ni}_3(\text{PO}_4)_2 \cdot 8\text{H}_2\text{O}$  grown NF was take off and washed 3 times using deionized water, Ethanol and Acetone, and dried in an oven at  $120^\circ\text{C}$  for 12 h. The mass loading on NF was carefully estimated from the mass difference before and after  $\text{Ni}_3(\text{PO}_4)_2 \cdot 8\text{H}_2\text{O}$  growth and found to be  $\sim 2.4 \text{ mg cm}^{-2}$ .

### 3.4.2 Structure Analysis (XRD and Raman)

The XRD pattern of the  $\text{Ni}_3(\text{PO}_4)_2 \cdot 8\text{H}_2\text{O}/\text{NF}$  is illustrated in Figure 3.22a. The strong peak at  $44^\circ$  and  $51^\circ$  of  $2\theta$  is due to pure NF substrate. The intense diffraction peaks located at  $14.3^\circ$ ,  $18.5^\circ$ ,  $29.1^\circ$ ,  $31.2^\circ$ , and  $34.5^\circ$  correspond to the hydrated nickel phosphate phase (JCPDS No. 33-951). There is no peaks from other phosphides or phosphates, confirming a single monoclinic phase of  $\text{Ni}_3(\text{PO}_4)_2 \cdot 8\text{H}_2\text{O}$  with  $I_2/m$  space group is successfully grown over the 3D NF<sup>259</sup>. The intense and narrow diffraction peaks demonstrates high crystallinity of the material. The average crystallite size of  $\text{Ni}_3(\text{PO}_4)_2 \cdot 8\text{H}_2\text{O}$  flakes was estimated from the Debye-Scherrer equation,  $D = \frac{K\lambda}{\beta \cos \theta}$ , where  $D$  is the mean size of crystallites (nm),  $K$  is crystallite shape factor (a good approximation is 0.9),  $\lambda$  is the X-ray wavelength ( $\lambda = 1.5406 \text{ \AA}$ ),  $\beta$  is the full width at half the maximum (FWHM) in radians of the X-ray diffraction peak and  $\theta$  is the Bragg's angle (degree). The calculated  $D$  value for (0 2 0) plane is found to be  $\sim 35 \text{ nm}$ .

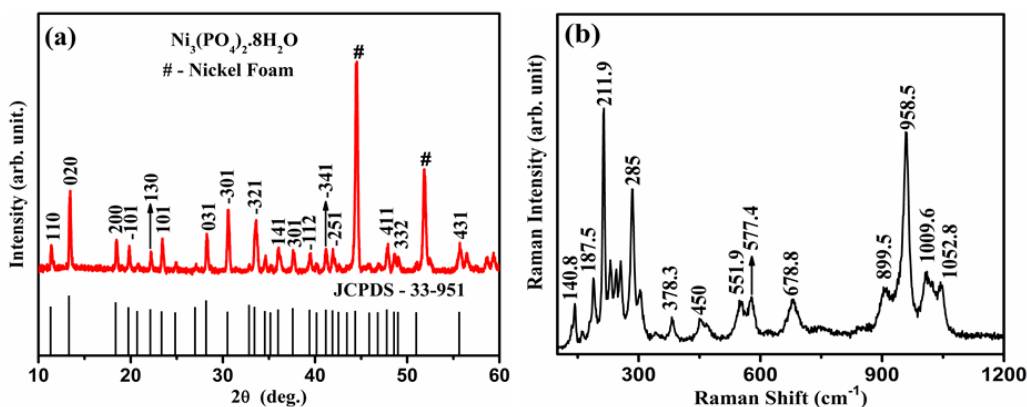


**Figure 3.22** (a) XRD and (b) Raman spectra of  $\text{Ni}_3(\text{PO}_4)_2 \cdot 8\text{H}_2\text{O}/\text{NF}$  nano/ microflakes.

Typical Raman spectra in Figure 3.22b consists of three ranges of vibrations including  $140 - 300$ ,  $350 - 700$  and  $900 - 1100 \text{ cm}^{-1}$  <sup>66,243-245,247,260,261</sup>. Raman shifts at  $958.5$  and  $1052.8 \text{ cm}^{-1}$  are assigned to the respective  $\nu_1 \text{ PO}_4^{3-}$  symmetric and  $\nu_3 \text{ PO}_4^{3-}$  antisymmetric stretching modes. There is also a band at  $1009.6 \text{ cm}^{-1}$  corresponds to the NiOH deformations modes. A low intensity band at  $899.5 \text{ cm}^{-1}$  can be a water liberation mode as reported by Breitingner et al.<sup>260</sup> Raman shift at  $678.8 \text{ cm}^{-1}$  (within the  $350$  to  $700 \text{ cm}^{-1}$  range) is assigned to the  $\nu_4$  bending modes of  $\text{PO}_4^{3-}$  unit<sup>247</sup>. Other peaks at  $378.5$  and  $577.4 \text{ cm}^{-1}$  indicate the deformation modes of  $\text{PO}_4$  and P-O-P, respectively<sup>243</sup>. The corresponding O-P-O bending modes is observed at  $450 \text{ cm}^{-1}$ . At the low wavenumber region, Raman band at  $211.9$  and  $285 \text{ cm}^{-1}$  can be assigned for P-O-P (bridge) bending and M-O stretching (i.e. Ni-O and O-Ni-O) vibrations, respectively. As the metal oxygen stretching occurs in the P-O-P bending region, it is difficult to assign this vibration unambiguously<sup>261</sup>. Also it can be seen that the Raman shifts at  $140.8$  and  $187.5 \text{ cm}^{-1}$  are due to external vibrations<sup>244,245</sup>. All these modes further confirms the growth of single phase  $\text{Ni}_3(\text{PO}_4)_2 \cdot 8\text{H}_2\text{O}$  monoclinic structure over NF support, without any secondary phases.

### 3.4.3 Morphology under SEM and TEM

The surface morphology and microstructure of the nickel phosphate hydrate were analyzed with electron microscope. The SEM images of the  $\text{Ni}_3(\text{PO}_4)_2 \cdot 8\text{H}_2\text{O}/\text{NF}$

captured at different magnifications are shown in Figure 3.23a-b. Low magnification SEM image confirms 3D growth of  $\text{Ni}_3(\text{PO}_4)_2 \cdot 8\text{H}_2\text{O}/\text{NF}$  nano/ microflakes layers radiating around all the directions. Each layer is randomly assembled and forming the multilayer structure. High magnification SEM image Figure 3.23b shows interconnected 2D micro flakes, where the average length and thickness of the flakes vary from 5-10  $\mu\text{m}$  and 100-200 nm, respectively. HR-TEM image Figure 3.23c confirms the interconnected disordered layer structure.

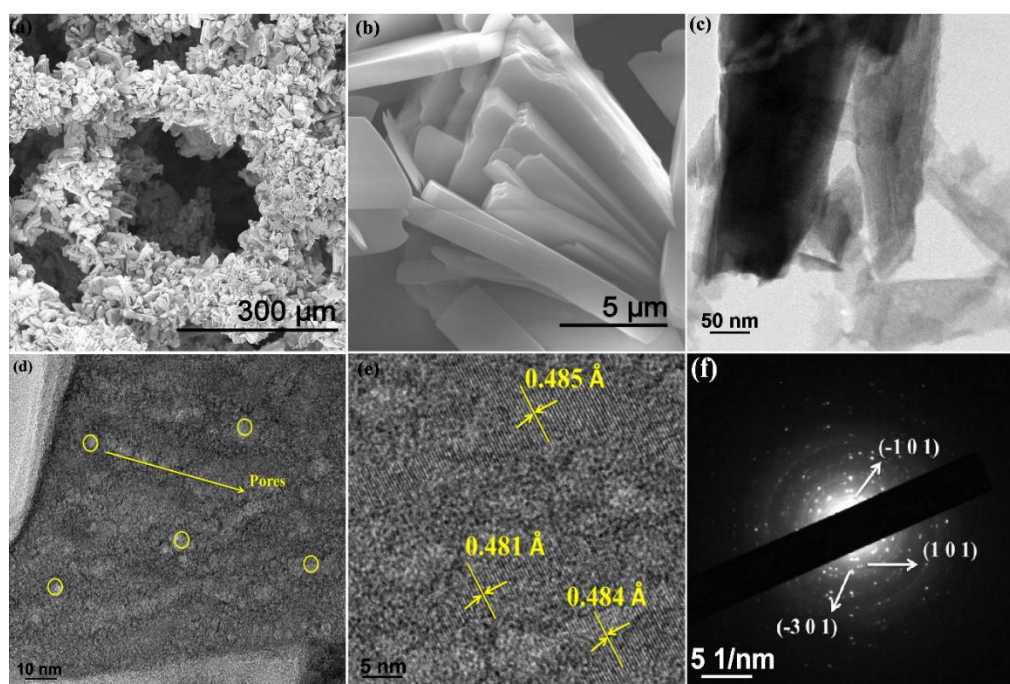


**Figure 3.23** (a-b) SEM images of  $\text{Ni}_3(\text{PO}_4)_2 \cdot 8\text{H}_2\text{O}/\text{NF}$  captured at different magnifications, (c) HRTEM image of  $\text{Ni}_3(\text{PO}_4)_2 \cdot 8\text{H}_2\text{O}$  nano/ microflakes, (d) Individual flake consists of pores, (e) Measured lattice space in layered flakes, and (f) the corresponding SAED pattern.

Further TEM analysis (Figure 3.23d) shows visible pores with an average size of 4 nm, reveals mesoporous microstructure of the materials. A well-resolved lattice fringe of  $\sim 0.48 \text{ \AA}$  as shown in Figure 3.23e can be assigned to (020) plane of monoclinic  $\text{Ni}_3(\text{PO}_4)_2 \cdot 8\text{H}_2\text{O}$  crystal structure (JCPDS No. 33-951). The selected area electron diffraction pattern in Figure 3.23f elucidate polycrystalline nature of the composite,

whereas energy dispersive spectroscopy (EDS) analysis in Figure 3.24a reveals the existence of primary Ni, P, and O elements with composition, asserting successful growth of nickel phosphate without impurities.

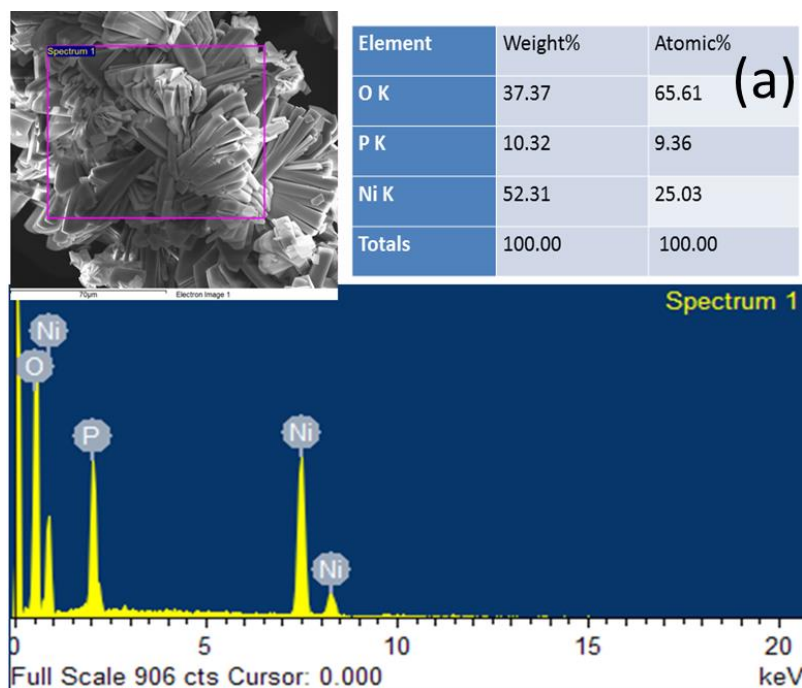


**Figure 3.24** EDS spectrum of  $\text{Ni}_3(\text{PO}_4)_2 \cdot 8\text{H}_2\text{O}$  nano/ microflakes and their corresponding elemental composition

### 3.4.4 XPS Analysis

X-ray photoelectron spectroscopy was carried out to investigate the atomic valence state of the nickel phosphate multilayer nano/ microflakes. From the XPS survey spectrum in Figure 3.25a, it has been perceived that the primary elements of Ni, P and O are present in the material, which is consistent with the EDS analysis. XPS spectra of Ni 2p, P 2p and O 1s of the sample are shown in Figure 3.25b-c. As seen from Figure 3.25b, Ni 2p consists of two peaks with their respective satellite peaks. The peaks centered at 856.2 and 873.9 eV correspond to the  $2p_{3/2}$  and  $2p_{1/2}$  splitting of  $\text{Ni}^{2+}$ , which possibly interacting with the phosphate and oxygen ions<sup>64,262</sup>. Besides, the presence of two additional deconvoluted peaks at higher binding energies of 858.1 and 875.9 eV in

the Ni2p XPS spectra can be assigned to the core levels of Ni<sup>3+</sup> cations, which indicates the presence of Ni-(OH)<sub>2</sub> in the Ni<sub>3</sub>(PO<sub>4</sub>)<sub>2</sub>·8H<sub>2</sub>O structure<sup>263,264</sup>. In addition, the satellite peaks at 858.1 and 875.9 eV further reveals the existence of Ni at their main +2 state. The corresponding P 2p spectra in Figure 3.25c shows the major peak at 133.1 eV and can be assigned to P-O interactions in nickel phosphate<sup>255</sup>. This XPS results is further supported with O 1s spectra shown in Figure 3.25d. The strong and intense peak at 531.2 eV is associated to the Ni-O and P-O bonding. The small intensity peak positioned at 532.8 eV mainly arises from the hydrates and moisture<sup>238</sup>.

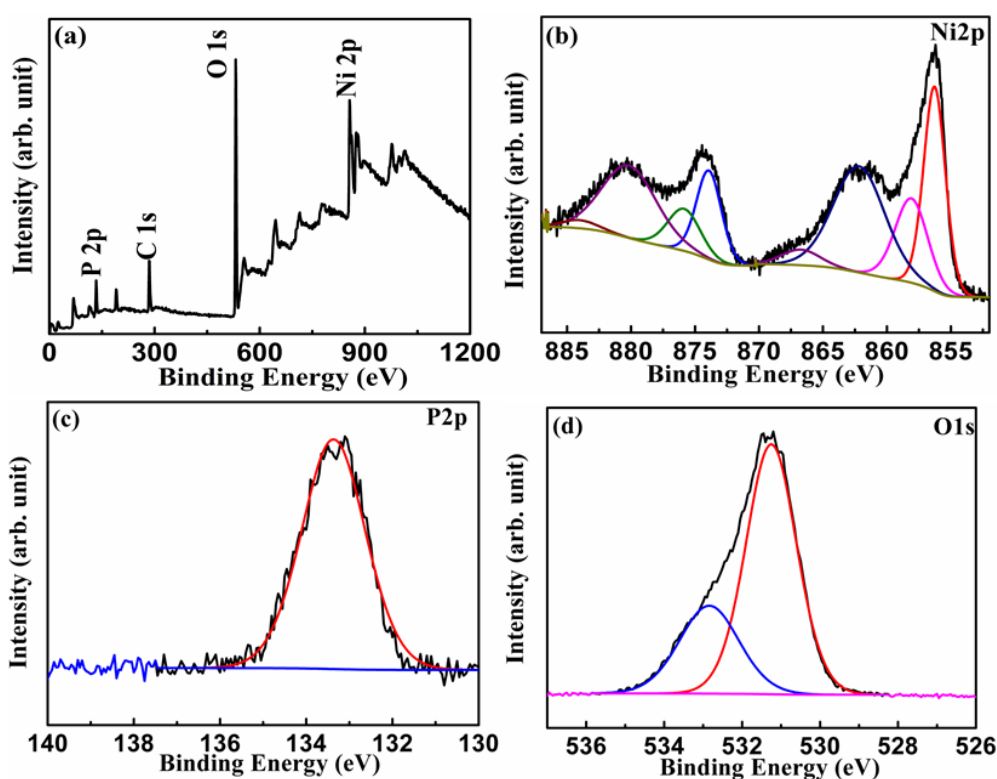


**Figure 3.25** (a-d) XPS survey and core level XPS spectra of nickel phosphate multilayer nano/ microflakes.

## 3.5 Co<sub>3</sub>(PO<sub>4</sub>)<sub>2</sub>·8H<sub>2</sub>O Nanoflakes/ Microflower on NF

### 3.5.1 Synthesis and growth mechanism

Co<sub>3</sub>(PO<sub>4</sub>)<sub>2</sub> nanoflakes/ flower was grown over nickel foam via hydrothermal method. More specifically, 2.5 mM Co(NO<sub>3</sub>)<sub>2</sub>·6H<sub>2</sub>O and 2.5 mM NH<sub>4</sub>H<sub>2</sub>PO<sub>4</sub> were dissolved in

the deionized (DI) water under stirring for 15 min to form the transparent light pink solution. The pre-treated nickel foam and light pink solution were transferred to a 100 mL autoclave, and then kept at 120 °C for 8 h in an oven. After cooled down to the room temperature naturally, the sample was washed with DI water, ethanol and acetone with the assistance of ultrasonication three times. After drying, the sample was annealed at 120 °C for 12 h in the oven. The loading mass of the  $\text{Co}_3(\text{PO}_4)_2$  nanoflakes/ flower was calculated by subtracting the weight of pure nickel foam from the weight of nickel foam with  $\text{Co}_3(\text{PO}_4)_2$  after the growth process. Typical mass of  $\text{Co}_3(\text{PO}_4)_2$  nanoflakes/ flower was  $\sim 4.5 \text{ mg cm}^{-2}$ . Figure 3.26 shows a photograph of  $\text{Co}_3(\text{PO}_4)_2 \cdot 8\text{H}_2\text{O}/\text{NF}$  samples before (pink-purple colour) and after (purple colour) annealing.



**Figure 3.26** Digital photograph of  $\text{Co}_3(\text{PO}_4)_2$  grown on NF substrate before (left) and after (right) annealing.

To comprehend the growth mechanism of the cobalt phosphate, the time dependent analysis was carried out and samples were synthesized via same fabrication procedure with different timings of 2, 4, 6 and 8 h. These samples were investigated with SEM (Figure 3.27) and EDX (Figure 3.28) analysis to view the nanoflakes/ microflower growth over nickel foam. In summary, cobalt phosphate nucleated on the nickel foam and grew in different directions to form the flower, which started to grow initially at the

edges of the NF then further grew towards the centre.

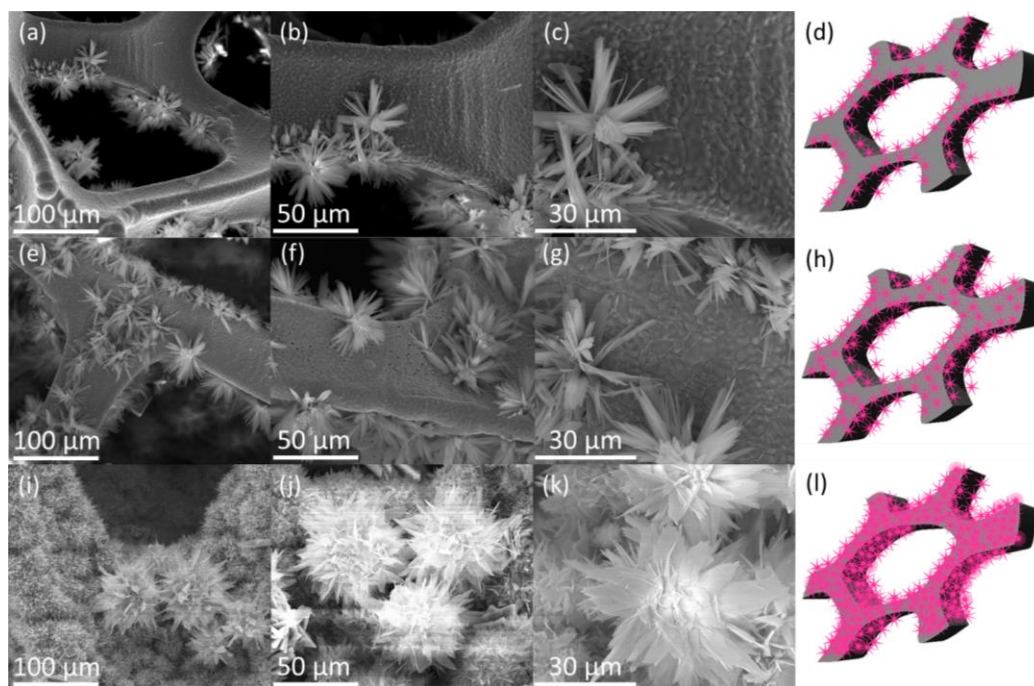
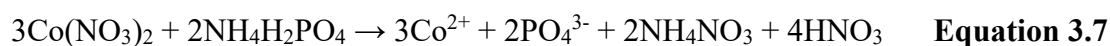


**Figure 3.27** SEM images of 2, 4 and 8 hours growth at different magnifications. (d,h,l) schematic of growth process.

Initially, the release of ammonium from phosphate precursor could drive the solution pH towards neutral/ alkaline conditions where the nucleation has been started, which is followed by the growth of  $\text{Co}_3(\text{PO}_4)_2$  granules at the edges of the NF. After two hours of reaction, granules are axially connected along different direction to form the flowers (Figure 3.27a-c). In this way, cobalt phosphate microflower nucleated further and started to grow towards the centre (Figure 3.27e-g) of the individual branch of the nickel foam, at the end of a 4 h reaction. Finally, the  $\text{Co}_3(\text{PO}_4)_2$  flowers completely covered the surface of the nickel foam substrate homogeneously after 8 h hydrothermal reaction at 120 °C (Figure 3.27 i-k). The schematic representation of the  $\text{Co}_3(\text{PO}_4)_2$  growth process is shown in Figure 3.27d, h, l. EDX and elemental mapping of 2, 4, 6 and 8 hour growth (Figure 3.28) further confirm this proposed growth process, where the growth can be explained by the following chemical reactions (Equation 3.7-3.8):





**Equation 3.8**

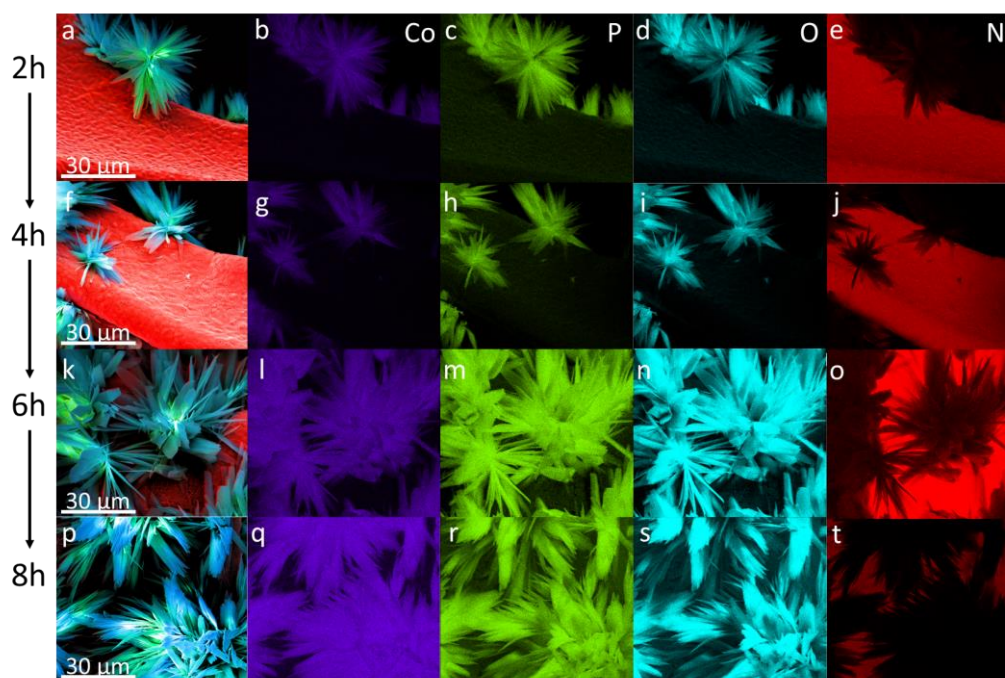


**Figure 3.28** Growth process identification by EDX mapping. (a) Phase distinguishable elemental mapping for 2h sample; (b-e) EDX elemental mapping for Co, P, O, Ni elements; (f-j), (k-o) and (p-t) are corresponding results for 4, 6 and 8h samples, respectively.

### 3.5.2 Structure Analysis (XRD and Raman)

The crystal structure and phase of nickel foam-supported cobalt phosphate was determined by XRD before and after annealing as shown in Figure 3.29a. Both samples can be indexed to cobalt phosphate hydrate (JCPDS 33-0432) with monoclinic crystal structure. After dehydrating at 120 °C for 12 h, the electrode colour changed from pink-purple to purple (Figure 3.26), which may be associated to the loss of surface water during annealing. However, reflections from the planes of cobalt phosphate became narrow and intense, which indicates that the low temperature annealing process enhanced the crystal quality.<sup>66</sup>

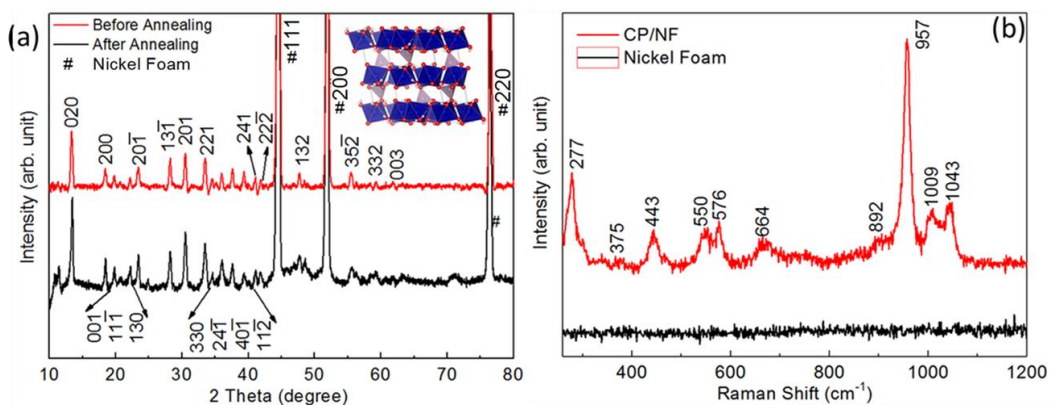


**Figure 3.29** (a) XRD patterns of cobalt phosphate electrode before and after annealing, (b) Raman spectra of cobalt phosphate electrode.

The observed room temperature Raman spectra in Figure 3.29b further support the growth of high quality cobalt phosphate hydrate structure on Ni Foam (NF). The peak at 277 cm<sup>-1</sup> is due to the O-Co-O bending<sup>244</sup>, and the high intensity peak at 957 cm<sup>-1</sup> assigned to the  $\nu_1$  PO<sub>4</sub><sup>-3</sup> symmetric stretching vibrations<sup>244,245</sup>, the peaks at 1009 and 1043 cm<sup>-1</sup> are assigned to  $\nu_3$  PO<sub>4</sub><sup>-3</sup> asymmetric stretching modes.<sup>245,261</sup> The low intensity peak at 664 cm<sup>-1</sup> corresponds to the  $\nu_4$  bending of the PO<sub>4</sub><sup>-3</sup> unit. The O-P-O and P-O-P bending modes are located at 443 and 894 cm<sup>-1</sup><sup>243,245</sup>, respectively. Raman bands at 550 and 576 cm<sup>-1</sup> are attributed to the  $\nu_2$  PO<sub>4</sub> and H<sub>2</sub>PO<sub>4</sub> bending modes.<sup>242</sup> All these Raman modes apparently confirm the formation of cobalt phosphate hydrate structure and corroborate with the XRD analysis.<sup>244,245,247,248,261</sup>

### 3.5.3 Morphology under SEM and TEM

The low magnification SEM image in Figure 3.30a1 shows a homogenous distribution of the cobalt phosphate nano/ microflower over the nickel foam. Figure 3.30a2 confirms the cobalt phosphate nanoflake (with an average thickness from 100 to 400 nm) outward growth in different directions, forming a flower-like microstructure. The EDX (Figure 3.30b) analysis clearly evidences the presence of the Co, P, and O elements in cobalt phosphate sample. In addition, Figure 3.30c shows the TEM image of cobalt phosphate powder, which has been scratched off from the nickel foam. Figure 3.30c1 shows the

substrate-delaminated few-nanoflake structures with an average thickness of 200 nm. Corresponding selected area electron diffraction (SAED) pattern in Figure 3.30c2 indicates good crystallinity of the multilayer structure of the cobalt phosphate nanoflakes and may be described as Bernal stacked single molecule layers with [001] growth direction<sup>175</sup>.

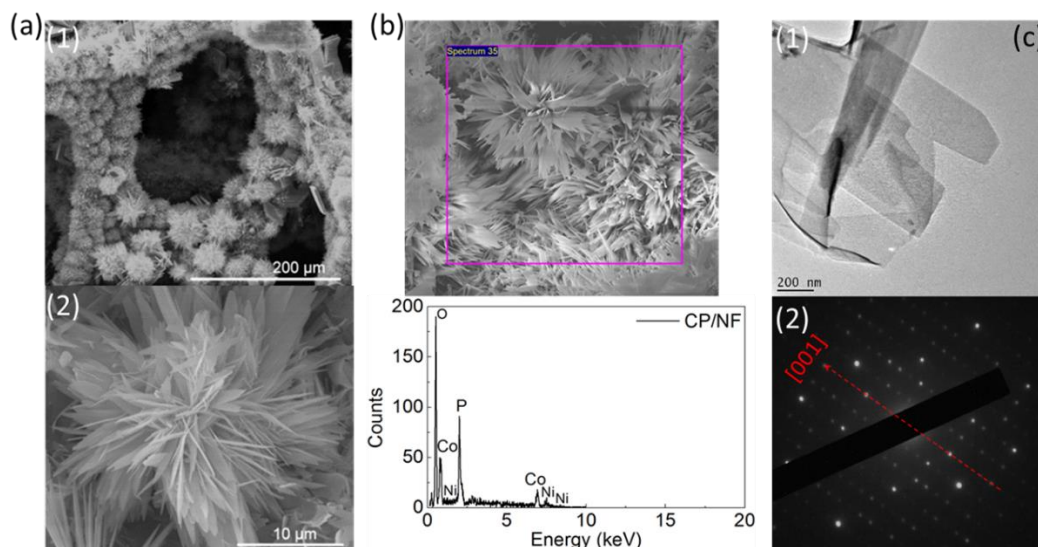


**Figure 3.30** (a) SEM images of cobalt phosphate electrode at different magnifications, (b) EDX analysis of cobalt phosphate electrode, (c) TEM image (1) and SAED pattern (2) of cobalt phosphate electrode.

### 3.5.4 XPS Analysis

The CP/NF sample was analyzed by X-ray photoelectron spectroscopy (XPS) to investigate the atomic valence state. The Ni2p, O1s, P2p and Co2p XPS spectra are shown in Figure 3.31. As presented in Figure 3.31a, the peaks at 856.1 eV ( $\text{Ni}(\text{OH})_2$ )<sup>265</sup> and 861.2 eV (satellite)<sup>266</sup> are may be due to the surface reaction on nickel foam during hydrothermal procedure. However, no peak observed at 854.3 eV<sup>267</sup> or 871.8 eV<sup>268</sup> indicated no nickel oxide formed. The peaks of O1s at 531.5 eV<sup>269</sup> in Figure 3.31b corresponds to the existence of  $\text{Ni}(\text{OH})_2$ . According to the P2p spectra in Figure 3.31c, the single bonding energy peak at 133.6 eV<sup>270</sup> is assigned to the P-O bonding, which corresponds with the O1s peak at 531.1 eV<sup>271</sup>. As expected, the peaks of Co2p (Figure

3.31d) correspond to  $\text{Co}2p_{3/2}$  at  $781.5 \text{ eV}^{272}$ , along with a satellite peak at  $786.8 \text{ eV}^{273}$ , indicates that +2 valence are the main state for cobalt.  $\text{Co}2p_{1/2}$  orbits at  $797.8 \text{ eV}^{274}$  and  $803.5 \text{ eV}^{273}$  further prove the +2 valence state.

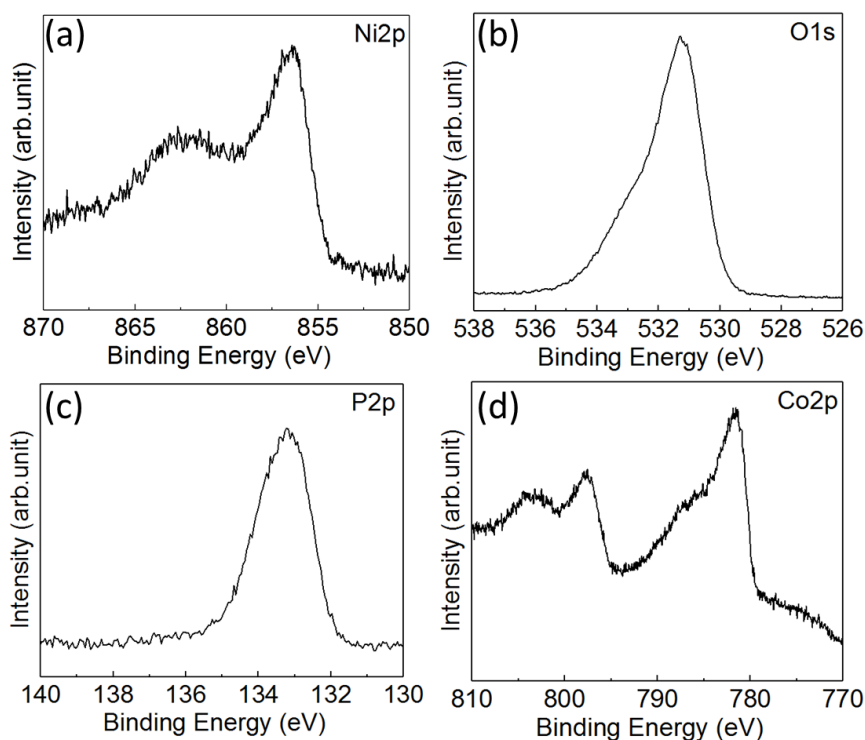


**Figure 3.31** (a-d) Ni2p, O1s, P2p and Co2p XPS spectra of CP/NF.

### 3.6 Conclusion

In this chapter, the fabrication process and material characterization of four different nanostructure materials were discussed. The materials were fabricated by simple hydrothermal method controlled by different concentration of cations and anions, temperature and pressure. Hierarchical 3D/1D hybrid  $\text{NiO-In}_2\text{O}_3$  hetero-structures were optimized using different ratio of two cations, and  $\text{Co}_3(\text{PO}_4)_2$  nanoflake/ microflower structure was improved by controlling the temperature rate and annealing process. In order to understand the growth mechanism of the fabricated materials, the time dependent analysis was carried out via same procedure. The morphology and microstructure of the fabricated materials were characterized using high resolution

scanning electron microscope, and high resolution transmission electron microscope, and structures were analysed by X-ray diffraction and Raman. X-ray photoelectron spectroscopy was carried out to investigate the valences of the electrode materials, which is conducive to understand the electrochemical mechanism. The fabricated novel nanostructure materials show the potential to be the promising electrodes for supercapattery application. The electrochemical performance studies are discussed in the following two chapters.

# Chapter 4 Electrochemical performances of materials

## 4.1 Introduction

In this chapter, the electrochemical properties of the four synthesized electrode materials were investigated in a three electrode configuration in-order to understand the charge-storage mechanism. The platinum wire (Pt) and saturated calomel electrode (SCE) as counter and reference electrodes, respectively. Electrode material along with the electrolyte determines the charge storage characteristics of materials. Different chemical valence and nano/ micro structure morphology of the electrode material can bring drastic variation in charge storage characteristic of the energy storage device. The surface to volume ratio of the nanostructure can be controlled by varying the synthesis parameter during the hydrothermal treatment, the more active sites on the electrode surface may consequently increase energy storage capacity. On the other hand, different types of electrolyte ions and their concentration also influence on the electrochemical properties due to the variation in electron/ ion transfer kinetics. The following Table 4.1 shows the electrochemical performances of fabricated materials in different electrolytes.

**Table 4.1** Electrochemical performances of fabricated materials in different electrolytes.

Electrode Material	Electrolyte	Capacity	Capacitance	Voltage Window	Cyclability
Composition		mAh g <sup>-1</sup>	F g <sup>-1</sup>	V	Cycles
NiO-In <sub>2</sub> O <sub>3</sub> /NF	3 M KOH	212.9	1096	0.75	89% after 5,000 cycles
Co <sub>3</sub> (PO <sub>4</sub> ) <sub>2</sub> ·8H <sub>2</sub> O/NF	1 M NaOH	241.2	1578	0.7	72.8% after 1,000 cycles
Ni <sub>3</sub> (PO <sub>4</sub> ) <sub>2</sub> ·8H <sub>2</sub> O/NF	1 M NaOH	301.8	1552.3	0.9	84% after 10,000 cycles
Co <sub>3</sub> (PO <sub>4</sub> ) <sub>2</sub> /NF	3 M KOH	215.6	1990	0.5	90.5% after 5,000 cycles

The four synthesized electrode materials all exhibit a non-capacitive Faradaic/ quasi-battery mechanism, the specific capacity in terms of  $C \text{ g}^{-1}/ \text{mAh g}^{-1}/ \text{mAh cm}^{-2}$  was calculated using Equation 4.1-3.

Specific capacity ( $C \text{ g}^{-1}$ ) of electrode material in three electrodes system

$$C = \frac{I \times t}{m} \quad \text{Equation 4.1}$$

where, I is the charge-discharge current (A), t is the discharge time (s), m is the mass loading of active material (g).

Specific capacity ( $\text{mAh g}^{-1}$ ) of electrode material in a three electrode system

$$C = \frac{I \times t}{3600 \times m} \quad \text{Equation 4.2}$$

where, I is the charge-discharge current (mA), t is the discharge time (s), m is the mass loading of active material (g).

Specific capacity ( $\text{mAh cm}^{-2}$ ) of electrode material in a three electrode system

$$C = \frac{I \times t}{3600 \times A} \quad \text{Equation 4.3}$$

where, I is the charge-discharge current (mA), t is the discharge time (s), A is the area of the electrode ( $\text{cm}^2$ ).

However, due to the misconception in the literature of the term “pseudocapacitance”, many researchers have classified their materials with a behaviour of a noticeable discharge plateau to be capacitive<sup>63,64</sup> and used the same equation to estimate the charge storage capacity. In order to compare with those results, the specific capacitance of the materials (in terms of  $\text{F g}^{-1}$ ) was calculated using Equation 4.4.

Specific capacitance ( $\text{F g}^{-1}$ ) of electrode material in three electrodes system

$$C_s = \frac{I \times t}{m \times U}$$

**Equation 4.4**

where, I is the charge-discharge current (A), t is the discharge time (s), m is the mass loading of active material (g), U is the potential (V).

## 4.2 Electrochemical performance of nickel foam

In order to understand the contribution of bare NF, CV measurements of the NF before and after acid treatment were carried out at a scan rate of  $10 \text{ mV s}^{-1}$  and shown in Figure 4.1. The estimated specific capacity of the bare NF is 0.021 and 0.023  $\text{mAh cm}^{-2}$  before and after the acid treatment, thus remaining essentially unchanged. Compare to the fabricated material, the capacity of NF is negligible. In addition, after acid treatment, the substrate indicate two reduction peaks may due to the formation of NiOOH metastable phase as:  $\text{Ni} \rightarrow \text{NiO} \rightarrow \text{Ni}(\text{OH})_2 \rightarrow \text{NiOOH} \rightarrow \text{Ni}(\text{OH})_2 \rightarrow \text{NiO}$ .

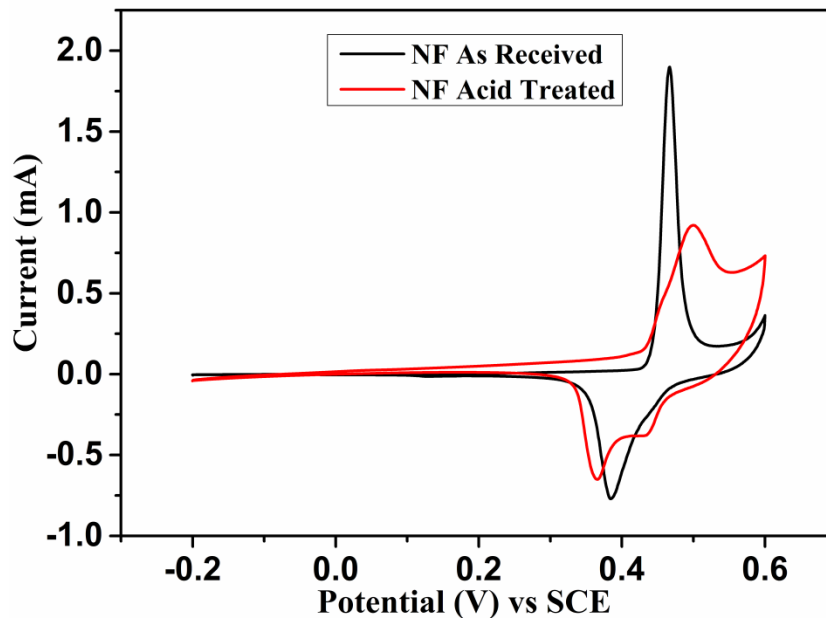


**Figure 4.1** CV curves of bare NF before (black) and after (red) acid treatment measured at  $10 \text{ mV s}^{-1}$  in 3M KOH solution.

During hydrothermal process, a thin layer of nickel hydroxide may synthesize on nickel foam surface. To confirm the conversion of the substrate, one piece of nickel foam ( $3 \times 3 \text{ cm}^2$ ) was kept in deionized water at  $120 \text{ }^\circ\text{C}$  for 8 hours. The obtained nickel hydroxide on nickel foam sample (NOH/NF) was investigated under SEM, EDX (Figure 4.2) and XPS (Figure 4.3a-b).

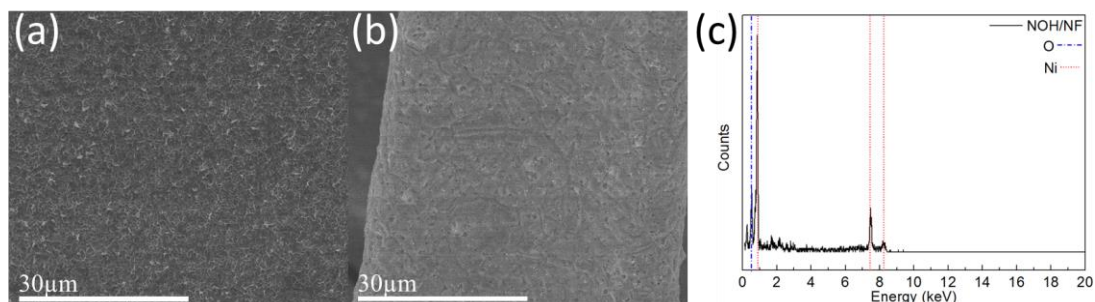


**Figure 4.2** (a-b) SEM images and (c) EDX analysis of NOH/NF sample.

Figure 4.2a-b shows the SEM images NOH/NF at different magnifications. A thin layer of homogeneous fibre-like morphology was observed on the NH/NF sample, and from the EDX analysis (Figure 4.2c), the elements detected from NOH/NF were nickel and oxide only.

To further investigate the growth mechanism, the NOH/NF samples was analyzed by X-ray photoelectron spectroscopy. The Ni2p and O1s spectra are shown in Figure 4.3a-b. As presented, the peaks at  $856.1 \text{ eV}$  ( $\text{Ni}(\text{OH})_2$ )<sup>265</sup>,  $852.6 \text{ eV}$  ( $\text{Ni}$ )<sup>267</sup> and  $861.2 \text{ eV}$  (satellite)<sup>266</sup> were obtained, which indicated the slow oxidation reaction of nickel foam in deionized water during hydrothermal procedure. However, no peak observed at  $854.3 \text{ eV}$ <sup>267</sup> or  $871.8 \text{ eV}$ <sup>268</sup> indicated no nickel oxide formed. The peaks of O1s at  $531.5 \text{ eV}$ <sup>271</sup> in Figure 4.3b corresponds to the existence of  $\text{Ni}(\text{OH})_2$ .

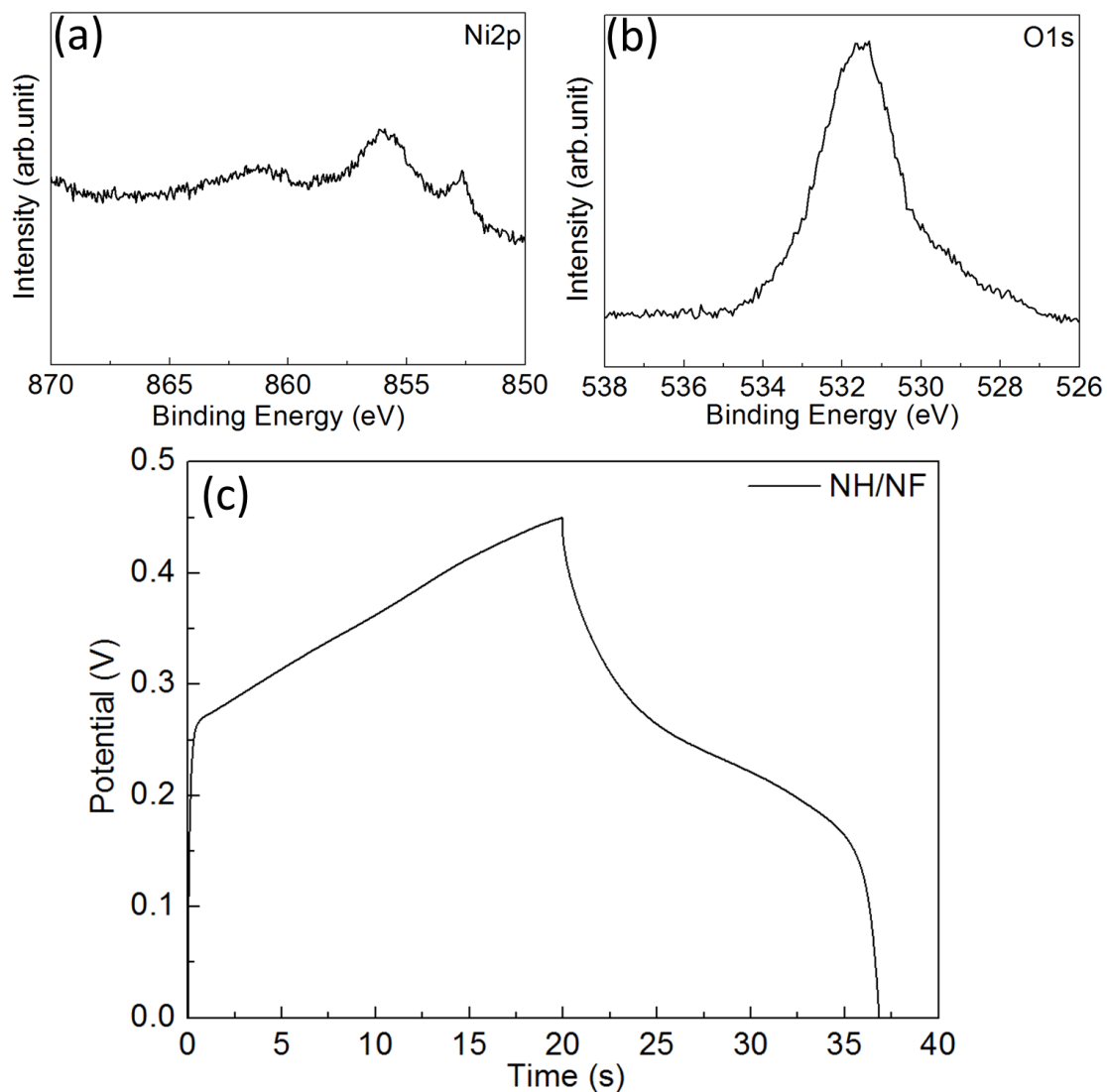


**Figure 4.3** (a-b) Ni2p and O1s XPS spectra of NOH/NF; (c) charge-discharge curves of NOH/NF sample at current density of  $5 \text{ mA cm}^{-2}$ .

The capacity of NOH/NF was found to be  $0.047 \text{ mAh cm}^{-2}$  using Equation 4.3. Overall, there is compelling evidence that the substrate contributes negligible capacity/capacitance which indicate that the nickel foam is not the principal contributor to the charge storage of the electrode.

### 4.3 Electrochemical performance of NiO-In<sub>2</sub>O<sub>3</sub>/NF hetero-microflower

To demonstrate this NiO-In<sub>2</sub>O<sub>3</sub> hetero-microflower as a supercapacitor electrode, a conventional three electrode cell was constructed and tested with electrochemical techniques such as cyclic voltammetry (CV), chronopotentiometry (CP) and electrochemical impedance spectroscopy (EIS). Typical CV curves of the NiO-NF, In<sub>2</sub>O<sub>3</sub>-NF and various compositions of NiO-In<sub>2</sub>O<sub>3</sub>-NF electrodes in 3 M KOH electrolyte at a scan rate of 10 mV s<sup>-1</sup> are shown in Figure 4.4a, which show the non-capacitive or battery-like redox characteristic of the electrodes.

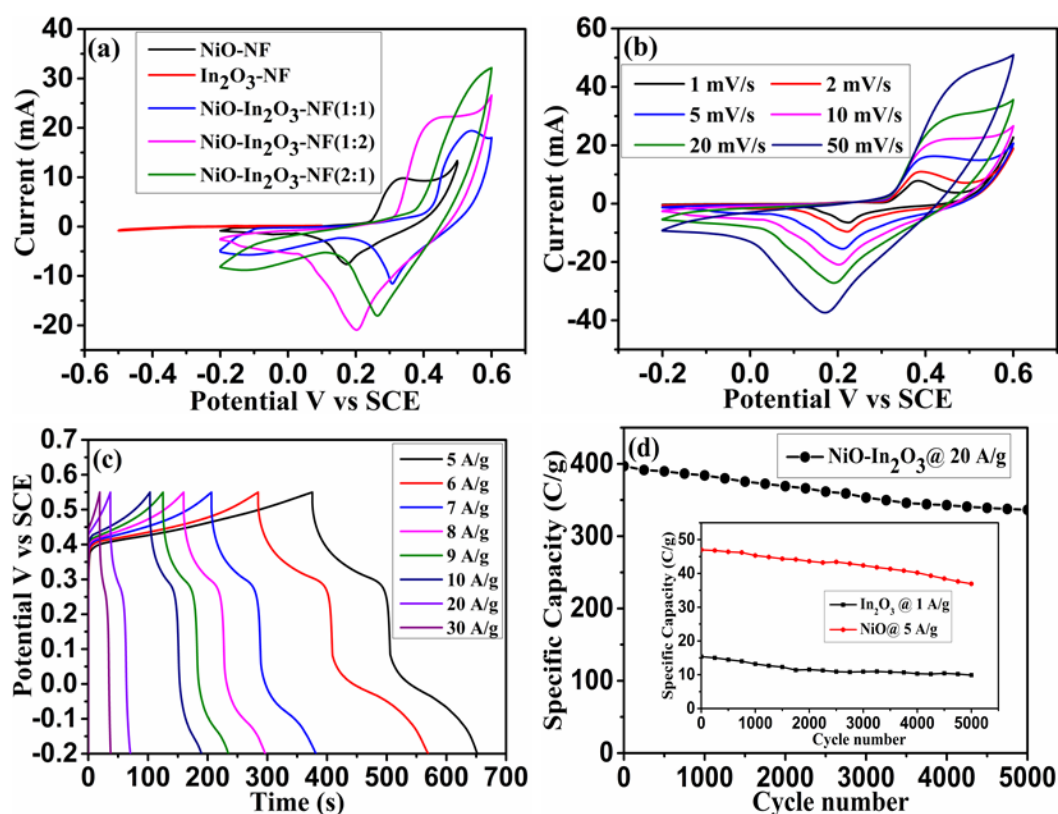


**Figure 4.4** (a) Cyclic voltammograms of individual oxides and NiO-In<sub>2</sub>O<sub>3</sub>-NF hybrid oxides measured at 10 mVs<sup>-1</sup> in 3 M KOH. (b) Scan rate dependent cyclic voltammograms of NiO-In<sub>2</sub>O<sub>3</sub>-NF (1:2) hybrid electrode. (c) Charge-discharge profile of NiO-In<sub>2</sub>O<sub>3</sub>-NF (1:2) hybrid structure (d) Cyclic stability of NiO-In<sub>2</sub>O<sub>3</sub>-NF (1:2) at 20 A g<sup>-1</sup> and the inset represents the cyclic stability curves of pristine oxides.

The comparison among the CVs in Figure 4.4a indicates that the NiO-In<sub>2</sub>O<sub>3</sub>-NF (1:2) electrode possess a significantly higher specific capacity than its individual oxides as well as the other NiO-In<sub>2</sub>O<sub>3</sub> composites. This can be attributed to the synergistic contribution of both NiO and In<sub>2</sub>O<sub>3</sub> to the specific capacitance associated to the hybrid microstructure. Figure 4.4b shows the CVs of the NiO-In<sub>2</sub>O<sub>3</sub>-NF (1:2) heterostructure over a range of scan rates of 1-50 mV s<sup>-1</sup>. The pair of redox peaks between the potential limit of -0.2 to 0.6 V present in the CVs of mixed oxide indicate the dominant non-capacitive Faradaic energy storage behavior<sup>63</sup>, which mainly originated from the Faradaic reaction over the nickel oxide surfaces based on the following reaction:

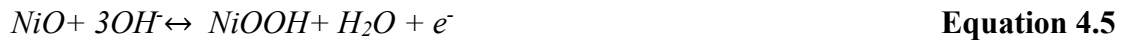


Figure 4.4c shows the charge-discharge profile of the NiO-In<sub>2</sub>O<sub>3</sub>-NF over a range of current 5-30 A g<sup>-1</sup>. Typical battery features in the charge-discharge curves indicate good pseudo-electrochemical characteristic of the electrode, which stays symmetric even at a high current density of 30 A g<sup>-1</sup>, representing a high rate performance of the electrode. The charge-discharge profile clearly evidences the contribution of In<sub>2</sub>O<sub>3</sub> to the redox process. It can be seen that the second redox process occurring between 0 and -0.2 V is due to the redox reaction over the In<sub>2</sub>O<sub>3</sub> surface. The investigation of In<sub>2</sub>O<sub>3</sub> electrodes for supercapacitors is limited in the literature and therefore related reaction mechanism is not mentioned.<sup>275-277</sup> However, the measurements demonstrate that in addition to the redox process, In<sub>2</sub>O<sub>3</sub> acts as an electron conducting channel between the NF and NiO microflower. Furthermore, the partial incorporation of In<sup>3+</sup> into NiO can increase the electrical conductivity of the NiO, which can increase the kinetics of NiO surface significantly in the hybrid electrode. It is well known that the electrical conductivity of pure NiO is poor ( $\sim \sigma < 10^{-13} \Omega^{-1} \text{ cm}^{-1}$ ) at room temperature. However, it can behave as semiconductor when the acceptor level situated near 3d<sub>8</sub> levels. In this case the holes from 3d<sub>8</sub> bands can migrate through lattice by Ni<sup>2+</sup> ions hopping, which raise the electrical conduction significantly.<sup>278</sup> The incorporation of In<sup>3+</sup> creates more surface oxygen through oxidation of Ni<sup>2+</sup> into Ni<sup>3+</sup> in the hybrid composite, followed by holes

migration based on the following reaction:<sup>278,279</sup>



This results the formation of nonstoichiometric disorder in NiO surface and thereby conductivity increased significantly.<sup>48</sup> These observations are further supported by Raman and XPS analysis as discussed in Chapter 3. Hence, it can be concluded that the observed nonstoichiometric phase in NiO is related to the amount of  $In^{3+}$  incorporation and the  $Ni^{2+}/Ni^{3+}$  ratio. In this case, among three compositions, the NiO- $In_2O_3$  (1:2) exhibits  $Ni^{2+}/Ni^{3+}$  intensity ratio of 0.66 (see Chapter 3.3.4), which is slightly higher than the other compositions and indicates a low amount of  $In^{3+}$  incorporation. This result is also matched to the captured In percentage in EDX analysis. Thereby, NiO- $In_2O_3$  (1:2) electrode showed better electrochemical performance due to their improved electrical conductivity. Even though, the measured potential drop during discharge is slightly higher than the acceptable value of  $\sim 1$  mV due to ion depletion effects in the electrolyte, which increases the ionic resistance during redox processes.<sup>49,280,281</sup>

As the energy storage mechanism is non-capacitive Faradaic/ quasi-battery like, the appropriate way to measure the amount charge stored in the electrode is specific capacity in terms of mAh  $g^{-1}$  rather than the specific capacitance  $F g^{-1}$ .<sup>65</sup> Hence the specific capacity (Cs) of the electrode was estimated using Equation 4.2.<sup>81</sup> The best specific capacity values of this hybrid composite electrode are found to be 212.9 mAh  $g^{-1}$  at the current of 5 A  $g^{-1}$ . Moreover, the electrode can retain 37.1% (79.2 mAh  $g^{-1}$ ) of its initial value for 6 times (30 A  $g^{-1}$ ) of initial current. For the sake of consistency with the reported literatures where they have measured the amount of charge in terms of specific capacitance ( $F g^{-1}$ ), authors have calculated the specific capacitance from Equation 4.4. Figure 4.5 shows the variation in specific capacitance with the current ranging from 5-30 A  $g^{-1}$  in 3.0 M KOH solution in three electrode configuration. The estimated maximum specific capacitance is 1096.8  $F g^{-1}$  at 5 A  $g^{-1}$  and decreased to 407.1  $F g^{-1}$  at 30 A  $g^{-1}$ .

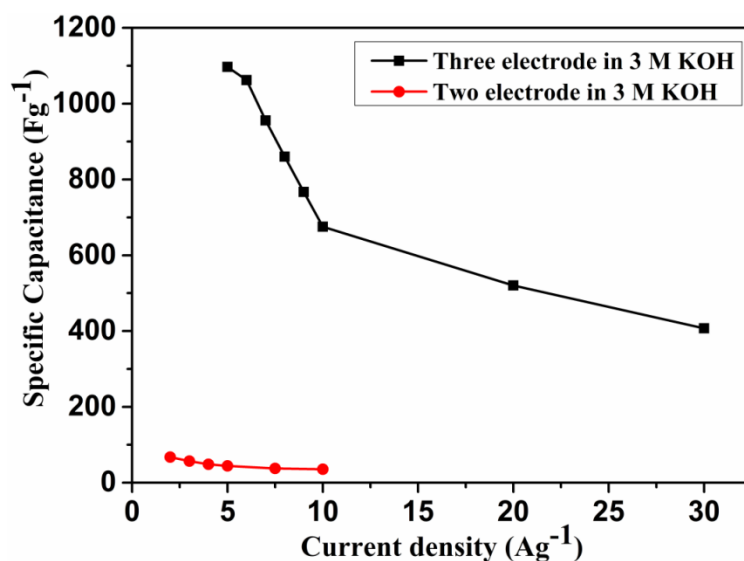


**Figure 4.5** Variation of specific capacitance with respect current density for NiO-In<sub>2</sub>O<sub>3</sub>-NF (1:2) hybrid electrode in both three and two electrode configurations.

The observed specific capacitance value for the NiO-In<sub>2</sub>O<sub>3</sub>-NF are far better than the similar hetero-composite oxide and chalcogenides based electrode materials as shown in Table 4.2. Pu *et al.* achieved ultra-high specific capacitance of 2028 F g<sup>-1</sup> at 10 A g<sup>-1</sup> with Ni(OH)<sub>2</sub>@ZnO, but the cyclic stability was limited to 68% after 500 cycles.<sup>282</sup> Similarly, Xing *et al.* reported 1529 F g<sup>-1</sup> at 2 A g<sup>-1</sup> with 42% capacity retention after 2,000 cycles in Ni<sub>3</sub>S<sub>2</sub>@ZnO hetero-structure.<sup>283</sup> Furthermore, Wang *et al.* showed 1716 F g<sup>-1</sup> at 1 A g<sup>-1</sup> in the NiCo<sub>2</sub>O<sub>4</sub>@Ni<sub>3</sub>S<sub>2</sub> core/ shell nanothorn array electrode with 83.7% capacity retention.<sup>284</sup>

**Table 4.2** Comparison of electrochemical performance for different hetero-composite electrodes in three electrode configuration

Materials	Specific Capacitance (F g <sup>-1</sup> )	Current Density	Potential Window (V)	Cyclic Stability	Ref
ZnO@MnO <sub>2</sub>	423.5	0.5 Ag <sup>-1</sup>	1	90.5% after 3000 cycles	285
Mn <sub>3</sub> O <sub>4</sub> @PbO <sub>2</sub>	338	10 mAcm <sup>-2</sup>	~2.5	-	286
CuO@MnO <sub>2</sub>	167.2	0.3 Ag <sup>-1</sup>	1	88.6% after 5000 cycles	287
WO <sub>3</sub> @MnO <sub>2</sub>	363	0.5 Ag <sup>-1</sup>	1	93.8% after 5000 cycles	288
ZnO@Co <sub>3</sub> O <sub>4</sub>	857.7	2 mAcm <sup>-2</sup>	0.5	96.8% after 6000 cycles	289
TiO <sub>2</sub> @Co(OH) <sub>2</sub>	199 mFcm <sup>-2</sup>	0.2 mAcm <sup>-2</sup>	0.6	82.5% after 4000 cycles	290
ZnO@Ni <sub>3</sub> S <sub>2</sub>	1529	2 Ag <sup>-1</sup>	0.5	42% after 2000 cycles	283
NiCo <sub>2</sub> O <sub>4</sub> @Ni <sub>3</sub> S <sub>2</sub>	1716	1 Ag <sup>-1</sup>	0.6	83.7% after 2000 cycles	284
Ni <sub>3</sub> S <sub>2</sub> @MoS <sub>2</sub>	848	5 Ag <sup>-1</sup>	0.8	91% after 2000 cycles	291
Ni@Ni <sub>3</sub> S <sub>2</sub>	1293	5 Ag <sup>-1</sup>	0.5	69% after 1000 cycles	292
ZnO@Ni(OH) <sub>2</sub>	2028	10 Ag <sup>-1</sup>	0.5	68% after 500 cycles	282
CuO@NiO	296.2	10 mVs <sup>-1</sup>	0.6	97% after 500 cycles	293
Ni(OH) <sub>2</sub> @Fe <sub>2</sub> O <sub>3</sub>	908	21.8 Ag <sup>-1</sup>	0.6	85.7% after 5000 cycles	230
ZnO@MoO <sub>3</sub>	241	5 mVs <sup>-1</sup>	1.5	89.7% after 100 cycles	294
<b>NiO-In<sub>2</sub>O<sub>3</sub>-NF</b>	<b>1096.8</b>	<b>5 Ag<sup>-1</sup></b>	<b>0.75</b>	<b>89.5% after 5000 cycle</b>	<b>This Work</b>

When compared to these electrodes, the NiO-In<sub>2</sub>O<sub>3</sub> electrode exhibit acceptable specific capacitance (1096.8 F g<sup>-1</sup> at 5 A g<sup>-1</sup>) but delivers excellent capacity retention of 89.5% after 5000 cycles. Also, these values are much higher than the electrodes made from individual compounds as can be seen from the charge-discharge curves in Figure

4.6a-b, with measured specific capacitances of  $450 \text{ F g}^{-1}$  ( $292.5 \text{ C g}^{-1}$  @  $1 \text{ A g}^{-1}$ ) and  $49 \text{ F g}^{-1}$  ( $29.4 \text{ C g}^{-1}$  @  $0.7 \text{ A g}^{-1}$ ) for NiO-NF and  $\text{In}_2\text{O}_3$ -NF respectively. The low specific capacitance for NiO and  $\text{In}_2\text{O}_3$  can be attributed to their unfavourable microstructure for ion diffusion and low intrinsic electrical conductivity.

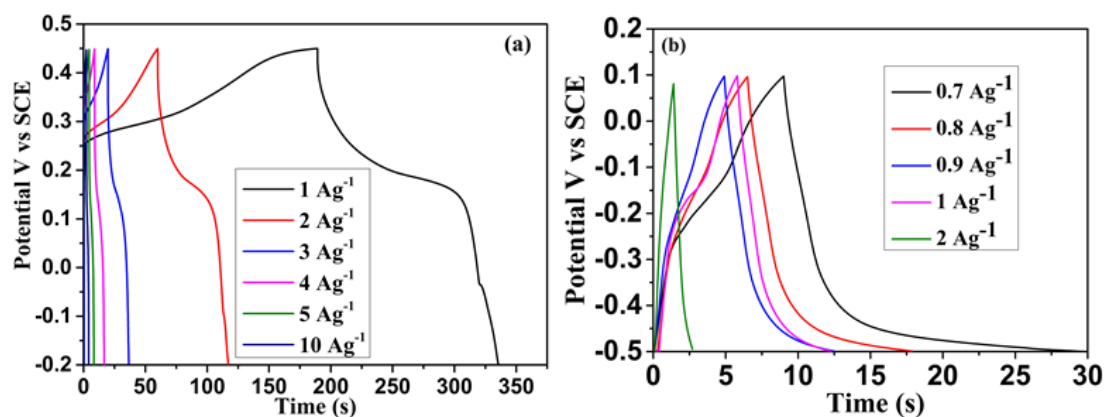


**Figure 4.6** Charge-discharge curves of (a) NiO-NF and (b)  $\text{In}_2\text{O}_3$ -NF at various current densities.

The electrical conductivity was further investigated by EIS analysis and presented in Figure 4.7. From the extended view of Nyquist plot in Figure 4.7 inset, it can be seen that the NiO- $\text{In}_2\text{O}_3$ -NF hybrid electrode showed negligible charge transfer resistance of  $\sim 0.08 \Omega$ , which indicates the incorporation of the  $\text{In}^{3+}$  ion has increased the electrical conductivity of hybrid electrode significantly. Whereas, pure NiO-NF electrode showed a dominant semicircle at high frequency region followed by sloped straight line resulting in a charge transfer resistance of  $0.45 \Omega$ .<sup>284,295,296</sup> However, the pristine  $\text{In}_2\text{O}_3$ -NF showed a distinct EIS spectra. Due to limited measurement frequency, there is incomplete depressed semicircle at high frequency region, visible semicircle at middle frequency range and a sloped line in the low frequency region.<sup>297,298</sup> Here in the Nyquist plot, the high-frequency intercept on the real axis is mainly composed of the bulk resistance of electrode materials, resistance of the current collector and contact resistance.<sup>297</sup> The sloping line in the low-frequency range ascribes the proton diffusion into the bulk electrodes.<sup>295</sup> From EIS results, it can be confirmed that the hybrid

electrode possess better electrical conductivity than the pristine materials and thereby enhanced electrochemical performance have been observed.

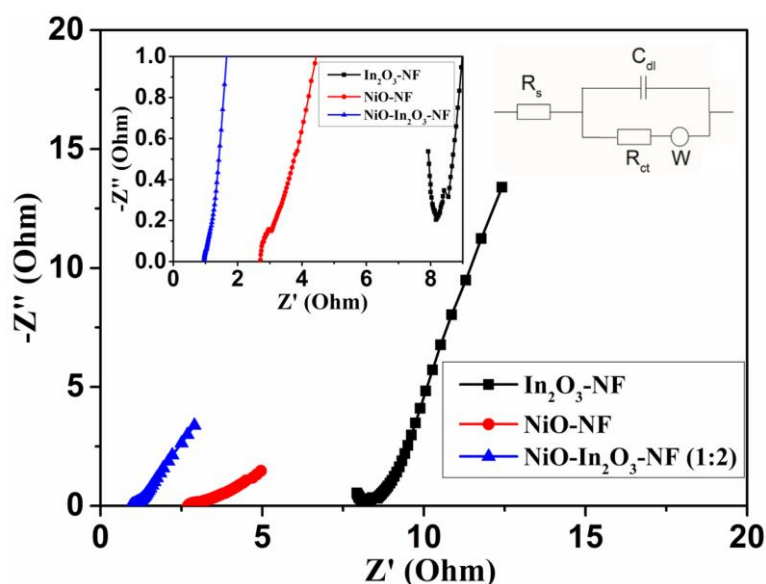


**Figure 4.7** Nyquist plot of  $\text{In}_2\text{O}_3$ -NF, NiO-NF and NiO- $\text{In}_2\text{O}_3$ -NF electrode measured at 3 M KOH in three electrode configuration.

Similarly, the electrochemical performance of other compositions namely, NiO- $\text{In}_2\text{O}_3$  (1:1) and (2:1) were also measured using 3 M KOH electrolyte. Typical charge-discharge curves of the samples measured at different current densities are shown in Figure 4.8a-b. Non-linear charge-discharge profile indicates the pseudocapacitive behaviour of the electrodes. However, the rate performance and specific capacitances were drastically varied when compared to the NiO- $\text{In}_2\text{O}_3$ -NF(1:2) electrode. This may be due to the detachment of NiO from the  $\text{In}_2\text{O}_3$  surface during electrochemical reactions owing to their inadequate hybridization and microstructure.

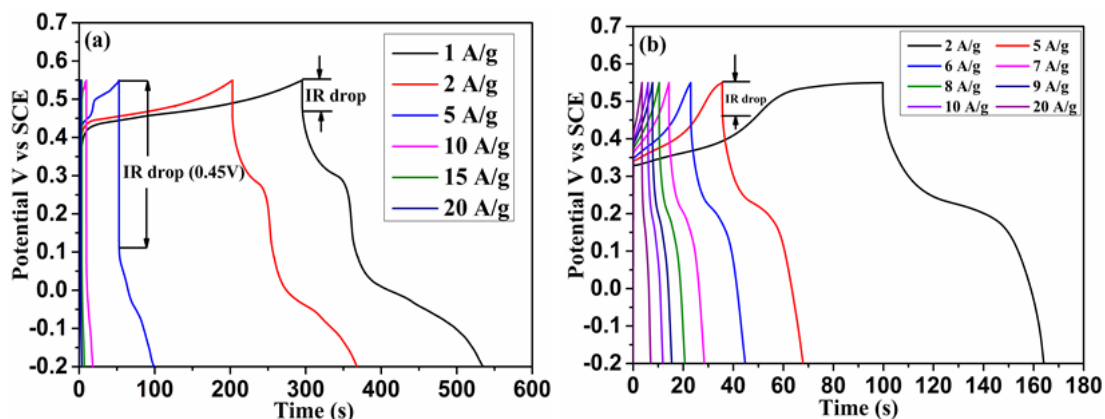


**Figure 4.8** Charge-discharge curves of (a) NiO-In<sub>2</sub>O<sub>3</sub>-NF (1:1) composite and (b) NiO-In<sub>2</sub>O<sub>3</sub>-NF (2:1) composite at various current densities.

The observed large IR drop during discharge in positive potential (i.e. active potential region of NiO ~ 0.55 to -0.2 V) in Figure 4.8a further reveals the disintegration of NiO. The specific capacitance values for these composites are found to be 404.1 Cg<sup>-1</sup> (538.8 Fg<sup>-1</sup>) for NiO-In<sub>2</sub>O<sub>3</sub>-NF (1:1) and 203.1 Cg<sup>-1</sup> (270.8 Fg<sup>-1</sup>) for NiO-In<sub>2</sub>O<sub>3</sub>-NF (2:1) at 5 Ag<sup>-1</sup>, which are quite low than the NiO-In<sub>2</sub>O<sub>3</sub>-NF(1:2) electrode at the same current density. In case of NiO-In<sub>2</sub>O<sub>3</sub>-NF (2:1), the electron kinetics between NiO and In<sub>2</sub>O<sub>3</sub> is not sufficient enough for complete utilization of NiO active sites. This is due to the formation of more Ni<sup>3+</sup>O<sub>x</sub> phase via the adsorption of negatively charged oxygen on the NiO surface as evidenced from the XPS analysis.<sup>280</sup> Thereby, only part of the NiO has been involved to redox process, resulting low specific capacitance.

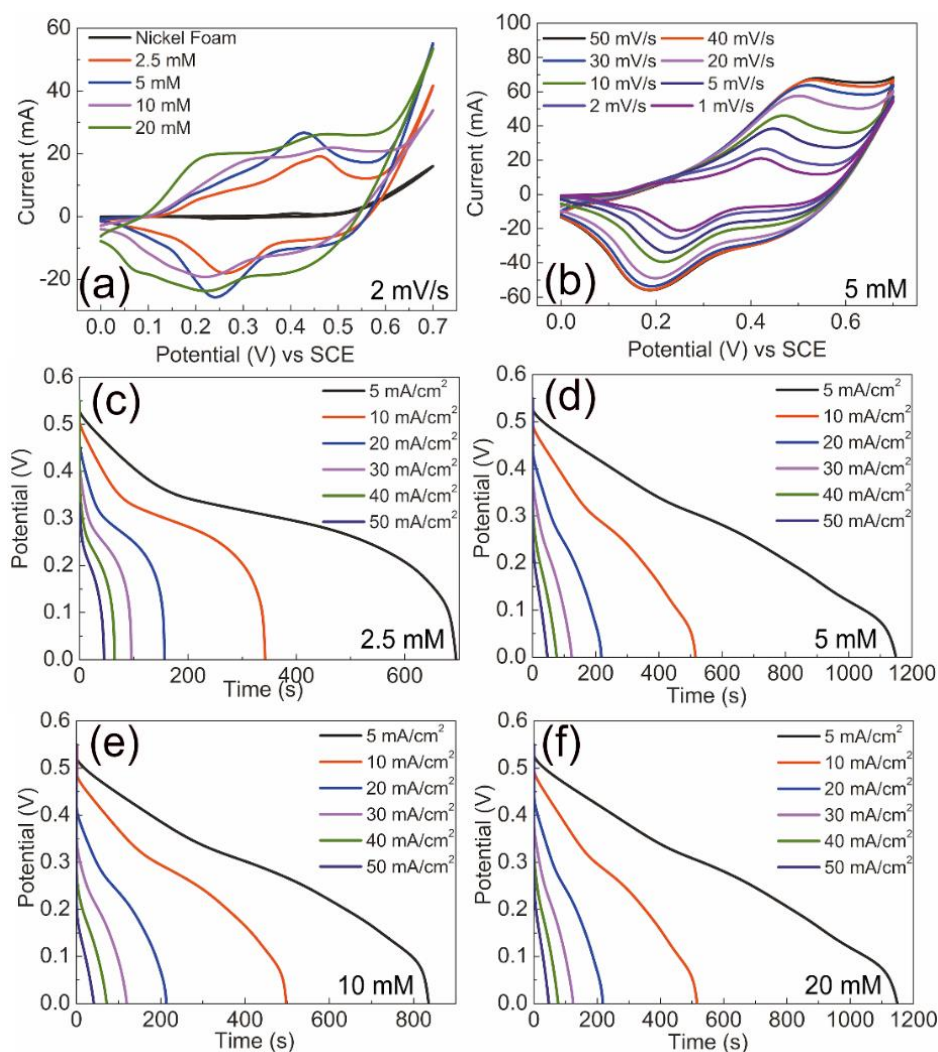
Interestingly, among the three compositions, NiO-In<sub>2</sub>O<sub>3</sub>-NF (1:2) showed the best electrochemical performance in terms of specific capacitance and rate capability, which is mainly attributed to their well-integrated 3D-1D hybrid microstructure. When compared to the monometallic oxides, the mixed NiO-In<sub>2</sub>O<sub>3</sub>-NF (1:2) electrode has delivered two orders of magnitude increased specific capacity (when compared to In<sub>2</sub>O<sub>3</sub>-NF) and three order superior rate performance. Interestingly, the observed specific capacity is even higher than the synergistic limit of individual oxides further revealing the extra-ordinary performance of the hetero-structured electrode, driven by

the three dimensional hierarchical microstructure. The nanorods-supported microflower heterostructure provides improved electron transfer kinetics and thus significantly increased specific capacity. One dimensional nanorods not only served as a scaffold for electrochemically active materials, but also served as effective channels for electron transfer between the active nano/ microflower and the NF substrate.<sup>285</sup>

Another important requirement for supercapacitor applications is its long term cyclic stability. Hence, the charge-discharge cycle was repeated up to 5,000 cycles at  $20 \text{ A g}^{-1}$  as depicted in Figure 4.4d. When compared to individual oxides, the hybrid electrode shows only 10.5% capacity loss after 5,000 cycles, while it was 21.5% and 35.6% for NiO-NF and  $\text{In}_2\text{O}_3$ -NF (Inset of Figure 4.4d). Due to the unique structural and conductive support, the NiO- $\text{In}_2\text{O}_3$ -NF (1:2) is expected to retain excellent electrochemical properties as supercapacitor electrodes.

#### **4.4 Electrochemical performance of $\text{Co}_3(\text{PO}_4)_2 \cdot 8\text{H}_2\text{O}$ /NF nanoflakes**

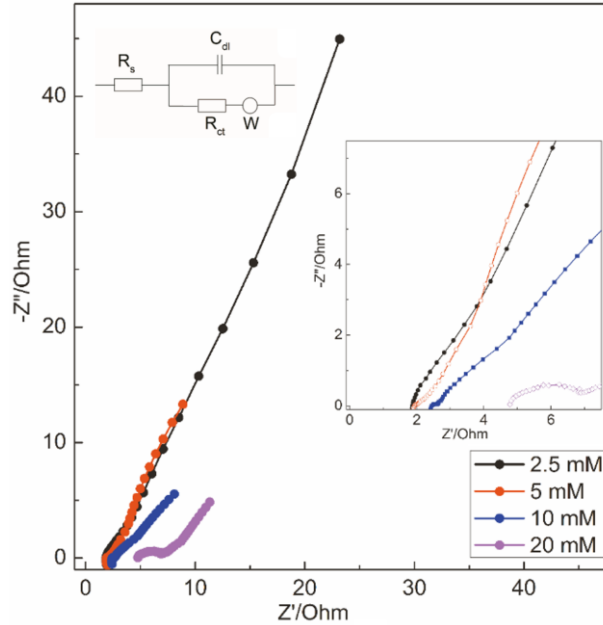
To investigate the electrochemical performance of the  $\text{Co}_3(\text{PO}_4)_2 \cdot 8\text{H}_2\text{O}$ /NF, a three electrode system was used. Figure 4.9a shows the CV curves of pure nickel foam, 2.5, 5, 10 and 20 mM  $\text{Co}_3(\text{PO}_4)_2 \cdot 8\text{H}_2\text{O}$ /NF at a scan rate of 2 mV/s in 1.0 M NaOH solution. The contribution of bare nickel foam is negligible compare to the  $\text{Co}_3(\text{PO}_4)_2 \cdot 8\text{H}_2\text{O}$ . Clear current peaks are observed in all the samples, indicating the non-capacitive Faradaic energy storage properties of the electrode material.



**Figure 4.9** (a) Cyclic voltammograms of nickel foam, 2.5, 5, 10 and 20 mM  $\text{Co}_3(\text{PO}_4)_2 \cdot 8\text{H}_2\text{O}/\text{NF}$  at a scan rate of 2 mV/s in 1 M NaOH. (b) Cyclic voltammograms of 5 mM  $\text{Co}_3(\text{PO}_4)_2 \cdot 8\text{H}_2\text{O}/\text{NF}$  at different scan rate from 1 to 50 mV/s. (c-f) Discharge profile of 2.5, 5, 10 and 20 mM samples at different current densities.

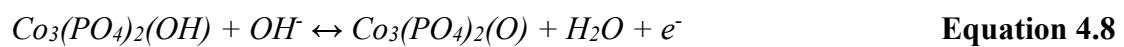
With increasing concentration (i.e., with increased mass loading of the active material), the main peaks around 0.45 and 0.25 V broaden and the peak current varies. This may be due to the higher mass loading, which results in more activate material to take part in the redox reaction but on the other hand reduces the conductivity of the electrode as can be observed from the Nyquist plots in Figure 4.10. The resistance of the electrodes are found to be 1.90, 1.94, 2.47 and 4.8  $\Omega$  with increased mass loading. The 2.5 and 5 mM CVs are nearly symmetrical, indicating good redox property of the material.

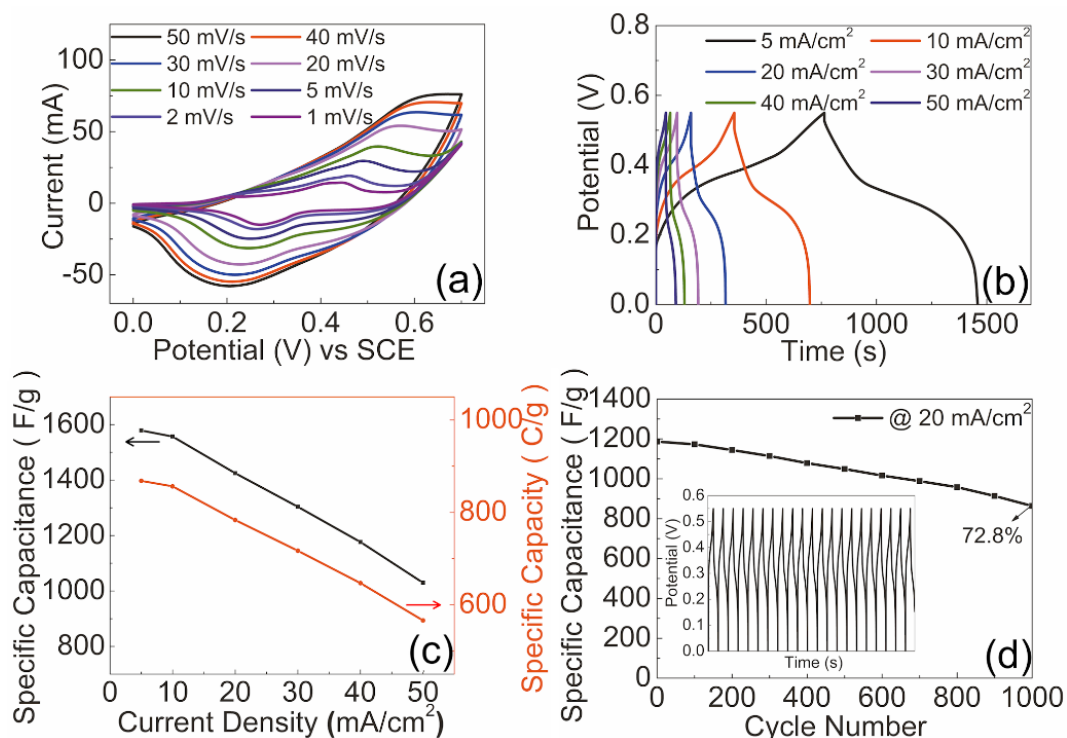
However, for higher concentration samples, the secondary peaks (around 0.25 and 0.55 V) become more obvious because of the larger mass loading enhanced the first step of the redox reactions (shown as Equation 4.7). Two pairs of oxidation and reduction peaks indicate the transform between the different states of  $\text{Co}^{2+}$  and  $\text{Co}^{3+}$ .



**Figure 4.10** Nyquist plot for 2.5, 5, 10 and 20 mM  $\text{Co}_3(\text{PO}_4)_2 \cdot 8\text{H}_2\text{O}/\text{NF}$

Figure 4.11a shows the CV curves of 2.5 mM sample at different scan rate from 1 to 50 mV/s. With increasing scan rate, the oxidation and reduction peaks started to shift from each other, indicating quasi-reversible reaction and the shape of the CVs tends to be asymmetric. Figure 4.9b shows that the peak shift in 5 mM sample is less than 2.5 mM sample, which may be due to the larger loading ( $2\times$  compared to 2.5 mM) of cobalt phosphate, resulted in more active materials to be involved in the Faradaic reactions as follows<sup>289,294</sup>:





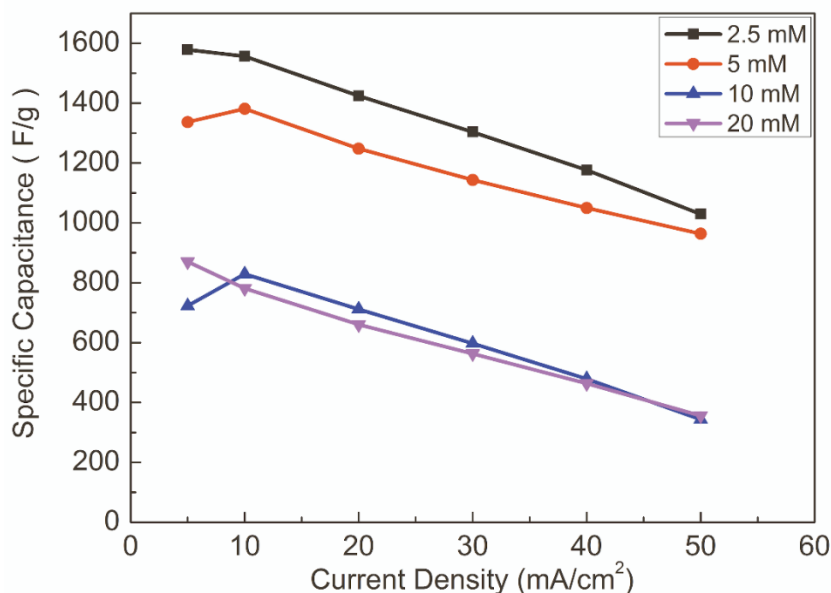
**Figure 4.11** (a) Cyclic voltammograms of 2.5 mM  $\text{Co}_3(\text{PO}_4)_2 \cdot 8\text{H}_2\text{O}/\text{NF}$  at different scan rate from 1 to 50 mV/s in 1 M NaOH. (b) Charge-discharge profile of the electrode at different current densities. (c) Specific capacitance and capacity variation at different current densities. (d) Cyclic stability of the electrode. Inset represents continuous charge-discharge profile at 20 mA  $\text{cm}^{-2}$ .

Figure 4.11b shows the charge-discharge profile of 2.5 mM  $\text{Co}_3(\text{PO}_4)_2 \cdot 8\text{H}_2\text{O}/\text{NF}$ . In both 2.5 and 5 mM discharging curves (Figure 4.9c-d), distinct potential plateaus are observed, which demonstrate the battery-like characteristics of the electrodes. The nearly symmetric charging and discharging curves at low current density indicate the reversible redox reaction. 5 mM sample shows nearly twice discharging time than the 2.5 mM sample at similar current density, which may be due to double mass loading in case of 5 mM sample. However, for 10 and 20 mM samples (Figure 4.9e-f), the discharge time does not increase with larger mass loading. As shown in the SEM image analysis in Figure 3.19f, the multilayer structures for higher-concentration samples grew thicker and larger in a disorderly fashion, which reduces the overall surface area of the electrode accessible by the electrolyte and thereby less active material is taking

part in storing the charge. These results are in good agreement with the CV analysis presented in Figure 4.11a and Figure 4.9a.

Due to the non-capacitive Faradaic/ quasi-battery mechanism, the specific capacity in terms of  $\text{mAh g}^{-1}$  was calculated using Equations 4.2. A maximum specific capacity of  $241.2 \text{ mAh g}^{-1}$  at an applied current density of  $5 \text{ mA cm}^{-2}$  was found for the  $2.5 \text{ mM}$  sample. The capacity variation as a function of current density is shown in Figure 4.11c. With a 10 times increase in the current density (from  $5$  to  $50 \text{ mA cm}^{-2}$ ), the capacity retention is  $65.2\%$  and  $72.1\%$  of the initial value for  $2.5$  and  $5 \text{ mM}$  samples, which are much better than the state of the art ( $48\%$ ) cobalt phosphate electrodes.<sup>199</sup>

However, to be comparable with reported literatures, specific capacitance in terms of  $\text{F g}^{-1}$  was calculated using Equation 4.4. An ultra-high specific capacitance of  $1578.7 \text{ F g}^{-1}$  was achieved from  $2.5 \text{ mM Co}_3(\text{PO}_4)_2 \cdot 8\text{H}_2\text{O/NF}$  at  $5 \text{ mA cm}^{-2}$  ( $1.25 \text{ A g}^{-1}$ ) and  $1336.9 \text{ F g}^{-1}$  was attained for  $5 \text{ mM}$  sample at  $5 \text{ mA cm}^{-2}$  ( $0.625 \text{ A g}^{-1}$ ), and reduced to  $1029.5 \text{ F g}^{-1}$  ( $65.2\%$ ) for  $2.5 \text{ mM}$  and  $963.6 \text{ F g}^{-1}$  ( $72.1\%$ ) for  $5 \text{ mM}$  sample for a current density of  $50 \text{ mA cm}^{-2}$  (Figure 4.11c and Figure 4.12).



**Figure 4.12** Specific capacitance as a function of applied current densities for  $2.5$ ,  $5$ ,  $10$  and  $20 \text{ mM}$  samples.

The reduction in specific capacitance in the 5 mM and higher concentration samples are due to the larger mass loading, which resulted in a thicker layer formation as compared to low concentration sample that ultimately reduced the active sites for ion diffusion from the electrolyte. However, the specific capacitance for 2.5 mM electrode is found to be better than the work reported by Tang et al., where a specific capacitance of 1409.8 F g<sup>-1</sup> at 0.25 A g<sup>-1</sup> was obtained for a honeycomb-like mesoporous cobalt nickel phosphate nanospheres, whereas for Co<sub>3</sub>(PO<sub>4</sub>)<sub>2</sub>, only 247.7 F g<sup>-1</sup> was reported<sup>205</sup>. Similarly, Li et al. showed 350 F g<sup>-1</sup> at 1 A g<sup>-1</sup> for a 3D Co<sub>3</sub>(PO<sub>4</sub>)<sub>2</sub>·8H<sub>2</sub>O architecture with flower-like morphologies assembled from 2D microsheets.<sup>199</sup> Furthermore, Pang et al. reported three different phosphate microstructures, and achieved 312 F g<sup>-1</sup> for Co<sub>11</sub>(HPO<sub>3</sub>)<sub>8</sub>(OH)<sub>6</sub> nanoribbons<sup>206</sup>, 413 F g<sup>-1</sup> for CoHPO<sub>4</sub>·3H<sub>2</sub>O nanosheets and 369.4 F g<sup>-1</sup> for NH<sub>4</sub>CoPO<sub>4</sub>·H<sub>2</sub>O nano/ microstructures. Whereas, the 2.5 mM electrode showed ~4 times better specific capacitance as compared to the best reported cobalt phosphate based electrodes. Another important requirement for supercapattery application is the long term cyclic stability. Figure 4.11d shows the cyclic stability of the 2.5 mM sample and the inset shows the continuous charge-discharge profile at 20 mA cm<sup>-2</sup>. The electrode exhibited a capacitance of 1149 F g<sup>-1</sup> (72.8% retention) after 1000 cycles, which is more than twice of the best capacitance value reported for cobalt phosphate based electrodes.<sup>175,199,205,206</sup> The decrease of the capacitance after 1000 charge-discharge cycles may be due to the morphology transformation and the dissolution of the active material as shown in Figure 4.13. After 1000 charge-discharge cycles, the Co<sub>3</sub>(PO<sub>4</sub>)<sub>2</sub>·8H<sub>2</sub>O micro/ nanoflakes started to fissure and fall off. The typical mass loading of Co<sub>3</sub>(PO<sub>4</sub>)<sub>2</sub>·8H<sub>2</sub>O/NF electrode after 1000 charge-discharge cycles is 3.45 mg cm<sup>-2</sup>, which confirm the speculation of dissolution.

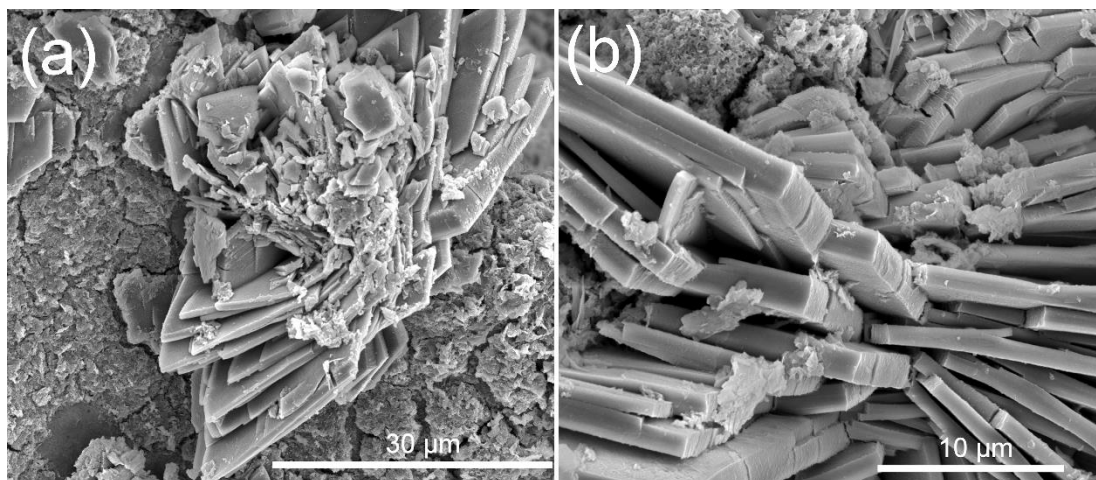


**Figure 4.13** (a-b) SEM images of  $\text{Co}_3(\text{PO}_4)_2 \cdot 8\text{H}_2\text{O}/\text{NF}$  electrode after 1000 charge-discharge cycles.

It is noteworthy that the observed specific capacity (or capacitance) is higher than the theoretical value ( $533 \text{ C g}^{-1}$  or  $969 \text{ F g}^{-1}$ <sup>299</sup>) for the cobalt phosphate electrode. This may be attributed to the contribution of electric double layer capacitance in addition to the battery-like Faradaic contributions.<sup>210</sup> When crystalline water is removed from the  $\text{Co}_3(\text{PO}_4)_2 \cdot 8\text{H}_2\text{O}$  during electrochemical reaction, a large amount of void space is available for redox reaction. The interconnected  $\text{Co}_3(\text{PO}_4)_2$  nanosheets are favorable for electrolyte penetration to the interior surfaces via the intercalated water molecules. After oxidation of crystalline water, there is a possibility of forming abundant pores within the  $\text{Co}_3(\text{PO}_4)_2$  nano/ microsheets as can be seen in Figure. 3.20 (e), which provide large surface area and numerous electroactive sites for effective ion adsorption.

## 4.5 Electrochemical performance of $\text{Ni}_3(\text{PO}_4)_2 \cdot 8\text{H}_2\text{O}/\text{NF}$ nanoflakes

In order to explore the potential application as a supercapattery electrode, the  $\text{Ni}_3(\text{PO}_4)_2 \cdot 8\text{H}_2\text{O}/\text{NF}$  was examined with cyclic voltammetry, galvanostatic charge-discharge, cyclic stability and EIS measurements in a three electrode configuration. Figure 4.14a shows the cyclic voltammogram (CV) at different scan rates ranging from

2-100 mVs<sup>-1</sup>. The CV curves are different from the ideal supercapacitor suggesting that energy storage mechanism is non-capacitive in nature, which is due to the Faradaic pseudo-battery property of the Ni<sub>3</sub>(PO<sub>4</sub>)<sub>2</sub>·8H<sub>2</sub>O/NF nano/ microflakes layers related to the Ni<sup>2+</sup>/Ni<sup>3+</sup> redox mechanism<sup>69</sup>. The pairs of the redox peaks are attributed to the oxidation of nickel phosphate and the reverse reduction processes as suggested by the following chemical reactions<sup>66,300</sup>:



According to Bajdich et al.<sup>300</sup> the adsorption of OH and O species on the surface lead to the oxygen evolution during electrochemical reaction in alkaline conditions. Since phosphate is not involved to the redox process, during electrochemical reaction there is an adsorption of OH<sup>-</sup> ions on the electrode [i. e., Ni(OH)<sub>2</sub>] surface leads to the oxidation of existing Ni<sup>3+</sup> to Ni<sup>4+</sup> and allows the formation of OH\* followed by the O\* and thus results the oxygen evolution at the end.<sup>300,301</sup> The high current response in the CV curves is mainly due to the contribution of more active sites from the Ni<sub>3</sub>(PO<sub>4</sub>)<sub>2</sub>·8H<sub>2</sub>O layers and implies the excellent charge storage capacity of the electrode. As the scan rate increases, the peak current increases and the redox potential start to shift more positive and negative regions, indicating quasi-reversibility of the electrode.

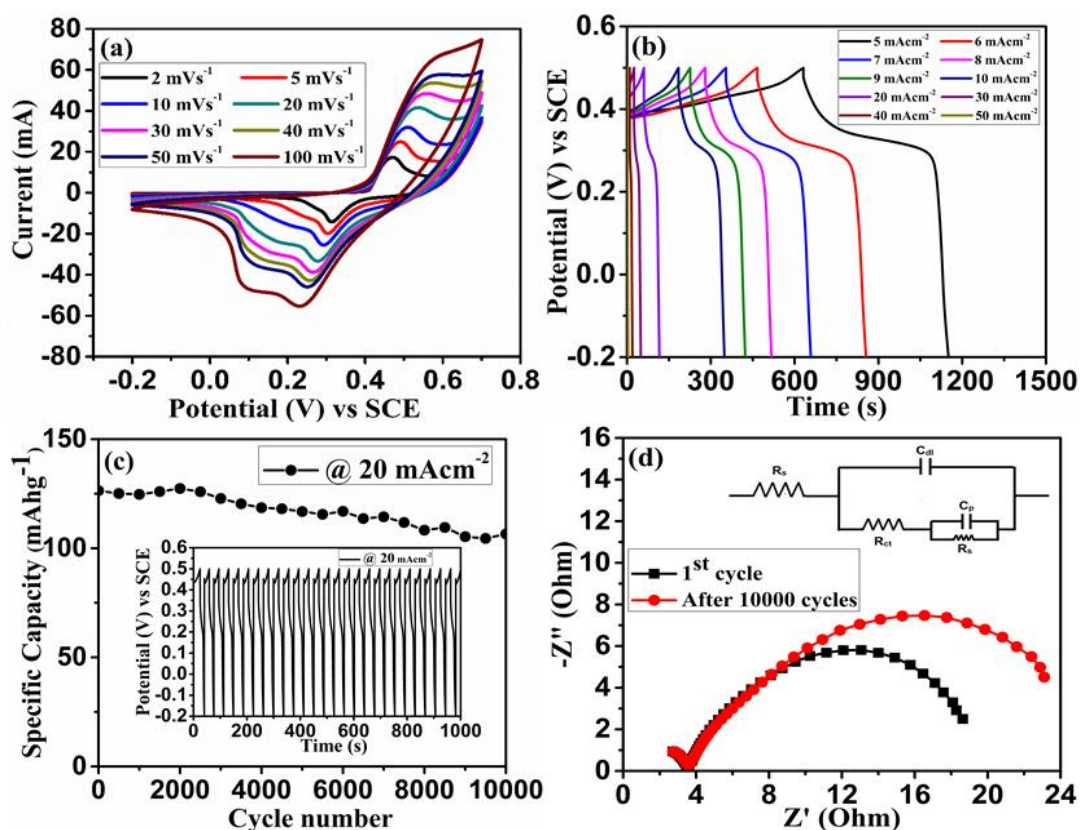


**Figure 4.14** (a) Cyclic voltammogram of  $\text{Ni}_3(\text{PO}_4)_2 \cdot 8\text{H}_2\text{O}$  nano/ microflakes electrode at different scan rates of 2 – 100  $\text{mVs}^{-1}$ , (b) Charge-discharge profile at various applied current of 5 – 50  $\text{mAcm}^{-2}$ , (c) Cyclic stability of the electrode at 20  $\text{mAcm}^{-2}$  and inset represents the continuous charge discharge curve, (d) Nyquist plot of the electrode before and after 10,000 charge-discharge cycles and the corresponding equivalent circuit (inset).

The charge-discharge (CD) studies under different specific current further supports the electrochemical response, observed from the CV analysis. The CD curve with distinct plateaus as shown in Figure 4.14b confirms the Faradaic pseudo-battery type energy storage with quasi-reversibility of the  $\text{Ni}_3(\text{PO}_4)_2 \cdot 8\text{H}_2\text{O}$  nano/ microflakes layered electrode. Since the observed energy storage phenomenon is non-capacitive, the average charge storage capacity and capacitance at the electrode surface was calculated using equation 4.2 and equation 4.4.<sup>64,81</sup>

The measured specific capacity of the electrode was found to be 301.8  $\text{mAh g}^{-1}$  (1552.3

F g<sup>-1</sup>), 270.4 mAh g<sup>-1</sup> (1390.8 F g<sup>-1</sup>), 246.9 mAh g<sup>-1</sup> (1270.1 F g<sup>-1</sup>), 220.2 mAh g<sup>-1</sup> (1132.4 F g<sup>-1</sup>), 203.8 mAh g<sup>-1</sup> (1048.3 F g<sup>-1</sup>) and 189.5 mAh g<sup>-1</sup> (974.7 F g<sup>-1</sup>) for 5, 6, 7, 8, 9 and 10 mA cm<sup>-2</sup> respectively. Recently, Chen et al. showed a specific capacitance of 964 F g<sup>-1</sup> at 5 Ag<sup>-1</sup> for NH<sub>4</sub> intercalated Ni<sub>3</sub>(PO<sub>4</sub>)<sub>2</sub>·H<sub>2</sub>O@NF.<sup>204</sup> Similarly, layered NH<sub>4</sub>Co<sub>x</sub>Ni<sub>1-x</sub>PO<sub>4</sub>·H<sub>2</sub>O nanostructures exhibit specific capacitance of 1567 and 1212 F g<sup>-1</sup> at 1 A g<sup>-1</sup> with and without Co.<sup>209</sup> In earlier, Zhao et al. showed a capacitance of 1497 F g<sup>-1</sup> at 1.25 Ag<sup>-1</sup> for Ni<sub>20</sub> [(OH)<sub>12</sub>(H<sub>2</sub>O)<sub>6</sub>][(HPO<sub>4</sub>)<sub>8</sub>(PO<sub>4</sub>)<sub>4</sub>]·12H<sub>2</sub>O nanorods.<sup>302</sup> It is worth mentioning that all these reports are for mostly intercalated metal phosphates or pyrophosphates and Ni<sub>3</sub>(PO<sub>4</sub>)<sub>2</sub>·8H<sub>2</sub>O is rarely been reported. Thereby with such a high energy storage capacity (e.g., 1552.3 F g<sup>-1</sup> at 5 mAcm<sup>-2</sup>), the Ni<sub>3</sub>(PO<sub>4</sub>)<sub>2</sub>·8H<sub>2</sub>O based electrode is superior to other nickel phosphate and metal phosphate based electrodes reported so far.<sup>200,214,303,304</sup>

The cyclic stability of the electrode was evaluated by continuous charge-discharge measurements at 20 mAcm<sup>-2</sup> (Figure 4.14c). The proposed nickel phosphate nano/microflake layered structure possesses excellent cyclic stability with 84% retention capacity even after 10,000 cycles. Typical reaction kinetics of the electrode was further interrogated by EIS and presented in a Nyquist plot in Figure 4.14d. These spectra show typical two-time-constants behavior: one appearing as large semicircle in the low frequency region and other as an incomplete semicircle at high frequency. Noticeably, the impedance which is related to charge transfer at the electrode surface is quite similar for before and after cycling, demonstrating consistent electrical conductivity of the electrode. An increment in the high frequency semicircle after 10,000 cycles reveals the adsorption of reaction intermediates. The existence of these two characteristic processes are associated with the adsorption/ desorption of intermediates and the diffusion controlled Faradaic reactions (electron/ ion transfer) at the electrode/ electrolyte interface. The observed Nyquist plot was fitted with an equivalent circuit as described by Ho et al.<sup>305</sup> and shown in the inset of Figure 4.14). Here the  $R_s$ ,  $R_{ct}$  and  $C_{dl}$ , represents the solution resistance, charge transfer resistance and double layer capacitance.<sup>64</sup> The elements  $C_p$  and  $R_p$  are associated with adsorption and desorption of reaction

intermediates as quoted in electrochemical reaction 4.7-9.<sup>305</sup> These reactions are commonly interpreted in terms of Faradaic reaction in the presence of adsorption of the reaction intermediates (i.e. OH<sup>•</sup> radical). The occurrence of the two depressed semicircles in the complex-plane plot in the presence of Faradaic reactions is not well-understood for real porous electrode and need more investigations. However, it can be seen that the time constant associated with the adsorption of intermediates is large compared to that of the charge transfer kinetics and hence the low frequency semicircle is typically associated with the adsorption process whereas the high frequency semicircle is associated with the redox kinetics.<sup>305</sup>

#### **4.6 Electrochemical performance of Co<sub>3</sub>(PO<sub>4</sub>)<sub>2</sub>/NF nanoflakes/microflower structure**

The electrochemical properties of the CP/NF nanoflakes/ microflower structure were investigated using a three electrode system. In order to exclude the contribution of nickel foam substrate, CV and charge-discharge studies were carried out for the NF and CP/NF as shown in Figure 4.15a-b. The capacity of NF and CP/NF were found to be 0.023 and 0.970 mAh cm<sup>-2</sup> ( $C=It/a$ , where  $I$  is applied current,  $t$  is discharge time and  $a$  is the area of the electrode), which indicate that cobalt phosphate is the principal contributor to the charge storage of the electrode.

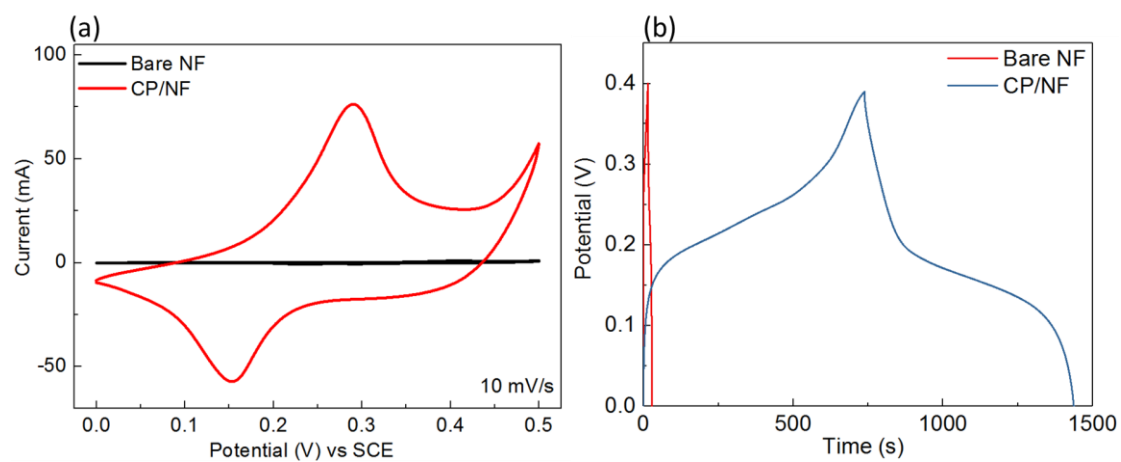


**Figure 4.15** (a) Cyclic voltammograms of NF and CP/NF samples at a scan rate of 10 mV/s in 3.0 M KOH, (b) charge-discharge curves of NF and CP/NF samples at current density of 5 mA cm<sup>-2</sup>.

Figure 4.16a shows the CV curves of CP/NF at different scan rates from 1 to 50 mV s<sup>-1</sup>. The pair of oxidation and reduction peaks indicate the Faradaic energy storage mechanism of the electrode material. With faster scan rate the peak separation increased, representing quasi-reversible Faradaic reaction on the electrode surface.

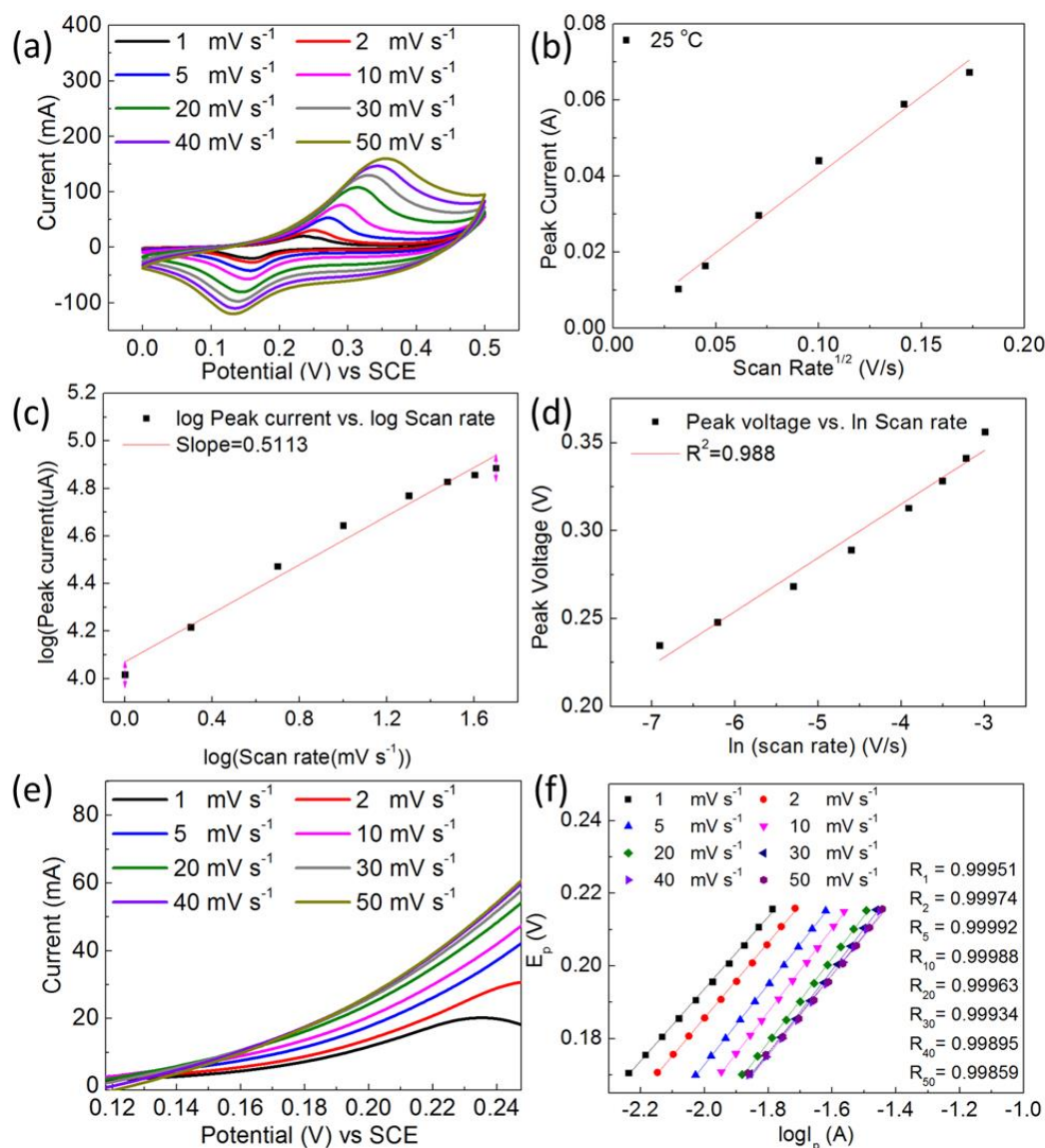
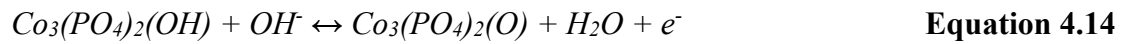


**Figure 4.16** (a) Cycle voltammograms, (b) plot of forward anodic peak current density and the square root of the scan rate, (c) the plot of log peak currents ( $I_{pa}$ ) against the log scan rate ( $v$ ), (d) the plot of peak voltage vs.  $\ln$  scan rate for CP/NF in three electrode system, (e) raising part of CV curve of the cobalt phosphate electrode at different scan rates and the corresponding Tafel plot (f).

The observed peak currents ( $I_{pa}$ ) are proportional to the square root of the scan rate ( $v$ ) (as shown in Figure 4.16b), with the equation of  $I_{pa}(A) = 0.3518 \times \sqrt{v (V/s)} + 0.00369$  and  $R^2 = 0.9862$ . Thereby, it can be realized that the process is diffusion-controlled process rather than surface-controlled process. From the theoretical point of

view, a slope of 0.5 or 1.0 is expected for the plot of  $\log I_{pa}$  vs.  $\log v$  under diffusion or adsorption-controlled process, respectively.<sup>306</sup> As can be observed, a linear curve was shown in the plot of  $\log I_{pa}$  vs.  $\log v$  (Figure 4.16c) with the slope of 0.5113, which is close to the theoretically predicted value of 0.5 for a purely diffusion-controlled process.<sup>306</sup> Furthermore, the plot of peak voltage vs.  $\ln v$  shows a linear behaviour (Figure 4.16d), which confirm the diffusion-limited transfer process.

The peak shifting (1 mV/s vs. 50 mV/s) for the oxidation peaks (121 mV) is larger than the reduction peaks (29 mV), which may be due to the quasi reversible oxidation and reduction of  $Co^{+2} \leftrightarrow Co^{+3/+4}$ . In general,  $OH^-$  ions are adsorbed upon oxidation and expelled during reduction, and thereby it is observed that the hydroxide ions are the dominant mobile species. Quasi or nearly symmetric nature of the CV curves at each scan rate signpost the good redox property of the material. The Faradaic reactions in the overall process are<sup>300,307</sup>:



The electrochemical redox reaction mechanism was further supported by the Tafel equation<sup>308</sup>:

$$b = 2.303 \frac{RT}{\alpha n F} \quad \text{Equation 4.16}$$

where  $b$  is Tafel slope, obtained from the Tafel plot ( $\log I_p$  vs.  $E_p$ ) as shown in Fig. 3e-f,  $\alpha$  is charge transfer coefficient,  $n$  is electron transfer number,  $F$  is Faraday constant (96485 C mol<sup>-1</sup>),  $R$  is gas constant (8.314 J mol<sup>-1</sup> K<sup>-1</sup>) and  $T$  is temperature (298 K).

$\alpha$  is often around 0.5, which is equal proportional of electrical energy for favouring forward reaction and suppressing the reverse reaction<sup>308</sup>, then the electron transfer

number is estimated to be 1.2, which indicated  $\text{Co}^{+2}$  had been oxidized to  $\text{Co}^{+3}$  and  $\text{Co}^{+4}$ . Furthermore, the diffusion coefficient was calculated using the Randles-Sevcik equation<sup>309</sup>:

$$I_p = 2.687 \times 10^5 \times n^{3/2} \times A \times \sqrt{D} \times C \times \sqrt{\nu} \quad \text{Equation 4.17}$$

where  $n$  is electron transfer number,  $A$  is the working area of the electrode ( $\text{cm}^2$ ),  $C$  is the concentration ( $\text{mol}/\text{cm}^3$ ),  $D$  is the diffusion coefficient ( $\text{cm}^2 \text{ s}^{-1}$ ), and  $\nu$  is the scan rate ( $\text{mV s}^{-1}$ ). The calculated diffusion coefficient is  $1.1 \times 10^{-13}$ , further confirmed hydroxide ions are the dominant mobile species.

Figure 4.17 a shows the charge-discharge profile of the CP/NF at different applied current from 5 to 50  $\text{mA cm}^{-2}$ . The quasi-reversible curves with distinct potential plateaus demonstrate the battery-type redox reaction on the electrode surface. The nearly symmetric charge-discharge curves at wide range of specific current indicate quasi reversible Faradaic reaction of the electrode. At a high current, the cation mobility is enhanced by the interlayer gallery spacing between the lamellar sheets of  $\text{Co}_3(\text{PO}_4)_2$  on the porous Ni foam current collector, which prevents significant ohmic drop ( $< 0.7$  mV) in the electrolyte and results the high electrochemical activity.

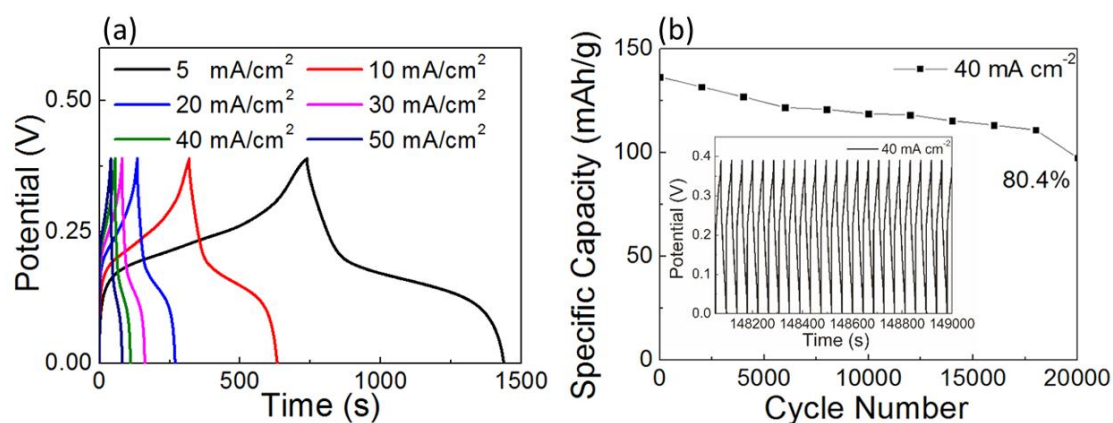


**Figure 4.17** (a) charge-discharge profiles and (b) cyclic stability of the cobalt phosphate electrode in three electrode system.

Due to the typical Faradaic charge compensation, the specific capacity was calculated using  $C=It/m$ , where  $I$  is applied current,  $t$  is discharge time and  $m$  is the mass of the active material. A maximum specific capacity was found to be 215.6 mAh g<sup>-1</sup> at an applied current of 5 mA. The value was reduced to 124.6 mAh g<sup>-1</sup> at a higher current of 50 mA showing a capacity retentions of 57.8% of the initial value with a 10-fold increase in applied current.

The word “pseudocapacitance” is used to describe those electrode materials, which demonstrate a linear dependence of electrochemical charge storage properties like carbon based capacitor, but with Faradaic chemical reaction<sup>63,65,310</sup>. However, due to the misconception in the literature of the term “pseudocapacitance”, many researchers have classified their materials with a behaviour of a noticeable discharge plateau to be capacitive<sup>63,64</sup> and used the same equation to estimate the charge storage capacity. In order to compare with those results, the specific capacitance ( $C=It/mV$ ) was calculated for the electrode, which showed a maximum capacitance of 1990 F g<sup>-1</sup> at a current of 5 mA, which is much higher than the state of the art (1578.7 F g<sup>-1</sup>)<sup>66</sup> cobalt phosphate electrode and other metal phosphate based materials<sup>311-313</sup>. This may due to the 3D network architecture along with the thin nanoflakes offered the large contact area with electrolyte for more efficient ion and charge transport. Also the interconnected nanoflakes provided lots of nano/ microscale gaps, which were favorable for electrolyte penetration to the interior surfaces. The stability of cobalt phosphate electrode was tested with a continuous charge-discharge cycles at a specific current of 40 mA as shown in Figure 4.17b. The interconnected nanoflakes provided a rigid structure so that the electrode showed an excellent stability of 90.5% after first 5,000 cycles, and retains 80.4% of its initial capacity after 20,000 cycles. These results are much better than the reported cobalt<sup>86,314</sup> and phosphate<sup>208,210,311</sup> based electrodes in terms of capacitance (up to 1492 F g<sup>-1</sup>) and cyclability (up to 10,000 cycles).

## 4.7 Conclusion

In this chapter, the Faradaic energy storage mechanism of each fabricated materials was discussed. Among all the five different electrode materials, phosphate based materials exhibited high capacity/ capacitance.  $\text{Ni}_3(\text{PO}_4)_2 \cdot 8\text{H}_2\text{O}/\text{NF}$  nano/ microflakes and  $\text{Co}_3(\text{PO}_4)_2/\text{NF}$  nanoflakes/ microflower structure shows the highest capacity of  $301.8 \text{ mAh g}^{-1}$  and  $1990 \text{ F g}^{-1}$ , respectively. The electrochemical properties improved by optimizing the nanostructure as discussed in Chapter 3. Table 4.3 and Table 4.4 compares the specific capacity and capacitance of all the phosphate based electrodes fabricated in this work and other similar metal phosphate and cobalt oxide based electrode materials and from published literature.

**Table 4.3** Comparison of electrochemical performance for different metal phosphate based electrode in three electrode configuration.

Electrode materials	Capacitance (F g <sup>-1</sup> )	Retention	Reference
Ni <sub>3</sub> (PO <sub>4</sub> ) <sub>2</sub> ·8H <sub>2</sub> O/NF	1552.3	10,000 (84%)	This work
Co <sub>3</sub> (PO <sub>4</sub> ) <sub>2</sub> /NF	1990	5,000 (90.5%)	This work
2.5 mM Co <sub>3</sub> (PO <sub>4</sub> ) <sub>2</sub> ·8H <sub>2</sub> O	1578.7	72.8% after 1000 cycles	This work
5 mM Co <sub>3</sub> (PO <sub>4</sub> ) <sub>2</sub> ·8H <sub>2</sub> O	1336.9	-	This work
10 mM Co <sub>3</sub> (PO <sub>4</sub> ) <sub>2</sub> ·8H <sub>2</sub> O	722.9	-	This work
20 mM Co <sub>3</sub> (PO <sub>4</sub> ) <sub>2</sub> ·8H <sub>2</sub> O	870.3	-	This work
Co <sub>11</sub> (HPO <sub>3</sub> ) <sub>8</sub> (OH) <sub>6</sub>	312	3,000 (89.4%)	206
CoHPO <sub>3</sub> ·3H <sub>2</sub> O	413	3,000 (100%)	175
NH <sub>4</sub> CoPO <sub>4</sub> ·H <sub>2</sub> O	369.4	400 (99.7%)	200
Co <sub>3</sub> (PO <sub>4</sub> ) <sub>2</sub> ·8H <sub>2</sub> O	350	1,000 (102%)	199
Co <sub>0.86</sub> Ni <sub>2.14</sub> (PO <sub>4</sub> ) <sub>2</sub>	1409	Not mentioned	205
NH <sub>4</sub> NiPO <sub>4</sub> ·H <sub>2</sub> O	1072	3,000 (95%)	315
Ni <sub>20</sub> [(OH) <sub>12</sub> (H <sub>2</sub> O) <sub>6</sub> ][(HPO <sub>4</sub> ) <sub>8</sub> (PO <sub>4</sub> ) <sub>4</sub> ]·12H <sub>2</sub> O	1497	Not mentioned	302
(NH <sub>4</sub> )(Ni, Co)(PO <sub>4</sub> ·0.67H <sub>2</sub> O)	1128	Not mentioned	203
Mn <sub>3</sub> (PO <sub>4</sub> ) <sub>2</sub> ·3H <sub>2</sub> O	320	2,000 (87%)	303
NaMnPO <sub>4</sub>	219	1,000 (93%)	316
NaCoPO <sub>4</sub>	279	1,000 (96%)	316
NaNiPO <sub>4</sub>	390	1,000 (88%)	316
NH <sub>4</sub> CoPO <sub>4</sub> ·H <sub>2</sub> O	662	3,000 (92.7%)	210
Mn <sub>3</sub> (PO <sub>4</sub> ) <sub>2</sub>	194	1,000 (91.1%)	161

**Table 4.4** Comparison of electrochemical performance for fabricated phosphate based electrode and other nickel or/ and cobalt oxide based electrode in three electrode configuration.

Electrode materials	Capacitance (F g <sup>-1</sup> )	Capacity (C g <sup>-1</sup> )	Retention	Reference
Ni <sub>3</sub> (PO <sub>4</sub> ) <sub>2</sub> ·8H <sub>2</sub> O/NF	1552.3	301.8	10,000 (84%)	This work
Co <sub>3</sub> (PO <sub>4</sub> ) <sub>2</sub> /NF	1990	215.6	5,000 (90.5%)	This work
2.5 mM Co <sub>3</sub> (PO <sub>4</sub> ) <sub>2</sub> ·8H <sub>2</sub> O	1578.7	868.3	1,000 (72.8%)	This work
5 mM Co <sub>3</sub> (PO <sub>4</sub> ) <sub>2</sub> ·8H <sub>2</sub> O	1336.9	735.3		This work
10 mM Co <sub>3</sub> (PO <sub>4</sub> ) <sub>2</sub> ·8H <sub>2</sub> O	722.9	397.6		This work
20 mM Co <sub>3</sub> (PO <sub>4</sub> ) <sub>2</sub> ·8H <sub>2</sub> O	870.3	478.7		This work
Pongam seed shells-derived activated carbon/CoO	94		1,000 (88%)	<sup>317</sup>
Co <sub>3</sub> O <sub>4</sub> nanobeads-carbon nanotubes-graphene nanpsheets	600.19		550 (95.4%)	<sup>318</sup>
NiO/Ni		1204	10,000 (90%)	<sup>319</sup>
Co <sub>3</sub> O <sub>4</sub> -MnO <sub>2</sub> -NiO	2525		5,700 (80%)	<sup>320</sup>
Co <sub>3</sub> O <sub>4</sub>	504		Not mentioned	<sup>321</sup>
Co <sub>3</sub> O <sub>4</sub> -RuO <sub>2</sub>	905		5,000 (96%)	<sup>322</sup>
Co <sub>3</sub> O <sub>4</sub>	407.5		2,000 (97.5%)	<sup>323</sup>

# Chapter 5 Electrochemical performances of devices

## 5.1 Introduction

In this chapter, a symmetric and three asymmetric supercapatteries were assembled using synthesized electrode materials and activated carbon. The electrodes and Celgard separator (porosity 55%, average pore size 64 nm) were cut to  $1 \times 1 \text{ cm}^2$  and then assembled to a sandwich-type supercapattery as shown in the schematic Figure 5.1. The total thickness of the supercapattery is  $\sim 0.2 \text{ cm}$  and the total volume of the supercapattery is  $\sim 0.2 \text{ cm}^3$ .

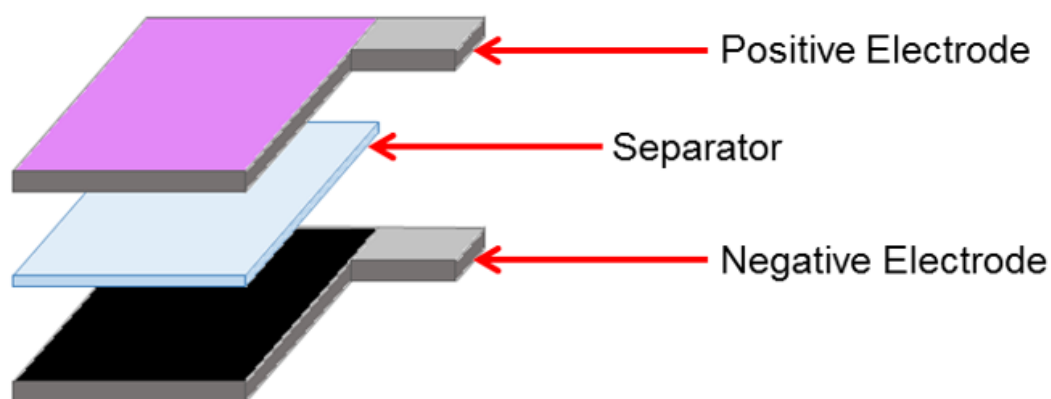


**Figure 5.1** Schematic of sandwich-type supercapattery ( $1 \times 1 \times 0.2 \text{ cm}^3$ ).

Specific capacity and capacitance of the assembled supercapatteries were calculated by Equation 5.1-4, based on the total mass of total active materials loading mass or the total measured volume of the supercapattery.

$$C = \frac{I \times t}{3.6 \times m} \quad \text{Equation 5.1}$$

$$C = \frac{I \times t}{3.6 \times V} \quad \text{Equation 5.2}$$

$$C_s = \frac{I \times t}{m \times \Delta U} \quad \text{Equation 5.3}$$

$$C_s = \frac{I \times t}{V \times \Delta U} \quad \text{Equation 5.4}$$

where,  $C$  is the specific capacity (mAh g<sup>-1</sup> based on total active materials loading mass, or mAh cm<sup>-3</sup> based on total volume of the fabricated supercapattery),  $C_s$  is the specific capacitance (F g<sup>-1</sup> based on total active materials loading mass, or F cm<sup>-3</sup> based on total volume of the fabricated supercapattery),  $I$  is the charge-discharge current (A),  $t$  is the discharge time (s),  $V$  is the total measured volume of the supercapattery) (1 × 1 × 0.2 cm<sup>-3</sup>),  $\Delta U = V_{max} - V_{min}$ , where  $V_{max}$  is the voltage at the beginning of discharge after the IR drop and  $V_{min}$  is the voltage at the end of discharge, 3.6 is due to the conversion of seconds to hours.

In addition, the specific energy and power are two important factors to evaluate the performance of a supercapattery cell. Since the charge-discharge is a non-linear function, the specific energy and power of the symmetric cell were calculated using the following equations:<sup>63,310</sup>

$$E = I \int_{t=0}^{t=t} V(t) dt \quad \text{Equation 5.5}$$

$$P = E/t \quad \text{Equation 5.6}$$

Where,  $E$  is the specific energy (Wh kg<sup>-1</sup>),  $P$  is the specific power (W kg<sup>-1</sup>),  $I$  is the specific Current (A g<sup>-1</sup>),  $V$  is the potential (V) and  $t$  is discharge time (s).

It's important to note that for asymmetric supercapatteries, the balancing of the charge flow between the positive and negative electrodes is critical for optimum performance. The charge stored by individual electrode is:

$$Q = C_s \times \Delta E \times m \quad \text{Equation 5.7}$$

where,  $C_s$  is the specific capacitance of the electrode,  $\Delta E$  is the potential range of the charging-discharging process and  $m$  is the mass loading of the active materials on the current collector.

So the mass loading ratio of positive electrode ( $m_P$ ) and negative electrode ( $m_N$ ) can be calculated as following:

$$\frac{m_P}{m_N} = \frac{C_N \times \Delta E_N}{C_P \times \Delta E_P}$$

**Equation 5.8**

Herein, the electrochemical properties of the four assembled supercapatteries were investigated in inorganic electrolytes. The summarized characteristics of these supercapatteries are shown in Table 5.1.

**Table 5.1** Electrochemical characteristics of the assembled supercapatteries.

Electrode Material		Electrolyte	Voltage Window	Energy Density	Power Density	Cyclability
Positive	Negative					
Composition	Composition	V	V	Wh kg <sup>-1</sup>	W kg <sup>-1</sup>	Cycles
NiO-In <sub>2</sub> O <sub>3</sub> /NF	NiO-In <sub>2</sub> O <sub>3</sub> /NF	3 M KOH	1.5	26.24	9624.5	89% after 5,000 cycles
Co <sub>3</sub> (PO <sub>4</sub> ) <sub>2</sub> ·8H <sub>2</sub> O/NF	AC/NF	1 M NaOH	1.6	29.29	4687	72.8% after 1,000 cycles
Ni <sub>3</sub> (PO <sub>4</sub> ) <sub>2</sub> ·8H <sub>2</sub> O/NF	AC/NF	1 M NaOH	1.5	33.4	2058	84% after 10,000 cycles
Co <sub>3</sub> (PO <sub>4</sub> ) <sub>2</sub> /NF	AC/NF	3 M KOH	1.7	43.2	5800	90.5% after 5,000 cycles

## 5.2 NiO-In<sub>2</sub>O<sub>3</sub>/NF symmetric supercapattery

For practical application, sandwich type symmetric cell was fabricated using two pieces of NiO-In<sub>2</sub>O<sub>3</sub>-NF electrodes separated by Celgard separator and tested in 3 M KOH aqueous electrolyte. Figure 5.2a shows the CV curves of the symmetric cell at scan rates extending from 5 to 50 mV s<sup>-1</sup>. Distinct CV curves indicate the battery like characteristic of the device as a function of scan rate. Further increasing the scan rate from 75 to 500 mV s<sup>-1</sup> did not result any obvious changes (Figure 5.3), implying the high rate capability of the device.

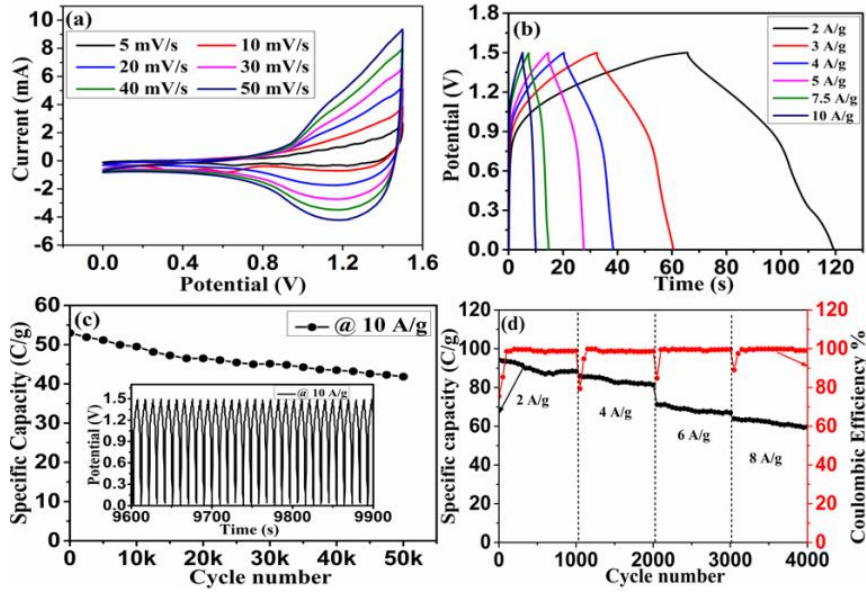


**Figure 5.2** (a) Cyclic voltammograms of symmetric supercapacitor fabricated with NiO-In<sub>2</sub>O<sub>3</sub>-NF (1:2) hybrid structure at different scan rates in 3 M KOH; (b) Charge-discharge curves of NiO-In<sub>2</sub>O<sub>3</sub>-NF (1:2) based symmetric supercapacitor at various current densities; (c) Cyclic stability of the symmetric supercapacitor and inset represents continuous charge-discharge profile at 10 A g<sup>-1</sup>; (d) Capacity retention and coulombic efficiency of the device at different current density.

Figure 5.2b shows the galvanostatic charge-discharge curves of the symmetric cell, which is carried out at different current densities (2-10 A g<sup>-1</sup>). Nearly symmetric charge-discharge behaviour envisages the non-capacitive Faradaic nature of the charge storage, consistent with the CV results. The specific capacity of the device is evaluated using equation 5.1. The estimated specific capacity for the symmetric cell is found to be 101.4 C g<sup>-1</sup> (28.2 mAh g<sup>-1</sup>) 67.6 F g<sup>-1</sup> at a constant current density of 2 A g<sup>-1</sup>. When the current density is increased, the specific capacity decreases due to the fact that insufficient active materials involve in the redox reaction. However, the device still exhibits 52.95 C g<sup>-1</sup> (14.7 mAh g<sup>-1</sup>) 35.3 F g<sup>-1</sup> of specific capacity even at a high current of 10 A g<sup>-1</sup>, which is 52% of the initial capacity when the current is increased by a factor of 5. With increasing current, the specific capacitance varies significantly. The observed Cs value is much higher than the earlier reported values of 23 C g<sup>-1</sup> (23 F g<sup>-1</sup>) for Ni|KOH|Ni

symmetric device,<sup>324</sup> 52.8 C g<sup>-1</sup> (44 F g<sup>-1</sup>) for Co(OH)<sub>2</sub>/SS(stainless steel) electrodes<sup>325</sup> and quite comparable to the Co(OH)<sub>2</sub>/GF (graphene foam) electrode of 82.8 C g<sup>-1</sup> (69 F g<sup>-1</sup>)<sup>326</sup> in symmetric cell configurations. Furthermore, the symmetric cell shows outstanding cyclic stability (Figure 5.2c), with only 21% capacity loss after 50,000 cycles. The excellent cyclic stability may be attributed to a well-integrated and strongly adhered NiO-In<sub>2</sub>O<sub>3</sub> hierarchical nano/ micro architecture on the nickel foam substrate and their synergistic effect.

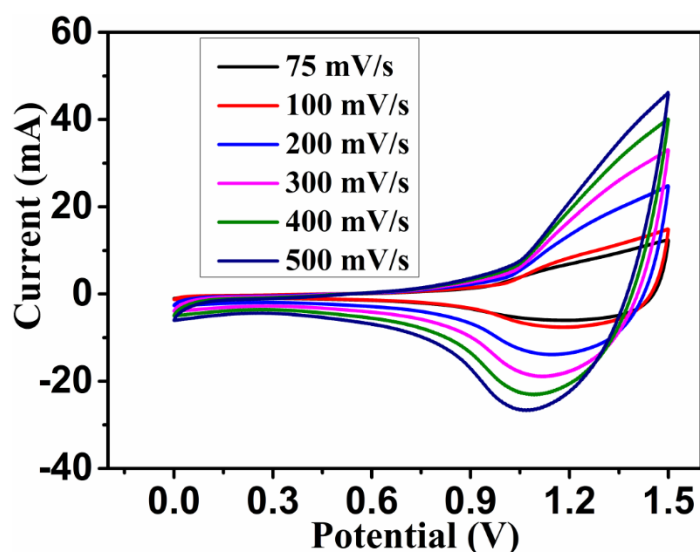


**Figure 5.3** Cyclic voltammograms of NiO-In<sub>2</sub>O<sub>3</sub>-NF (1:2) based symmetric supercapacitor at high scan rates.

Figure 5.4a-d shows the SEM images of NiO-In<sub>2</sub>O<sub>3</sub> hetero-structure after 50,000 charge-discharge cycles. There is noticeable destruction in the microstructure for this NiO-In<sub>2</sub>O<sub>3</sub> hetero-composite when compared to before cycling as shown in Figure 3.9 (chapter 3). It seems that some diffusion/ dissolution reaction between In<sub>2</sub>O<sub>3</sub> and NiO during charge/ discharge and resulted in the formation intermetallic compound between NiO and In<sub>2</sub>O<sub>3</sub> after long cyclic process.

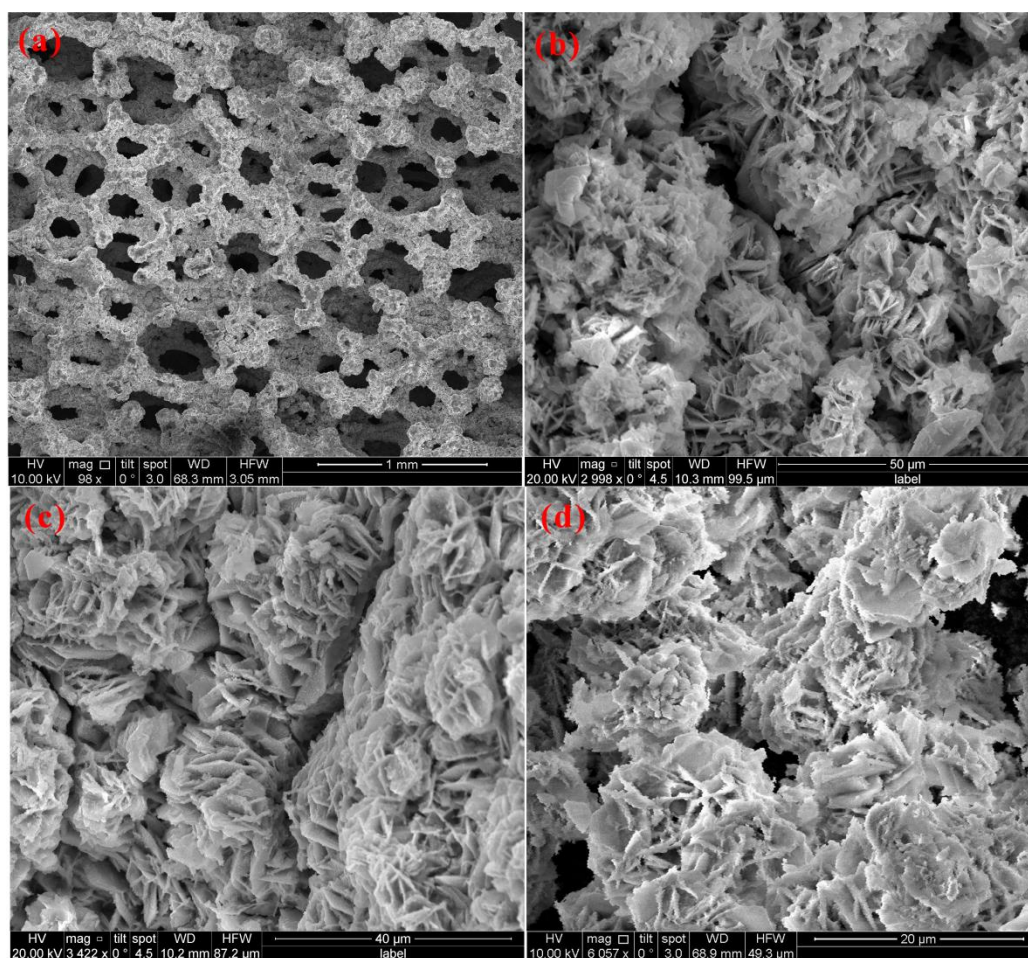


**Figure 5.4** (a-d) SEM images of NiO-In<sub>2</sub>O<sub>3</sub>-NF (1:2) electrode after 50,000 charge-discharge cycles.

In terms of coulombic efficiency, the device has showed significant variations based on the applied current. Figure 5.2d shows the variation of specific capacity and the corresponding coulombic efficiency measured at various current of 2 – 8 A g<sup>-1</sup>. Worth mentioning, the estimated capacity retentions were about ~94% for all current densities after 1000 cycles. However, the coulombic efficiency varied significantly during initial few cycles. Figure 5.5a-d shows the initial charge/ discharge cycles of fabricated symmetric cell measured at before and after 1000 cycling. The calculated efficiency values for first 5 cycles are 75.5%, 79.4%, 84.76% and 89.1% for the current of 2, 4, 6 and 8 A g<sup>-1</sup>, respectively. It reaches to ~98% of the maximum value after prolonged cycling. This can be explained by the effect of solid electrolyte interphase (SEI) layer formation over electrode materials during redox reaction. It is well demonstrated that

the generation of SEI layer plays a crucial role in batteries and hybrid supercapacitors or supercapatteries.<sup>327-329</sup> Generally, the SEI layer is created on an electrode surface due to the reaction between solid electrode and liquid electrolyte. In this case, it is believed that typical SEI layer is formed on the electrode surface during initial charge/ discharge cycles as reported earlier.<sup>328,329</sup> The detailed mechanism of SEI layer formation is not clear and needs further investigations. The same trend in efficiency was observed for all the measured current as shown Figure 5.2d, which indicates that the formation of SEI layer is independent to the applied current. However, the SEI formation requires only few 10s of cycles at high current, whereas it is nearly 100 cycles for low current. The variation in efficiency can be directly related to the electrode kinetics during redox process. Since the NiO and In<sub>2</sub>O<sub>3</sub> have different kinetic potentials, the redox process is also different during charging/ discharging process, thereby asymmetric behaviour is observed in Figure 5.2b. Also, the formation of stable SEI layer ensures the long term cyclic stability of the device.<sup>327</sup>

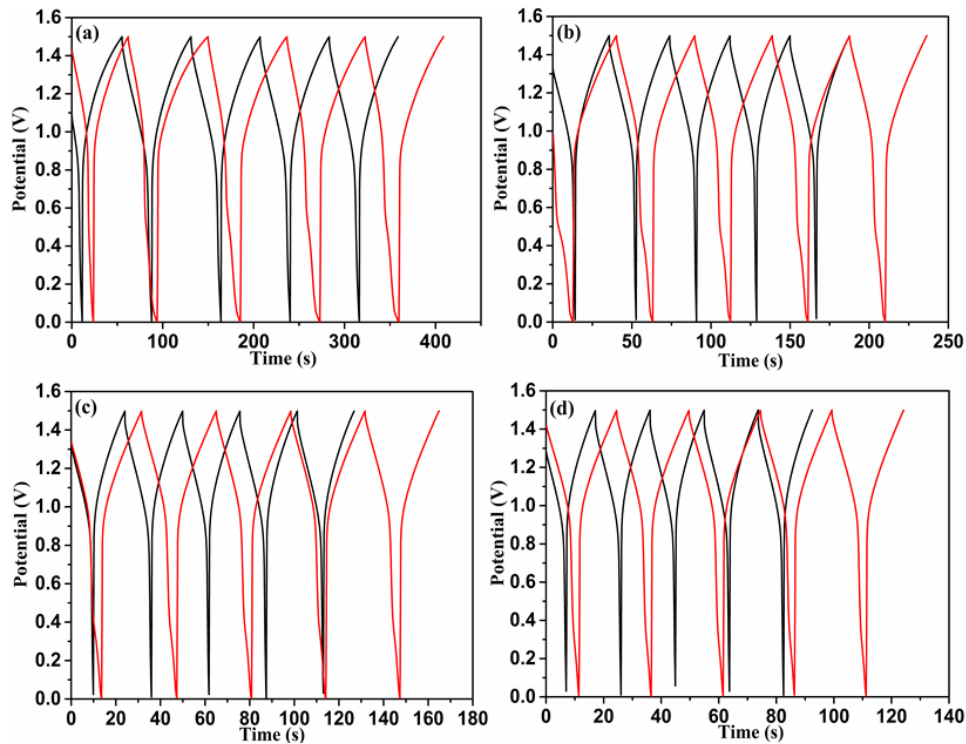


**Figure 5.5** First few charge-discharge cycles of NiO-In<sub>2</sub>O<sub>3</sub>-NF (1:2) based symmetric supercapacitor measured before (black line) and after (red line) 1000 cycles at different current density (a) 2 A g<sup>-1</sup>, (b) 4 A g<sup>-1</sup>, (c) 6 A g<sup>-1</sup> and (d) 8 A g<sup>-1</sup>.

In general, the amount of energy stored in the electrochemical energy storage devices is directly related to the voltage applied between the electrodes. So, a stable potential window should be fixed appropriately for the symmetric cell. However, in two electrode configuration, controlling the potential range of each electrode is not possible since there is no reference electrode.<sup>330,331</sup> In this case, the observed potential is  $\sim 1.5$  V which is significantly higher than the limit of water splitting voltage ( $\sim 1.23$  V) in aqueous electrolyte.<sup>330</sup> Therefore to understand the electrode behaviour and stable potential window, the cyclic voltammogram study was carried out for the symmetric cell using SCE as reference electrode. Typical CV curves of symmetric cell are shown in Figure 5.6a-b, indicates the potential window of each electrode at different voltage limits. It is important to point out that the positive electrode operates between 0 and 0.6 V vs. SCE and the negative one between 0 and -1 V vs. SCE. So, the water reduction potential of the negative electrode shifted beyond -1 V from the theoretical value of -0.38 V. Meantime the positive potential is slightly under the thermodynamic limit of water oxidation ( $\sim 0.85$  V). This result further confirms that the symmetric cell can be able to reach the stable potential of 1.5 V as shown in Figure 5.2a-b.

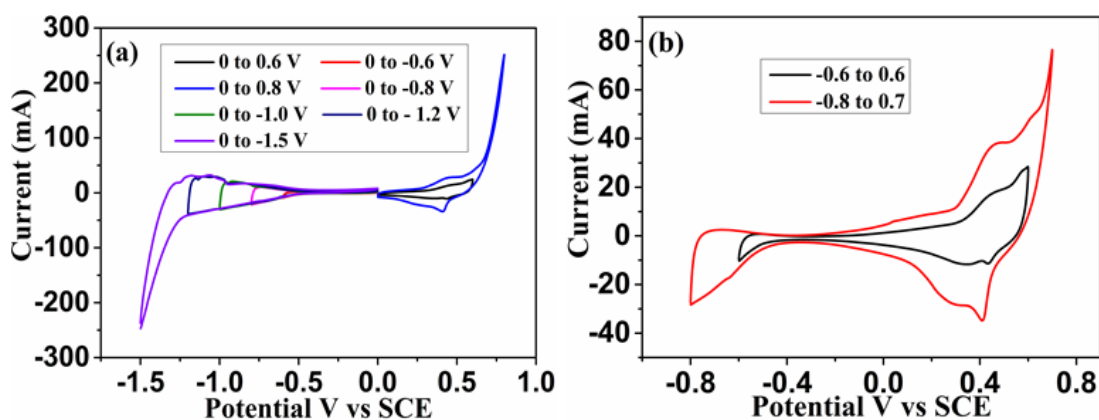


**Figure 5.6** (a) Cyclic voltammograms of NiO-In<sub>2</sub>O<sub>3</sub>-NF symmetric cell at different potential range and (b) the stable potential window of the device with respect to reference electrode.

According to the Ragone plot shown in Figure 5.7, the highest specific energy for this cell is 26.24 Wh kg<sup>-1</sup> with a power density of 1752.8 W kg<sup>-1</sup> and remained 13.1 Wh kg<sup>-1</sup> at a maximum power density of 9624.5 W kg<sup>-1</sup>. The corresponding volumetric energy

and power density for the symmetric supercapacitor is about  $3.56 \text{ Wh cm}^{-3}$  and  $438.1 \text{ W cm}^{-3}$ . The observed energy and power performance for the NiO-In<sub>2</sub>O<sub>3</sub> hybrid structure is higher than most of the reported symmetric supercapacitors.<sup>324,326,332</sup>

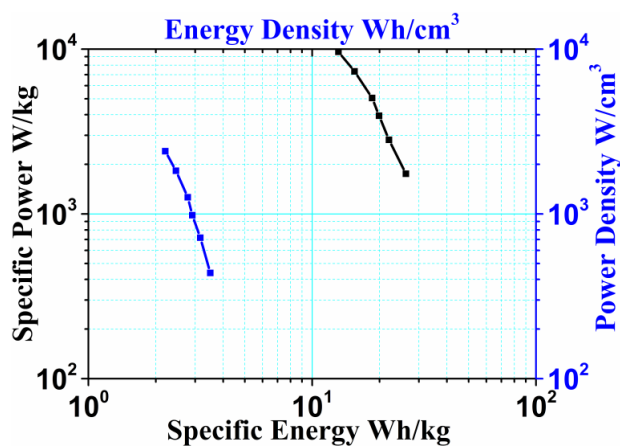


**Figure 5.7** Ragone plot for NiO-In<sub>2</sub>O<sub>3</sub>-NF (1:2) based symmetric supercapacitor.

In order to demonstrate practical usability of the device, three symmetric cells were connected in series and lighting a red LED for 10 seconds while discharging (Figure 5.8a). Furthermore, the device which fabricated with NiO-In<sub>2</sub>O<sub>3</sub> was lighting an LED with the same power (Figure 5.8b) even a month after the initial test. Thus further confirms the long-term activity of the electrode for high performance supercapacitor applications.

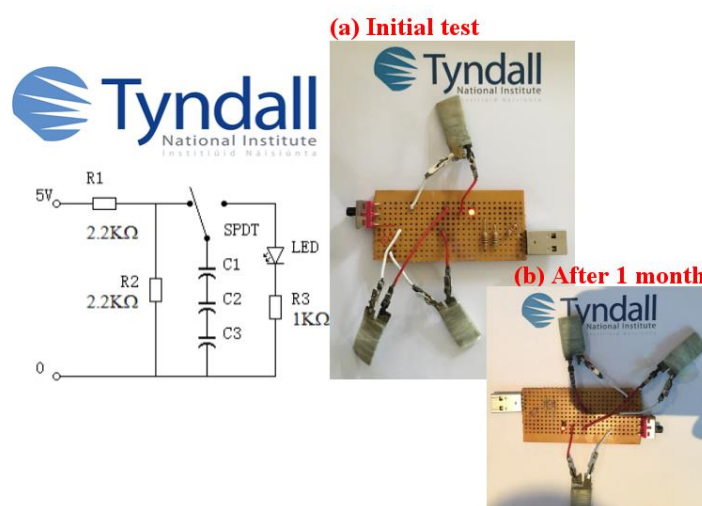


**Figure 5.8** NiO-In<sub>2</sub>O<sub>3</sub>-NF (1:2) based symmetric supercapacitor connected in series and their practical application of LED lighting.

The electrochemical impedance spectroscopy was performed to study the resistance of the supercapacitor device before and after 50,000 cycles (Figure 5.9). Both plots consists of semicircle arcs at high to middle frequency region and straight lines at low frequency range. The observed EIS data can be fitted with the equivalent circuit (inset of Figure 5.9) consisting of solution resistance ( $R_s$ ), charge transfer resistance ( $R_{ct}$ ), diffusion resistance ( $W$ ) and electrochemical capacitance ( $C_{dl}$ ).<sup>296</sup> The Nyquist plot revealed no obvious resistance change of the device even after 50,000 cycles, which is remarkable. However, the deviation in the slope of the straight line confirms the increased internal resistance at the electrode. Thereby, the EIS results further confirm the excellent stability of the symmetric capacitor.

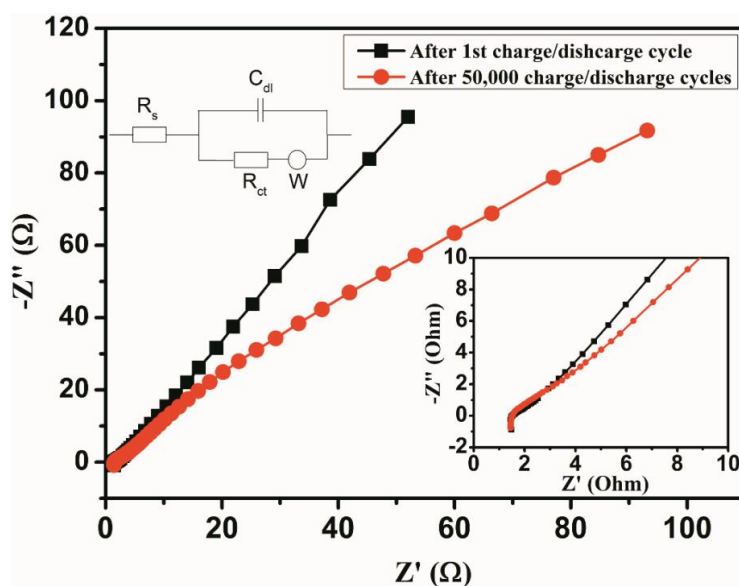


**Figure 5.9** Nyquist plot for NiO-In<sub>2</sub>O<sub>3</sub>-NF (1:2) based symmetric supercapacitor before and after 50,000 cycles. Inset on the left is the equivalent circuit and inset on the right is showing the expanded view of the high frequency region.

The superior electrochemical performance of the NiO-In<sub>2</sub>O<sub>3</sub> heterostructured electrode could be attributed to the following structural benefits: First, 3D mesoporous NF has superior electrical conductivity and this leads to rapid electron transport during charge-discharge process at high current density. Second, the 3D-1D hybrid micro/ nano structure gives more active sites for redox reactions due to the existence of more surface defects on the oxide surface as observed in the XPS analysis (section 3.2.4) and their

synergistic contribution. Third, 1D nanorod integrated hierarchical microflower structure increases the cyclic stability for long term applications due to strong mechanical integrity with Ni support. Moreover, these 1D nanorods not only support the electroactive materials, but also serve as effective channels for electron transfer and act as an intermediate buffer layer between the highly active NiO flower and the Ni foam substrate. Finally, formation of strongly coupled NiO-In<sub>2</sub>O<sub>3</sub> heterostructures with mesoporous Ni foam resulted in a large contact area between active materials and the electrolyte, leading to more efficient ion and charge transport, resulting in significant increases in the specific capacitance and rate capability at high current densities over longer cycle times.

### **5.3 Co<sub>3</sub>(PO<sub>4</sub>)<sub>2</sub>·8H<sub>2</sub>O/NF hybrid supercapattery**

In order to evaluate the performance of the Co<sub>3</sub>(PO<sub>4</sub>)<sub>2</sub>·8H<sub>2</sub>O/NF electrode, a hybrid supercapattery (Co<sub>3</sub>(PO<sub>4</sub>)<sub>2</sub>·8H<sub>2</sub>O//AC) was assembled with 2.5 mM Co<sub>3</sub>(PO<sub>4</sub>)<sub>2</sub>·8H<sub>2</sub>O/NF as positive electrode and AC/NF as negative electrode in 1 M NaOH solution. Figure 5.10a-b shows the cyclic voltammograms graphs and charge-discharge curves of activated carbon electrode in a three electrode system where saturated calomel electrode was used as a reference electrode in 1 M NaOH solution. The activated carbon electrode presents a wide potential window of -1 to 0.2 V. Typical carbon rectangular-shaped CV curves were obtained at low scan rate from 1 to 10 mV/s. Linear charge-discharge curves at different currents indicate the non-Faradaic energy storage properties of the electrode material.

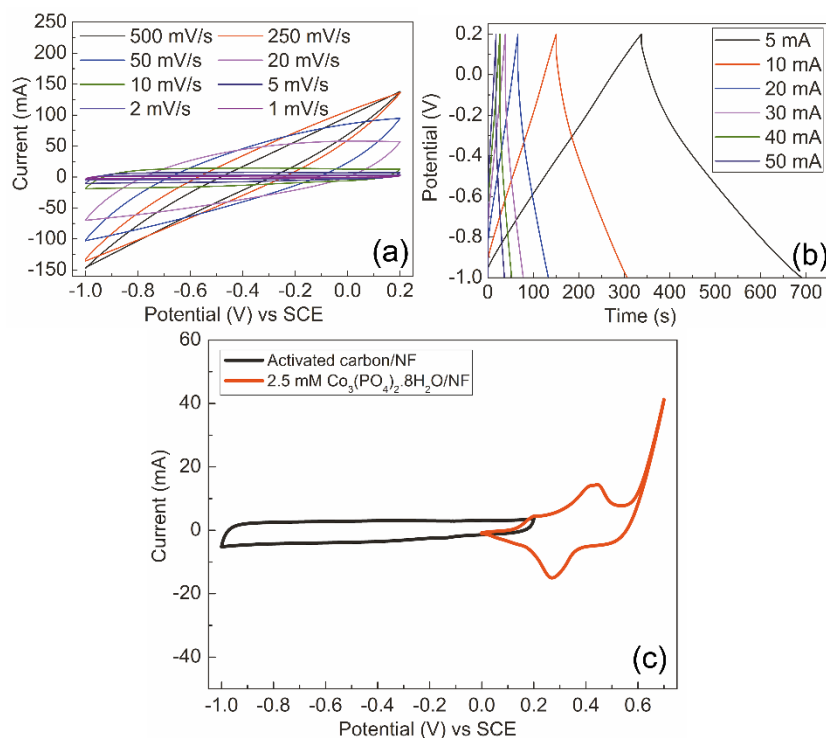


**Figure 5.10** (a) Cyclic voltammograms of activated carbon at different scan rates in 1 M NaOH. (b) Charge-discharge curves of activated carbon at different current in 1 M NaOH. (c) Cyclic voltammograms of 2.5 mM  $\text{Co}_3(\text{PO}_4)_2 \cdot 8\text{H}_2\text{O}/\text{NF}$  and activated carbon in a three electrode system where saturated calomel electrode (SCE) was used as a reference electrode (scan rate: 2 mV/s).

However, to further investigate the optimization of positive and negative electrodes for hybrid supercapattery, three negative electrodes with different mass loading of activated carbon of 2, 4, 6  $\text{mg cm}^{-2}$  were fabricated and assemble hybrid supercapattery with 2.5 mM  $\text{Co}_3(\text{PO}_4)_2 \cdot 8\text{H}_2\text{O}/\text{NF}$  as positive electrode. Among those, 4  $\text{mg cm}^{-2}$  mass loading of activated carbon showed the best performance due to the balance of the charge flow between the positive electrode and the negative electrode. Figure 5.11a shows the CV curves of the  $\text{Co}_3(\text{PO}_4)_2 \cdot 8\text{H}_2\text{O}/\text{AC}$  supercapattery at different scan rates from 5 to 50 mV/s. The quasi-rectangle shapes of these CV curves demonstrate the dominant capacitive behaviour rather than battery characteristic. The CV curves retain the same shape with increasing scan rate, which exhibited a good rate capability of the hybrid supercapattery.

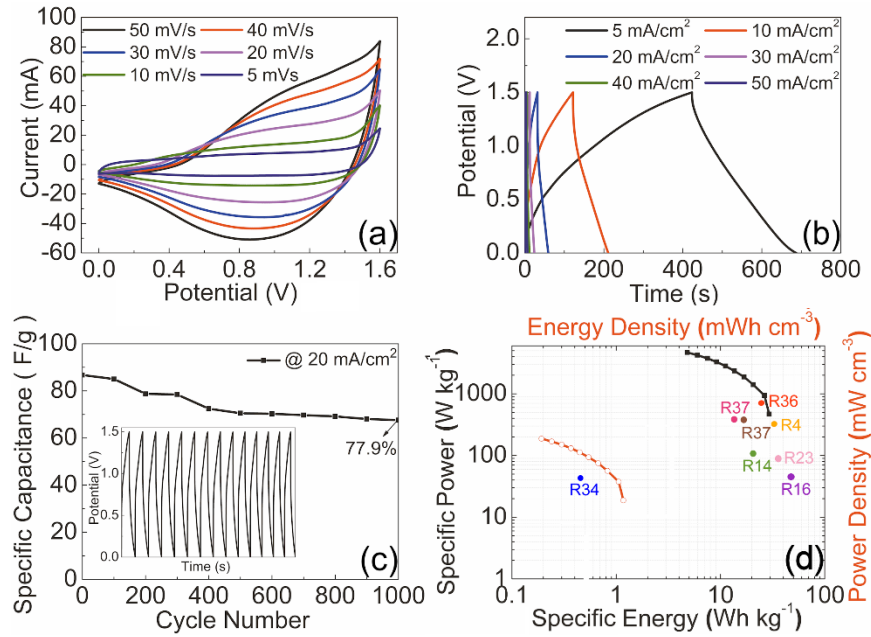


**Figure 5.11** (a) Cyclic voltammograms of the  $\text{Co}_3(\text{PO}_4)_2 \cdot 8\text{H}_2\text{O} // \text{AC}$  hybrid supercapattery at different scan rates in 1 M NaOH. (b) Charge-discharge curves of supercapattery at different current densities. (c) Cyclic stability of supercapattery. Inset represents continuous charge-discharge profile at  $20 \text{ mA cm}^{-2}$  (d) Ragone plots of supercapattery.<sup>161,201,205,210,303,312,316</sup>

The individual CV curves of positive ( $\text{Co}_3(\text{PO}_4)_2 \cdot 8\text{H}_2\text{O} / \text{NF}$ ) and negative ( $\text{AC} / \text{NF}$ ) electrodes are shown in Figure 5.10c. The negative electrode demonstrated a typical electric double layer charge-discharge profile, with hydrogen storage at deep cathodic conditions. On the other hand, the positive electrode has a capacity of redox reversible reaction. Thereby, a potential window of 1.6 V was achieved in this hybrid supercapattery.

Figure 5.11b shows the charge-discharge curves of the  $\text{Co}_3(\text{PO}_4)_2 \cdot 8\text{H}_2\text{O} // \text{AC}$  supercapattery at different current densities with a cell voltage up to 1.5 V. Quasi-lined charge and discharge curves rather than potential plateaus confirm the capacitive characteristic of the hybrid supercapattery.

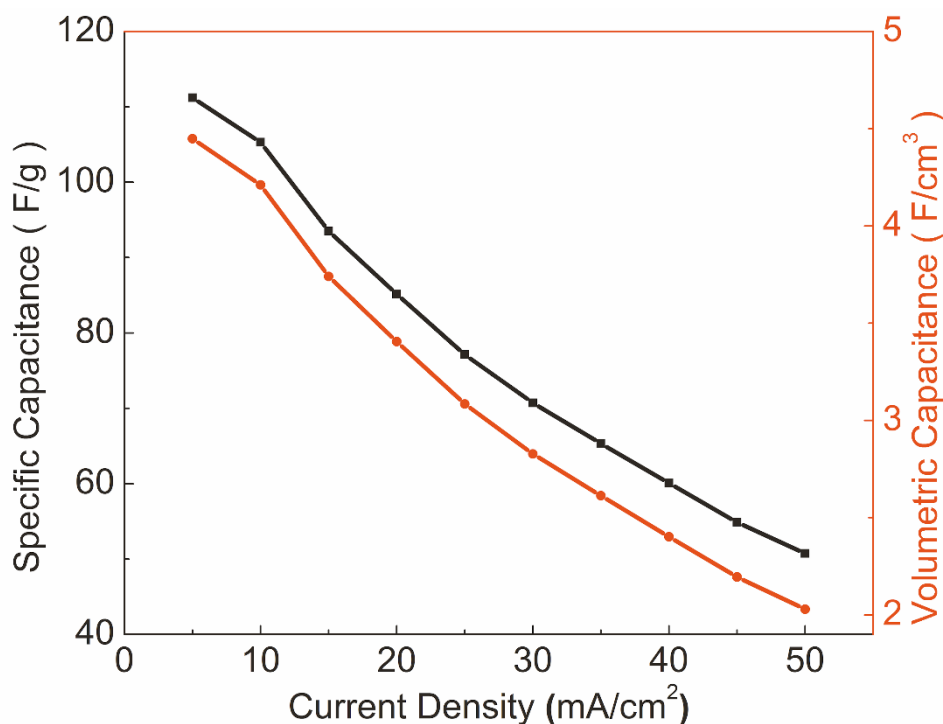


**Figure 5.12** Specific capacitance as a function of applied current densities for hybrid supercapattery.

The device showed a specific capacitance of  $111.2 \text{ F g}^{-1}$  ( $4.44 \text{ F cm}^{-3}$ ) at a current density of  $5 \text{ mA cm}^{-2}$ . Even at  $50 \text{ mA cm}^{-2}$ , it showed a specific capacitance of  $50.7 \text{ F g}^{-1}$  ( $2.03 \text{ F cm}^{-3}$ ). Thereby, this hybrid device could retain a remarkable 45.6% of the initial value for ten times of initial current density. Furthermore, the hybrid supercapattery showed better cyclic stability of 77.9% (Figure 5.11c) after 1000 cycles as compared to the earlier reported work (66.5% and 57.8%)<sup>205</sup>. Compared to three electrode system, the hybrid supercapattery exhibits a better cyclic stability, which may be due to the synergistic effect of the positive supercapattery electrode with the negative carbon based electrode, which reduced the dissolution of active material.

Due to the non-linear function of the charge-discharge curves, the specific energy (density) and specific power (density) were calculated by equations 5.5-6. As in the Ragone plots shown in Figure 5.11d, the highest specific energy was found to be  $29.29 \text{ Wh kg}^{-1}$  (energy density of  $1.17 \text{ mWh cm}^{-3}$ ) at a specific power of  $468.75 \text{ W kg}^{-1}$  (power density of  $18.75 \text{ mW cm}^{-3}$ ) for the hybrid device using  $2.5 \text{ mM Co}_3(\text{PO}_4)_2 \cdot 8\text{H}_2\text{O/NF}$  as

positive and AC/NF as negative electrode. Even at a high specific power of  $4687 \text{ W kg}^{-1}$  (power density of  $187.5 \text{ mW cm}^{-3}$ ), the device could retain a specific energy of  $5.33 \text{ Wh kg}^{-1}$  (energy density of  $0.21 \text{ mWh cm}^{-3}$ ). The Nyquist plot of the hybrid supercapattery before and after 1000 cycles is shown in Figure 5.13. From the two plots, resistance was found to be only  $0.80 \text{ } \Omega$  and  $5.06 \text{ } \Omega$  for the hybrid supercapattery before and after cyclability test, which indicate acceptable conductivity for the device even after 1000 cycles.

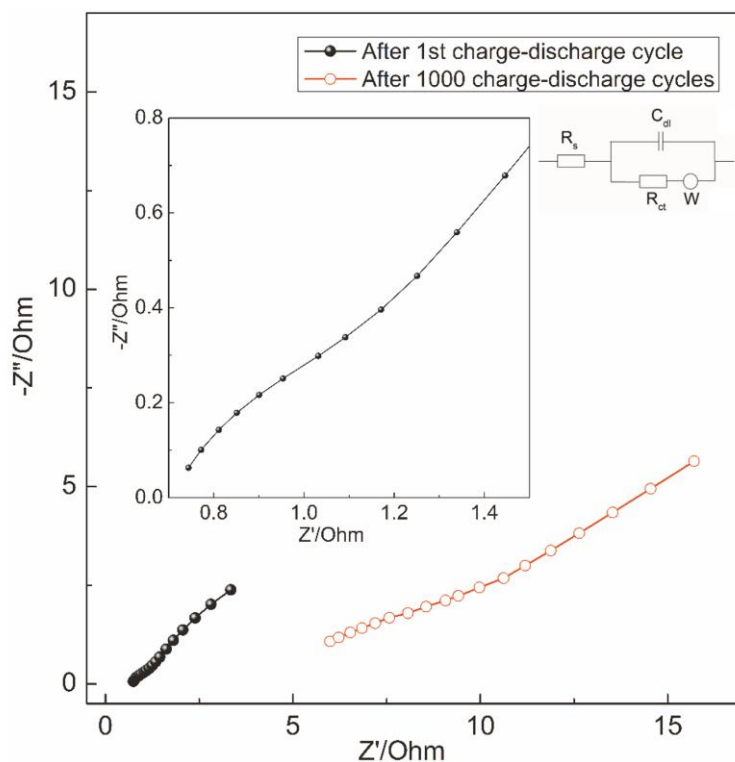


**Figure 5.13** Nyquist plot for  $\text{Co}_3(\text{PO}_4)_2 \cdot 8\text{H}_2\text{O} // \text{AC}$  hybrid supercapattery before and after 1000 cycles.

Overall, cobalt phosphate hydrate multilayer nano/ microflakes structure showed interesting properties as a positive electrode for supercapattery application. Lower concentration samples exhibited better electrochemical performance due to the less mass loading and thinner layer and showed state of the art specific capacitance for this composite. Formation of  $\text{Co}_3(\text{PO}_4)_2 \cdot 8\text{H}_2\text{O}$  nano/ microflakes coupled with mesoporous Ni foam resulted in a large contact area between active materials and the electrolyte, leading to more efficient ion and charge transport, resulting in significant increases in

the specific capacitance and rate capability at high current densities. Thereby, the hybrid device showed excellent specific capacitance with very good energy and power density, acceptable retention capability and good cyclability.

#### 5.4 $\text{Ni}_3(\text{PO}_4)_2 \cdot 8\text{H}_2\text{O}/\text{NF}$ hybrid supercapattery

Considering the high performance of the  $\text{Ni}_3(\text{PO}_4)_2 \cdot 8\text{H}_2\text{O}$  micro/ nanoflakes electrode at three electrode configuration, several hybrid supercapatteries were fabricated with  $\text{Ni}_3(\text{PO}_4)_2 \cdot 8\text{H}_2\text{O}/\text{NF}$  (NP/NF) as the positive and activated carbon/NF (AC/NF) as the negative electrodes. The different operating voltages of the NP (-0.2 to +0.5 V) and AC (-1 to 0 V) indicate a good match in the potential windows for an asymmetric supercapattery (Figure 5.14).

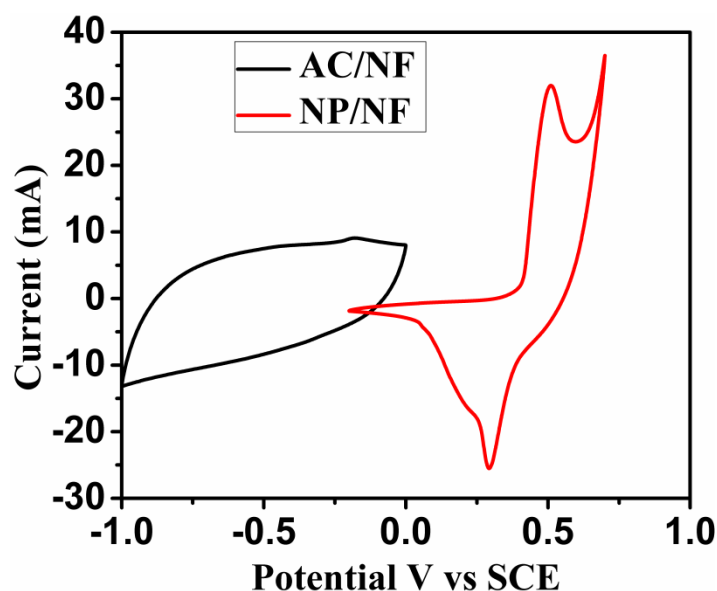


**Figure 5.14** CV curves of AC/NF and  $\text{Ni}_3(\text{PO}_4)_2 \cdot 8\text{H}_2\text{O}/\text{NF}$  at  $10 \text{ mV s}^{-1}$  in 1 M NaOH.

Figure 5.15a-d summarizes the performance of the hybrid supercapattery in 1 M NaOH electrolyte. The CV curves (Figure 5.15a) retaining their battery like characteristic even at a high scan rate of  $100 \text{ mVs}^{-1}$  indicate excellent rate capacity of the device. Figure 5.15b shows the charge-discharge profile of the  $\text{Ni}_3(\text{PO}_4)_2 \cdot 8\text{H}_2\text{O}/\text{NF} \parallel \text{AC}/\text{NF}$  hybrid supercapattery at various specific current ranging from 2.5 to  $20 \text{ mAcm}^{-2}$ . The specific capacity of the device was calculated from the discharge curve based on the active

material masses of the device ( $\sim 7.5 \text{ mg cm}^{-2}$ ) using equation (5.1). The specific capacities are 67.4, 58.9, 52.3, 52.7, 46.3, 41.7, 26.8 and 16  $\text{mAh g}^{-1}$  for 2.5, 3, 3.5, 4, 4.5, 5, 10 and 20  $\text{mA cm}^{-2}$ , respectively. In addition, the supercapattery showed excellent cyclic stability of up to 10,000 cycles as shown in Fig. 5(c) and retained 89% of initial capacity at 20  $\text{mA cm}^{-2}$ . The coulombic efficiency of the device was found to be 96.5% for the first few cycles and reached to  $\sim 99\%$ , and was quite stable up to 10,000 cycles (Figure 5.15c), indicating steady redox process at the electrode surface.

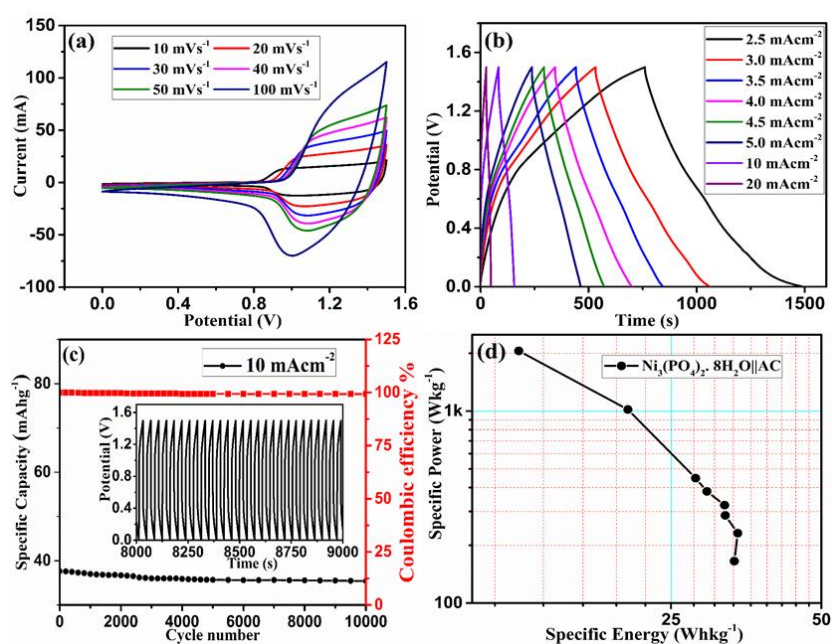


**Figure 5.15** (a) Cyclic voltammogram of  $\text{Ni}_3(\text{PO}_4)_2 \cdot 8\text{H}_2\text{O}/\text{NF} \parallel \text{AC}/\text{NF}$  supercapattery at different scan rates of 10 – 100  $\text{mVs}^{-1}$ , (b) Charge-discharge profile for the device at different specific current of 2.5 – 20  $\text{mA cm}^{-2}$ , (c) Cyclic stability and coulombic efficiency of the device at 10  $\text{mA cm}^{-2}$  and inset represents the corresponding charge discharge profile, (d) Ragone plot related to the specific energy and power of the device.

Since the electrode kinetics are pseudo-battery type behaviour, the specific energy and power of the device were calculated according to Equation 5.5-5.6. Ragone plot for the hybrid cell at different currents are shown in Figure 5.15d. At 2.5  $\text{mA cm}^{-2}$  current, the supercapattery delivers a specific energy of 33.5  $\text{Wh kg}^{-1}$  with a specific power of 165.5  $\text{W kg}^{-1}$ . At a high current of 20  $\text{mA cm}^{-2}$ , the specific energy and power values are 16  $\text{Wh kg}^{-1}$  and 2058.7  $\text{W kg}^{-1}$ , respectively. The observed specific energy and power

output of the device is quite comparable with the value (35.3 Wh kg<sup>-1</sup> and 101 W kg<sup>-1</sup>) reported by Zhao et al. for (Ni, Co)<sub>3</sub>(PO<sub>4</sub>)<sub>2</sub>·8H<sub>2</sub>O<sup>312</sup> and nearly equal to the nickel-cobalt pyrophosphates based asymmetric cell (33.4 Wh kg<sup>-1</sup> and 399 W kg<sup>-1</sup>)<sup>333</sup>. Interestingly, this supercapattery shows comparable and in some cases better properties than other reported works for similar materials (Table 5.2).

**Table 5.2** Comparison of electrochemical performance for various metal-phosphate based asymmetric cell.

Supercapacitor/ Supercapatteries	Specific capacitance /Capacity	Specific Energy (Whkg <sup>-1</sup> )	Specifi c Power (Wkg <sup>-1</sup> )	Stability (Retention %)	Ref
<b>Ni<sub>3</sub>(PO<sub>4</sub>)<sub>2</sub>·8H<sub>2</sub>O AC</b>	<b>(161.8 F g<sup>-1</sup>) 67.4 mAh g<sup>-1</sup></b>	<b>33.5</b>	<b>165.5</b>	<b>10,000 (89%)</b>	<b>This work</b>
Ni <sub>3</sub> P <sub>2</sub> O <sub>8</sub> -Co <sub>3</sub> P <sub>2</sub> O <sub>8</sub> ·8H <sub>2</sub> O AC	94 F g <sup>-1</sup>	33.4	399	5,000 (83%)	333
Co <sub>3</sub> (PO <sub>4</sub> ) <sub>2</sub> ·8H <sub>2</sub> O AC	111.2 F g <sup>-1</sup>	29.29	468.75	1,000 (77.9%)	66
CoNiPO   AC	149.9 F g <sup>-1</sup>	45.8	42.4	2,500 (7.8%)	205
NaNiPO <sub>4</sub>  AC	56 F g <sup>-1</sup>	20	138	500 (70%)	316
NH <sub>4</sub> CoPO <sub>4</sub> ·H <sub>2</sub> O AC	-	26.6	852	-	210
Mn <sub>3</sub> (PO <sub>4</sub> ) <sub>2</sub>  AC	41.9 F g <sup>-1</sup>	14.89	400	10,000 (90%)	161
Mn <sub>3</sub> (PO <sub>4</sub> ) <sub>2</sub> ·8H <sub>2</sub> O   AC	80.53 F g <sup>-1</sup>	32.32	426.25	-	303
Mn <sub>3</sub> (PO <sub>4</sub> ) <sub>2</sub> / Graphene foam   AC	28 F g <sup>-1</sup>	7.6	360	10,000 (96%)	334
NiCoP   AC	164 C g <sup>-1</sup>	32	351	3,000 (91.8%)	335
Ni-P   AC	105 F g <sup>-1</sup>	29.2	400	1,000 (84.5%)	336

The Nyquist plots for the supercapattery before and after 10,000 charge- discharge cycles are shown in Figure 5.16. The electrical conductivity of the electrode is quite good for the hybrid device and the equivalent series resistance is 0.78 Ω and 5.25 Ω before and after 10,000 cycles. The observed low ESR values confirm the high

conductivity and excellent electrical contact between the active material and current collector. From this study it can be concluded that  $\text{Ni}_3(\text{PO}_4)_2 \cdot 8\text{H}_2\text{O}$  micro/ nanoflakes could be an excellent candidate as positive electrode for future energy storage devices.

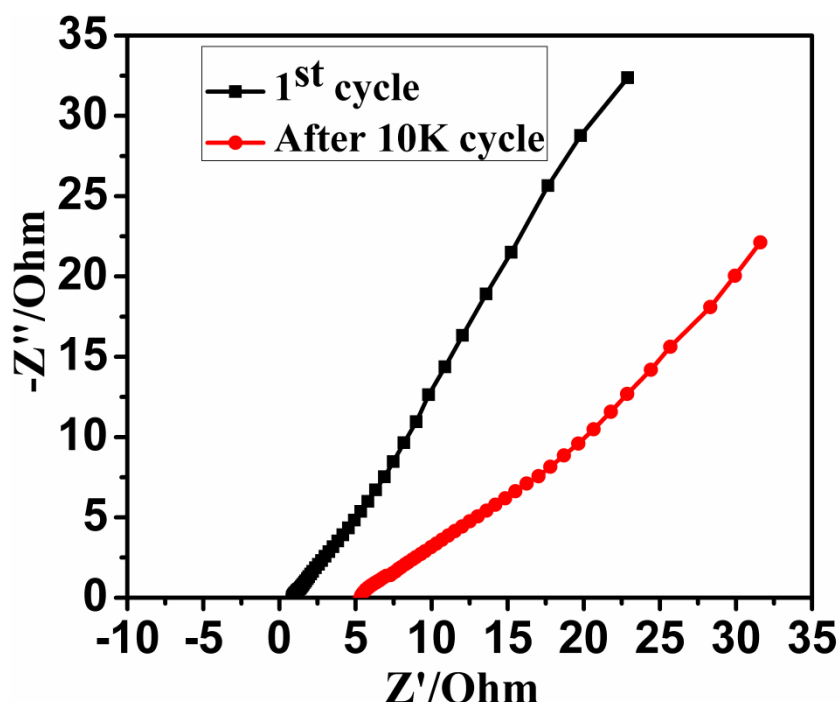
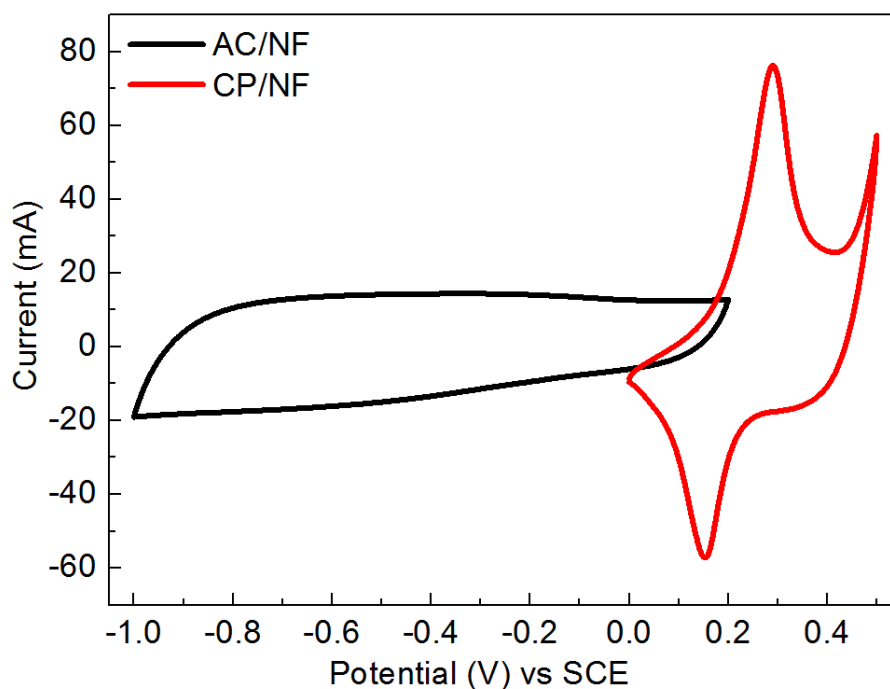


**Figure 5.16** Nyquist Plot of  $\text{Ni}_3(\text{PO}_4)_2 \cdot 8\text{H}_2\text{O}$  /NF ||AC/NF supercapattery before and after 10,000 charge-discharge cycles.

## 5.5 $\text{Co}_3(\text{PO}_4)_2$ /NF supercapattery

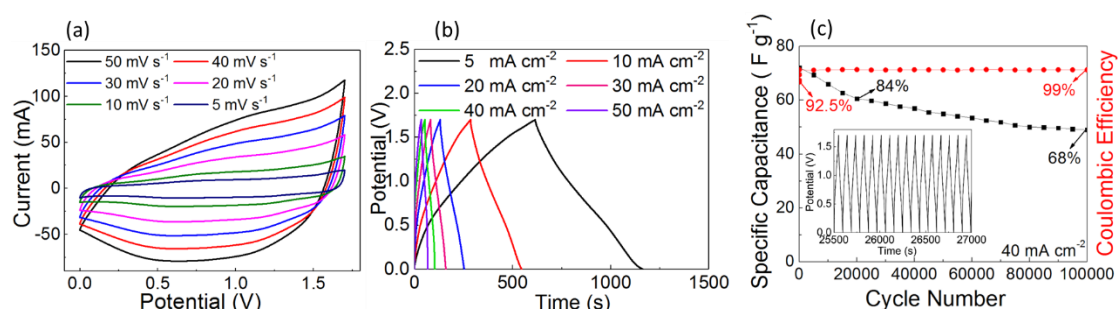
### 5.5.1 Supercapattery performance

Considering the outstanding electrochemical activity of cobalt phosphate on nickel foam, a supercapattery were fabricated using the CP/NF as positive electrode and activated carbon on nickel foam (AC/NF) as negative electrode and tested in 3.0 M KOH solution. Figure 5.17 depicts the individual CV curves of positive and negative electrodes, where the CP/NF shows a non-capacitive Faradaic mechanism in the potential range 0 - 0.5 V. The AC/NF electrode demonstrated a typical capacitive behavior between -1.0 - 0.2 V, due to physical electrostatic adsorption of ions at the interface between electrode and electrolyte.



**Figure 5.17** Cyclic voltammograms of CP/NF and activated carbon in a three electrode system where saturated calomel electrode (SCE) was used as a reference electrode (scan rate: 10 mV/s).

Thereby, a large potential window of 1.7 V was obtained in the supercapattery as shown in Figure 5.18a. Due to the combination of two different charge storage mechanisms, the CV response shows quasi-rectangular shape at low scan rate, and further shape deviation at higher scan rate. This may be due to the electron/ ion transport restricted to certain limit on the electrode surface at high scan rate (current flowing) during the redox process.



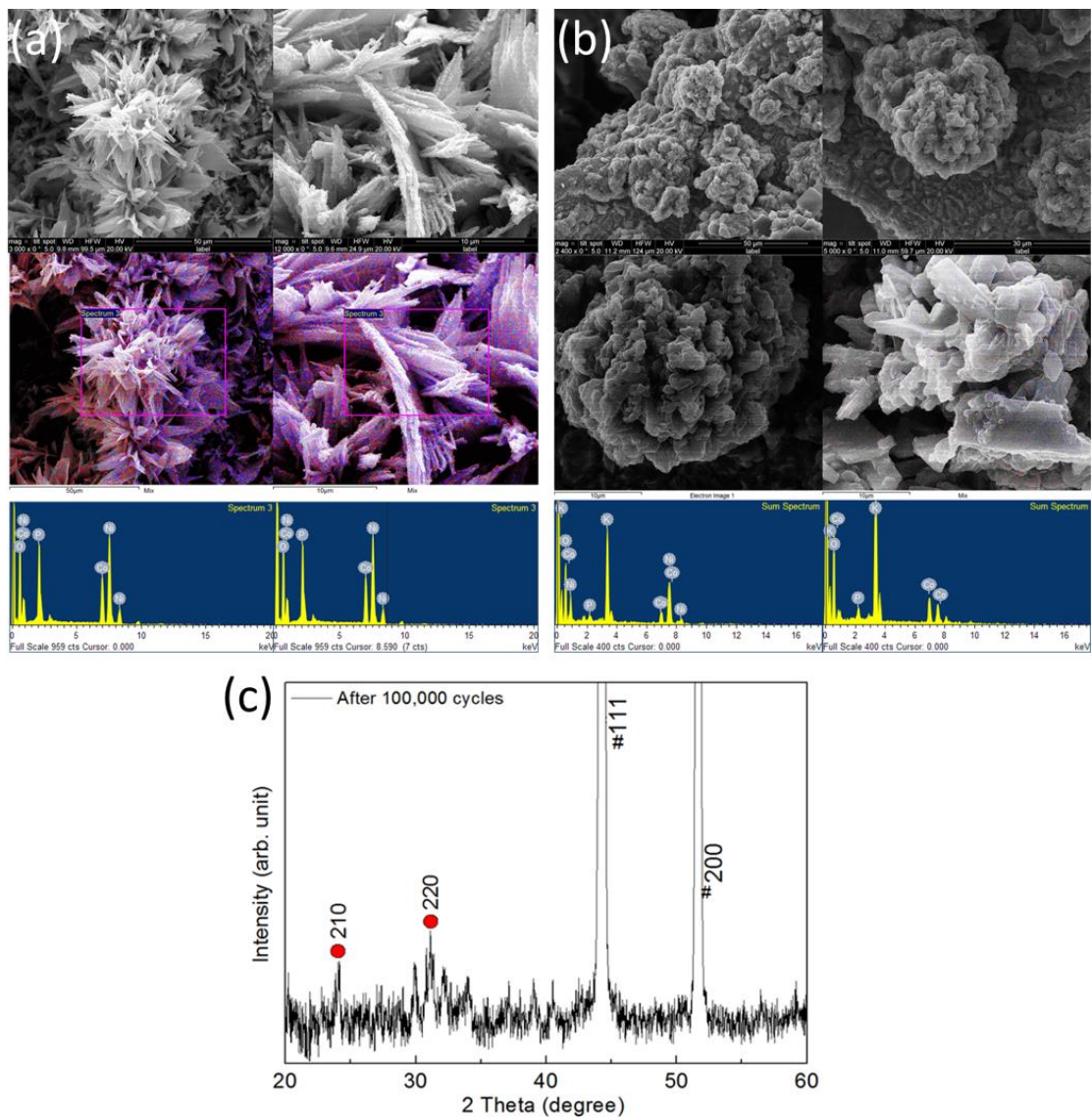
**Figure 5.18** (a) Cycle voltammograms, (b) charge-discharge profiles and (c) cyclic stability of the CP/NF // AC/NF supercapattery.

Figure 5.18b shows the charge-discharge curves of the supercapattery at different applied currents. Quasi-linear charge-discharge curves confirm both the capacitive and

battery like characteristic of the device, which is in good agreement with the CV analysis. A maximum specific capacity of 50.84 mAh g<sup>-1</sup> (capacitance 107.7 F g<sup>-1</sup>) at an applied current of 5 mA is observed, using the active materials' weight of the device. Increasing the applied current by an order of magnitude (up to 50 mA), decreased the capacity to 30.71 mAh g<sup>-1</sup> (capacitance 65.0 F g<sup>-1</sup>). Even at a high current of 100 mA, the capacity remained stable at 24.26 mAh g<sup>-1</sup>, which is 47.7% of the initial value for 20× the initial current. Due to the non-linear charge-discharge behavior, the specific energy and power were calculated according to Equation 5.5-6. A maximum energy density of 3.53 mWh cm<sup>-3</sup> (43.2 Wh kg<sup>-1</sup>) was observed at a specific power of 8.5 mW cm<sup>-3</sup> (293.1 W kg<sup>-1</sup>), which is nearly 50% of the Lithium iron phosphate based battery (90-110 Wh kg<sup>-1</sup>).<sup>337</sup> Even at a high current of 100 mA, the energy density remains at 1.49 mWh cm<sup>-3</sup> (20.6 Wh kg<sup>-1</sup>) and reached to a peak power density of 425 mW cm<sup>-3</sup> (5.8 kW kg<sup>-1</sup>), which is similar to the maximum specific energy reported for most cobalt based devices.<sup>86,314,338</sup>

To replace the pacemaker battery system with this supercapattery, its storage performance must be comparable with the battery in an actual pacemaker. Assuming the pacemaker has to deliver 10 (usually it is twice per day for the pacemaker battery life estimation)<sup>339</sup> impulses per day, then for 20 years lifetime the device has to be operational for at least 73,000 charge-discharge cycles. Thereby, the hybrid device was investigated 100,000 cycles at a charge-discharge current of 40 mA with no loss after 2,000 cycles (100% retention capability), and the device suffered just a 9.5% capacity loss after 10,000 cycles, and retaining 84% of the initial value (Figure 5.18c) after 20,000 cycles. Surprisingly, after 100,000 cycles, the capacity dropped to 68%, while the voltage remained at 1.5 V which confirms excellent cyclability of the device. The shelf life of a lithium battery is typically equivalent to 90% capacity retention over 5 years.<sup>339</sup> With similar retention, this hybrid device survived 10,000 cycles, which means 14 years of operability, according to two pulses delivered per day for the pacemaker battery life estimation.<sup>339</sup> Furthermore, a battery is determined to be invalid when its capacity retention is below 80%.<sup>340</sup> The CP/NF // AC/NF supercapattery can retain 84% capacity over 20,000 cycles and thereby can be active for more than 24 years (at two

pulses per day), meeting the stringent requirement of the pacemaker (20 years lifetime). The coulombic efficiency of the device was calculated to be 92.5%, 93.5%, 96.2% for the 10<sup>th</sup>, 20<sup>th</sup>, 30<sup>th</sup> cycles and this may be due to the formation of solid electrolyte interphase. After 100 charge-discharge cycles, the coulombic efficiency is ~99% and quite stable (Figure 5.18c), indicating the redox process repeats in a consistent manner. SEM and EDX analysis (Figure 5.19a) of cobalt phosphate electrode after 20,000 cycles, showed no major change in nanoflakes/ microflower structure aside from some granular particles, likely due to the partial dissolution (0.15 mg loss) of the active material. The formation of potassium cobalt phosphate at the electrode surface after 100,000 cycles and the more granular morphology are confirmed by the SEM, EDX (Figure 5.19b) and XRD analysis (Figure 5.19c red spot marked peaks are assigned to potassium cobalt phosphate (JCPDS 39-0261) and the peaks marked with # are from Ni foam.).



**Figure 5.19** (a) SEM and EDX images of cobalt phosphate electrode after 20,000 charge-discharge cycles, (b) SEM and EDX images of cobalt phosphate electrode after 100,000 charge-discharge cycles, (c) XRD patterns of cobalt phosphate electrode after 100,000 charge-discharge cycles.

The 3D Ragone plot of Figure 5.20a compares CP/NF // AC/NF supercapattery with state of the art metal oxide and phosphate based devices, and displays the retention of the initial capacitance/ capacity after certain numbers of cycles from green (100%), blue (95%), purple (90%), and pink (85%) to white (<85%). Obviously, the  $\text{MnO}_2/\text{Au}$  based device achieved a high specific energy of  $57 \text{ Wh kg}^{-1}$  but only survives 1,000 cycles with a decay of 15%.<sup>341</sup> Among all the cobalt and phosphate based devices summarised

in Figure 5.20a, the cobalt phosphate based supercapattery shows the best specific energy with beyond state of the art cyclability. In terms of volumetric density (Figure 5.20b),  $\text{LiTi}_2(\text{PO}_4)_3$  based batteries<sup>342</sup> can obtain a high energy density of 26-31  $\text{mWh cm}^{-3}$  however, the retention is limited to 2,000 cycles. The device exhibits a higher power density than other battery/ supercapattery devices with an acceptable energy density. The space allocated (5 mm inner diameter  $\times$  13 mm height) for the energy storage device can accommodate six layers of supercapattery cells (5 mm  $\times$  2 mm) connected in series and should be able to store 0.175  $\text{mWh}$  energy and deliver 49.98  $\text{mW}$  (equivalent to 49.98  $\text{mJ/s}$ ) power, which is nearly 2,000 times the pacemaker pulse requirements of 25  $\mu\text{J}$ .<sup>339</sup>

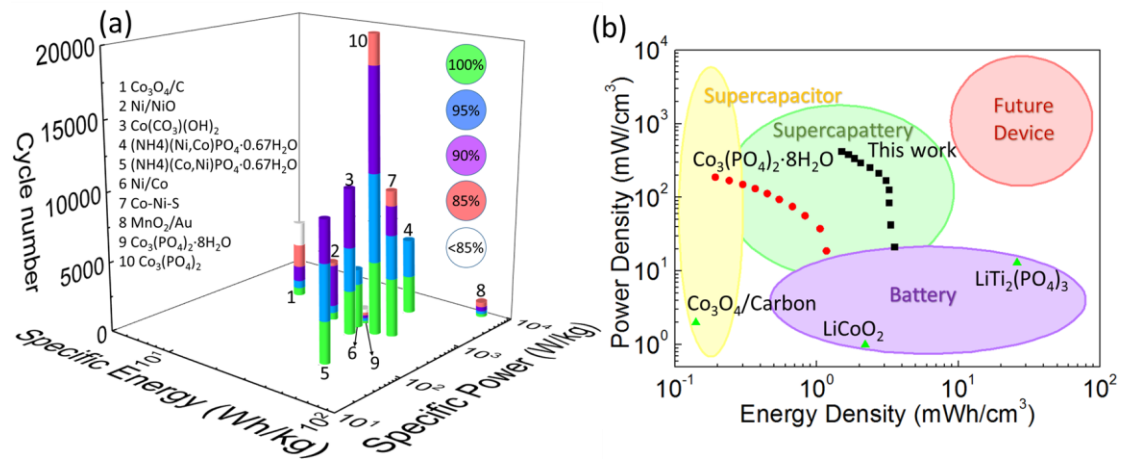


**Figure 5.20** (a) 3D gravimetric Ragone plots of the supercapattery and comparison with other works, the z-axis indicates the charge-discharge cycles reported for each device and the colour-gradient map,<sup>66,68,86,311,314,319,338,341</sup> (b) volumetric Ragone plots of the CP/NF//AC/NF supercapattery and comparison with other energy devices.

In order to demonstrate the usability of the device, two supercapatteries were connected in series to power an LED. By charging the devices through a USB port for 1 min, the LED remained lit for up to 20 mins with no loss in brightness in the first minute as shown in Figure 5.21. The cobalt phosphate supercapatteries were connected in series and charged through 5 V USB port as shown in the circuit (left). The charging current is around 10 mA controlled by current-limiting resistance R1 (470  $\Omega$ ). The working voltage of the LED is around 3 V. Even after 5,000 charge-discharge cycles, the devices were still capable of powering the LED with similar brightness to the initial test, which

confirms the long-term usability of the proposed supercapattery device.

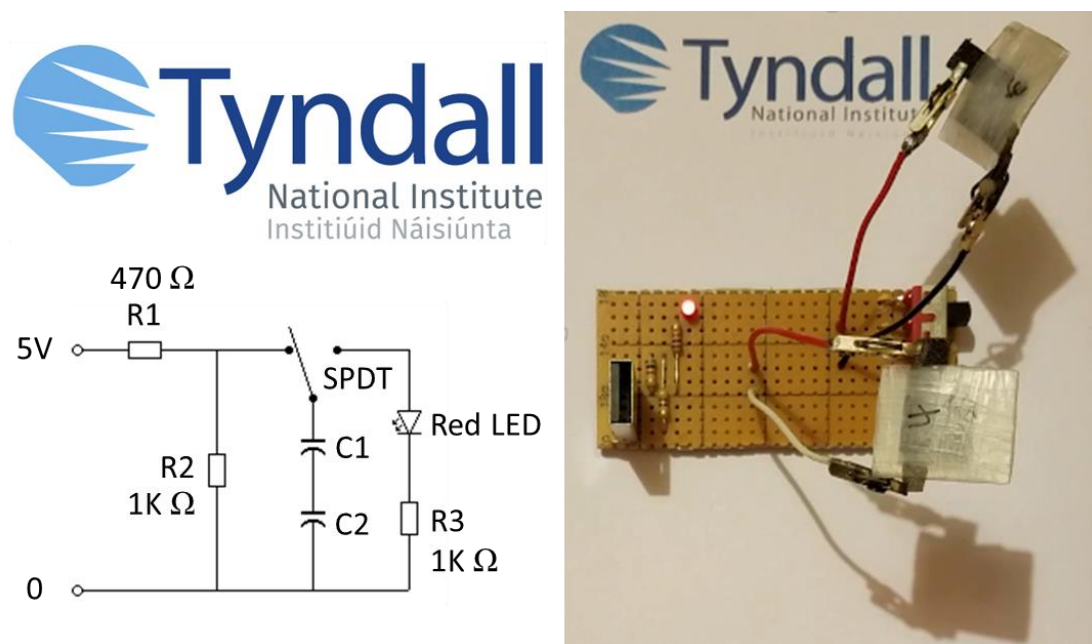


**Figure 5.21** Cobalt phosphate based hybrid supercapatteries connected in series and the application of LED lighting.

### 5.5.2 Self-discharge avoidance in pacemaker supercapattery

To ensure that a pacemaker retains enough energy to provide electrical impulses during emergency, the self-discharge behaviour and leakage current of CP/NF//AC/NF supercapattery device were investigated by measuring the open-circuit voltage, immediately after the device was fully charged with a charging current of 5 mA, as shown in Figure 5.22a. The self-discharge is mainly due to the migration of active electrolyte between two electrodes and the Faradaic redox reaction from some depolarizing impurity.<sup>147</sup> The oxidation and reduction reaction, if it occurs on the surface of either electrode, could cause a voltage leak. Since clinical brain death occurs from oxygen starvation in four minutes after the heart stops beating, a supercapattery such as developed in this work remains at 1.35 V (79.4% of the fully charged voltage) after 237 s, indicating that the device can provide enough power during cardiac emergencies. In addition, the device maintained more than 66% of the initial voltage after 1100 seconds, and remains stable for another 700 seconds.

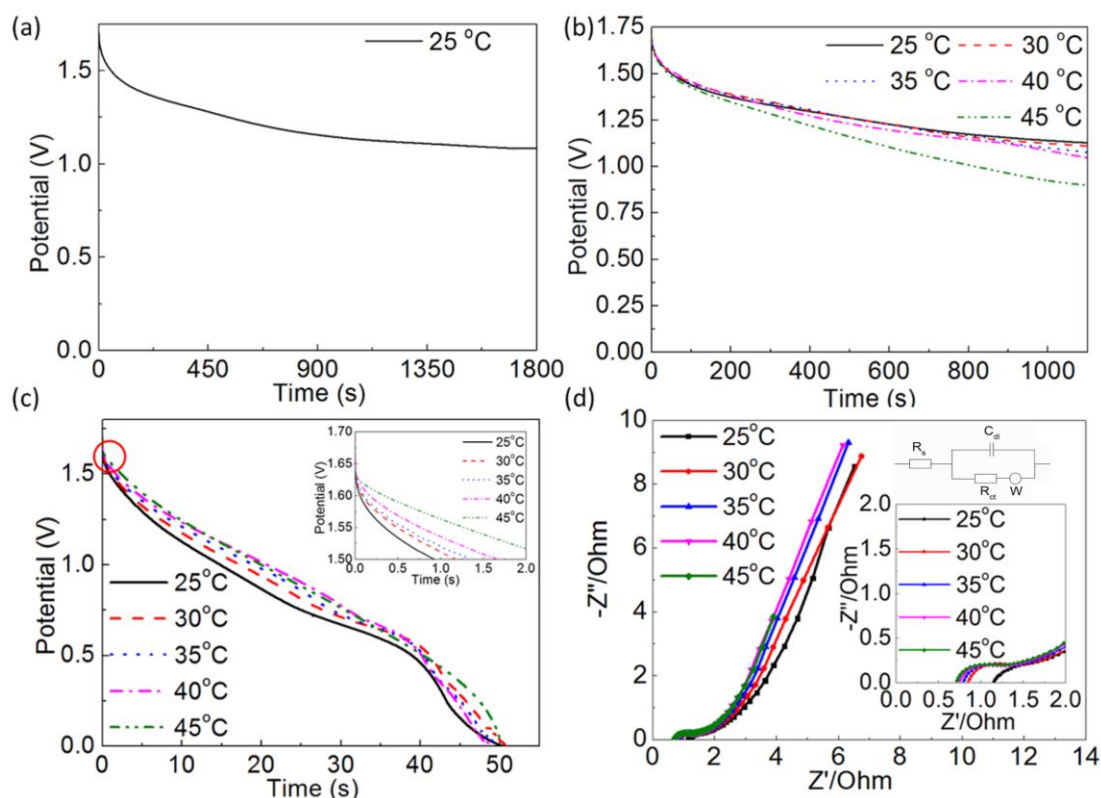


**Figure 5.22** (a) self-discharge curves of supercapattery at different temperature from 25 °C to 45 °C, (b) Plot of forward anodic peak current density and the square root of the scan rate for CP/NF at different temperature from 25 °C to 45 °C in three electrode system, (c-d) discharge curve (at 40 mA cm<sup>-2</sup>) and Nyquist plots of the hybrid device at different temperature from 25 °C to 45 °C.

### 5.5.3 Operation under physiological conditions (25 - 45 °C)

For use under physiological conditions inside human body, studies on the electrochemical properties were carried out between 25 - 45 °C. Besides the electrochemical properties and purity of the reagents, temperature is another important factor that determines the self-discharge current ( $I = A \exp[-\Delta E^+ / RT]$ , where  $\Delta E^+$  is a positive quantity around 16-20 kJ mol<sup>-1</sup> for diffusion controlled reactions).<sup>147</sup> As shown in Figure 5.22b, the leakage current of the device increase noticeably with increasing temperature, indicating the enhanced mobility of the electrolyte ions.

In order to understand the mechanism, individual electrode (CP/NF and AC/NF) were

investigated between 25 - 45 °C. For individual electrodes in a three electrode system, the diffusion coefficient (Figure 5.23 slopes) is amplified with increasing the temperature, showing slightly improved activation energy. Thereby, in case of the complete hybrid device (Figure 5.22c), it is observed a slight increase in specific capacity (from 29.51 to 34.88 mAh g<sup>-1</sup>) due to the thermal activation of the electrode material. As presented in the Figure 5.22c inset, the IR drop decreased from 0.079 to 0.034 V for 25 to 45 °C, indicating slight decrease of the device resistance. From the Nyquist plots (Figure 5.22d) acquired in 5 °C increments from 25 to 45 °C, the resistance of the device were found to be 1.13 to 0.70 Ω, which is consistent with the discharge behaviour and leakage current. Overall, the device is very stable and its capacity and voltage stability are within operational and safety norms for pacemaker power sources under nominal human body temperature (25-45 °C).

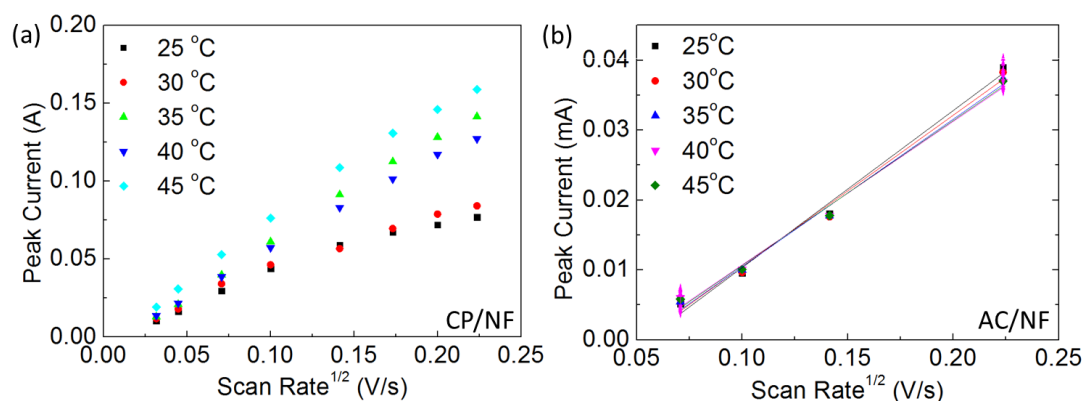


**Figure 5.23** (a) Plot of forward anodic peak current density and the square root of the scan rate for CP/NF at different temperature from 25 °C to 45 °C in three electrode system, (b) plot of forward anodic peak current density and the square root of the scan rate for AC/NF at different temperature from 25 °C to 45 °C in three electrode system.

In addition, a charge-discharge study for 20,000 cycles at 38 °C showed only 18.5% decay in the initial capacity, similar to room temperature, indicating excellent electrochemical properties and stability for the cobalt phosphate based supercapattery for the pacemaker implanted inside the human body. This rechargeable supercapattery with a high energy density of 3.53 mWh cm<sup>-3</sup> (43.2 Wh kg<sup>-1</sup>) and retention of 68% after

100,000 cycles, should be able to power the pacemaker for 20 years. The devices with single cell voltage of 1.7 V can be connected in series to meet the requirement of 2.8 V and would hold enough voltage (1.35 V) after the first 4 minutes with minimal self-discharge, which should be sufficient time for a piezoelectric energy harvester to recharge the device completely. The device exhibited good electrochemical properties at normothermia (38 °C), so that it is a promising forerunner for the development of a long-life rechargeable energy source for powering and operating next-generation self-charging pacemakers in conjunction with suitable energy harvesting technology.

## 5.6 Conclusion

In summary, among all the fabricated nanomaterials in this work, cobalt phosphate-nickel foam nanoflakes/ microflower structure based supercapattery exhibited the highest energy density of 3.53 mWh cm<sup>-3</sup> (43.2 Wh kg<sup>-1</sup>) and remained at 1.49 mWh cm<sup>-3</sup> (20.6 Wh kg<sup>-1</sup>) at a high power density of 425 mW cm<sup>-3</sup> (5.8 kW kg<sup>-1</sup>). Moreover, the device demonstrated an excellent cyclability of 84% after 20,000 cycles, and even after 100,000 cycles, the capacitance only dropped to 68% on initial value, confirming a long-time reliability of this device. Furthermore, the cobalt phosphate based supercapattery is stable at room temperature and above body temperature (25 to 45 °C). The energy and power performance of this hybrid device exceeded the stringent requirements of a leadless pacemaker system. Furthermore, in terms of power delivery, cycle life, self-discharge stability and compatibility with human body temperature, the device exhibits state of the art performance. This relatively simple technology is being developed as a long-life rechargeable energy source for powering and operating next-generation self-charging pacemakers in conjunction with suitable energy harvesting technology. With further biological evaluation and device miniaturization, the concept of a higher energy density, fast charging power source for cardiac care in patients will be accomplished. This device is also adaptable to a range of other wearable technologies and for internet of Things (IoT) applications requiring rechargeable power sources for wireless sensor nodes.

# Chapter 6 Conclusions and Future Work

## 6.1 Thesis Summary and Main Results

The prompt development of miniaturized implanted medical devices like an artificial cardiac pacemaker has increased the demand for power sources that can last for more than 20 years. The conventional rechargeable batteries with high energy density are very expensive with limited cycle life and cannot survive beyond 12 years. The supercapattery that combines high power capability and short charging/ discharging times of supercapacitor associated with greater energy density of batteries could be an attractive power source for the next generation pacemaker. Such supercapatteries fabricated using low-cost and abundant electrode materials could be the perfect alternative to batteries. It is the aim of this study is to develop novel nanostructured materials with enhanced electrochemical performance to be used as supercapattery electrodes. In this thesis, the design, fabrication, and characterization of the four different nickel foam supported materials have been systematically investigated. The structure, morphology, and elemental valence was studied using XRD, Raman, SEM, EDX, TEM, and XPS analysis, and these materials were electrochemically analysed in a three electrode system. Moreover, different configuration supercapatteries have been assembled and tested. The achievement of high energy density and high power density with excellent cyclic stability of supercapatteries fills the gap in the Ragone plot between conventional capacitor and batteries.

Important findings from the study are listed below:

- i. Commercially available nickel foam with a porosity of 95% was used as substrate, which offers a large active surface area and highly conductive 3D network architecture. Moreover, the direct growth of active materials on nickel foam also improved the morphology of the material therefore enhancing the efficient electron transport for energy storage processes.

- ii. Hydrothermal synthesis was carried out for the nanomaterial fabrication. The material structure and morphology was controlled by altering solution concentration, surface active agent, temperature, and holding time. Five different cobalt phosphate nanostructures were obtained under several processing variables, and optimized cobalt phosphate nanoflakes/ nanoflowers were synthesized in 8 hours at 120 °C in a 2.5 mM cobalt solution.
- iii. The supercapatteries were assembled in both symmetric and asymmetric configuration using Celgard membrane (porosity 55%, average pore size 64 nm) as separator. In the case of asymmetric cell, activated carbon was used as negative electrode. It was observed that for each pair of electrode materials, the mass loading balancing was a crucial factor to optimize the electrochemical performance of the complete device along with the specific electrolyte.
- iv. 3D/ 1D hybrid NiO–In<sub>2</sub>O<sub>3</sub> hetero-structures allow the synergistic contribution of both nanostructure as well as materials leading to better electrochemical performance as a supercapattery electrode. Noticeably, by varying compositions these hetero-structured electrodes showed distinct electrochemical performances due to their diverse electron/ ion transfer kinetics and microstructure. Among them, the hierarchical hybrid structures of NiO– In<sub>2</sub>O<sub>3</sub> (1 : 2) delivered a high specific capacity of 766.65 C g<sup>-1</sup> at 5 A g<sup>-1</sup> in 3 M KOH electrolyte. Moreover, the assembled symmetric supercapattery showed a high specific energy of 26.24 W h kg<sup>-1</sup> and a high specific power of 9624.5 W kg<sup>-1</sup> with a long term cyclic stability of 79% after 50,000 cycle testing.
- v. Binder-free Co<sub>3</sub>(PO<sub>4</sub>)<sub>2</sub>·8H<sub>2</sub>O multilayer nano/ microflakes structures were fabricated under different concentrations of the synthesis process with an average thickness of 400 nm to 1 μm. Among all the samples, the highest specific capacity of 868.3 C g<sup>-1</sup> (241.2 mAh g<sup>-1</sup>) at a current density of 5 mA cm<sup>-2</sup> was exhibited from 2.5 mM sample, with a rate capability of 65.2% for 10 times of the initial current density. The hybrid supercapattery fabricated using Co<sub>3</sub>(PO<sub>4</sub>)<sub>2</sub>·8H<sub>2</sub>O/NF as positive and AC/NF as the negative electrode demonstrated a maximum specific energy of 29.29 Wh kg<sup>-1</sup> (energy density of 1.17 mWh cm<sup>-3</sup>) and a maximum

specific power of  $4687 \text{ W kg}^{-1}$  (power density of  $187.5 \text{ mW cm}^{-3}$ ), with good cyclic stability of 77.9% after 1000 cycles.

- vi. 3D nano/ microflakes of  $\text{Ni}_3(\text{PO}_4)_2 \cdot 8\text{H}_2\text{O}$  structure were grown on nickel foam and delivered a specific capacity of  $301.8 \text{ mAh g}^{-1}$  at a current density of  $5 \text{ mA cm}^{-2}$ . The fabricated supercapattery based on the  $\text{Ni}_3(\text{PO}_4)_2 \cdot 8\text{H}_2\text{O}/\text{NF}$  and  $\text{AC}/\text{NF}$  as the positive and negative electrodes showed an specific energy and power of  $33.4 \text{ Wh kg}^{-1}$  and  $165.5 \text{ W kg}^{-1}$  with impressive cyclic stability of 89% after 10,000 cycles.
- vii. The optimized cobalt phosphate nanoflakes/ nanoflowers displayed a specific capacity of  $215.6 \text{ mAh g}^{-1}$  ( $1990 \text{ F g}^{-1}$ ) at an applied current of  $5 \text{ mA cm}^{-2}$  and 80.4% of initial capacity retention after 20,000 cycles, which is significantly better than the state of the art. The assembled asymmetric supercapattery delivered a high energy density of  $3.53 \text{ mWh cm}^{-3}$  ( $43.2 \text{ Wh kg}^{-1}$ ) and retains  $1.49 \text{ mWh cm}^{-3}$  ( $20.6 \text{ Wh kg}^{-1}$ ) even at a high power density of  $425 \text{ mW cm}^{-3}$  ( $5.8 \text{ kW kg}^{-1}$ ). The cyclic stability of the device was found to be over 68% retention after 100,000 cycles.
- viii. The quantify self-leakage and the performance of the cobalt phosphate nanoflakes/ nanoflowers based supercapattery were tested under a temperature range from 25 to  $45 \text{ }^\circ\text{C}$ . The cell remains  $1.35 \text{ V}$  (79.4% of the fully charged voltage) after 237 s and the retention is 81.5% after 20,000 charge-discharge cycles at physiological temperature ( $38 \text{ }^\circ\text{C}$ ). Thereby, supercapattery may provide a new platform to the bioelectronics industry, material scientists, engineers and the wider scientific community for the development of power sources for next generation biomedical devices and Internet of Things.

## **6.2 Recommendations for Future Work**

### **6.2.1 Development of Novel Materials**

There are still many promising materials have not been widely investigated for supercapattery applications, including chromium, copper, fluorides, phosphides, and chlorides. These material are commonly used as intercalation electrodes, thus should have the potential to extend the application as new type supercapattery. Besides, to further improve the electrochemical properties of the electrode, new developments in structure design are desired. There are many existing techniques to modify the surface and structure such as nitrogen doping, multilayer synthesis, core-shell design, and metal–organic frameworks. Further investigation on different composites and unique structure development are required. Overall, the target is to improve the electrochemical performance by increasing the surface active area of the activated material, enhancing the electrochemical kinetics between electrode and electrolyte, and developing stable structure.

### **6.2.2 Optimization of the Complete Supercapattery Cell**

Supercapatteries can be classified into different categories according to their electrode materials as discussed in section 1.2.2, but not all of them have been widely investigated. With the development of materials, novel supercapatteries will be assembled using different materials, such as pairing one battery type material with one pseudocapacitive material, or pairing two different pseudo-battery type materials with different potential window. On the other hand, it should be pointed out that the studies on electrolyte is lacking. Only several kinds of aqueous solution, organic electrolyte, and ionic liquid have been investigated. However, the understanding and evidence of the mechanism is limited. Therefore, more research is required on in-situ studies to further analyse the electrochemical performance of both electrode and electrolyte. Moreover, since most of the metal base materials exhibit higher capacity/ capacity compare to carbon, the

discovery of negative electrode material is needed to extend the working potential of the complete supercapattery cell. Furthermore, besides carbon fibre, nickel foam, and graphene sheets, other investigation on substrate are required to assemble different types/ shapes of supercapatteries for various applications. Silicon may be an alternative option for future energy storage devices. The future supercapattery may have the potential to offer both high energy and high power with excellent cyclic stability and wide working potential, so that would be suitable for various implanted medical devices and other existing electronic devices.

# Bibliography

- 1 Rathore, H., Mohamed, A., Al-Ali, A., Du, X. & Guizani, M. in *Wireless Communications and Mobile Computing Conference (IWCMC), 2017 13th International*. 1495-1501 (IEEE).
- 2 Bradley, P. D. in *ESSCIRC (ESSCIRC), 2011 Proceedings of the*. 37-41 (IEEE).
- 3 Marc Goodman, Who does the autopsy, [http://www.slate.com/articles/technology/future\\_tense/2015/03/implantable\\_medical\\_devices\\_hacking\\_who\\_does\\_the\\_autopsy.html](http://www.slate.com/articles/technology/future_tense/2015/03/implantable_medical_devices_hacking_who_does_the_autopsy.html), (2015)
- 4 Sarina A van der Zee, Shephal K. Doshi, Permanent leadless cardiac pacing, <http://www.acc.org/latest-in-cardiology/articles/2016/03/23/08/09/permanent-leadless-cardiac-pacing>, (2016)
- 5 Shepard, R. K. & Ellenbogen, K. A. (Eur Heart Rhythm Assoc, 2008).
- 6 Mallela, V. S., Ilankumaran, V. & Rao, S. N. Trends in cardiac pacemaker batteries. *Indian pacing and electrophysiology journal* **4**, 201-212 (2004).
- 7 Reynolds, D. *et al.* A leadless intracardiac transcatheter pacing system. *New England Journal of Medicine* **374**, 533-541 (2016).
- 8 Kerzenmacher, S., Ducrée, J., Zengerle, R. & Von Stetten, F. Energy harvesting by implantable abiotically catalyzed glucose fuel cells. *Journal of Power Sources* **182**, 1-17 (2008).
- 9 Goto, H., Sugiura, T., Harada, Y. & Kazui, T. Feasibility of using the automatic generating system for quartz watches as a leadless pacemaker power source. *Medical & biological engineering & computing* **37**, 377-380 (1999).
- 10 Parsonnet, V., Berstein, A. D. & Perry, G. Y. The nuclear pacemaker: Is renewed interest warranted? *The American journal of cardiology* **66**, 837-842 (1990).
- 11 Jackson, N. *et al.* Widening the bandwidth of vibration energy harvesters using a liquid-based non-uniform load distribution. *Sensors and Actuators A: Physical* **246**, 170-179 (2016).
- 12 Nitta, N., Wu, F., Lee, J. T. & Yushin, G. Li-ion battery materials: present and future. *Materials today* **18**, 252-264 (2015).

- 13 Maaroufi, S., Parrain, F., Lefeuvre, E., Boutaud, B. & Dal Molin, R. in *Journal of Physics: Conference Series*. 012103 (IOP Publishing).
- 14 Galaxy S9/S9+, <https://www.samsung.com/us/smartphones/galaxy-s9/specs/>, (2018)
- 15 Lin, M.-C. *et al.* An ultrafast rechargeable aluminium-ion battery. *Nature* **520**, 324 (2015).
- 16 Bullock, K. R. Lead/acid batteries. *Journal of power sources* **51**, 1-17 (1994).
- 17 Bode, H. Lead-acid batteries. (1977).
- 18 Henderson, I. H. & Ladan, S. G. (Google Patents, 1967).
- 19 Reddy, B. R. & Priya, D. N. Chloride leaching and solvent extraction of cadmium, cobalt and nickel from spent nickel–cadmium, batteries using Cyanex 923 and 272. *Journal of Power Sources* **161**, 1428-1434 (2006).
- 20 Etacheri, V., Marom, R., Elazari, R., Salitra, G. & Aurbach, D. Challenges in the development of advanced Li-ion batteries: a review. *Energy & Environmental Science* **4**, 3243-3262 (2011).
- 21 Aurbach, D. Review of selected electrode–solution interactions which determine the performance of Li and Li ion batteries. *Journal of Power Sources* **89**, 206-218 (2000).
- 22 McNulty, D., Buckley, D. N. & O'Dwyer, C. Synthesis and electrochemical properties of vanadium oxide materials and structures as Li-ion battery positive electrodes. *Journal of Power Sources* **267**, 831-873 (2014).
- 23 Palacin, M. R. Recent advances in rechargeable battery materials: a chemist's perspective. *Chemical Society Reviews* **38**, 2565-2575 (2009).
- 24 Kim, D. K. *et al.* Spinel LiMn<sub>2</sub>O<sub>4</sub> nanorods as lithium ion battery cathodes. *Nano letters* **8**, 3948-3952 (2008).
- 25 Lee, H.-W. *et al.* Ultrathin spinel LiMn<sub>2</sub>O<sub>4</sub> nanowires as high power cathode materials for Li-ion batteries. *Nano letters* **10**, 3852-3856 (2010).
- 26 Zhao, L., Hu, Y. S., Li, H., Wang, Z. & Chen, L. Porous Li<sub>4</sub>Ti<sub>5</sub>O<sub>12</sub> Coated with N-Doped Carbon from Ionic Liquids for Li-Ion Batteries. *Advanced Materials* **23**, 1385-1388 (2011).

- 27 Park, K.-S., Benayad, A., Kang, D.-J. & Doo, S.-G. Nitridation-driven conductive  $\text{Li}_4\text{Ti}_5\text{O}_{12}$  for lithium ion batteries. *Journal of the American Chemical Society* **130**, 14930-14931 (2008).
- 28 Liu, Y. *et al.* Effect of carbon nanotube on the electrochemical performance of C-LiFePO<sub>4</sub>/graphite battery. *Journal of Power Sources* **184**, 522-526 (2008).
- 29 Li, B. *et al.* A novel electrolyte with the ability to form a solid electrolyte interface on the anode and cathode of a LiMn<sub>2</sub>O<sub>4</sub>/graphite battery. *Journal of Materials Chemistry A* **1**, 12954-12961 (2013).
- 30 Groot, J., Swierczynski, M., Stan, A. I. & Kær, S. K. On the complex ageing characteristics of high-power LiFePO<sub>4</sub>/graphite battery cells cycled with high charge and discharge currents. *Journal of Power Sources* **286**, 475-487 (2015).
- 31 Ge, H., Li, N., Li, D., Dai, C. & Wang, D. Study on the theoretical capacity of spinel lithium titanate induced by low-potential intercalation. *The Journal of Physical Chemistry C* **113**, 6324-6326 (2009).
- 32 Chan, C. K. *et al.* High-performance lithium battery anodes using silicon nanowires. *Nature nanotechnology* **3**, 31 (2008).
- 33 Fisher, C. A., Hart Prieto, V. M. & Islam, M. S. Lithium Battery Materials LiMPO<sub>4</sub> (M= Mn, Fe, Co, and Ni): Insights into Defect Association, Transport Mechanisms, and Doping Behavior. *Chemistry of Materials* **20**, 5907-5915 (2008).
- 34 Yamada, A., Chung, S.-C. & Hinokuma, K. Optimized LiFePO<sub>4</sub> for lithium battery cathodes. *Journal of the electrochemical society* **148**, A224-A229 (2001).
- 35 Tao, T. *et al.* MoO<sub>3</sub> nanoparticles dispersed uniformly in carbon matrix: a high capacity composite anode for Li-ion batteries. *Journal of Materials Chemistry* **21**, 9350-9355 (2011).
- 36 Armand, M. & Tarascon, J.-M. Building better batteries. *nature* **451**, 652 (2008).
- 37 Poizot, P., Laruelle, S., Grugeon, S. & Tarascon, J.-M. Rationalization of the low-potential reactivity of 3d-metal-based inorganic compounds toward Li. *Journal of The Electrochemical Society* **149**, A1212-A1217 (2002).
- 38 McDowell, M. T., Xia, S. & Zhu, T. The mechanics of large-volume-change

- transformations in high-capacity battery materials. *Extreme Mechanics Letters* **9**, 480-494 (2016).
- 39 Jin, S. *et al.* Facile synthesis of hierarchically structured Fe<sub>3</sub>O<sub>4</sub>/carbon microflowers and their application to lithium-ion battery anodes. *Journal of Power Sources* **196**, 3887-3893 (2011).
- 40 Xue, X.-Y. *et al.* Porous Co<sub>3</sub>O<sub>4</sub> nanoneedle arrays growing directly on copper foils and their ultrafast charging/discharging as lithium-ion battery anodes. *Chemical communications* **47**, 4718-4720 (2011).
- 41 Zhang, W.-J. A review of the electrochemical performance of alloy anodes for lithium-ion batteries. *Journal of Power Sources* **196**, 13-24 (2011).
- 42 Lee, K.-M., Lee, Y.-S., Kim, Y.-W., Sun, Y.-K. & Lee, S.-M. Electrochemical characterization of Ti-Si and Ti-Si-Al alloy anodes for Li-ion batteries produced by mechanical ball milling. *Journal of Alloys and Compounds* **472**, 461-465 (2009).
- 43 Kravchyk, K. *et al.* Monodisperse and inorganically capped Sn and Sn/SnO<sub>2</sub> nanocrystals for high-performance Li-ion battery anodes. *Journal of the American Chemical Society* **135**, 4199-4202 (2013).
- 44 Xu, L. *et al.* Monodisperse Sn nanocrystals as a platform for the study of mechanical damage during electrochemical reactions with Li. *Nano letters* **13**, 1800-1805 (2013).
- 45 Hwang, S.-M. *et al.* Lithium insertion in SiAg powders produced by mechanical alloying. *Electrochemical and Solid-State Letters* **4**, A97-A100 (2001).
- 46 Roberts, G., Cairns, E. & Reimer, J. Magnesium silicide as a negative electrode material for lithium-ion batteries. *Journal of power sources* **110**, 424-429 (2002).
- 47 Liu, Y., He, Y., Ma, R., Gao, M. & Pan, H. Improved lithium storage properties of Mg<sub>2</sub>Si anode material synthesized by hydrogen-driven chemical reaction. *Electrochemistry Communications* **25**, 15-18 (2012).
- 48 Ardizzone, S., Fregonara, G. & Trasatti, S. "Inner" and "outer" active surface of RuO<sub>2</sub> electrodes. *Electrochimica Acta* **35**, 263-267 (1990).
- 49 Zheng, J., Cygan, P. & Jow, T. Hydrous ruthenium oxide as an electrode material

- for electrochemical capacitors. *Journal of the Electrochemical Society* **142**, 2699-2703 (1995).
- 50 Lee, H. Y. & Goodenough, J. B. Supercapacitor behavior with KCl electrolyte. *Journal of Solid State Chemistry* **144**, 220-223 (1999).
- 51 Brousse, T. *et al.* Crystalline MnO<sub>2</sub> as possible alternatives to amorphous compounds in electrochemical supercapacitors. *Journal of the Electrochemical Society* **153**, A2171-A2180 (2006).
- 52 Mohapatra, S., Acharya, A. & Roy, G. The role of nanomaterial for the design of supercapacitor. *Lat. Am. J. Phys. Educ. Vol* **6**, 380 (2012).
- 53 Chen, S.-M., Ramachandran, R., Mani, V. & Saraswathi, R. Recent advancements in electrode materials for the high-performance electrochemical supercapacitors: a review. *Int. J. Electrochem. Sci* **9**, 4072-4085 (2014).
- 54 Beidaghi, M. & Wang, C. Micro-supercapacitors based on interdigital electrodes of reduced graphene oxide and carbon nanotube composites with ultrahigh power handling performance. *Advanced Functional Materials* **22**, 4501-4510 (2012).
- 55 Chen, T. & Dai, L. Carbon nanomaterials for high-performance supercapacitors. *Materials Today* **16**, 272-280 (2013).
- 56 Yao, J., Pan, Q., Yao, S., Duan, L. & Liu, J. Mesoporous MnO<sub>2</sub> Nanosphere/Graphene Sheets as Electrodes for Supercapacitor Synthesized by a Simple and Inexpensive Reflux Reaction. *Electrochimica Acta* **238**, 30-35 (2017).
- 57 Mutlu, A. T. characterization of CNTs and CNTs/MnO<sub>2</sub> composite for supercapacitor application. (2010).
- 58 Zhang, F., Tang, J., Shinya, N. & Qin, L.-C. Hybrid graphene electrodes for supercapacitors of high energy density. *Chemical Physics Letters* **584**, 124-129 (2013).
- 59 Makgopa, K. *et al.* A high-rate aqueous symmetric pseudocapacitor based on highly graphitized onion-like carbon/birnessite-type manganese oxide nanohybrids. *Journal of Materials Chemistry A* **3**, 3480-3490 (2015).

- 60 Fan, L., Tang, L., Gong, H., Yao, Z. & Guo, R. Carbon-nanoparticles encapsulated in hollow nickel oxides for supercapacitor application. *Journal of Materials Chemistry* **22**, 16376-16381 (2012).
- 61 Lu, Z., Chang, Z., Liu, J. & Sun, X. Stable ultrahigh specific capacitance of NiO nanorod arrays. *Nano research* **4**, 658 (2011).
- 62 Rakhi, R., Chen, W., Cha, D. & Alshareef, H. N. Substrate dependent self-organization of mesoporous cobalt oxide nanowires with remarkable pseudocapacitance. *Nano letters* **12**, 2559-2567 (2012).
- 63 Chen, G. Z. Understanding supercapacitors based on nano-hybrid materials with interfacial conjugation. *Progress in Natural Science: Materials International* **23**, 245-255 (2013).
- 64 Padmanathan, N., Shao, H., McNulty, D., O'Dwyer, C. & Razeeb, K. M. Hierarchical NiO–In<sub>2</sub>O<sub>3</sub> microflower (3D)/nanorod (1D) hetero-architecture as a supercapattery electrode with excellent cyclic stability. *Journal of Materials Chemistry A* **4**, 4820-4830 (2016).
- 65 Brousse, T., Bélanger, D. & Long, J. W. To be or not to be pseudocapacitive? *Journal of The Electrochemical Society* **162**, A5185-A5189 (2015).
- 66 Shao, H., Padmanathan, N., McNulty, D., O' Dwyer, C. & Razeeb, K. M. Supercapattery Based on Binder-Free Co<sub>3</sub>(PO<sub>4</sub>)<sub>2</sub>·8H<sub>2</sub>O Multilayer Nano/Microflakes on Nickel Foam. *ACS applied materials & interfaces* **8**, 28592-28598 (2016).
- 67 Chen, G. Z., presented at *ECS Meeting*, Boston, Massachusetts, US, 559-559 (The Electrochemical Society) (2011).
- 68 Dubal, D. P., Ayyad, O., Ruiz, V. & Gomez-Romero, P. Hybrid energy storage: the merging of battery and supercapacitor chemistries. *Chemical Society Reviews* **44**, 1777-1790 (2015).
- 69 Chen, G. Z. Supercapacitor and supercapattery as emerging electrochemical energy stores. *International Materials Reviews* **62**, 173-202 (2017).
- 70 Stoller, M. D., Park, S., Zhu, Y., An, J. & Ruoff, R. S. Graphene-based ultracapacitors. *Nano letters* **8**, 3498-3502 (2008).

- 71 Vivekchand, S., Rout, C. S., Subrahmanyam, K., Govindaraj, A. & Rao, C. Graphene-based electrochemical supercapacitors. *Journal of Chemical Sciences* **120**, 9-13 (2008).
- 72 Zhang, L. L. & Zhao, X. Carbon-based materials as supercapacitor electrodes. *Chemical Society Reviews* **38**, 2520-2531 (2009).
- 73 Ma, Y. *et al.* Conductive graphene fibers for wire-shaped supercapacitors strengthened by unfunctionalized few-walled carbon nanotubes. *ACS nano* **9**, 1352-1359 (2015).
- 74 Härmas, M. *et al.* in *ECSSMeeting*, National Harbor, DC, US, 652-652. (The Electrochemical Society) (2017).
- 75 Padmanathan, N., Selladurai, S., Rahulan, K. M., O'Dwyer, C. & Razeeb, K. M. NiO hybrid nanoarchitecture-based pseudocapacitor in organic electrolyte with high rate capability and cycle life. *Ionics* **21**, 2623-2631 (2015).
- 76 Padmanathan, N., Selladurai, S. & Razeeb, K. M. Ultra-fast rate capability of a symmetric supercapacitor with a hierarchical Co<sub>3</sub>O<sub>4</sub> nanowire/nanoflower hybrid structure in non-aqueous electrolyte. *RSC Advances* **5**, 12700-12709 (2015).
- 77 Padmanathan, N. *et al.* Pseudocapacitance of  $\alpha$ -CoMoO<sub>4</sub> nanoflakes in non-aqueous electrolyte and its bi-functional electro catalytic activity for methanol oxidation. *international journal of hydrogen energy* **40**, 16297-16305 (2015).
- 78 Dsoke, S., Fuchs, B., Gucciardi, E. & Wohlfahrt-Mehrens, M. The importance of the electrode mass ratio in a Li-ion capacitor based on activated carbon and Li<sub>4</sub>Ti<sub>5</sub>O<sub>12</sub>. *Journal of Power Sources* **282**, 385-393 (2015).
- 79 Arun, N. *et al.* Nanostructured spinel LiNi<sub>0.5</sub>Mn<sub>1.5</sub>O<sub>4</sub> as new insertion anode for advanced Li-ion capacitors with high power capability. *Nano Energy* **12**, 69-75 (2015).
- 80 Jian, Z. *et al.* A High-Power Symmetric Na-Ion Pseudocapacitor. *Advanced Functional Materials* **25**, 5778-5785 (2015).
- 81 Ding, J. *et al.* Peanut shell hybrid sodium ion capacitor with extreme energy-power rivals lithium ion capacitors. *Energy & Environmental Science* **8**, 941-

- 955 (2015).
- 82 Gao, S. *et al.* Na<sub>2</sub>CoSiO<sub>4</sub> as a novel positive electrode material for sodium-ion capacitors. *Materials Letters* **158**, 300-303 (2015).
- 83 Lin, T. *et al.* Nitrogen-doped mesoporous carbon of extraordinary capacitance for electrochemical energy storage. *Science* **350**, 1508-1513 (2015).
- 84 Cakici, M., Kakarla, R. R. & Alonso-Marroquin, F. Advanced electrochemical energy storage supercapacitors based on the flexible carbon fiber fabric-coated with uniform coral-like MnO<sub>2</sub> structured electrodes. *Chemical Engineering Journal* **309**, 151-158 (2017).
- 85 Yu, L. & Chen, G. Z. Redox electrode materials for supercapatteries. *Journal of Power Sources* **326**, 604-612 (2016).
- 86 Liu, S. *et al.* Ultrafine nickel–cobalt alloy nanoparticles incorporated into three-dimensional porous graphitic carbon as an electrode material for supercapacitors. *Journal of Materials Chemistry A* **4**, 17080-17086 (2016).
- 87 Frackowiak, E., Khomenko, V., Jurewicz, K., Lota, K. & Béguin, F. Supercapacitors based on conducting polymers/nanotubes composites. *Journal of Power Sources* **153**, 413-418 (2006).
- 88 He, W. *et al.* Flexible and high energy density asymmetrical supercapacitors based on core/shell conducting polymer nanowires/manganese dioxide nanoflakes. *Nano Energy* **35**, 242-250 (2017).
- 89 Wang, L. *et al.* Metal–organic frameworks for energy storage: Batteries and supercapacitors. *Coordination Chemistry Reviews* **307**, 361-381 (2016).
- 90 Liu, B., Shioyama, H., Jiang, H., Zhang, X. & Xu, Q. Metal–organic framework (MOF) as a template for syntheses of nanoporous carbons as electrode materials for supercapacitor. *Carbon* **48**, 456-463 (2010).
- 91 Sheberla, D. *et al.* Conductive MOF electrodes for stable supercapacitors with high areal capacitance. *Nature materials* **16**, 220 (2017).
- 92 Liu, R., Duay, J. & Lee, S. B. Heterogeneous nanostructured electrode materials for electrochemical energy storage. *Chemical Communications* **47**, 1384-1404 (2011).

- 93 Zhi, M. *et al.* Effects of pore structure on performance of an activated-carbon supercapacitor electrode recycled from scrap waste tires. *ACS Sustainable Chemistry & Engineering* **2**, 1592-1598 (2014).
- 94 Kim, M.-H., Kim, K.-B., Park, S.-M. & Roh, K. C. Hierarchically structured activated carbon for ultracapacitors. *Scientific reports* **6**, 21182 (2016).
- 95 Faraji, S. & Ani, F. N. The development supercapacitor from activated carbon by electroless plating—A review. *Renewable and Sustainable Energy Reviews* **42**, 823-834 (2015).
- 96 Zhao, J. *et al.* Hierarchical NiMn layered double hydroxide/carbon nanotubes architecture with superb energy density for flexible supercapacitors. *Advanced Functional Materials* **24**, 2938-2946 (2014).
- 97 Gu, W. & Yushin, G. Review of nanostructured carbon materials for electrochemical capacitor applications: advantages and limitations of activated carbon, carbide-derived carbon, zeolite-templated carbon, carbon aerogels, carbon nanotubes, onion-like carbon, and graphene. *Wiley Interdisciplinary Reviews: Energy and Environment* **3**, 424-473 (2014).
- 98 Ke, Q. & Wang, J. Graphene-based materials for supercapacitor electrodes—A review. *Journal of Materiomics* **2**, 37-54 (2016).
- 99 Chee, W. *et al.* Flexible graphene-based supercapacitors: a review. *The Journal of Physical Chemistry C* **120**, 4153-4172 (2016).
- 100 Gao, Y. Graphene and polymer composites for supercapacitor applications: a review. *Nanoscale research letters* **12**, 387 (2017).
- 101 Shi, K., Ren, M. & Zhitomirsky, I. Activated carbon-coated carbon nanotubes for energy storage in supercapacitors and capacitive water purification. *ACS Sustainable Chemistry & Engineering* **2**, 1289-1298 (2014).
- 102 Evanoff, K. *et al.* Towards ultrathick battery electrodes: Aligned carbon nanotube-enabled architecture. *Advanced Materials* **24**, 533-537 (2012).
- 103 Evanoff, K., Magasinski, A., Yang, J. & Yushin, G. Nanosilicon-Coated Graphene Granules as Anodes for Li-Ion Batteries. *Advanced Energy Materials* **1**, 495-498 (2011).

- 104 Yang, S.-Y. *et al.* Design and tailoring of a hierarchical graphene-carbon nanotube architecture for supercapacitors. *Journal of Materials Chemistry* **21**, 2374-2380 (2011).
- 105 Li, X., Han, C., Chen, X. & Shi, C. Preparation and performance of straw based activated carbon for supercapacitor in non-aqueous electrolytes. *Microporous and Mesoporous Materials* **131**, 303-309 (2010).
- 106 Wang, R. *et al.* Promising porous carbon derived from celtuce leaves with outstanding supercapacitance and CO<sub>2</sub> capture performance. *ACS applied materials & interfaces* **4**, 5800-5806 (2012).
- 107 Zhang, J., Gong, L., Sun, K., Jiang, J. & Zhang, X. Preparation of activated carbon from waste *Camellia oleifera* shell for supercapacitor application. *Journal of Solid State Electrochemistry* **16**, 2179-2186 (2012).
- 108 Li, Q.-Y., Wang, H.-Q., Dai, Q.-F., Yang, J.-H. & Zhong, Y.-L. Novel activated carbons as electrode materials for electrochemical capacitors from a series of starch. *Solid State Ionics* **179**, 269-273 (2008).
- 109 Balathanigaimani, M. *et al.* Highly porous electrodes from novel corn grains-based activated carbons for electrical double layer capacitors. *Electrochemistry Communications* **10**, 868-871 (2008).
- 110 Yang, H., Yoshio, M., Isono, K. & Kuramoto, R. Improvement of commercial activated carbon and its application in electric double layer capacitors. *Electrochemical and solid-state letters* **5**, A141-A144 (2002).
- 111 Teng, H., Chang, Y.-J. & Hsieh, C.-T. Performance of electric double-layer capacitors using carbons prepared from phenol-formaldehyde resins by KOH etching. *Carbon* **39**, 1981-1987 (2001).
- 112 Pandolfo, A. & Hollenkamp, A. Carbon properties and their role in supercapacitors. *Journal of power sources* **157**, 11-27 (2006).
- 113 Alonso, A. *et al.* Activated carbon produced from Sasol-Lurgi gasifier pitch and its application as electrodes in supercapacitors. *Carbon* **44**, 441-446 (2006).
- 114 Hulicova-Jurcakova, D. *et al.* Highly stable performance of supercapacitors from phosphorus-enriched carbons. *Journal of the American Chemical Society*

- 131**, 5026-5027 (2009).
- 115 Nandhini, R., Mini, P., Avinash, B., Nair, S. & Subramanian, K. Supercapacitor electrodes using nanoscale activated carbon from graphite by ball milling. *Materials Letters* **87**, 165-168 (2012).
- 116 Simon, P. & Burke, A. Nanostructured carbons: double-layer capacitance and more. *The electrochemical society interface* **17**, 38 (2008).
- 117 Huang, C.-W., Hsieh, C.-T., Kuo, P.-L. & Teng, H. Electric double layer capacitors based on a composite electrode of activated mesophase pitch and carbon nanotubes. *Journal of Materials Chemistry* **22**, 7314-7322 (2012).
- 118 Hulicova-Jurcakova, D. *et al.* Nitrogen-Enriched Nonporous Carbon Electrodes with Extraordinary Supercapacitance. *Advanced Functional Materials* **19**, 1800-1809 (2009).
- 119 Guo, S. *et al.* Preparation and performance of polyvinyl alcohol-based activated carbon as electrode material in both aqueous and organic electrolytes. *Journal of Solid State Electrochemistry* **16**, 3355-3362 (2012).
- 120 Chen, H. *et al.* An activated carbon derived from tobacco waste for use as a supercapacitor electrode material. *Carbon* **130**, 848 (2018).
- 121 Thubsuang, U., Laebang, S., Manmuanpom, N., Wongkasemjit, S. & Chaisuwan, T. Tuning pore characteristics of porous carbon monoliths prepared from rubber wood waste treated with H<sub>3</sub>PO<sub>4</sub> or NaOH and their potential as supercapacitor electrode materials. *Journal of Materials Science* **52**, 6837-6855 (2017).
- 122 Seo, M.-K. & Park, S.-J. Electrochemical characteristics of activated carbon nanofiber electrodes for supercapacitors. *Materials Science and Engineering: B* **164**, 106-111 (2009).
- 123 Yu, M., Li, J. & Wang, L. KOH-activated carbon aerogels derived from sodium carboxymethyl cellulose for high-performance supercapacitors and dye adsorption. *Chemical engineering journal* **310**, 300-306 (2017).
- 124 Elmouwahidi, A., Zapata-Benabithe, Z., Carrasco-Marín, F. & Moreno-Castilla, C. Activated carbons from KOH-activation of argan (*Argania spinosa*) seed

- shells as supercapacitor electrodes. *Bioresource technology* **111**, 185-190 (2012).
- 125 Frackowiak, E. *et al.* Enhanced capacitance of carbon nanotubes through chemical activation. *Chemical Physics Letters* **361**, 35-41 (2002).
- 126 Niu, C., Sichel, E. K., Hoch, R., Moy, D. & Tennent, H. High power electrochemical capacitors based on carbon nanotube electrodes. *Applied Physics Letters* **70**, 1480-1482 (1997).
- 127 Yoon, B.-J. *et al.* Electrical properties of electrical double layer capacitors with integrated carbon nanotube electrodes. *Chemical Physics Letters* **388**, 170-174 (2004).
- 128 Wan, K. *et al.* Supramolecular Assembly of 1D Pristine Carbon Nanotubes and 2D Graphene Oxides into Macroscopic All-Carbon Hybrid Sponges for High-Energy-Density Supercapacitors. *ChemNanoMat* **3**, 447-453 (2017).
- 129 Lu, W., Qu, L., Henry, K. & Dai, L. High performance electrochemical capacitors from aligned carbon nanotube electrodes and ionic liquid electrolytes. *Journal of Power Sources* **189**, 1270-1277 (2009).
- 130 González, A., Goikolea, E., Barrena, J. A. & Mysyk, R. Review on supercapacitors: technologies and materials. *Renewable and Sustainable Energy Reviews* **58**, 1189-1206 (2016).
- 131 Bhuyan, M. S. A., Uddin, M. N., Islam, M. M., Bipasha, F. A. & Hossain, S. S. Synthesis of graphene. *International Nano Letters* **6**, 65-83 (2016).
- 132 Ghosh, S., Gupta, B., Mathews, T., Das, A. & Kamruddin, M. Influence of aqueous electrolytes on electrochemical performance of vertical graphene nanosheets supercapacitor electrode. *arXiv preprint arXiv:1603.08320* (2016).
- 133 Liu, C., Yu, Z., Neff, D., Zhamu, A. & Jang, B. Z. Graphene-based supercapacitor with an ultrahigh energy density. *Nano letters* **10**, 4863-4868 (2010).
- 134 Du, Q. *et al.* Preparation of functionalized graphene sheets by a low-temperature thermal exfoliation approach and their electrochemical supercapacitive behaviors. *Electrochimica Acta* **55**, 3897-3903 (2010).
- 135 Wang, Y. *et al.* Supercapacitor devices based on graphene materials. *The*

- Journal of Physical Chemistry C* **113**, 13103-13107 (2009).
- 136 Zhu, Y. *et al.* Microwave assisted exfoliation and reduction of graphite oxide for ultracapacitors. *Carbon* **48**, 2118-2122 (2010).
- 137 Jeong, H. M. *et al.* Nitrogen-doped graphene for high-performance ultracapacitors and the importance of nitrogen-doped sites at basal planes. *Nano letters* **11**, 2472-2477 (2011).
- 138 Sui, Z.-Y. *et al.* Nitrogen-doped graphene aerogels as efficient supercapacitor electrodes and gas adsorbents. *ACS applied materials & interfaces* **7**, 1431-1438 (2015).
- 139 Kota, M., Yu, X., Yeon, S.-H., Cheong, H.-W. & Park, H. S. Ice-templated three dimensional nitrogen doped graphene for enhanced supercapacitor performance. *Journal of Power Sources* **303**, 372-378 (2016).
- 140 Portet, C., Taberna, P., Simon, P. & Flahaut, E. Influence of carbon nanotubes addition on carbon-carbon supercapacitor performances in organic electrolyte. *Journal of power sources* **139**, 371-378 (2005).
- 141 Xia, H., Wang, Y., Lin, J. & Lu, L. Hydrothermal synthesis of MnO<sub>2</sub>/CNT nanocomposite with a CNT core/porous MnO<sub>2</sub> sheath hierarchy architecture for supercapacitors. *Nanoscale research letters* **7**, 33 (2012).
- 142 Wang, Z., Zhang, C., Xu, C., Zhu, Z. & Chen, C. Hollow polypyrrole nanosphere embedded in nitrogen-doped graphene layers to obtain a three-dimensional nanostructure as electrode material for electrochemical supercapacitor. *Ionics* **23**, 147-156 (2017).
- 143 Quan, H., Cheng, B., Chen, D., Su, X., Xiao, Y., and Lei, S. One-pot synthesis of  $\alpha$ -MnS/nitrogen-doped reduced graphene oxide hybrid for high-performance asymmetric supercapacitors. *Electrochimica Acta* **210**, 557-566 (2016).
- 144 Patake, V., Lokhande, C. & Joo, O. S. Electrodeposited ruthenium oxide thin films for supercapacitor: Effect of surface treatments. *Applied Surface Science* **255**, 4192-4196 (2009).
- 145 Ghodbane, O., Pascal, J.-L. & Favier, F. Microstructural effects on charge-storage properties in MnO<sub>2</sub>-based electrochemical supercapacitors. *ACS*

- applied materials & interfaces* **1**, 1130-1139 (2009).
- 146 Hu, C.-C., Lee, C.-H. & Wen, T.-C. Oxygen evolution and hypochlorite production on Ru-Pt binary oxides. *Journal of applied electrochemistry* **26**, 72-82 (1996).
- 147 Conway, B. E. *Electrochemical supercapacitors: scientific fundamentals and technological applications*. (Springer Science & Business Media, 2013).
- 148 Jia, Q. *et al.* Epitaxial growth of highly conductive RuO<sub>2</sub> thin films on (100) Si. *Applied physics letters* **68**, 1069-1071 (1996).
- 149 Chen, L. *et al.* Toward the theoretical capacitance of RuO<sub>2</sub> reinforced by highly conductive nanoporous gold. *Advanced Energy Materials* **3**, 851-856 (2013).
- 150 Yong-gang, W. & Xiao-gang, Z. Preparation and electrochemical capacitance of RuO<sub>2</sub>/TiO<sub>2</sub> nanotubes composites. *Electrochimica Acta* **49**, 1957-1962 (2004).
- 151 Pico, F. *et al.* Understanding RuO<sub>2</sub>·xH<sub>2</sub>O/carbon nanofibre composites as supercapacitor electrodes. *Journal of Power Sources* **176**, 417-425 (2008).
- 152 Song, R. Y. *et al.* Supercapacitive properties of polyaniline/Nafion/hydrous RuO<sub>2</sub> composite electrodes. *Journal of power sources* **166**, 297-301 (2007).
- 153 Bi, R.-R. *et al.* Highly dispersed RuO<sub>2</sub> nanoparticles on carbon nanotubes: facile synthesis and enhanced supercapacitance performance. *The Journal of Physical Chemistry C* **114**, 2448-2451 (2010).
- 154 Zang, J. *et al.* Well-aligned cone-shaped nanostructure of polypyrrole/RuO<sub>2</sub> and its electrochemical supercapacitor. *The Journal of Physical Chemistry C* **112**, 14843-14847 (2008).
- 155 Chang, J.-K. *et al.* Physicochemical factors that affect the pseudocapacitance and cyclic stability of Mn oxide electrodes. *Electrochimica Acta* **54**, 3278-3284 (2009).
- 156 Wei, W., Cui, X., Chen, W. & Ivey, D. G. Manganese oxide-based materials as electrochemical supercapacitor electrodes. *Chemical society reviews* **40**, 1697-1721 (2011).
- 157 Lei, Z., Zhang, J. & Zhao, X. Ultrathin MnO<sub>2</sub> nanofibers grown on graphitic carbon spheres as high-performance asymmetric supercapacitor electrodes.

- Journal of Materials Chemistry* **22**, 153-160 (2012).
- 158 Kundu, M. & Liu, L. Direct growth of mesoporous MnO<sub>2</sub> nanosheet arrays on nickel foam current collectors for high-performance pseudocapacitors. *Journal of Power Sources* **243**, 676-681 (2013).
- 159 Tang, Y. *et al.* Synthesis of graphene oxide anchored porous manganese sulfide nanocrystals via the nanoscale Kirkendall effect for supercapacitors. *Journal of Materials Chemistry A* **3**, 12913-12919 (2015).
- 160 Chen, T. *et al.* All-solid-state high performance asymmetric supercapacitors based on novel MnS nanocrystal and activated carbon materials. *Scientific reports* **6**, 23289 (2016).
- 161 Ma, X.-J., Zhang, W.-B., Kong, L.-B., Luo, Y.-C. & Kang, L. Electrochemical performance in alkaline and neutral electrolytes of a manganese phosphate material possessing a broad potential window. *RSC Advances* **6**, 40077-40085 (2016).
- 162 Simon, P. & Gogotsi, Y. Materials for electrochemical capacitors. *Nature materials* **7**, 845 (2008).
- 163 Wang, F. *et al.* Latest advances in supercapacitors: from new electrode materials to novel device designs. *Chemical Society Reviews* **46**, 6816-6854 (2017).
- 164 Li, J. *et al.* LiMn<sub>2</sub>O<sub>4</sub>/graphene composites as cathodes with enhanced electrochemical performance for lithium-ion capacitors. *RSC Advances* **6**, 54866-54873 (2016).
- 165 Satish, R., Aravindan, V., Ling, W. C. & Madhavi, S. Carbon-coated Li<sub>3</sub>V<sub>2</sub>(PO<sub>4</sub>)<sub>3</sub> as insertion type electrode for lithium-ion hybrid electrochemical capacitors: An evaluation of anode and cathodic performance. *Journal of Power Sources* **281**, 310-317 (2015).
- 166 Kim, H.-K. *et al.* TiO<sub>2</sub>-reduced graphene oxide nanocomposites by microwave-assisted forced hydrolysis as excellent insertion anode for Li-ion battery and capacitor. *Journal of Power Sources* **327**, 171-177 (2016).
- 167 Jeżowski, P., Fic, K., Crosnier, O., Brousse, T. & Béguin, F. Lithium rhenium (VII) oxide as a novel material for graphite pre-lithiation in high performance

- lithium-ion capacitors. *Journal of Materials Chemistry A* **4**, 12609-12615 (2016).
- 168 Zhao, X., Wang, H.-E., Cao, J., Cai, W. & Sui, J. Amorphous/crystalline hybrid MoO<sub>2</sub> nanosheets for high-energy lithium-ion capacitors. *Chemical Communications* **53**, 10723-10726 (2017).
- 169 Mhamane, D. *et al.* Silica-assisted bottom-up synthesis of graphene-like high surface area carbon for highly efficient ultracapacitor and Li-ion hybrid capacitor applications. *Journal of Materials Chemistry A* **4**, 5578-5591 (2016).
- 170 Zhao, Y. *et al.* Two-dimensional biomass-derived carbon nanosheets and MnO/carbon electrodes for high-performance Li-ion capacitors. *Journal of Materials Chemistry A* **5**, 15243-15252 (2017).
- 171 Xu, X. *et al.* Sorghum core-derived carbon sheets as electrodes for a lithium-ion capacitor. *RSC Advances* **7**, 17178-17183 (2017).
- 172 Zhou, L. *et al.* Prussian blue as positive electrode material for aqueous sodium-ion capacitor with excellent performance. *RSC Advances* **6**, 109340-109345 (2016).
- 173 Chen, Y. *et al.* Organic electrode for non-aqueous potassium-ion batteries. *Nano Energy* **18**, 205-211 (2015).
- 174 Dubal, D., Fulari, V. & Lokhande, C. Effect of morphology on supercapacitive properties of chemically grown  $\beta$ -Ni(OH)<sub>2</sub> thin films. *Microporous and Mesoporous Materials* **151**, 511-516 (2012).
- 175 Pang, H. *et al.* Few-layered CoHPO<sub>4</sub>·3H<sub>2</sub>O ultrathin nanosheets for high performance of electrode materials for supercapacitors. *Nanoscale* **5**, 5752-5757 (2013).
- 176 Vangari, M., Pryor, T. & Jiang, L. Supercapacitors: review of materials and fabrication methods. *Journal of Energy Engineering* **139**, 72-79 (2012).
- 177 Jamal, M. *et al.* A non enzymatic glutamate sensor based on nickel oxide nanoparticle. *Microsystem Technologies*, 1-7 (2017).
- 178 Hu, C.-C., Chen, J.-C. & Chang, K.-H. Cathodic deposition of Ni(OH)<sub>2</sub> and Co(OH)<sub>2</sub> for asymmetric supercapacitors: importance of the electrochemical

- reversibility of redox couples. *Journal of Power Sources* **221**, 128-133 (2013).
- 179 Kong, D.-S., Wang, J.-M., Shao, H.-B., Zhang, J.-Q. & Cao, C.-n. Electrochemical fabrication of a porous nanostructured nickel hydroxide film electrode with superior pseudocapacitive performance. *Journal of Alloys and Compounds* **509**, 5611-5616 (2011).
- 180 Deng, M.-J., Huang, F.-L., Sun, I.-W., Tsai, W.-T. & Chang, J.-K. An entirely electrochemical preparation of a nano-structured cobalt oxide electrode with superior redox activity. *Nanotechnology* **20**, 175602 (2009).
- 181 Gund, G. S., Dubal, D. P., Jambure, S. B., Shinde, S. S. & Lokhande, C. D. Temperature influence on morphological progress of Ni(OH)<sub>2</sub> thin films and its subsequent effect on electrochemical supercapacitive properties. *Journal of Materials Chemistry A* **1**, 4793-4803 (2013).
- 182 Liang, K., Tang, X. & Hu, W. High-performance three-dimensional nanoporous NiO film as a supercapacitor electrode. *Journal of Materials Chemistry* **22**, 11062-11067 (2012).
- 183 Xu, J., Gao, L., Cao, J., Wang, W. & Chen, Z. Preparation and electrochemical capacitance of cobalt oxide (Co<sub>3</sub>O<sub>4</sub>) nanotubes as supercapacitor material. *Electrochimica Acta* **56**, 732-736 (2010).
- 184 Xiong, S., Yuan, C., Zhang, X., Xi, B. & Qian, Y. Controllable synthesis of mesoporous Co<sub>3</sub>O<sub>4</sub> nanostructures with tunable morphology for application in supercapacitors. *Chemistry-A European Journal* **15**, 5320-5326 (2009).
- 185 Yu, Z.-Y., Chen, L.-F. & Yu, S.-H. Growth of NiFe<sub>2</sub>O<sub>4</sub> nanoparticles on carbon cloth for high performance flexible supercapacitors. *Journal of Materials Chemistry A* **2**, 10889-10894 (2014).
- 186 Mohamed, S. G., Chen, C.-J., Chen, C. K., Hu, S.-F. & Liu, R.-S. High-performance lithium-ion battery and symmetric supercapacitors based on FeCo<sub>2</sub>O<sub>4</sub> nanoflakes electrodes. *ACS applied materials & interfaces* **6**, 22701-22708 (2014).
- 187 Lu, X. *et al.* Controllable synthesis of porous nickel–cobalt oxide nanosheets for supercapacitors. *Journal of Materials Chemistry* **22**, 13357-13364 (2012).

- 188 Li, L. *et al.* The facile synthesis of hierarchical porous flower-like NiCo<sub>2</sub>O<sub>4</sub> with superior lithium storage properties. *Journal of Materials chemistry A* **1**, 10935-10941 (2013).
- 189 Yang, F. *et al.* Ni–Co oxides nanowire arrays grown on ordered TiO<sub>2</sub> nanotubes with high performance in supercapacitors. *Journal of Materials Chemistry A* **1**, 594-601 (2013).
- 190 Zhao, Y., Hu, L., Zhao, S. & Wu, L. Preparation of MnCo<sub>2</sub>O<sub>4</sub>@Ni(OH)<sub>2</sub> core–shell flowers for asymmetric supercapacitor materials with ultrahigh specific capacitance. *Advanced Functional Materials* **26**, 4085-4093 (2016).
- 191 Kong, W., Lu, C., Zhang, W., Pu, J. & Wang, Z. Homogeneous core–shell NiCo<sub>2</sub>S<sub>4</sub> nanostructures supported on nickel foam for supercapacitors. *Journal of Materials Chemistry A* **3**, 12452-12460 (2015).
- 192 Li, J. *et al.* An electrochemical–thermal model based on dynamic responses for lithium iron phosphate battery. *Journal of Power Sources* **255**, 130-143 (2014).
- 193 Ye, Y., Shi, Y. & Tay, A. A. Electro-thermal cycle life model for lithium iron phosphate battery. *Journal of Power Sources* **217**, 509-518 (2012).
- 194 Li, X., Elshahawy, A. M., Guan, C. & Wang, J. Metal Phosphides and Phosphates-based Electrodes for Electrochemical Supercapacitors. *Small* (2017).
- 195 Bendi, R., Kumar, V., Bhavanasi, V., Parida, K. & Lee, P. S. Metal Organic Framework-Derived Metal Phosphates as Electrode Materials for Supercapacitors. *Advanced Energy Materials* **6** (2016).
- 196 Pang, H. *et al.* Cobalt pyrophosphate nano/microstructures as promising electrode materials of supercapacitor. *Journal of Solid State Electrochemistry* **17**, 1383-1391 (2013).
- 197 Zhang, Y., Zheng, M., Qu, M., Sun, M. & Pang, H. Core–shell Co<sub>11</sub>(HPO<sub>3</sub>)<sub>8</sub>(OH)<sub>6</sub>–Co<sub>3</sub>O<sub>4</sub> hybrids for high-performance flexible all-solid-state asymmetric supercapacitors. *Journal of Alloys and Compounds* **651**, 214-221 (2015).
- 198 Omar, F. S. *et al.* Ultrahigh capacitance of amorphous nickel phosphate for

- asymmetric supercapacitor applications. *RSC Advances* **6**, 76298-76306 (2016).
- 199 Li, H. *et al.* Self-assembled 3D cobalt phosphate octahydrate architecture for supercapacitor electrodes. *Materials Letters* **152**, 25-28 (2015).
- 200 Pang, H. *et al.* Facile fabrication of  $\text{NH}_4\text{CoPO}_4 \cdot \text{H}_2\text{O}$  nano/microstructures and their primarily application as electrochemical supercapacitor. *Nanoscale* **4**, 5946-5953 (2012).
- 201 Pang, H. *et al.* Nickel phosphite superstructures assembled by nanotubes: original application for effective electrode materials of supercapacitors. *ChemPlusChem* **78**, 546-553 (2013).
- 202 Liu, M.-C., Li, J.-J., Hu, Y.-X., Yang, Q.-Q. & Kang, L. Design and Fabrication of  $\text{Ni}_3\text{P}_2\text{O}_8\text{-Co}_3\text{P}_2\text{O}_8 \cdot 8\text{H}_2\text{O}$  as Advanced Positive Electrodes for Asymmetric Supercapacitors. *Electrochimica Acta* **201**, 142-150 (2016).
- 203 Zhao, Y. *et al.* Hybridized Phosphate with Ultrathin Nanoslices and Single Crystal Microplatelets for High Performance Supercapacitors. *Scientific reports* **6**, 17613 (2016).
- 204 Chen, C. *et al.* Polypyrrole-Modified  $\text{NH}_4\text{NiPO}_4 \cdot \text{H}_2\text{O}$  Nanoplate Arrays on Ni Foam for Efficient Electrode in Electrochemical Capacitors. *ACS Sustainable Chemistry & Engineering* **4**, 5578-5584 (2016).
- 205 Tang, Y. *et al.* Honeycomb-like mesoporous cobalt nickel phosphate nanospheres as novel materials for high performance supercapacitor. *Electrochimica Acta* **190**, 118-125 (2016).
- 206 Pang, H. *et al.* Cobalt phosphite microarchitectures assembled by ultralong nanoribbons and their application as effective electrochemical capacitor electrode materials. *Nanoscale* **5**, 503-507 (2012).
- 207 Theerthagiri, J. *et al.* Synthesis of hierarchical cobalt phosphate nanoflakes and their enhanced electrochemical performances for supercapacitor applications. *ChemistrySelect* **2**, 201-210 (2017).
- 208 Xi, Y. *et al.* Well-defined, nanostructured, amorphous metal phosphate as electrochemical pseudocapacitor materials with high capacitance. *Chemistry of Materials* **28**, 1355-1362 (2016).

- 209 Li, Q. *et al.* Layered  $\text{NH}_4\text{Co}_x\text{Ni}_{1-x}\text{PO}_4 \cdot \text{H}_2\text{O}$  ( $0 \leq x \leq 1$ ) nanostructures finely tuned by Co/Ni molar ratios for asymmetric supercapacitor electrodes. *Journal of Materials Science* **51**, 9946-9957 (2016).
- 210 Wang, S. *et al.*  $\text{NH}_4\text{CoPO}_4 \cdot \text{H}_2\text{O}$  microbundles consisting of one-dimensional layered microrods for high performance supercapacitors. *RSC Advances* **4**, 340-347 (2014).
- 211 Gao, Y., Zhao, J., Run, Z., Zhang, G. & Pang, H. Microporous  $\text{Ni}_{11}(\text{HPO}_3)_8(\text{OH})_6$  nanocrystals for high-performance flexible asymmetric all solid-state supercapacitors. *Dalton Transactions* **43**, 17000-17005 (2014).
- 212 Pang, H., Zhang, Y.-Z., Run, Z., Lai, W.-Y. & Huang, W. Amorphous nickel pyrophosphate microstructures for high-performance flexible solid-state electrochemical energy storage devices. *Nano Energy* **17**, 339-347 (2015).
- 213 Pramanik, M., Salunkhe, R. R., Imura, M. & Yamauchi, Y. Phosphonate-Derived Nanoporous Metal Phosphates and Their Superior Energy Storage Application. *ACS applied materials & interfaces* **8**, 9790-9797 (2016).
- 214 Zhang, J., Yang, Y., Zhang, Z., Xu, X. & Wang, X. Rapid synthesis of mesoporous  $\text{Ni}_x\text{Co}_{3-x}(\text{PO}_4)_2$  hollow shells showing enhanced electrocatalytic and supercapacitor performance. *Journal of Materials Chemistry A* **2**, 20182-20188 (2014).
- 215 Li, B. *et al.* Ultrathin Nickel–Cobalt Phosphate 2D Nanosheets for Electrochemical Energy Storage under Aqueous/Solid-State Electrolyte. *Advanced Functional Materials* **27** (2017).
- 216 Yang, J. *et al.* A flexible and high-performance all-solid-state supercapacitor device based on  $\text{Ni}_3\text{S}_2$  nanosheets coated ITO nanowire arrays on carbon fabrics. *RSC Advances* **6**, 75186-75193 (2016).
- 217 Wang, X. *et al.* A  $\text{Ni}_{1-x}\text{Zn}_x\text{S}/\text{Ni}$  foam composite electrode with multi-layers: one-step synthesis and high supercapacitor performance. *Journal of Materials Chemistry A* **4**, 12929-12939 (2016).
- 218 Chen, X., Cheng, M., Chen, D. & Wang, R. Shape-controlled synthesis of  $\text{Co}_2\text{P}$  nanostructures and their application in supercapacitors. *ACS applied materials*

- & interfaces* **8**, 3892-3900 (2016).
- 219 Lukatskaya, M. R., Dunn, B. & Gogotsi, Y. Multidimensional materials and device architectures for future hybrid energy storage. *Nature communications* **7**, 12647 (2016).
- 220 Yang, Y., Ruan, G., Xiang, C., Wang, G. & Tour, J. M. Flexible three-dimensional nanoporous metal-based energy devices. *Journal of the American Chemical Society* **136**, 6187-6190 (2014).
- 221 Wang, Y., Song, Y. & Xia, Y. Electrochemical capacitors: mechanism, materials, systems, characterization and applications. *Chemical Society Reviews* **45**, 5925-5950 (2016).
- 222 Xia, L., Yu, L., Hu, D. & Chen, G. Z. Electrolytes for electrochemical energy storage. *Materials Chemistry Frontiers* **1**, 584-618 (2017).
- 223 Rabenau, A. The role of hydrothermal synthesis in preparative chemistry. *Angewandte Chemie International Edition* **24**, 1026-1040 (1985).
- 224 Simon, P. & Gogotsi, Y. Capacitive energy storage in nanostructured carbon-electrolyte systems. *Accounts of chemical research* **46**, 1094-1103 (2012).
- 225 Liu, J. *et al.* Porous hierarchical In<sub>2</sub>O<sub>3</sub> micro-/nanostructures: preparation, formation mechanism, and their application in gas sensors for noxious volatile organic compound detection. *The Journal of Physical Chemistry C* **114**, 4887-4894 (2010).
- 226 Du, H., Jiao, L., Cao, K., Wang, Y. & Yuan, H. Polyol-mediated synthesis of mesoporous  $\alpha$ -Ni(OH)<sub>2</sub> with enhanced supercapacitance. *ACS applied materials & interfaces* **5**, 6643-6648 (2013).
- 227 Padmanathan, N. & Selladurai, S. Controlled growth of spinel NiCo<sub>2</sub>O<sub>4</sub> nanostructures on carbon cloth as a superior electrode for supercapacitors. *RSC Advances* **4**, 8341-8349 (2014).
- 228 Ren, Y. & Gao, L. From Three-Dimensional Flower-Like  $\alpha$ -Ni(OH)<sub>2</sub> Nanostructures to Hierarchical Porous NiO Nanoflowers: Microwave-Assisted Fabrication and Supercapacitor Properties. *Journal of the American Ceramic Society* **93**, 3560-3564 (2010).

- 229 Hsu, K.-H. & Chen, K.-S. Photoluminescence of ZnGa<sub>2</sub>O<sub>4</sub> phosphor prepared by a microencapsulation method. *Ceramics international* **26**, 469-473 (2000).
- 230 Tian, W. *et al.* Ni(OH)<sub>2</sub> nanosheet@ Fe<sub>2</sub>O<sub>3</sub> nanowire hybrid composite arrays for high-performance supercapacitor electrodes. *Nano energy* **2**, 754-763 (2013).
- 231 Chu, D., Masuda, Y., Ohji, T. & Kato, K. Shape-controlled growth of In(OH)<sub>3</sub>/In<sub>2</sub>O<sub>3</sub> nanostructures by electrodeposition. *Langmuir* **26**, 14814-14820 (2010).
- 232 Wang, C., Chen, D., Jiao, X. & Chen, C. Lotus-root-like In<sub>2</sub>O<sub>3</sub> nanostructures: fabrication, characterization, and photoluminescence properties. *The Journal of Physical Chemistry C* **111**, 13398-13403 (2007).
- 233 Kim, H.-J. *et al.* Enhanced ethanol sensing characteristics of In<sub>2</sub>O<sub>3</sub>-decorated NiO hollow nanostructures via modulation of hole accumulation layers. *ACS applied materials & interfaces* **6**, 18197-18204 (2014).
- 234 Sun, X. *et al.* Nanocasting synthesis of In<sub>2</sub>O<sub>3</sub> with appropriate mesostructured ordering and enhanced gas-sensing property. *ACS applied materials & interfaces* **6**, 401-409 (2013).
- 235 Cao, C.-Y., Guo, W., Cui, Z.-M., Song, W.-G. & Cai, W. Microwave-assisted gas/liquid interfacial synthesis of flowerlike NiO hollow nanosphere precursors and their application as supercapacitor electrodes. *Journal of Materials Chemistry* **21**, 3204-3209 (2011).
- 236 Lin, F. *et al.* Origin of electrochromism in high-performing nanocomposite nickel oxide. *ACS applied materials & interfaces* **5**, 3643-3649 (2013).
- 237 Dong, C., Li, Q., Chen, G., Xiao, X. & Wang, Y. Enhanced formaldehyde sensing performance of 3D hierarchical porous structure Pt-functionalized NiO via a facile solution combustion synthesis. *Sensors and Actuators B: Chemical* **220**, 171-179 (2015).
- 238 Zhao, B. *et al.* Synthesis of flower-like NiO and effects of morphology on its catalytic properties. *The Journal of Physical Chemistry C* **113**, 14440-14447 (2009).
- 239 Tseng, W. J., Tseng, T. T., Wu, H. M., Her, Y. C. & Yang, T. J. Facile synthesis

- of monodispersed In<sub>2</sub>O<sub>3</sub> hollow spheres and application in photocatalysis and gas sensing. *Journal of the American Ceramic Society* **96**, 719-725 (2013).
- 240 Meng, X., Tang, L. & Li, J. Room-temperature ferromagnetism in Co-doped In<sub>2</sub>O<sub>3</sub> nanocrystals. *The Journal of Physical Chemistry C* **114**, 17569-17573 (2010).
- 241 Mu, J. *et al.* Enhancement of the visible-light photocatalytic activity of In<sub>2</sub>O<sub>3</sub>-TiO<sub>2</sub> nanofiber heteroarchitectures. *ACS applied materials & interfaces* **4**, 424-430 (2011).
- 242 Kostecki, R. & McLarnon, F. Electrochemical and in situ raman spectroscopic characterization of nickel hydroxide electrodes I. pure nickel hydroxide. *Journal of The Electrochemical Society* **144**, 485-493 (1997).
- 243 Chapman, A. & Thirlwell, L. Spectra of phosphorus compounds—I the infra-red spectra of orthophosphates. *Spectrochimica Acta* **20**, 937-947 (1964).
- 244 Bontchev, R. P., Iliev, M. N., Dezaneti, L. M. & Jacobson, A. J. Two new open framework cobalt phosphates: NaCo<sub>3</sub>(OH)(PO<sub>4</sub>)<sub>2.1</sub>·4H<sub>2</sub>O and Na(NH<sub>4</sub>)Co<sub>2</sub>(PO<sub>4</sub>)<sub>2</sub>·H<sub>2</sub>O. *Solid state sciences* **3**, 133-142 (2001).
- 245 Baril, M., Assaaoudi, H. & Butler, I. S. Pressure-tuning Raman microspectroscopic study of cobalt (II), manganese (II), zinc (II) and magnesium (II) pyrophosphate dihydrates. *Journal of molecular structure* **751**, 168-171 (2005).
- 246 Tuschel, D. Raman Spectroscopy and Imaging of Low Energy Phonons. (2015).
- 247 Preston, C. M. & Adams, W. A laser Raman spectroscopic study of aqueous orthophosphate salts. *Journal of Physical Chemistry* **83**, 814-821 (1979).
- 248 Tomimatsu, Y., Kint, S. & Scherer, J. R. Resonance Raman spectra of iron (III)-, copper (II)-, cobalt (III)-, and manganese (III)-transferrins and of bis (2, 4, 6-trichlorophenolato) diimidazolecopper (II) monohydrate, a possible model for copper (II) binding to transferrins. *Biochemistry* **15**, 4918-4924 (1976).
- 249 Liu, D., Jing, L., Luan, P., Tang, J. & Fu, H. Enhancement effects of cobalt phosphate modification on activity for photoelectrochemical water oxidation of TiO<sub>2</sub> and mechanism insights. *ACS applied materials & interfaces* **5**, 4046-4052

- (2013).
- 250 Liu, Q., Ding, D., Ning, C. & Wang, X. Cobalt-phosphate/Ni-doped TiO<sub>2</sub> nanotubes composite photoanodes for solar water oxidation. *Materials Science and Engineering: B* **202**, 54-60 (2015).
- 251 Zhao, S., Li, C., Huang, H., Liu, Y. & Kang, Z. Carbon nanodots modified cobalt phosphate as efficient electrocatalyst for water oxidation. *Journal of Materiomics* **1**, 236-244 (2015).
- 252 Ge, L., Han, C., Xiao, X. & Guo, L. In situ synthesis of cobalt-phosphate (Co-Pi) modified C<sub>3</sub>N<sub>4</sub> photocatalysts with enhanced photocatalytic activities. *Applied Catalysis B: Environmental* **142**, 414-422 (2013).
- 253 Carriazo, D. *et al.* Phosphate-Functionalized Carbon Monoliths from Deep Eutectic Solvents and their Use as Monolithic Electrodes in Supercapacitors. *ChemSusChem* **5**, 1405-1409 (2012).
- 254 Shih, P., Yung, S. & Chin, T. Thermal and corrosion behavior of P<sub>2</sub>O<sub>5</sub>-Na<sub>2</sub>O-CuO glasses. *Journal of Non-Crystalline Solids* **224**, 143-152 (1998).
- 255 Barr, T. L. Recent advances in x-ray photoelectron spectroscopy studies of oxides. *Journal of Vacuum Science & Technology A: Vacuum, Surfaces, and Films* **9**, 1793-1805 (1991).
- 256 Chai, J. *et al.* Thermal behaviour of ultra-thin Co overlayers on rutile TiO<sub>2</sub> (100) surface. *Surface science* **589**, 32-41 (2005).
- 257 Zhao, Z.-G. *et al.* In-situ formation of cobalt-phosphate oxygen-evolving complex-anchored reduced graphene oxide nanosheets for oxygen reduction reaction. *Scientific reports* **3** (2013).
- 258 Zsoldos, Z. & Guczi, L. Structure and catalytic activity of alumina supported platinum-cobalt bimetallic catalysts. 3. Effect of treatment on the interface layer. *The Journal of Physical Chemistry* **96**, 9393-9400 (1992).
- 259 Kullyakool, S., Danvirutai, C., Siriwong, K. & Noisong, P. Determination of kinetic triplet of the synthesized Ni<sub>3</sub>(PO<sub>4</sub>)<sub>2</sub>·8H<sub>2</sub>O by non-isothermal and isothermal kinetic methods. *Journal of Thermal Analysis and Calorimetry* **115**, 1497-1507 (2014).

- 260 Breitingner, D. *et al.* Combined vibrational spectra of natural wardite. *Journal of molecular structure* **706**, 95-99 (2004).
- 261 Viswanathan, K., Nayar, V. & Aruldas, G. Infrared and Raman spectra of three tetrametaphosphates  $M_2P_4O_{12}$  (M= Fe, Ni, Zn). *Journal of Chemical Sciences* **95**, 463-469 (1985).
- 262 Yu, M. *et al.* Scalable self-growth of Ni@ NiO core-shell electrode with ultrahigh capacitance and super-long cyclic stability for supercapacitors. *NPG Asia Materials* **6**, e129 (2014).
- 263 Senthilkumar, V. *et al.* NiO nanoarrays of a few atoms thickness on 3D nickel network for enhanced pseudocapacitive electrode applications. *Journal of Power Sources* **303**, 363-371 (2016).
- 264 Sathiya, M. *et al.*  $Li_4NiTeO_6$  as a positive electrode for Li-ion batteries. *Chemical Communications* **49**, 11376-11378 (2013).
- 265 Mansour, A. Characterization of NiO by XPS. *Surface Science Spectra* **3**, 231-238 (1994).
- 266 Venezia, A., Bertocello, R. & Deganello, G. X-ray photoelectron spectroscopy investigation of pumice-supported nickel catalysts. *Surface and interface analysis* **23**, 239-247 (1995).
- 267 Lorenz, P. *et al.* ESCA investigations of some NiO/SiO<sub>2</sub> and NiO-Al<sub>2</sub>O<sub>3</sub>/SiO<sub>2</sub> catalysts. *Journal of Electron Spectroscopy and Related Phenomena* **16**, 267-276 (1979).
- 268 Khawaja, E. *et al.* XPS, auger, electrical and optical studies of vanadium phosphate glasses doped with nickel oxide. *Journal of non-crystalline solids* **110**, 33-43 (1989).
- 269 Lo, P. H., Tsai, W. T., Lee, J. T. & Hung, M. P. The Electrochemical Behavior of Electroless Plated Ni-P Alloys in Concentrated NaOH Solution. *Journal of the Electrochemical Society* **142**, 91-96 (1995).
- 270 Barbaux, Y. *et al.* Bulk and surface analysis of a Fe-PO oxydehydrogenation catalyst. *Applied Catalysis A: General* **90**, 51-60 (1992).
- 271 Demri, B. & Muster, D. XPS study of some calcium compounds. *Journal of*

- materials processing technology* **55**, 311-314 (1995).
- 272 Kasztelan, S. *et al.* Preparation of Co-Mo- $\gamma$ -Al<sub>2</sub>O<sub>3</sub> and Ni-Mo- $\gamma$ -Al<sub>2</sub>O<sub>3</sub> catalysts by pH regulation of molybdenum solution. characterization of supported species and hydrogenation activities. *Applied Catalysis* **7**, 91-112 (1983).
- 273 Strydom, C. & Strydom, H. X-ray photoelectron spectroscopy studies of some cobalt (II) nitrate complexes. *Inorganica Chimica Acta* **159**, 191-195 (1989).
- 274 Rao, C., Sarma, D., Vasudevan, S. & Hegde, M. in *Proceedings of the Royal Society of London A: Mathematical, Physical and Engineering Sciences*. 239-252 (The Royal Society).
- 275 Prasad, K. R., Koga, K. & Miura, N. Electrochemical deposition of nanostructured indium oxide: high-performance electrode material for redox supercapacitors. *Chemistry of materials* **16**, 1845-1847 (2004).
- 276 Chen, P.-C., Shen, G., Sukcharoenchoke, S. & Zhou, C. Flexible and transparent supercapacitor based on In<sub>2</sub>O<sub>3</sub> nanowire/carbon nanotube heterogeneous films. *Applied Physics Letters* **94**, 043113 (2009).
- 277 Chang, J., Lee, W., Mane, R. S., Cho, B. W. & Han, S.-H. Morphology-dependent electrochemical supercapacitor properties of indium oxide. *Electrochemical and Solid-State Letters* **11**, A9-A11 (2008).
- 278 Nachman, M., Cojocar, L. & Ribco, L. Electrical Properties of Non-Stoichiometric Nickel Oxide. *physica status solidi (b)* **8**, 773-783 (1965).
- 279 Eror, N. & Wagner, J. Electrical conductivity of single crystalline nickel oxide. *physica status solidi (b)* **35**, 641-651 (1969).
- 280 Kim, I.-H., Kim, J.-H. & Kim, K.-B. Electrochemical characterization of electrochemically prepared ruthenium oxide/carbon nanotube electrode for supercapacitor application. *Electrochemical and Solid-State Letters* **8**, A369-A372 (2005).
- 281 Nagarajan, N. & Zhitomirsky, I. Cathodic electrosynthesis of iron oxide films for electrochemical supercapacitors. *Journal of applied electrochemistry* **36**, 1399-1405 (2006).
- 282 Pu, Z. *et al.* Fabrication of Ni(OH)<sub>2</sub> coated ZnO array for high-rate

- pseudocapacitive energy storage. *Electrochimica Acta* **109**, 252-255 (2013).
- 283 Xing, Z. *et al.* Ni<sub>3</sub>S<sub>2</sub> coated ZnO array for high-performance supercapacitors. *Journal of Power Sources* **245**, 463-467 (2014).
- 284 Wang, J., Wang, S., Huang, Z. & Yu, Y. High-performance NiCo<sub>2</sub>O<sub>4</sub>@Ni<sub>3</sub>S<sub>2</sub> core/shell mesoporous nanothorn arrays on Ni foam for supercapacitors. *Journal of Materials Chemistry A* **2**, 17595-17601 (2014).
- 285 Huang, M. *et al.* Hierarchical ZnO@ MnO<sub>2</sub> core-shell pillar arrays on Ni foam for binder-free supercapacitor electrodes. *Electrochimica Acta* **152**, 172-177 (2015).
- 286 Dan, Y. *et al.* Porous quasi three-dimensional nano-Mn<sub>3</sub>O<sub>4</sub>+ PbO<sub>2</sub> composite as supercapacitor electrode material. *Electrochimica Acta* **83**, 175-182 (2012).
- 287 Zhang, Y. X., Li, F. & Huang, M. One-step hydrothermal synthesis of hierarchical MnO<sub>2</sub>-coated CuO flower-like nanostructures with enhanced electrochemical properties for supercapacitor. *Materials Letters* **112**, 203-206 (2013).
- 288 Yuan, C. *et al.* Anodic deposition and capacitive property of nano-WO<sub>3</sub>·H<sub>2</sub>O/MnO<sub>2</sub> composite as supercapacitor electrode material. *Materials Letters* **148**, 167-170 (2015).
- 289 Cai, D. *et al.* High-performance supercapacitor electrode based on the unique ZnO@Co<sub>3</sub>O<sub>4</sub> core/shell heterostructures on nickel foam. *ACS applied materials & interfaces* **6**, 15905-15912 (2014).
- 290 Ramadoss, A. & Kim, S. J. Enhanced supercapacitor performance using hierarchical TiO<sub>2</sub> nanorod/Co(OH)<sub>2</sub> nanowall array electrodes. *Electrochimica Acta* **136**, 105-111 (2014).
- 291 Wang, J. *et al.* Ni<sub>3</sub>S<sub>2</sub>@ MoS<sub>2</sub> core/shell nanorod arrays on Ni foam for high-performance electrochemical energy storage. *Nano Energy* **7**, 151-160 (2014).
- 292 Krishnamoorthy, K., Veerasubramani, G. K., Radhakrishnan, S. & Kim, S. J. One pot hydrothermal growth of hierarchical nanostructured Ni<sub>3</sub>S<sub>2</sub> on Ni foam for supercapacitor application. *Chemical Engineering Journal* **251**, 116-122 (2014).

- 293 Yin, J. & Park, J. Y. Electrochemical investigation of copper/nickel oxide composites for supercapacitor applications. *International Journal of Hydrogen Energy* **39**, 16562-16568 (2014).
- 294 Li, G.-R., Wang, Z.-L., Zheng, F.-L., Ou, Y.-N. & Tong, Y.-X. ZnO@ MoO<sub>3</sub> core/shell nanocables: facile electrochemical synthesis and enhanced supercapacitor performances. *Journal of Materials Chemistry* **21**, 4217-4221 (2011).
- 295 Li, J. *et al.* Coprecipitation fabrication and electrochemical performances of coral-like mesoporous NiO nanobars. *Journal of Materials Chemistry A* **2**, 4690-4697 (2014).
- 296 Li, S. *et al.* Three-dimensional MnO<sub>2</sub> nanowire/ZnO nanorod arrays hybrid nanostructure for high-performance and flexible supercapacitor electrode. *Journal of Power Sources* **256**, 206-211 (2014).
- 297 Zhang, B. *et al.* Platinum@ regular indium oxide nanooctahedra as difunctional counter electrodes for dye-sensitized solar cells. *Journal of Materials Chemistry A* **2**, 6331-6336 (2014).
- 298 Yue, L. *et al.* One-step solvothermal process of In<sub>2</sub>O<sub>3</sub>/C nanosheet composite with double phases as high-performance lithium-ion battery anode. *Electrochimica Acta* **160**, 123-130 (2015).
- 299 Zhi, M., Xiang, C., Li, J., Li, M. & Wu, N. Nanostructured carbon–metal oxide composite electrodes for supercapacitors: a review. *Nanoscale* **5**, 72-88 (2013).
- 300 Bajdich, M., García-Mota, M., Vojvodic, A., Nørskov, J. K. & Bell, A. T. Theoretical investigation of the activity of cobalt oxides for the electrochemical oxidation of water. *Journal of the American chemical Society* **135**, 13521-13530 (2013).
- 301 Wu, G., Li, N., Zhou, D.-R., Mitsuo, K. & Xu, B.-Q. Anodically electrodeposited Co+ Ni mixed oxide electrode: preparation and electrocatalytic activity for oxygen evolution in alkaline media. *Journal of Solid State Chemistry* **177**, 3682-3692 (2004).
- 302 Zhao, J. *et al.* Hydrothermal Synthesis of Nickel Phosphate Nanorods for High-

- Performance Flexible Asymmetric All-Solid-State Supercapacitors. *Particle & Particle Systems Characterization* **32**, 880-885 (2015).
- 303 Dai, Y.-H. *et al.* Facile fabrication of manganese phosphate nanosheets for supercapacitor applications. *Ionics* **22**, 1461-1469 (2016).
- 304 Hassaninejad-Darzi, S. K. & Gholami-Esfidvajani, M. Preparation of nanoporous nickel phosphate VSB-5 nanorods carbon paste electrode as glucose non-enzymatic sensor. *Journal of Porous Materials* **24**, 85-95 (2017).
- 305 Ho, J., Tremiliosi Filho, G., Simpraga, R. & Conway, B. Structure influence on electrocatalysis and adsorption of intermediates in the anodic O<sub>2</sub> evolution at dimorphic  $\alpha$ - and  $\beta$ -PbO<sub>2</sub>. *Journal of Electroanalytical Chemistry* **366**, 147-162 (1994).
- 306 Kissinger, P. & Heineman, W. R. *Laboratory Techniques in Electroanalytical Chemistry, revised and expanded.* (CRC press, 1996).
- 307 Kim, H. *et al.* Coordination tuning of cobalt phosphates towards efficient water oxidation catalyst. *Nature communications* **6**, 8253-8253 (2015).
- 308 Deshpande, P. P. & Sazou, D. *Corrosion protection of metals by intrinsically conducting polymers.* (CRC Press, Marcel Dekker, New York, 2016).
- 309 Zanello, P. *Inorganic electrochemistry: theory, practice and application.* (Royal Society of Chemistry, 2007).
- 310 Akinwolemiwa, B., Peng, C. & Chen, G. Z. Redox electrolytes in supercapacitors. *Journal of The Electrochemical Society* **162**, A5054-A5059 (2015).
- 311 Chen, Z. *et al.* Construction of a novel hierarchical structured NH<sub>4</sub>-Co-Ni phosphate toward an ultrastable aqueous hybrid capacitor. *Nanoscale* **8**, 6636-6645 (2016).
- 312 Zhao, Y. *et al.* Hybridized Phosphate with Ultrathin Nanoslices and Single Crystal Microplatelets for High Performance Supercapacitors. *Scientific reports* **6** (2016).
- 313 Raju, K. & Ozoemena, K. I. Hierarchical one-dimensional ammonium nickel phosphate microrods for high-performance pseudocapacitors. *Scientific reports*

- 5, 17629 (2015).
- 314 Yang, J. *et al.* Electroactive edge site-enriched nickel–cobalt sulfide into graphene frameworks for high-performance asymmetric supercapacitors. *Energy & Environmental Science* **9**, 1299-1307 (2016).
- 315 Zhao, J. *et al.* Mesoporous uniform ammonium nickel phosphate hydrate nanostructures as high performance electrode materials for supercapacitors. *CrystEngComm* **15**, 5950-5955 (2013).
- 316 Senthilkumar, B., Sankar, K. V., Vasylechko, L., Lee, Y.-S. & Selvan, R. K. Synthesis and electrochemical performances of maricite-NaMPO<sub>4</sub> (M= Ni, Co, Mn) electrodes for hybrid supercapacitors. *RSC Advances* **4**, 53192-53200 (2014).
- 317 Madhu, R. *et al.* Honeycomb-like porous carbon–cobalt oxide nanocomposite for high-performance enzymeless glucose sensor and supercapacitor applications. *ACS applied materials & interfaces* **7**, 15812-15820 (2015).
- 318 Kumar, R., Singh, R. K., Dubey, P. K., Singh, D. P. & Yadav, R. M. Self-Assembled hierarchical formation of conjugated 3D cobalt oxide nanobead–CNT–graphene nanostructure using microwaves for high-performance supercapacitor electrode. *ACS applied materials & interfaces* **7**, 15042-15051 (2015).
- 319 Lai, H. *et al.* Mesostructured NiO/Ni composites for high-performance electrochemical energy storage. *Energy & Environmental Science* **9**, 2053-2060 (2016).
- 320 Singh, A. K., Sarkar, D., Karmakar, K., Mandal, K. & Khan, G. G. High-Performance Supercapacitor Electrode Based on Cobalt Oxide–Manganese Dioxide–Nickel Oxide Ternary 1D Hybrid Nanotubes. *ACS applied materials & interfaces* **8**, 20786-20792 (2016).
- 321 Salunkhe, R. R. *et al.* Asymmetric supercapacitors using 3D nanoporous carbon and cobalt oxide electrodes synthesized from a single metal–organic framework. *ACS nano* **9**, 6288-6296 (2015).
- 322 Rakhi, R., Chen, W., Hedhili, M. N., Cha, D. & Alshareef, H. N. Enhanced rate

- performance of mesoporous Co<sub>3</sub>O<sub>4</sub> nanosheet supercapacitor electrodes by hydrous RuO<sub>2</sub> nanoparticle decoration. *ACS applied materials & interfaces* **6**, 4196-4206 (2014).
- 323 Dam, D. T. & Lee, J.-M. Three-dimensional cobalt oxide microstructures with brush-like morphology via surfactant-dependent assembly. *ACS applied materials & interfaces* **6**, 20729-20737 (2014).
- 324 Ganesh, V., Pitchumani, S. & Lakshminarayanan, V. New symmetric and asymmetric supercapacitors based on high surface area porous nickel and activated carbon. *Journal of Power Sources* **158**, 1523-1532 (2006).
- 325 Jagadale, A., Kumbhar, V., Dhawale, D. & Lokhande, C. Potentiodynamically deposited nickel oxide (NiO) nanoflakes for pseudocapacitors. *Journal of Electroanalytical Chemistry* **704**, 90-95 (2013).
- 326 Patil, U. *et al.* Enhanced symmetric supercapacitive performance of Co(OH)<sub>2</sub> nanorods decorated conducting porous graphene foam electrodes. *Electrochimica Acta* **129**, 334-342 (2014).
- 327 Gourdin, G., Zheng, D., Smith, P. H. & Qu, D. In situ electrochemical-mass spectroscopic investigation of solid electrolyte interphase formation on the surface of a carbon electrode. *Electrochimica Acta* **112**, 735-746 (2013).
- 328 Wang, Y., Guo, X., Greenbaum, S., Liu, J. & Amine, K. Solid electrolyte interphase formation on lithium-ion electrodes: a <sup>7</sup>Li nuclear magnetic resonance study. *Electrochemical and Solid-State Letters* **4**, A68-A70 (2001).
- 329 Lee, J. H., Shin, W. H., Lim, S. Y., Kim, B. G. & Choi, J. W. Modified graphite and graphene electrodes for high-performance lithium ion hybrid capacitors. *Materials for Renewable and Sustainable Energy* **3**, 22 (2014).
- 330 Bichat, M., Raymundo-Piñero, E. & Béguin, F. High voltage supercapacitor built with seaweed carbons in neutral aqueous electrolyte. *Carbon* **48**, 4351-4361 (2010).
- 331 Demarconnay, L., Raymundo-Pinero, E. & Béguin, F. A symmetric carbon/carbon supercapacitor operating at 1.6 V by using a neutral aqueous solution. *Electrochemistry Communications* **12**, 1275-1278 (2010).

- 332 Jagadale, A., Kumbhar, V., Dhawale, D. & Lokhande, C. Performance evaluation of symmetric supercapacitor based on cobalt hydroxide  $\text{Co}(\text{OH})_2$  thin film electrodes. *Electrochimica Acta* **98**, 32-38 (2013).
- 333 Liu, M.-C., Li, J.-J., Hu, Y.-X., Yang, Q.-Q. & Kang, L. Design and Fabrication of  $\text{Ni}_3\text{P}_2\text{O}_8\text{-Co}_3\text{P}_2\text{O}_8\cdot 8\text{H}_2\text{O}$  as Advanced Positive Electrodes for Asymmetric Supercapacitors. *Electrochimica Acta* **201**, 142-150 (2016).
- 334 Mirghni, A. A. *et al.* Hydrothermal synthesis of manganese phosphate/graphene foam composite for electrochemical supercapacitor applications. *Journal of Colloid and Interface Science* **494**, 325-337 (2017).
- 335 Hu, Y.-M. *et al.* One-pot hydrothermal synthesis of porous nickel cobalt phosphides with high conductivity for advanced energy conversion and storage. *Electrochimica Acta* **215**, 114-125 (2016).
- 336 Wang, D. *et al.* Amorphous Ni-P materials for high performance pseudocapacitors. *Journal of Power Sources* **274**, 1107-1113 (2015).
- 337 Omar, N. *et al.* Lithium iron phosphate based battery—assessment of the aging parameters and development of cycle life model. *Applied Energy* **113**, 1575-1585 (2014).
- 338 Leng, X. *et al.* A novel open architecture built by ultra-fine single-crystal  $\text{Co}_2(\text{CO}_3)(\text{OH})_2$  nanowires and reduced graphene oxide for asymmetric supercapacitors. *Journal of Materials Chemistry A* **4**, 17171-17179 (2016).
- 339 Mallela, V. S., Ilankumaran, V. & Rao, N. S. Trends in cardiac pacemaker batteries. *Indian pacing and electrophysiology journal* **4**, 201 (2004).
- 340 Lindemark, B. in *Telecommunications Energy Conference, 1991. INTELEC'91., 13th International*. 196-201 (IEEE).
- 341 Lang, X., Hirata, A., Fujita, T. & Chen, M. Nanoporous metal/oxide hybrid electrodes for electrochemical supercapacitors. *Nature nanotechnology* **6**, 232 (2011).
- 342 Weng, G.-M., Tam, L.-Y. S. & Lu, Y.-C. High-performance  $\text{LiTi}_2(\text{PO}_4)_3$  anodes for high-areal-capacity flexible aqueous lithium-ion batteries. *Journal of Materials Chemistry A* **5**, 11764-11771 (2017).